Spin Physics of Novel Chiral Electron Gases

Spinphysik in neuartigen chiralen Elektronengasen

Der Naturwissenschaftlichen Fakultät
Der Friedrich-Alexander-Universität
Erlangen-Nürnberg

zur

Erlangung des Doktorgrades Dr. rer. nat.

vorgelegt von Nicolas Klier aus Erlangen Als Dissertation genehmigt von der Naturwissenschaftlichen Fakultät der Friedrich-Alexander-Universität Erlangen-Nürnberg

Tag der mündlichen Prüfung: 30.01.2018

Vorsitzender des Promotionsorgans: Prof. Dr. Georg Kreimer

Gutachter: Prof. Dr. Oleg Pankratov

Prof. Dr. Florian Marquardt

Abstract

Using analytical band structure models we study in this thesis the spin physics in few layer graphenes and on the surface of topological insulators of the SnTe class. A common feature of both systems is that they host chiral low energy excitations that are described by a Dirac-Weyl-type equation and can be probed via the indirect exchange interaction. In order to derive the indirect exchange interaction we deploy a Green's function approach. We find that the interaction between two magnetic impurities, which are intercalated in AB-stacked bilayer graphene, changes its period discontinuously as the Fermi level passes through the edge of the bonding-antibonding band gap and is significantly enhanced for higher Fermi energies. This is associated with a transition of the impurity spin coupling from oscillatory to antiferromagnetic at small impurity separations. A similar effect can be also achieved by increasing the temperature or by applying an interlayer bias voltage. To study the spin texture and the indirect exchange interaction in the crystalline topological insulator of the SnTe class we use an analytical model which explicitly links the electron spectrum to the microscopic parameters of the bulk, i.e. the crystal field and the spin orbit interaction. In this model, we derive the topological states on the (111) surface and find that the in-plane spin texture is always tangential to a conic section curve which can be in its form controlled by the band bending at the surface. While the interaction in a spin unpolarized host such as the few layer graphenes is either purely ferro- or antiferromagnetic, the crystalline topological insulator of the SnTe class enables with its spin-polarized surface states a much richer RKKY interaction. The indirect exchange interaction consists of a Heisenberg-type, a Dzyaloshinskii-Moriyatype and a XY-type term. We show that the weight of the different terms depends on the impurity separation, the Fermi energy and in the ternary alloy $Pb_{1-x}Sn_xTe$ the weight can be also controlled by varying the Pb content.

Contents

1	\mathbf{Intr}	roduction	1
	1.1	The RKKY Interaction in Bilayer Graphene	2
	1.2	Topological Insulators	
	1.3	Outline of the Thesis	6
2	The	e Indirect Exchange Interaction	8
	2.1	The Indirect Exchange Interaction at Zero Temperature	8
		2.1.1 Spin-unpolarized Electron Gas	13
		2.1.2 Lowest-Order Approximation	15
	2.2	The Indirect Exchange Interaction at Finite Temperature	15
		2.2.1 Spin-unpolarized Electron Gas	17
		2.2.2 Lowest-Order Approximation	18
	2.3	Other Coupling Schemes	18
		2.3.1 The Coherent Coupling Scheme	19
		2.3.2 The Incoherent Coupling Scheme	19
3	The	RKKY Interaction in Monolayer Graphene	21
	3.1	Monolayer Graphene	22
		3.1.1 The Zero Temperature Green's function	23
		3.1.2 The Finite Temperature Green's Function	24
	3.2	The RKKY Interaction in Monolayer Graphene at Zero Temperature $$.	25
		3.2.1 Undoped Monolayer Graphene	26
		3.2.2 Doped Monolayer Graphene	27
	3.3	The RKKY Interaction in Monolayer Graphene at Finite Temperature	28
		3.3.1 Asymptotic Expansion	29
		3.3.2 Zero Temperature Limit	31
	3.4	The RKKY Interaction between Plaquette Impurities	32
4	The	e RKKY Interaction in Bilayer Graphene	36
	4.1	AA-stacked Bilayer Graphene	37
		4.1.1 The RKKY Interaction at Zero Temperature	38
	4.2	AB-stacked Bilayer Graphene	41

CONTENTS

		4.2.1 The RKKY Interaction at Zero Temperature	42
		4.2.2 The RKKY Interaction at Finite Temperature	53
		4.2.3 The RKKY Interaction between Intercalated Impurities	55
	4.3	Biased AB-stacked Bilayer Graphene	62
		4.3.1 The RKKY Interaction at Finite Temperature	64
		4.3.2 The RKKY Interaction between Intercalated Impurities	66
5	The	e Bulk Band Structure of a IV-VI Semiconductor	71
	5.1	Tight Binding Approach for the Parent Phase	72
	5.2	Formation of the Semiconductor: Dielectrization of the Parent Phase $$.	74
	5.3	The Band Structure at the L Point	74
	5.4	The $\mathbf{k}.\mathbf{p}$ Hamiltonian	78
	5.5	The Band Structure in Vicinity of the L Point	81
6	The	e Topological Surface States of a Topological Insulator of the SnTe	
	Clas	SS	83
	6.1	The Topological Surface States	84
	6.2	The Spin Texture	89
7	The	RKKY Interaction on the Surface of a Topological Insulator of	
	the	SnTe Class	94
	7.1	The Interaction Energy	94
	7.2	The RKKY Interaction on the Pristine Surface	97
	7.3	The RKKY Interaction on the Doped Surface	98
8	Con	nclusions 1	.02
A	ppe	ndix 1	.09
\mathbf{A}			00
	The	e Indirect Exchange Interaction 1	.09
		e Indirect Exchange Interaction 1 The Spin Product $(\mathbf{S}_i.\boldsymbol{\sigma})(\mathbf{S}_{i_1}.\boldsymbol{\sigma})\cdots(\mathbf{S}_{i_m}.\boldsymbol{\sigma})$. 09 109
	A.1	The Spin Product $(\mathbf{S}_i.\boldsymbol{\sigma})$ $(\mathbf{S}_{i_1}.\boldsymbol{\sigma})\cdots(\mathbf{S}_{i_m}.\boldsymbol{\sigma})$	109 . 12
	A.1	The Spin Product $(\mathbf{S}_i.\boldsymbol{\sigma})$ $(\mathbf{S}_{i_1}.\boldsymbol{\sigma}) \cdots (\mathbf{S}_{i_m}.\boldsymbol{\sigma})$	109 1 12
	A.1 Bes	The Spin Product $(\mathbf{S}_i.\boldsymbol{\sigma})$ $(\mathbf{S}_{i_1}.\boldsymbol{\sigma})\cdots(\mathbf{S}_{i_m}.\boldsymbol{\sigma})$	109 1 12
	A.1 Bes B.1	The Spin Product $(\mathbf{S}_i.\boldsymbol{\sigma})$ $(\mathbf{S}_{i_1}.\boldsymbol{\sigma}) \cdots (\mathbf{S}_{i_m}.\boldsymbol{\sigma})$	109 1 12 112

CONTENTS

	B.5	Integrals of Bessel functions
\mathbf{C}	The	RKKY Interaction in Bilayer Graphene 119
	C.1	The Green's Function of AA-stacked Bilayer Graphene
	C.2	The Green's Function of AB-stacked Bilayer Graphene
	C.3	The Green's Function of Biased AB-stacked Bilayer Graphene 121
	C.4	The DOS of Biased AB-stacked Bilayer Graphene
	C.5	The RKKY Interaction in Biased AB-stacked Bilayer Graphene
		at Zero Temperature
D	The	Topological Surface States of a Topological Insulator of the SnTe
	Clas	126
	D.1	The Spin Operator in the Basis of the Bulk Band Edge States 126
	D.2	The Absolute Value of the Spin
\mathbf{B}	iblic	graphy 129

CHAPTER 1

Introduction

In the last decade there have emerged two broad classes of condensed matter systems that feature electron gases for which chirality is a good low energy quantum number. In the first case we have low dimensional materials such as graphene and its derivatives, for which the low energy physics is described by a Dirac-Weyl-type electron fluid, but for which the physical spin, due to the very weak spin-orbit coupling, does not play a prominent role. Nevertheless, the novel underlying electronic structure leads to a rich and interesting physics of spin impurities, driven by the unusual form of the static spin susceptibility [1, 2, 3, 4, 5, 6, 7]. In another new class of two and three dimensional materials that are known as topological insulators the Dirac-Weyl states occur at the surface. For these materials, which are insulating in the bulk but metallic on the surface, spin plays a crucial role. They can be characterized by a coupling that exists between the crystal momentum and the spin direction of the quasiparticles known as the spin texture. Henceforth in both new groups of materials one expects a rich and fundamentally new spin physics which is potentially useful for technological applications, e.g. in spintronics.

Graphene, a honeycomb lattice of carbon, was for a long period of time considered as a convenient theoretical model which was helpful for understanding existing carbon allotropes, for example carbon nanotubes. This model was considered especially interesting due to its remarkable analogy to quantum electrodynamics [8, 9, 10, 11] (QED), but was not expected to be realized in nature. The latter scepticism was driven both by theory, namely by a theorem stating that two-dimensional materials are thermodynamically unstable [12, 13], and by the widespread experimental finding that thin metal films crumple on an insulation substrate [14]. The more surprising was its experimental discovery by a simple exfoliation technique in 2004 [15]. This and subsequent experiments confirmed many of the remarkable physical properties expected on the basis of the low energy QED analogy and uncovered many remarkable mechanical and chemical properties [16, 17, 18, 19, 20] of this genuine two-dimensional solid.

The low energy electronic structure of graphene features two inequivalent conical band intersections situated at the K and K' high symmetry points of the hexagonal Brillouin zone [8, 9, 15]. Quasiparticles on these low energy manifolds are described by an effective Dirac-Weyl equation, the same equation that governs massless neutrinos but with the speed of light c replaced by the Fermi velocity of graphene $v_F \approx c/300$. Similar to neutrinos these quasiparticles are endowed with a pseudospin degree of freedom and with a new good quantum number, the chirality, that takes on the values

+1 for positive energy, and -1 for negative energies. From this emergent low energy physics many of the remarkable properties of graphene can immediately be deduced. In particular, chirality leads to a suppression of back scattering and, as a consequence, to very high electron mobilities with near ballistic transport as observed in graphene nanoribbons [15, 21, 22]. The presence of positive as well as negative energy branches, implied by the Dirac-Weyl Hamiltonian, fundamentally alters transition and reflexion of quasiparticles on potential barriers: for certain directions of incidence electrons can tunnel through arbitrarily high barriers with unity probability. This, of course, is just a condensed matter physics realization of the famous Klein paradox which is well known in QED [23, 24]. In a magnetic field, the Landau spectrum of graphene shows a $E_n \propto \pm \sqrt{n}$ quantization sequence with the proportionality constant involving v_F , and hence much larger than the ordinary quantization scale involving the cyclotron mass. As a consequence, the quantum Hall effect (QHE) can be observed in graphene at room temperatures [21, 22], in contrast to the common QHE in semiconductor heterostructures which require temperatures below 70 K [25, 26]. Some of these effects are expected to play an important role in future technological applications: today the first graphene-based field effect transistors are in operation and could represent, after optimization for industrial use, an alternative to the common Si devices [27, 28, 29].

The RKKY Interaction in Bilayer Graphene

The indirect exchange interaction between magnetic moments through a non-magnetic host (known in the leading order as the RKKY interaction) was first studied by Ruderman and Kittel in the context of the coupling of nuclear spins in silver, and was successfully used to explain the broad spin resonance line in this metal [30]. Kasuya and Yosida further generalized the theory to the case of impurity spins in a nonmagnetic host, as occurs for instance in the classic example of CuMn alloys [31, 32]. Later the research in this field included impurities in two-dimensional electron gases, e.g. the surface state of Cu(111), where also the Friedel oscillations of the electron density were directly observed with scanning tunnelling microscopy (STM) [33, 34]. With the experimental discovery of graphene, the attention of theorists was drawn to the question of how the RKKY interaction would manifest in this novel Dirac-Weyl election gas. Two key differences from the case of the two-dimensional Schrödinger electron gas were noted: (i) at the Dirac point one has an unusual envelope decay $1/R^3$ [1, 3, 4, 5, 6, 7, 35] as opposed to the expected $1/R^2$ [36, 37, 38, 39] with R the impurity separation and (ii) the multivalley low energy spectrum leads to an intervalley component of the RKKY which is fast oscillating on the scale of the lattice constant, and which is also responsible for a sensitivity of the RKKY to the local impurity environment [1, 2, 3, 4, 5, 6, 35]. A number of subsequent publications have addressed further generalizations of the RKKY problem in graphene: the RKKY in spin-polarized graphene [40], the effect of disorder [41, 42], strain [43], and different impurity types [2, 3, 5, 6]. One of the most natural generalizations which has been missing is the one from a single-layer to few layer graphenes.

Multilayer graphenes are of interest for two reasons. Firstly, the multilayer situation

offers the possibility of an intercalated impurity geometry. Since the ionic radius of a typical magnetic impurity is comparable to the interlayer separation one expects a strong impurity-bilayer coupling, a situation not realized for physisorbed surface impurities. Secondly, it is known that the low energy spectrum depends sensitively on the stacking order in few layer graphene systems. This should be reflected in the spin susceptibility and hence in a rich RKKY physics associated with few layer graphenes. Investigating the RKKY in few layer graphene forms the first part of this thesis.

The simplest structural generalization of the multilayered structures is a bilayer which, due to the weak van-der-Waals bonding of the layers, can be realized in a number of different stacking arrangements [8, 44, 45, 46]. The lowest energy stacking configuration is the so called Bernal stacking in which the two layers are arranged in the same AB fashion as found in graphite [Fig. (4.3)]. The band structure at low energies is characterized by a parabolic dispersion and at (lower) higher energies by (bonding) antibonding bands, also with parabolic dispersion, that are separated by an energy of $\approx 0.8 \text{eV}$ [47, 48]. Furthermore, both theory and experiment report the opening of a band gap at the Dirac point by an out-of-plane electric field [49, 50, 51]. At zero doping and zero electric field the RKKY interaction is described by an algebraic $1/R^n$ decay where the power n depends sensitively on the sublattice position of both impurities [52], reflecting the more complex structure of the wave function in the bilayer material. For two impurities on the A(B) sublattice a $1/R^6(1/R^2)$ decay is found, while impurities on different sublattices are described by an intermediate $1/R^4$ envelope. For finite doping the interaction has been addressed via a downfolded two-band Hamiltonian that projects the full bilayer wave function onto a subspace involving only the B sublattices [53, 54]. The resulting two-band model, however, cannot treat the complex sublattice dependence of the RKKY interaction in bilayer graphene.

All these previous works focused on the interaction between impurities that couple to a single lattice site. However, as we have mentioned above, from the physical point of view it is much more realistic to consider an intercalated impurity geometry which involves multiple sites. In the first part of this thesis we investigate such intercalated impurities for two different physical situations: (i) the RKKY interaction in undoped material in the presence of a layer perpendicular electric field, and (ii) a highly doped bilayer at zero field. The latter case is particularly interesting as a change of the Fermi surface topology occurs when the Fermi energy crosses the antibonding band edge E_q . For $E_F < E_q$ one has a single Fermi circle, while for $E_F > E_q$ a double Fermi circle and, as we show in Chapter 4, this change in topology is associated with a discontinuous change of the RKKY period. For energies arbitrarily close to E_q , but still less than E_q , the interaction oscillates with the wave vector of the low energy band, giving an oscillation period $\lambda \to 15a$ as E_F approaches E_q from below (a is the graphene lattice constant). However, once E_F is equal or greater than E_g the oscillation is governed entirely by the Fermi vector of the antibonding band, giving an osculation period $\lambda \to \infty$ as E_F approaches E_g from above. In short, as the Fermi energy crosses the antibonding gap edge the low energy manifold is "switched off" and the high energy manifold "switched on". This physics is seen

only for the intercalated impurity. This rapidly changing zero temperature RKKY is also manifest as an unusual temperature dependence of the RKKY interaction. At finite temperatures, for the Fermi energy close but still below the antibonding band edge, a low temperature oscillatory interaction goes over to a high temperature antiferromagnetic interaction. Needless to say, this is in sharp contrast to the usual behaviour of the RKKY interaction in which the same qualitative form is seen at all temperatures.

The second case we consider, also in Chapter 4, is the RKKY interaction close the Dirac point but in the presence of a layer symmetry breaking applied electric field. We find that RKKY interaction has three distinct band structure regimes: (i) a damped ferromagnetic interaction in the gap, (ii) an antiferromagnetic interaction "on the brim of the Mexican hat" E_0 , and (iii) an oscillatory interaction for energies greater than E_0 . This energy sensitivity is manifest in different ways depending on whether the physical situation fixes the Fermi energy or the particle number. For example, bilayer graphene epilayers grown on SiC have a chemical potential fixed by the substrate [55, 56], and this leads to an evolution from an oscillatory to an antiferromagnetic interaction as a function of the applied field – an effect that occurs as the Fermi energy is driven towards the "brim of the Mexican hat" as the gap opens in an applied field.

Topological Insulators

The second class of materials which feature chiral low energy excitations are topological insulators. In contrast to other solids topological insulators reveal their peculiar properties at their surfaces. These materials feature metallic surface states that are topologically protected. As in the case of graphene these states are described by a Dirac-Weyl equation close to the conical intersection point. However, in contrast to graphene there is no longer an obvious relation between the pseudospin degree of freedom and the atomic structure of the unit cell.

The protection of the surface state is guaranteed either by the time reversal symmetry T (the Z_2 topological insulators [57, 58, 59]) or by the point group symmetry of the crystal (the crystalline topological insulators [60, 61, 62, 63, 64]). In the former case the topological protection holds for *any* crystal face while for crystalline topological insulators the surface states are protected only on facets that feature the necessary point symmetry operation.

Characteristic of all topological insulators is the fact that momentum and spin of the quasiparticles are, in contrast to common materials, no longer independent but strictly coupled: the momentum direction unequivocally determines the spin direction. Such spin-momentum locking can be described by a vector field of spin directions in the momentum plane, known as the spin texture. This texture can be measured in angle-resolved photoemission spectroscopy (ARPES) experiments. Data exists, for example, for two of the most popular representatives of the strong topological insulators, the chalcogenides Bi_2Se_3 and Bi_2Te_3 [65, 66, 67, 68, 69]. Both materials possess T-protected surface states at the Γ point of the surface Brillouin zone, with only the former system featuring a distinct Dirac-Weyl cone (for Bi_2Te_3 a heavily

distorted cone is observed). The spin textures are very different: while spin and momentum in Bi₂Se₃ are, due to strong spin-orbit interaction, locked at right angles [66, 68, 70], the spin texture of the warped Dirac cone in Bi₂Te₃ is, according to Refs. [67, 71, 72], much more complex and has an out-of-plane component.

These examples highlight the non-universal spin structure of the topological surface state. This raises the question of how the bulk parameters – e.g. the spin-orbit interaction and crystal field in the bulk as well as the band-bending at the surface – determine the properties of the topological surface state and its spin texture. Understanding this relation requires a clear route from the microscopic physics of the bulk insulator (characterized by the corresponding quantum numbers, e.g. spin, angular momentum, parity, etc.) to the emergent effective pseudospin degrees of freedom of the topological Dirac-Weyl (DW) surface state. In this thesis, we analytically follow this route on example of IV-VI semiconductors.

The IV-VI semiconductor family adopt a simple rock salt crystal structure and, perhaps uniquely amongst the topological insulators, offers the possibility to trace the route from microscopic to emergent variables. The basic concept behind this route is, in fact, not new and dates back to the 1980s. At that time the L point band structure of the IV-VI semiconductors was derived analytically using the symmetry of the L point which includes the mirror symmetry and the threefold rotational symmetry around the (111) axis [73, 74]. In these works it was figured out that some materials such as SnTe have an inverted band gap while others such as PbTe have a conventional band ordering. When two materials with opposite band ordering are put together forming a band inversion contact, which can be realized e.g. by variation of the Pb content in the ternary compound $Pb_xSn_{1-x}Te$, linear dispersing interface states emerge [75, 76, 77, 78]. A similar situation occurs at the surface of SnTe, i.e. at the contact of the inverted band structure with vacuum, where the same effect, the mirror symmetry about the (110) plane, guarantees topological states on the (100), (110) and (111) surface [63, 64, 79, 80, 81, 82, 83]. This surface is particularly interesting and, as we will see in this work, it is analytically tractable: the (111) surface has in its hexagonal surface Brillouin zone two different types of Dirac points. The Dirac cone at the M-point has a slight anisotropy and is shifted in energy by 170meVrelative to the apex of the Dirac cone at the Γ point [79]. In recent works these topological surface states were treated phenomenologically in a generic Dirac-Weyl model which was not related to the bulk band structure. The link between the pseudospin degree of freedom of the Dirac-Weyl equation and the quantum numbers of the bulk thus could not be uncovered. In Refs. [81, 82], for example, it was assumed that the basis wave functions were pure spin up or spin down states which is certainly not true for SnTe [73, 74].

To fully reveal the nature of the Dirac-Weyl surface states we treat in this work the spin texture and the RKKY interaction using a microscopic model based on the proper description of the bulk electron spectrum. In Chapter 5 we discuss the bulk electronic structure of the IV-VI semiconductors. These materials feature a low energy spectrum that is described by an effective Dirac equation [73, 74, 84]. In Chapter 6 we "take the bulk Hamiltonian to the surface", using an appropriate boundary condition. The

latter involves the band inversion [75] and is now known as a "topological boundary conditio" [75, 81]. We find the topological surface state and express its wave function in terms of the fundamental edge states of the bulk insulator. Importantly, as the bulk Dirac equation is derived from the tight-binding model, the pseudospin degrees of freedom are not introduced ad hoc, but emerge from the low energy spectrum of the band edge states of the bulk insulator.

From this fully microscopic yet analytical approach two interesting observations follow. Firstly, there are two distinct mechanisms that act to entangle spin in the surface state: (i) spin-orbit induced spin mixing within the bulk wave functions and, (ii), an intrinsic topological spin entanglement arising from the superposition of bulk band edge states that comprise the topological surface state. Secondly, we find that the microscopically derived surface state wave function may possess, for the same crystal facet, a highly non-universal richness of spin structures. We find not only a helical spin texture – the "standard result" – but also hyperbolic and linear spin textures. Which of these is realized depends on the microscopic physics of the material: namely on the balance of spin-orbit and crystal field effects in the bulk, and on the band bending at the crystal-vacuum boundary.

Finally, in Chapter 7 we return to the RKKY interaction in the context of the IV-VI semiconductor surface state. While the RKKY interaction in TIs has been considered in the past on the basis of phenomenological Dirac-Weyl models [85, 86, 87], as well as with ab initio calculations for magnetic impurities in some specific materials [88], our focus is instead to investigate analytically the connection between the bulk physics and the topological surface state, viewing the RKKY interaction as a probe of this connection. To that end we consider the RKKY interaction on the (111) surface of the IV-VI semiconductors and investigate the effect that the bulk spin-orbit and crystal field interactions have on this interaction. We find that the qualitative form of the RKKY interaction is profoundly impacted by the balance of the spin-orbit and the crystal field. The relative weight of the various terms in the RKKY interaction, namely the XY-type, the Ising-type and the Dzyaloshinskii-Moriya-type is determined by the ratio of the spin-orbit and the crystal field parameters, the same factors that govern the spin texture of the topological surface state.

Outline of the Thesis

The thesis is structured as follows: first, in Chapter 2, we provide a short introduction to the indirect exchange interaction in a non-interacting electron gas and present an analytical derivation of the interaction energy at zero and at finite temperature. In the following two chapters we use these results in a study of the RKKY interaction in graphene monolayer and AA- and AB-stacked graphene bilayer. For all three cases we present a systematic analysis of the RKKY interaction as a function of the Fermi energy, impurity separation, temperature and for different electron impurity coupling schemes. The first part of the thesis ends with a discussion of the RKKY interaction in the biased AB-stacked bilayer graphene. In the second part of the thesis we address the low energy physics on the (111) surface of IV-VI semiconductor topological insulators.

CHAPTER 1. INTRODUCTION

Our presentation begins with a discussion of an analytical model that describes the bulk band structure close to the high symmetry L points (Chapter 5). Based on this model we derive the topological surface states and their spin texture. In the last chapter, we calculate the RKKY interaction mediated by these topological surface states.

The Indirect Exchange Interaction

This chapter gives a short introduction to the indirect exchange interaction. We begin with the standard electron gas model and derive the interaction energy at zero and at finite temperature using quantum field theory techniques. In this way we can express the interaction energy in terms of Green's functions, a strategy which leads in the lowest order to the well-known Green's function expression for the Ruderman-Kittel-Kasuya-Yosida (RKKY) interaction. We conclude the chapter with considering the RKKY interaction in other, non-standard coupling schemes, which are necessary to discuss the interaction in a realistic solid.

The Indirect Exchange Interaction at Zero Temperature

We consider N magnetic impurities embedded in a gas of non-interacting electrons. Each impurity spin is treated as a classical object that couples via a contact interaction to the electron spin density. The resulting spin polarization is felt by the neighboring impurities and in this way there arises a coupling between impurity spins that is known in literature as the indirect exchange interaction. The Hamiltonian of the interacting many-body system may be written as $H = H^0 + W$ where H^0 is taken for the Hamiltonian of the non-interacting system and the perturbation W is described by a contact interaction between the impurity spin \mathbf{S}_i and the itinerant electron spin density \mathbf{s}_i

$$W = -\lambda \sum_{i=1}^{N} \mathbf{S}_{i}.\mathbf{s}_{i}$$
 (2.1.1)

In a second quantization representation the single-particle operator for electron spin density is given by $\mathbf{s}_i = \hbar/2 \sum_{\mu,\nu} c^{\dagger}_{i\mu} \boldsymbol{\sigma}_{\mu\nu} c_{i\nu}$ where $c^{\dagger}_{i\mu}$ generates an electron at site $i \in \{1, \dots, N\}$ with spin $\mu \in \{\uparrow, \downarrow\}$ and $\boldsymbol{\sigma}$ is the vector of Pauli matrices. Here, our intention is to calculate the interaction energy that can be written as the expectation value of the Heisenberg operator $W_H(t) = \exp(iHt/\hbar)W\exp(-iHt/\hbar)$ in the ground state of the interacting many-body system $|\Psi_0\rangle$

$$E_{\text{int}} = \frac{\langle \Psi_0 \mid W_H(t) \mid \Psi_0 \rangle}{\langle \Psi_0 \mid \Psi_0 \rangle}$$
 (2.1.2)

For an analytical evaluation of the matrix element in the numerator it is convenient to use the interaction picture where Eq. (2.1.2) takes the form

$$E_{\text{int}} = \sum_{m=0}^{\infty} \frac{1}{m!} \left(-\frac{i}{\hbar} \right)^m \int_{-\infty}^{\infty} dt_1 \cdots \int_{-\infty}^{\infty} dt_m$$

$$\times \langle \Phi_0 \mid T \left[W_I(t_1) \cdots W_I(t_m) W_I(t) \right] \mid \Phi_0 \rangle_c \tag{2.1.3}$$

with $W_I(t) = \exp(iH^0t/\hbar)W\exp(-iH^0t/\hbar)$ and the ground state of the non-interacting system $|\Phi_0\rangle$. In the ground state of the non-interacting system all single-particle energy levels up to the Fermi energy ϵ_F are occupied. After inserting the perturbation in its second quantization representation $W_I(t) = -\hbar\lambda/2\sum_{\mu,\nu} (\boldsymbol{\sigma}_{\mu\nu}.\mathbf{S}_i) c_{i\mu}^{\dagger}(t^+)c_{i\nu}(t)$ we obtain the following expression

$$E_{\text{int}} = -\frac{\hbar\lambda}{2} \sum_{m=0}^{\infty} \frac{1}{m!} \left(\frac{i\lambda}{2}\right)^m \sum_{i,i_1,\dots,i_m} \sum_{\mu,\mu_1,\dots,\mu_m} \sum_{\nu,\nu_1,\dots,\nu_m} \sum_{\nu,\nu_1,\dots,\nu_m} \left(\mathbf{S}_{i}.\boldsymbol{\sigma}_{\mu\nu}\right) \left(\mathbf{S}_{i_1}.\boldsymbol{\sigma}_{\mu_1\nu_1}\right) \cdots \left(\mathbf{S}_{i_m}.\boldsymbol{\sigma}_{\mu_m\nu_m}\right) \int_{-\infty}^{\infty} dt_1 \cdots \int_{-\infty}^{\infty} dt_m \left(\mathbf{T}_{i_1\mu_1}^{\dagger}(t_1^+)c_{i_1\nu_1}(t_1) \cdots c_{i_m\mu_m}^{\dagger}(t_m^+)c_{i_m\nu_m}(t_m)c_{i\mu}^{\dagger}(t^+)c_{i\nu}(t)\right] |\Phi_0\rangle_c \quad (2.1.4)$$

where the time ordering operator T sorts the field operators from the left to the right in descending time order:

$$T[c_{i\mu}^{\dagger}(t)c_{j\nu}(t')] = \begin{cases} c_{i\mu}^{\dagger}(t)c_{j\nu}(t') & t > t' \\ -c_{j\nu}(t')c_{i\mu}^{\dagger}(t) & t' > t \end{cases}$$
(2.1.5)

In order to conserve the proper order of creation and annihilation operators within each $W_I(t)$ the creation operator $c_{i\mu}^{\dagger}(t^+) = \exp(iH^0t^+/\hbar)c_{i\mu}\exp(-iH^0t^+/\hbar)$ is evaluated at the time t^+ , a time that is infinitesimally later than t. At this point it is convenient to introduce another product, the normal ordered product, that places all annihilation operators to the left and all creation operators to the right:

$$N[c_{i\mu}^{\dagger}(t)c_{j\nu}(t')] = -c_{j\nu}(t')c_{i\mu}^{\dagger}(t) \tag{2.1.6}$$

The factor -1 comes, in Eq. (2.1.6) and in the second line of Eq. (2.1.5), from the interchange of the two fermion operators. The difference between the time ordered and the normal ordered product of two field operators is in literature well known as a contraction:

$$c_{i\mu}^{\dagger}(t)^{\bullet}c_{j\nu}(t')^{\bullet} = T[c_{i\mu}^{\dagger}(t)c_{j\nu}(t')] - N[c_{i\mu}^{\dagger}(t)c_{j\nu}(t')]$$
 (2.1.7)

This contraction defines the time ordered Green's function of the non-interacting electron gas:

$$G_{\mu\nu}^{0}(\mathbf{r}_{i}, t, \mathbf{r}_{j}, t') = -ic_{i\mu}(t)^{\bullet}c_{j\nu}^{\dagger}(t')^{\bullet}$$

$$= -i\frac{\langle \Phi_{0} \mid T[c_{i\mu}(t)c_{j\nu}^{\dagger}(t')] \mid \Phi_{0} \rangle}{\langle \Phi_{0} \mid \Phi_{0} \rangle}$$
(2.1.8)

Here we also want to define the retarded and the advanced Green's function that are easier to access and have, as will be seen later, a simpler analytical structure

$$G_{\mu\nu}^{0R}(\mathbf{r}_i, t, \mathbf{r}_j, t') = -i \frac{\langle \Phi_0 \mid \{c_{i\mu}(t), c_{j\nu}^{\dagger}(t')\} \mid \Phi_0 \rangle}{\langle \Phi_0 \mid \Phi_0 \rangle} \Theta(t - t')$$
 (2.1.9)

$$G_{\mu\nu}^{0A}(\mathbf{r}_i, t, \mathbf{r}_j, t') = i \frac{\langle \Phi_0 \mid \{c_{i\mu}(t), c_{j\nu}^{\dagger}(t')\} \mid \Phi_0 \rangle}{\langle \Phi_0 \mid \Phi_0 \rangle} \Theta(t' - t)$$
 (2.1.10)

where the braces $\{\ ,\ \}$ stand for the anti-commutator. Since the Hamiltonian H^0 has a translational invariance and no explicit time dependence all propagators are a function of the difference t'-t and $\mathbf{r}_i-\mathbf{r}_i$, only.

With these definitions in mind we go back to Eq. (2.1.4) and replace, for each order m, the expectation value according to Wick's theorem by the sum over all contractions. Each contraction is a product of time ordered single particle Green's functions and can

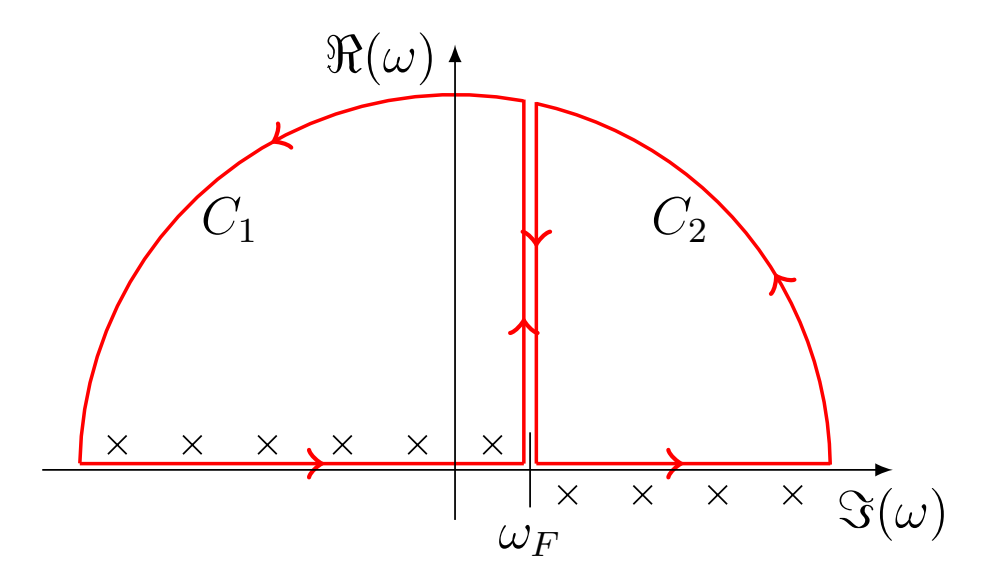


Figure 2.1: The integration contour for the function $f(\omega) = \exp(i\omega\eta) \ G^0(\mathbf{k},\omega)G^0(\mathbf{k}_1,\omega)\cdots G^0(\mathbf{k}_m,\omega)$ in the complex plane. The contour integral over the product of time ordered Green's functions in the upper half plane can be split into two sub-contours with $\Re(\omega) < \omega_F$ and $\Re(\omega) > \omega_F$ over the product of retarded and advanced Green's functions, respectively. The singularities of the retarded and advanced Green's functions are indicated in the respective energy range by black crosses.

be illustrated by a Feynman diagram with an on-site spin-flip at each space-time vertex (\mathbf{r}_i, t) and the propagation between two neighboring vertices described by a single particle Green's function. Note that the original expectation value, Eq. (2.1.2), may be written as a product of two factors: the first factor is the sum of all connected diagrams and the second factor is the sum of all disconnected diagrams. As indicated by the subscript c the contribution of all disconnected diagrams has been, in Eq. (2.1.3), cancelled with the normalization $\langle \Psi_0 | \Psi_0 \rangle$. For this reason we have to include only those diagrams that connect the space-time vertices $\{(\mathbf{r}_i, t), (\mathbf{r}_{i_1}, t_1), \cdots (\mathbf{r}_{i_m}, t_m)\}$ on a closed loop. This is achieved by summing over all permutations P of the indices $\{1, \dots, m\}$:

$$E_{\text{int}} = -i\hbar \sum_{m=0}^{\infty} \frac{1}{m!} \left(\frac{\lambda}{2}\right)^{m+1} \sum_{P} \sum_{i,i_{1},\dots,i_{m}} \sum_{\mu,\mu_{1},\dots,\mu_{m}} \sum_{\nu,\nu_{1},\dots,\nu_{m}} \sum_$$

By exchanging indices (such as $\mu_1 \leftrightarrow \mu_2$, $\nu_1 \leftrightarrow \nu_2$ and $i_1 \leftrightarrow i_2$) it can be seen easily that all permutations equally contribute to the interaction energy. Hence the factor 1/m! cancels with the total number of permutations. Then we perform the sum over the spin indices μ, μ_1, \dots, μ_m and ν, ν_1, \dots, ν_m and obtain a trace over the product of σ .S matrices and Green's functions.

$$E_{\text{int}} = -i\hbar \sum_{m=0}^{\infty} \left(\frac{\lambda}{2}\right)^{m+1} \sum_{i,i_1,\dots,i_m} \int_{-\infty}^{\infty} dt_1 \dots \int_{-\infty}^{\infty} dt_m$$

$$\times \text{Tr}\left[(\mathbf{S}_i \cdot \boldsymbol{\sigma}) \, \mathbf{G}^0(\mathbf{r}_i, t, \mathbf{r}_{i_1}, t_1^+) \, (\mathbf{S}_{i_1} \cdot \boldsymbol{\sigma}) \, G^0(\mathbf{r}_{i_1}, t_1, \mathbf{r}_{i_2}, t_2^+) \dots \right]$$

$$\times (\mathbf{S}_{i_m} \cdot \boldsymbol{\sigma}) \, G^0(\mathbf{r}_{i_m}, t_m, \mathbf{r}_i, t^+) \right]$$
(2.1.12)

After replacing each Green's function by its Fourier transform the energy takes the form

$$E_{\text{int}} = -\frac{i\hbar}{2\pi} \lim_{\eta \to 0} \sum_{m=0}^{\infty} \left(\frac{\lambda}{2N_0}\right)^{m+1} \sum_{i,i_1,\dots,i_m} \sum_{\mathbf{k},\mathbf{k}_1,\dots,\mathbf{k}_m}$$

$$\times e^{-i\mathbf{k}.(\mathbf{r}_{i_1}-\mathbf{r}_i)} e^{-i\mathbf{k}_1.(\mathbf{r}_{i_2}-\mathbf{r}_{i_1})} \cdots e^{-i\mathbf{k}_m.(\mathbf{r}_{i_m}-\mathbf{r}_i)} I(\mathbf{k},\mathbf{k}_1,\dots,\mathbf{k}_m)$$
(2.1.13)

with the number of unit cells N_0 and $I(\mathbf{k}, \mathbf{k}_1, \dots, \mathbf{k}_m)$ given by

$$I = \int_{-\infty}^{\infty} d\omega \ e^{i\omega\eta} \ \text{Tr} \left[(\mathbf{S}_{i}.\boldsymbol{\sigma}) \ G^{0}(\mathbf{k},\omega) \ (\mathbf{S}_{i_{1}}.\boldsymbol{\sigma}) \ G^{0}(\mathbf{k}_{1},\omega) \cdots (\mathbf{S}_{i_{m}}.\boldsymbol{\sigma}) \ G^{0}(\mathbf{k}_{m},\omega) \right]$$
(2.1.14)

The integration in Eq. (2.1.14) can be performed along a contour in the complex ω plane [Fig. (2.1)]. The convergence factor $\exp(i\omega\eta)$ indicates, with $\eta = t^+ - t > 0$,
that the contour must be closed in the upper half plane. In Fig. (2.1) the contour
in the upper half plane is drawn as a sum of the two sub-contours C_1 and C_2 with $\Re\omega < \omega_F$ and $\Re\omega > \omega_F$, respectively. Each of these sub-contours consists of three
sections: an integral over the real axis, an integral parallel to the imaginary axis and
an integral over the arc. Within these sub-contours the time ordered Green's function
is either given by the the retarded or by the advanced Green's function. The relation
between the three different Green's functions can be understood from the Lehmann
representation of their Fourier transforms

$$G_{\mu\nu}^{0}(\mathbf{k},\omega) = \hbar N_{0} \sum_{n} \left[\delta_{\mathbf{k},\mathbf{P}_{n}/\hbar} \frac{\langle \Psi_{0} \mid c_{0\mu}(0) \mid \Psi_{n} \rangle \langle \Psi_{n} \mid c_{0\nu}^{\dagger}(0) \mid \Psi_{0} \rangle}{\hbar \omega - (E_{n} - E_{0}) + i\eta} \right]$$

$$+ \delta_{\mathbf{k},-\mathbf{P}_{n}/\hbar} \frac{\langle \Psi_{0} \mid c_{0\nu}^{\dagger}(0) \mid \Psi_{n} \rangle \langle \Psi_{n} \mid c_{0\mu}(0) \mid \Psi_{0} \rangle}{\hbar \omega - (E_{n} - E_{0}) - i\eta} \right]$$

$$G_{\mu\nu}^{0R,A}(\mathbf{k},\omega) = \hbar N_{0} \sum_{n} \left[\delta_{\mathbf{k},\mathbf{P}_{n}/\hbar} \frac{\langle \Psi_{0} \mid c_{0\mu}(0) \mid \Psi_{n} \rangle \langle \Psi_{n} \mid c_{0\nu}^{\dagger}(0) \mid \Psi_{0} \rangle}{\hbar \omega - (E_{n} - E_{0}) \pm i\eta} \right]$$

$$+ \delta_{\mathbf{k},-\mathbf{P}_{n}/\hbar} \frac{\langle \Psi_{0} \mid c_{0\nu}^{\dagger}(0) \mid \Psi_{n} \rangle \langle \Psi_{n} \mid c_{0\mu}(0) \mid \Psi_{0} \rangle}{\hbar \omega - (E_{n} - E_{0}) \pm i\eta}$$

$$(2.1.16)$$

with the plus sign in Eq. (2.1.16) taken for the retarded and the minus sign for the advanced Green's function. In the expressions above, the wave functions $|\Psi_n\rangle$ form a complete set of common eigenstates to the Hamiltonian H and the momentum operator \mathbf{P} . The corresponding eigenvalues are given by E_n and \mathbf{P}_n with $n \in \mathbb{N}_0$, respectively. From Eq. (2.1.16) it can be seen that the Lehmann representation of the retarded and the advanced Green's function differ in the sign of the small imaginary part in the denominator. This is the reason why the retarded Green's function $G_{\mu\nu}^{0R}(\mathbf{k},\omega)$ has its poles in the lower half plane while the advanced Green's function $G_{\mu\nu}^{0R}(\mathbf{k},\omega)$ has its poles in the upper half plane. On the real axis the small, vanishing imaginary part requires that both Green's functions are adjoint operators: $G_{\mu\nu}^{0R}(\mathbf{k},\omega) = G_{\nu\mu}^{0A}(\mathbf{k},\omega)^*$. Another important consequence of the small imaginary part is that the time ordered Green's function corresponds, depending on the energy, either to the retarded or to the advanced Green's function

$$G_{\mu\nu}^{0}(\mathbf{k},\omega) = \begin{cases} G_{\mu\nu}^{0R}(\mathbf{k},\omega) & \omega > \omega_{F} \\ G_{\mu\nu}^{0A}(\mathbf{k},\omega) & \omega < \omega_{F} \end{cases} \quad \forall \omega \in \mathbb{R}$$
 (2.1.17)

In the complex plane, away from the real axis, the small imaginary part plays no role and all three Green's functions are equivalent

$$G_{\mu\nu}^{0}(\mathbf{k},\omega) = G_{\mu\nu}^{0R}(\mathbf{k},\omega) = G_{\mu\nu}^{0A}(\mathbf{k},\omega) \qquad \forall \Im(\omega) > 0$$
 (2.1.18)

From the analytic structure of the momentum space Green's function it can be seen easily that $I(\mathbf{k}, \mathbf{k}_1, \dots, \mathbf{k}_m)$ can be written for $\Re \omega < \omega_F$ as an integral over advanced Green's functions and for $\Re \omega > \omega_F$ as an integral over retarded Green's functions.

$$I = \int_{-\infty}^{\omega_F} d\omega \ e^{i\omega\eta} \ \text{Tr} \left[(\mathbf{S}_i.\boldsymbol{\sigma}) G^{0A}(\mathbf{k},\omega) (\mathbf{S}_{i_1}.\boldsymbol{\sigma}) G^{0A}(\mathbf{k}_1,\omega) \cdots (\mathbf{S}_{i_m}.\boldsymbol{\sigma}) G^{0A}(\mathbf{k}_m,\omega) \right]$$
$$+ \int_{\omega_F}^{\infty} d\omega \ e^{i\omega\eta} \ \text{Tr} \left[(\mathbf{S}_i.\boldsymbol{\sigma}) G^{0R}(\mathbf{k},\omega) (\mathbf{S}_{i_1}.\boldsymbol{\sigma}) G^{0R}(\mathbf{k}_1,\omega) \cdots (\mathbf{S}_{i_m}.\boldsymbol{\sigma}) G^{0R}(\mathbf{k}_m,\omega) \right]$$
(2.1.19)

Since the singularities of the retarded Green's function are in the lower half plane the integral over the upper half plane is zero.

$$\int_{-\infty}^{\infty} d\omega \ e^{i\omega\eta} \ \text{Tr} \left[(\mathbf{S}_{i}.\boldsymbol{\sigma}) \ G^{0R}(\mathbf{k},\omega) \left(\mathbf{S}_{i_{1}}.\boldsymbol{\sigma} \right) G^{0R}(\mathbf{k}_{1},\omega) \cdots \left(\mathbf{S}_{i_{m}}.\boldsymbol{\sigma} \right) G^{0R}(\mathbf{k}_{m},\omega) \right] = 0 \quad (2.1.20)$$

This identity allows us to change the range of integration in the second line of Eq. (2.1.19). The two integrals parallel to the imaginary axis cancel each other and due to the convergence factor $\exp(i\omega\eta)$ the integral over the arc vanishes. As a consequence the contour integral may be turned into an integral over the real axis where the retarded and advanced Green's functions are pairwise adjoint operators.

$$I = \int_{-\infty}^{\omega_F} d\omega \left(\text{Tr} \left[(\mathbf{S}_i \cdot \boldsymbol{\sigma}) G^{0R}(\mathbf{k}_m, \omega) (\mathbf{S}_{i_m} \cdot \boldsymbol{\sigma}) \cdots G^{0R}(\mathbf{k}_1, \omega) (\mathbf{S}_{i_1} \cdot \boldsymbol{\sigma}) G^{0R}(\mathbf{k}, \omega) \right]^* - \text{Tr} \left[(\mathbf{S}_i \cdot \boldsymbol{\sigma}) G^{0R}(\mathbf{k}, \omega) (\mathbf{S}_{i_1} \cdot \boldsymbol{\sigma}) G^{0R}(\mathbf{k}_1, \omega) \cdots (\mathbf{S}_{i_m} \cdot \boldsymbol{\sigma}) G^{0R}(\mathbf{k}_m, \omega) \right] \right)$$
(2.1.21)

Then we transform each Green's function back to real space and use the symmetry $G^{0R}(\mathbf{r}_i, \mathbf{r}_j, \omega) = G^{0R}(\mathbf{r}_j, \mathbf{r}_i, \omega)$ in order to bring the integrand to the form of two complex conjugate terms. In this way Eq. (2.1.13) reduces to the form

$$E_{\text{int}} = -\frac{\hbar}{\pi} \sum_{m=0}^{\infty} \left(\frac{\lambda}{2}\right)^{m+1} \sum_{i,i_1,\dots,i_m} \int_{-\infty}^{\omega_F} d\omega \,\,\Im\left(\text{Tr}\left[\left(\mathbf{S}_i.\boldsymbol{\sigma}\right)G^{0R}(\mathbf{r}_i,\mathbf{r}_{i_1},\omega)\right.\right.\right) \\ \times \left(\mathbf{S}_{i_1}.\boldsymbol{\sigma}\right)G^{0R}(\mathbf{r}_{i_1},\mathbf{r}_{i_2},\omega)\cdots\left(\mathbf{S}_{i_m}.\boldsymbol{\sigma}\right)G^{0R}(\mathbf{r}_{i_m},\mathbf{r}_{i},\omega)\right]\right)$$
(2.1.22)

It is important to stress that the trace must be generally taken over the product of σ . S_i matrices and Green's functions $G^{0R}(\mathbf{r}_{i_i}, \mathbf{r}_{i_j}, \omega)$. Only under certain circumstances, which are for example given in the spin-unpolarized electron gas, it is possible to reduce the complexity of that expression.

Spin-unpolarized Electron Gas

There are plenty of examples in nature where it is reasonable to assume that the interaction is mediated by a gas of spin unpolarized electrons. In this case the Green's function is diagonal in spin space and may be written as $G^{0R}_{\mu\nu}(\mathbf{r}_i,\mathbf{r}_j,\omega) = \delta_{\mu\nu} \mathbf{G}^{0R}(\mathbf{r}_i,\mathbf{r}_j,\omega)$. After a substitution of $G^{0R}_{\mu\nu}(\mathbf{r}_i,\mathbf{r}_j,\omega)$ into Eq. (2.1.22) each individual addend of the interaction energy factorizes into the product of an integral over retarded Green's

functions $G^{0R}(\mathbf{r}_i, \mathbf{r}_j, \omega)$ and a trace over $\boldsymbol{\sigma}$.S-matrices:

$$E_{\text{int}} = -\frac{\hbar}{\pi} \sum_{m=0}^{\infty} \left(\frac{\lambda}{2}\right)^{m+1} \sum_{i,i_1,\dots,i_m=1}^{N} \text{Tr}\left[\left(\mathbf{S}_i.\boldsymbol{\sigma}\right)\left(\mathbf{S}_{i_1}.\boldsymbol{\sigma}\right) \cdots \left(\mathbf{S}_{i_m}.\boldsymbol{\sigma}\right)\right]$$

$$\times \int_{-\infty}^{\omega_F} d\omega \,\Im\left[\mathbf{G}^{0R}(\mathbf{r}_i,\mathbf{r}_{i_1},\omega)\mathbf{G}^{0R}(\mathbf{r}_{i_1},\mathbf{r}_{i_2},\omega) \cdots \mathbf{G}^{0R}(\mathbf{r}_{i_m},\mathbf{r}_{i},\omega)\right]$$

$$(2.1.23)$$

The trace can be evaluated analytically and this leads, as shown in Appendix. A.1, for even m to the result

$$\operatorname{Tr}\left[\left(\mathbf{S}_{i_{0}}.\boldsymbol{\sigma}\right)\left(\mathbf{S}_{i_{1}}.\boldsymbol{\sigma}\right)\cdots\left(\mathbf{S}_{i_{m}}.\boldsymbol{\sigma}\right)\right]$$

$$=2i\sum_{\gamma}\operatorname{sgn}(\gamma)\left(\mathbf{S}_{i_{\gamma(0)}}.\mathbf{S}_{i_{\gamma(1)}}\right)\cdots\left(\mathbf{S}_{i_{\gamma(m-4)}}.\mathbf{S}_{i_{\gamma(m-3)}}\right)$$

$$\times\left(\left[\mathbf{S}_{i_{\gamma(m-2)}}\times\mathbf{S}_{i_{\gamma(m-1)}}\right].\mathbf{S}_{i_{m}}\right)$$
(2.1.24)

while for odd m the trace takes the form

$$\operatorname{Tr}\left[\left(\mathbf{S}_{i}.\boldsymbol{\sigma}\right)\left(\mathbf{S}_{i_{1}}.\boldsymbol{\sigma}\right)\cdots\left(\mathbf{S}_{i_{m}}.\boldsymbol{\sigma}\right)\right]$$

$$=2\sum_{\gamma}\operatorname{sgn}(\gamma)\left(\mathbf{S}_{i_{\gamma(0)}}.\mathbf{S}_{i_{\gamma(1)}}\right)\cdots\left(\mathbf{S}_{i_{\gamma(m-3)}}.\mathbf{S}_{i_{\gamma(m-2)}}\right)\left(\mathbf{S}_{i_{\gamma(m-1)}}.\mathbf{S}_{i_{\gamma(m)}}\right) \qquad (2.1.25)$$

with $i=i_0$ and the sum \sum_{γ} taken over all possibilities to make inequivalent pairs from the set of impurity spins $\{\mathbf{S}_i, \mathbf{S}_{i_1}, \cdots, \mathbf{S}_{i_m}\}$. Each pair of impurity spins is either connected by a dot or by a cross product. By convention, the interchange of indices within a pair and the exchange of factors in the product of pairs does not contribute to the sum with a new sequence. Provided that each pair is sorted by its indices in ascending order the sign of each sequence $\operatorname{sgn}(\gamma)$ is determined from the total number of interchanges of impurity spins. Due to the cross product the trace behaves, for even m, antisymmetric under an inversion of the order of the indices $\{1, \cdots, m\}$

$$\operatorname{Tr}\left[\left(\mathbf{S}_{i}.\boldsymbol{\sigma}\right)\left(\mathbf{S}_{i_{1}}.\boldsymbol{\sigma}\right)\cdots\left(\mathbf{S}_{i_{m}}.\boldsymbol{\sigma}\right)\right] = -\operatorname{Tr}\left[\left(\mathbf{S}_{i}.\boldsymbol{\sigma}\right)\left(\mathbf{S}_{i_{m}}.\boldsymbol{\sigma}\right)\cdots\left(\mathbf{S}_{i_{1}}.\boldsymbol{\sigma}\right)\right]$$
(2.1.26)

In contrast, for odd m, all spin pairs are connected by a dot product and the trace behaves symmetric

$$\operatorname{Tr}\left[\left(\mathbf{S}_{i}.\boldsymbol{\sigma}\right)\left(\mathbf{S}_{i_{1}}.\boldsymbol{\sigma}\right)\cdots\left(\mathbf{S}_{i_{m}}.\boldsymbol{\sigma}\right)\right] = \operatorname{Tr}\left[\left(\mathbf{S}_{i}.\boldsymbol{\sigma}\right)\left(\mathbf{S}_{i_{m}}.\boldsymbol{\sigma}\right)\cdots\left(\mathbf{S}_{i_{1}}.\boldsymbol{\sigma}\right)\right]$$
(2.1.27)

The antisymmetry of the trace and the symmetry of the Green's function $\mathbf{G}^{0R}(\mathbf{r}_i, \mathbf{r}_j, \omega) = \mathbf{G}^{0R}(\mathbf{r}_i, \mathbf{r}_i, \omega)$ require that in Eq. (2.1.23) all all even orders in m cancel.

Lowest-Order Approximation

In Section 2.1 we have derived the interaction energy for a system of N magnetic impurities. We have found an infinite series which may be interpreted as a sum of loop diagrams that consists in each order of 2m space time vertices that are connected by 2m propagators. For a homogeneous system as it is the case here, the Green's function decays with the impurity separation and we may truncate the series after a certain order. The crudest approximation is to cut the series after the lowest order (m = 1) which yields the following interaction energy

$$E_{\text{int}} = -\frac{\hbar}{\pi} \left(\frac{\lambda}{2}\right)^2 \sum_{i,i_1} \int_{-\infty}^{\omega_F} d\omega$$

$$\times \Im \left(\text{Tr} \left[(\mathbf{S}_i.\boldsymbol{\sigma}) \, \mathbf{G}^{0R}(\mathbf{r}_i, \mathbf{r}_{i_1}, \omega) \, (\mathbf{S}_{i_1}.\boldsymbol{\sigma}) \, \mathbf{G}^{0R}(\mathbf{r}_{i_1}, \mathbf{r}_{i}, \omega) \right] \right)$$
(2.1.28)

A minimization of the interaction energy with respect to the relative coordinates of both impurity spins is in general not possible since it requires information about the Green's function $\mathbf{G}^{0R}(\mathbf{r}_i, \mathbf{r}_j, \omega)$ and the $\mathbf{S}_i.\boldsymbol{\sigma}$ matrix. However, the situation is much simpler in the spin-unpolarized system: in this case the interaction energy reduces to the expression $E_{\text{int}} = \sum_{i,i_1} J(\mathbf{r}_i, \mathbf{r}_{i_1}) (\mathbf{S}_i.\mathbf{S}_{i_1})$ with the exchange integral $J(\mathbf{r}_i, \mathbf{r}_{i_1})$ given by

$$J(\mathbf{r}_{i}, \mathbf{r}_{i_{1}}) = -\frac{2\hbar}{\pi} \left(\frac{\lambda}{2}\right)^{2} \int_{-\infty}^{\omega_{F}} d\omega \,\Im\left[\mathbf{G}^{0R}(\mathbf{r}_{i}, \mathbf{r}_{i_{1}}, \omega)\mathbf{G}^{0R}(\mathbf{r}_{i_{1}}, \mathbf{r}_{i}, \omega)\right]$$
(2.1.29)

From this expression it can be immediately seen that depending on the sign of the exchange integral either a purely ferromagnetic or a purely antiferromagnetic coupling is preferred. This approach was first used by Ruderman, Kittel, Kasuya and Yosida to describe the nuclear spin coupling in the gas of conduction electrons and is in literature well known as the RKKY approximation. When we discuss in the following chapters the indirect exchange interaction in graphene or on the surface of a topological insulator we use the expression 'RKKY interaction' in order to indicate that we stay in a regime where the lowest order approximation is applicable.

The Indirect Exchange Interaction at Finite Temperature

Similar to the previous section we consider a system of N magnetic moments in a gas of non-interacting electrons. The system is in thermal equilibrium and has the possibility to exchange energy and particles with a reservoir. All possible equilibrium states of the system can be described by the grand canonical ensemble with the density matrix $\rho = \exp(-\beta K)/Z$ and the partition function $Z = \text{Tr} \left[\exp(-\beta K)\right]$. Here we have introduced the grand canonical Hamiltonian $K = H^0 + W - \mu N$ with the Hamiltonian of the non-interacting system H^0 , the contact interaction W, the

2.2. THE INDIRECT EXCHANGE INTERACTION AT FINITE TEMPERATURE

particle number operator N and the chemical potential μ . The temperature T enters into the density matrix through the parameter $\beta = 1/(k_BT)$ where k_B stands for the Boltzmann constant. For such a system the interaction energy is given by the expectation value $E_{\rm int} = {\rm Tr} \, (\rho W)$ and in the following we will evaluate this expression using finite temperature quantum field theory techniques. The first step is to rewrite the interaction energy in the interaction picture

$$E_{\text{int}} = \frac{\text{Tr}\left(e^{-\beta K^0} W_I(\hbar \beta) U(\hbar \beta, 0)\right)}{\text{Tr}\left(e^{-\beta K^0} U(\hbar \beta, 0)\right)}$$
(2.2.1)

where the perturbation takes the form $W_I(\tau) = exp(K^0\tau/\hbar)Wexp(-K^0\tau/\hbar)$ with $K^0 = H^0 - \mu N$. The imaginary time evolution operator $U(\tau, 0)$ satisfies the differential equation $-\partial/\partial\tau \ U(\tau, 0) = W_I(\tau)U(\tau, 0)$. The solution of the differential equation is given by $U(\tau, 0) = \exp(K^0\tau)\exp(-K\tau)$ which may be expanded as

$$U(\tau,0) = \sum_{m=0}^{\infty} \frac{1}{m!} \left(-\frac{1}{\hbar} \right)^m \int_0^{\tau} d\tau_1 \cdots \int_0^{\tau} d\tau_m \ T_{\tau} \left[W_I(\tau_1) \cdots W_I(\tau_m) \right]$$
 (2.2.2)

where T_{τ} stands for the temperature ordering operator. In the temperature ordered product the operator with the highest temperature stands farthest to the left. Eq. (2.2.2) allows us to rewrite the numerator and the denominator of Eq. (2.2.1) as a perturbation series which factorizes in both cases into the product of all connected and all disconnected diagrams. After cancellation there remains the following expression

$$E_{\text{int}} = \sum_{m=0}^{\infty} \frac{1}{m!} \left(-\frac{1}{\hbar} \right)^m \int_0^{\hbar\beta} d\tau_1 \cdots \int_0^{\hbar\beta} d\tau_m$$

$$\times \text{Tr} \left(\rho^0 T_\tau \left[W_I(\tau_1) \cdots W_I(\tau_m) W_I(\hbar\beta) \right] \right)_c \tag{2.2.3}$$

with $\rho^0 = \exp(-\beta K^0)/Z^0$ and $Z^0 = \text{Tr}[\exp(-\beta K^0)]$. Here it is important to stress that the creation and the annihilation operator are, for real τ , not a pair of adjoint operators. For a further analytical evaluation of the expectation value we insert the perturbation $W_I(\tau)$ in its second quantization representation

$$E_{\text{int}} = \sum_{m=0}^{\infty} \frac{1}{m!} \left(-\frac{1}{\hbar} \right)^m \left(-\frac{\lambda \hbar}{2} \right)^{m+1} \sum_{i,i_1,\dots,i_m} \sum_{\mu,\mu_1,\dots,\mu_m} \sum_{\nu,\nu_1,\dots,\nu_m} \sum_{\nu,\nu_1,\dots,\nu_m} \sum_{\nu,\nu_1,\dots,\nu_m} \left(\mathbf{S}_{i.}\boldsymbol{\sigma}_{\mu\nu} \right) \left(\mathbf{S}_{i_1}\boldsymbol{\sigma}_{\mu_1\nu_1} \right) \cdots \left(\mathbf{S}_{i_m}\boldsymbol{\sigma}_{\mu_m\nu_m} \right) \int_0^{\hbar\beta} d\tau_1 \cdots \int_0^{\hbar\beta} d\tau_m \right. \\ \times \left. \operatorname{Tr} \left(\rho^0 T_\tau \left[c_{i_1\mu_1}^{\dagger}(\tau_1) c_{i_1\nu_1}(\tau_1) \cdots c_{i_m\mu_m}^{\dagger}(\tau_m) c_{i_m\nu_m}(\tau_m) c_{i_{\dot{m}}\dot{\nu}_m}^{\dagger}(\hbar\beta) c_{i\nu}(\hbar\beta) \right] \right)_c$$
 (2.2.4)

Similar to the zero temperature formalism we have chosen the interaction picture where the two field operators are given by $c_{i\mu}(\tau) = \exp(K^0\tau/\hbar)c_{i\mu}\exp(-K^0\tau/\hbar)$ and $c_{i\mu}^{\dagger}(\tau) = \exp(K^0\tau/\hbar)c_{i\mu}^{\dagger}\exp(-K^0\tau/\hbar)$. Then we use Wick's theorem and replace the

trace over the field operators by the sum of all contractions. Each order consists of m! connected diagrams that all give an identical contribution to the interaction energy. Hence, the factor m! in the denominator of Eq. (2.2.4) cancels with the total number of contractions and the interaction energy can be brought to the form

$$E_{\text{int}} = \hbar \sum_{m=0}^{\infty} \left(-\frac{\lambda}{2} \right)^{m+1} \sum_{i,i_1,\dots,i_m} \int_0^{\hbar\beta} d\tau_1 \dots \int_0^{\hbar\beta} d\tau_m \operatorname{Tr} \left[(\mathbf{S}_i.\boldsymbol{\sigma}) \mathscr{G}^0(\mathbf{r}_i, \hbar\beta, \mathbf{r}_{i_1}, \tau_1) \right] \times (\mathbf{S}_{i_1}.\boldsymbol{\sigma}) \mathscr{G}^0(\mathbf{r}_{i_1}, \tau_1, \mathbf{r}_{i_2}, \tau_2) \dots (\mathbf{S}_{i_m}.\boldsymbol{\sigma}) \mathscr{G}^0(\mathbf{r}_{i_m}, \tau_m, \mathbf{r}_i, \hbar\beta)$$
(2.2.5)

with the finite temperature Green's function defined as follows:

$$\mathscr{G}^{0}_{\mu\nu}(\mathbf{r}_{i},\tau,\mathbf{r}_{j},\tau') = -c_{i\mu}(\tau)^{\bullet}c^{\dagger}_{j\nu}(\tau')^{\bullet}$$
$$= -\operatorname{Tr}\left(\rho^{0}T_{\tau}\left[c_{i\mu}(\tau)c^{\dagger}_{j\nu}(\tau')\right]\right) \tag{2.2.6}$$

For a system that is invariant under translations and has no explicit dependence on the temperature the Green's function is a function of the difference $\tau' - \tau$ and $\mathbf{r}_j - \mathbf{r}_i$, only.

In the final step we take Eq. (2.2.5) and replace the Green's function by its Fourier transform $\mathscr{G}^0(\mathbf{r}_i, \mathbf{r}_j, \tau) = 1/(\hbar\beta) \sum_n e^{-i\omega_n \tau} \mathscr{G}^0(\mathbf{r}_i, \mathbf{r}_j, i\omega_n)$ and obtain the following result

$$E_{\text{int}} = \frac{1}{\beta} \sum_{m=0}^{\infty} \left(\frac{\lambda}{2}\right)^{m+1} \sum_{i,i_1,\dots,i_m} \sum_{n=-\infty}^{\infty} \text{Tr}\left[(\mathbf{S}_i.\boldsymbol{\sigma}) \mathcal{G}^0(\mathbf{r}_i, \mathbf{r}_{i_1}, i\omega_n) \right.$$

$$\times (\mathbf{S}_{i_1}.\boldsymbol{\sigma}) \mathcal{G}^0(\mathbf{r}_{i_1}, \mathbf{r}_{i_2}, i\omega_n) \cdots (\mathbf{S}_{i_m}.\boldsymbol{\sigma}) \mathcal{G}^0(\mathbf{r}_{i_m}, \mathbf{r}_i, i\omega_n) \right]$$
(2.2.7)

where $\omega_n = \pi (2n+1)/(\hbar \beta)$ stands for the Matsubara frequency. In the zero temperature limit these discrete Matsubara frequencies go over into a continuum and the Matsubara sum turns into an integral

$$\frac{1}{\hbar\beta} \sum_{n=-\infty}^{+\infty} \to \frac{1}{2\pi} \int_{-\infty}^{+\infty} d\omega \tag{2.2.8}$$

Under these circumstances we recover the results that were derived in the zero temperature formalism.

Spin-unpolarized Electron Gas

In the finite temperature formalism we have derived with Eq. (2.2.7) an expression that allows to calculate the interaction energy as a function of the impurity configuration, the chemical potential μ and the temperature T up to any order. For a Green's function that is diagonal $\mathscr{G}^0_{\mu\nu}(\mathbf{r}_i,\mathbf{r}_j,i\omega_n) = \delta_{\mu\nu}\mathcal{G}^0(\mathbf{r}_i,\mathbf{r}_j,i\omega_n)$, as it is found for the

spin-unpolarized electron gas, the interaction energy reduces to the form

$$E_{\text{int}} = \frac{1}{\beta} \sum_{m=0}^{\infty} \left(\frac{\lambda}{2}\right)^{m+1} \sum_{i,i_1,\dots,i_m} \text{Tr}\left[\left(\mathbf{S}_i.\boldsymbol{\sigma}\right)\left(\mathbf{S}_{i_1}.\boldsymbol{\sigma}\right) \cdots \left(\mathbf{S}_{i_m}.\boldsymbol{\sigma}\right)\right]$$

$$\times \sum_{n=-\infty}^{\infty} \mathcal{G}^0(\mathbf{r}_i, \mathbf{r}_{i_1}, i\omega_n) \mathcal{G}^0(\mathbf{r}_{i_1}, \mathbf{r}_{i_2}, i\omega_n) \cdots \mathcal{G}^0(\mathbf{r}_{i_m}, \mathbf{r}_i, i\omega_n)$$
(2.2.9)

In analogy to the calculation in the zero temperature formalism we can replace the trace $\text{Tr}\left[\left(\mathbf{S}_{i}.\boldsymbol{\sigma}\right)\left(\mathbf{S}_{i_{1}}.\boldsymbol{\sigma}\right)\cdots\left(\mathbf{S}_{i_{m}}.\boldsymbol{\sigma}\right)\right]$ by Eq. (2.1.25) and restrict the sum \sum_{m} to odd order of m. But in contrast to Section 2.1 there is no need to introduce a real or imaginary part around the product of Green's functions since the Green's function $\mathcal{G}^{0}(\mathbf{r}_{i},\mathbf{r}_{j},i\omega_{n})$ is real itself

$$\mathcal{G}^{0}(\mathbf{r}_{i}, \tau, \mathbf{r}_{j}, \tau')^{*} = -\operatorname{Tr}\left(\rho^{0}T\left[c_{j}(\tau)c_{i}^{\dagger}(\tau')\right]\right)$$
$$= \mathcal{G}^{0}(\mathbf{r}_{i}, \tau, \mathbf{r}_{j}, \tau') \tag{2.2.10}$$

Here we made use of the cyclic invariance of the trace and the symmetry of the Green's function $\mathcal{G}^0(\mathbf{r}_i, \tau, \mathbf{r}_j, \tau') = \mathcal{G}^0(\mathbf{r}_j, \tau, \mathbf{r}_i, \tau')$.

Lowest-Order Approximation

In the lowest order we may approximate the interaction energy by

$$E_{\text{int}} = \frac{1}{\beta} \left(\frac{\lambda}{2} \right)^2 \sum_{i,i_1} \sum_{n=-\infty}^{\infty} \text{Tr} \left[(\mathbf{S}_i.\boldsymbol{\sigma}) \, \mathcal{G}^0(\mathbf{r}_i, \mathbf{r}_{i_1}, i\omega_n) \, (\mathbf{S}_{i_1}.\boldsymbol{\sigma}) \, \mathcal{G}^0(\mathbf{r}_{i_1}, \mathbf{r}_i, i\omega_n) \right] \quad (2.2.11)$$

For a system where the Green's function is diagonal the RKKY interaction energy reduces to the form $E_{\text{int}} = \sum_{i,i_1} \mathcal{J}(\mathbf{r}_i, \mathbf{r}_{i_1}) (\mathbf{S}_i.\mathbf{S}_{i_1})$ with the finite temperature exchange integral $\mathcal{J}(\mathbf{r}_i, \mathbf{r}_{i_1})$ defined as follows:

$$\mathcal{J}(\mathbf{r}_i, \mathbf{r}_{i_1}) = \frac{\lambda^2}{2\beta} \sum_{n=-\infty}^{\infty} \mathcal{G}^0(\mathbf{r}_i, \mathbf{r}_{i_1}, i\omega_n) \mathcal{G}^0(\mathbf{r}_{i_1}, \mathbf{r}_i, i\omega_n)$$
(2.2.12)

In the latter case the coupling of the two impurity spins is depending on the sign of $\mathcal{J}(\mathbf{r}_i, \mathbf{r}_{i_1})$ either ferro- or antiferromagnetic.

Other Coupling Schemes

Up to this point we focused on the indirect exchange interaction between impurities such that each impurity couples to the gas of delocalized electrons on a single site. However, as soon as the impurity couples to a selected set of lattice sites, which is usually the case in a solid, the situation gets more complicated.

The Coherent Coupling Scheme

In the most general case, which is known as the coherent coupling scheme, each impurity spin S_i couples to a set of surrounding lattice sites M_i and causes on-site as well as inter-site spin-flip processes in its environment. Each scattering process is weighted by an individual coupling constant $\lambda(a_i, d_i)$ that can be determined from abinitio calculation. Under these circumstances the Hamiltonian of the electron-impurity interaction is given by the coherent sum of all scattering processes

$$V = -\frac{\hbar}{2} \sum_{\mu,\nu} \sum_{i=1}^{N} \sum_{a_i,d_i \in M_i} \lambda\left(a_i, d_i\right) c_{a_i \mu}^{\dagger} c_{d_i \nu} \left(\boldsymbol{\sigma}_{\mu \nu}. \mathbf{S}_i\right)$$
(2.3.1)

with $\mu, \nu \in \{\uparrow, \downarrow\}$ and where a_i and d_i are lattice sites in the local environment of the impurity spin \mathbf{S}_i . In the zero temperature formalism we get the following expression for the interaction energy

$$E_{\text{int}} = -\frac{\hbar}{\pi} \sum_{m=0}^{\infty} \sum_{i,i_{1},\dots,i_{m}} \sum_{a_{i},a_{i_{1}}\dots,a_{i_{m}}} \sum_{d_{i},d_{i_{1}},\dots,d_{i_{m}}} \left(\frac{1}{2}\right)^{m+1} \int_{-\infty}^{\omega_{F}} d\omega$$

$$\times \lambda(a_{i},d_{i})\lambda(a_{i_{1}},d_{i_{1}})\dots\lambda(a_{i_{m}},d_{i_{m}})\Im\left(\text{Tr}\left[\left(\mathbf{S}_{i}.\boldsymbol{\sigma}\right)G^{0R}(\mathbf{r}_{a_{i}},\mathbf{r}_{d_{i_{1}}},\omega\right)\right.$$

$$\times \left(\mathbf{S}_{i_{1}}.\boldsymbol{\sigma}\right)G^{0R}(\mathbf{r}_{a_{i_{1}}},\mathbf{r}_{d_{i_{2}}},\omega)\dots\left(\mathbf{S}_{i_{m}}.\boldsymbol{\sigma}\right)G^{0R}(\mathbf{r}_{a_{i_{m}}},\mathbf{r}_{d_{i}},\omega)\right]\right) \qquad (2.3.2)$$

Even the lowest order includes scattering between four lattice sites and this makes the calculation of the interaction energy quite complicated.

The Incoherent Coupling Scheme

The complexity of the calculation reduces considerably in the incoherent coupling scheme where only on-site spin-flip processes are taken into account while inter-site spin-flip processes are neglected. The Hamiltonian for the electron-impurity interaction now reads

$$V = -\frac{\hbar}{2} \sum_{\mu,\nu} \sum_{i=1}^{N} \sum_{a_i \in M_i} \lambda(a_i) \ c_{a_i\mu}^{\dagger} c_{a_i\nu} \left(\boldsymbol{\sigma}_{\mu\nu}.\mathbf{S}_i\right)$$
 (2.3.3)

This coupling scheme leads to the following interaction energy

$$E_{\text{int}} = -\frac{\hbar}{\pi} \sum_{m=0}^{\infty} \sum_{i,i_1,\dots,i_m} \sum_{a_i,a_{i_1}\dots,a_{i_m}} \left(\frac{\lambda(a_i)}{2}\right)^{m+1} \int_{-\infty}^{\omega_F} d\omega \,\Im\left(\text{Tr}\left[\left(\mathbf{S}_i.\boldsymbol{\sigma}\right)\right]\right) \times G^{0R}(\mathbf{r}_{a_i},\mathbf{r}_{a_{i_1}},\omega) \left(\mathbf{S}_{i_1}.\boldsymbol{\sigma}\right) G^{0R}(\mathbf{r}_{a_{i_1}},\mathbf{r}_{a_{i_2}},\omega) \cdots \left(\mathbf{S}_{i_m}.\boldsymbol{\sigma}\right) G^{0R}(\mathbf{r}_{a_{i_m}},\mathbf{r}_{a_i},\omega)\right] \right)$$
(2.3.4)

2.3. OTHER COUPLING SCHEMES

In case that all impurity spins couple to the local environment in the same way the interaction energy reduces to the linear combination of several site-to-site interactions.

The RKKY Interaction in Monolayer Graphene

It is well known that the interaction between two magnetic impurities embedded in a two-dimensional electron gas oscillates with the period of the Fermi wave vector between a ferro- and an antiferromagnetic type and decays following an inverse square dependent envelope function [36, 37, 38, 39]. Graphene has, in contrast to a usual Schrödinger electron gas, a linear spectrum and a DOS that vanishes at the Dirac point. In this chapter we study the impact of these new features on the RKKY interaction. After an introduction to the graphene electronic properties we begin

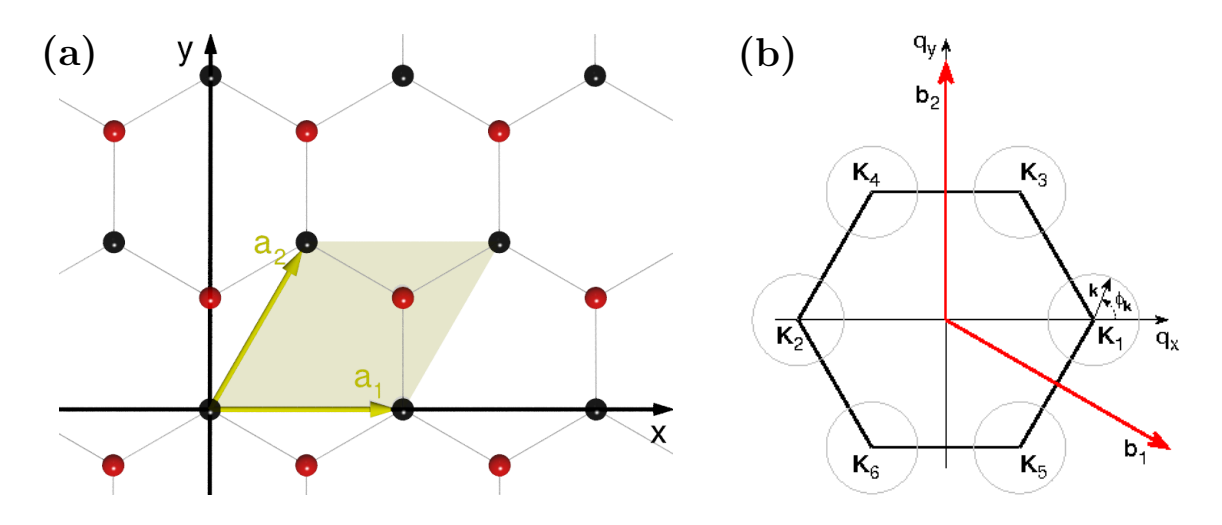


Figure 3.1: The crystal structure [Fig. (3.1a)] and the Brillouin zone [Fig. (3.1b)] of graphene.

with the RKKY interaction at zero temperature which, in fact, has already been addressed in recent publications [1, 2, 3, 4, 5, 6, 7]. We use the Green's function formalism that we established in the first chapter. Then we proceed with the RKKY interaction at finite temperature where we find an unusual increase of the interaction with temperature. We conclude the chapter with the situation which seems most realistic, namely the interaction between two plaquette impurities which we treat within different electron-impurity coupling schemes.

Monolayer Graphene

The crystal structure as well as the electronic properties of graphene derive from the remarkable ability of carbon to form various bonding configurations. In particular, for this allotrope the two 2p- and one 2s-orbital combine to three degenerate sp²-hybrid orbitals which form in-plane σ -bonds. With their bond angle of 120 degrees these are responsible for the planar honeycomb structure. The remaining valence electron contributes to a π -bond and can freely travel through the crystal. These π -electrons determine the low energy electronic properties of the material. In the simplest approximation where only the nearest-neighbor hopping of π -electrons is taken into account the Hamiltonian reads [8, 9, 48]

$$H^{0} = -t \sum_{\langle ij \rangle} (a_{j}^{\dagger} b_{i} + b_{i}^{\dagger} a_{j})$$

$$(3.1.1)$$

with the nearest-neighbor hopping amplitude $t \approx 2.8eV$ and the operators a_i^{\dagger} (b_i^{\dagger}) creating an electron on site i of sublattice A(B). The sum $\sum_{\langle ij \rangle}$ is taken over nearest-neighbor sites of carbon atoms. In order to solve the Schrödinger equation $H^0\Psi = \epsilon\Psi$ we introduce the two Bloch sums

$$|\Psi_A^{\mathbf{q}}\rangle = \frac{1}{\sqrt{N_0}} \sum_{i \in A} e^{i\mathbf{q} \cdot \mathbf{r}_i} a_i^{\dagger} |0\rangle$$
 (3.1.2)

$$|\Psi_B^{\mathbf{q}}\rangle = \frac{1}{\sqrt{N_0}} \sum_{i \in B} e^{i\mathbf{q}\cdot\mathbf{r}_i} b_i^{\dagger} |0\rangle$$
 (3.1.3)

where $| 0 \rangle$ is vacuum state and N_0 is the number of unit cells in the crystal. In the basis of the Bloch sums [Eqs. (3.1.2) and (3.1.3)] and a low energy expansion in vicinity of the corner of the hexagonal Brillouin zone \mathbf{K}_m the Hamiltonian becomes [89]

$$H_m^0(\mathbf{k}) = \begin{pmatrix} 0 & \tilde{\Phi}_m(\mathbf{k}) \\ \tilde{\Phi}_m^*(\mathbf{k}) & 0 \end{pmatrix}$$
 (3.1.4)

where we introduced the function $\tilde{\Phi}_m(\mathbf{k}) = \hbar v_F k \exp[i\gamma_m + i\delta_m\phi_{\mathbf{k}}]$ with the Fermi velocity $v_F = \sqrt{3}at/(2\hbar)$ and the phases γ_m and δ_m tabulated in Table (3.1). Here $a \approx 2.46 \text{Å}$ stands for graphene's lattice constant and the wave vector $\mathbf{k} = \mathbf{q} - \mathbf{K}_m$ for a small deviation from the K point which is specified by the wave vector \mathbf{K}_m with $m \in \{1, 2, \dots, 6\}$. Furthermore we have introduced k as a radius and $\phi_{\mathbf{k}} = \arctan(k_y/k_x)$ as a polar angle of \mathbf{k} . The position of the six K points may be seen in Fig. (3.1).

With help of the Bloch theorem the number of inequivalent K points can be reduced to two. Expanded in vicinity of \mathbf{K}_1 the Hamiltonian takes the simple form $H_1(\mathbf{k}) = \boldsymbol{\sigma}.\mathbf{k}$ while the expansion in vicinity of \mathbf{K}_2 yields $H_2(\mathbf{k}) = \boldsymbol{\sigma}^*.\mathbf{k}$ where $\boldsymbol{\sigma}$ stands for the vector of Pauli matrices and $\boldsymbol{\sigma}^*$ for its complex conjugate. From that

\overline{m}	1	2	3	4	5	6
$\mathbf{K} imes rac{3a}{2\pi}$	$\begin{pmatrix} 2 \\ 0 \end{pmatrix}$	$\begin{pmatrix} -2 \\ 0 \end{pmatrix}$	$\begin{pmatrix} 1 \\ \sqrt{3} \end{pmatrix}$	$\begin{pmatrix} -1\\\sqrt{3} \end{pmatrix}$	$\begin{pmatrix} 1 \\ -\sqrt{3} \end{pmatrix}$	$\begin{pmatrix} -1 \\ -\sqrt{3} \end{pmatrix}$
γ	0	π	$-\frac{\pi}{3}$	$\frac{2\pi}{3}$	$\frac{\pi}{3}$	$-\frac{2\pi}{3}$
δ	-1	+1	+1	-1	+1	-1

Table 3.1: The coefficients for the low energy expansion at each of the six high-symmetry K points of the graphene Brillouin zone [89].

representation it is immediately clear that the low energy spectrum consists of two linear dispersing bands

$$\epsilon_l(\mathbf{k}) = l\hbar v_F k \tag{3.1.5}$$

with the chirality $l \in \{\pm\}$. In addition to that it can be concluded that the eigenstates of H_m^0 are two-component spinors in a pseudospin space that is spanned by the Bloch sums $|\Psi_A\rangle$ and $|\Psi_B\rangle$ taken at a particular \mathbf{K}_m point.

$$\Psi_{ml}(\mathbf{k}) = \frac{1}{\sqrt{2}} \begin{pmatrix} 1\\ l\frac{\tilde{\Phi}_m^*(\mathbf{k})}{|\tilde{\Phi}_m(\mathbf{k})|} \end{pmatrix}$$
(3.1.6)

The corresponding density of states (DOS) is given by $D_{\alpha}(\mathbf{R}, E) = 2\pi |E|/(\hbar^2 v_F^2 \Omega_{BZ})$ where $\alpha \in \{A, B\}$ stands for the sublattice and $\Omega_{BZ} = 8\pi^2/(\sqrt{3}a^2)$ for the area of the Brillouin zone. In contrast to what one would expect for a common non-relativistic two-dimensional electron gas the DOS grows linear by |E| and equals to zero at the Dirac point.

The Zero Temperature Green's function

The spectral properties can be used in order to calculate the low energy Green's function of graphene. Here we proceed as follows: first we derive the momentum space Green's function

$$\mathbf{G}_{m}^{0R}(\mathbf{k}, E) = [E + i\eta - H_{m}^{0}(\mathbf{k})]^{-1}$$
 (3.1.7)

where η is a small, positive real number. A subsequent Fourier transform then yields the real space Green's function

$$\mathbf{G}^{0R}(\mathbf{R}, E) = \sum_{m=1}^{2} \mathbf{G}_{m}^{0R}(\mathbf{R}, E) e^{i(\mathbf{K}_{m}.\mathbf{R})}$$
(3.1.8)

with $G_m^{0R}(\mathbf{R}, E) = 1/\Omega_{BZ} \int d^2k \, \exp(i\mathbf{k}.\mathbf{R}) G_m^{0R}(\mathbf{k}, E)$. The latter integral can be taken with the help of Appendix B which then leads, as shown in Ref. [89], to the following result

$$\mathbf{G}_{m}^{0R}(\mathbf{R}, E) = -\frac{\pi^{2}i(E + i\eta)}{\hbar^{2}v_{F}^{2}\Omega_{BZ}}$$

$$\times \begin{pmatrix} H_{0}^{1}\left(\frac{E + i\eta}{\hbar v_{F}}R\right) & i\Phi_{m}(\mathbf{R})H_{1}^{1}\left(\frac{E + i\eta}{\hbar v_{F}}R\right) \\ i\Phi_{m}^{*}(\mathbf{R})H_{1}^{1}\left(\frac{E + i\eta}{\hbar v_{F}}R\right) & H_{0}^{1}\left(\frac{E + i\eta}{\hbar v_{F}}R\right) \end{pmatrix}$$
(3.1.9)

where we introduced the function $\Phi_m(\mathbf{R}) = \exp[i\gamma_m + i\delta_m\theta]$ with γ_m and δ_m tabulated in Table (3.1). Furthermore, the vector \mathbf{R} is in polar coordinates given by the radius R and the polar angle θ and $H^1_{\nu}(x)$ stands for the Hankel function of the first kind and ν^{th} -order.

The Finite Temperature Green's Function

Thermodynamic properties of the system are encoded in the finite temperature Green's function. The momentum space representation of the finite temperature Green's function can be obtained from the analytic continuation of Eq. (3.1.7), a procedure which requires to replace the energy $E + i\eta$ by $i\omega_n + \mu$ and yields

$$\mathcal{G}_m^0(\mathbf{k}, i\omega_n) = \hbar \left[i\hbar\omega_n + \mu - H_m^0(\mathbf{k}) \right]^{-1}$$
(3.1.10)

where $\omega_n = (2n+1)\pi/(\hbar\beta)$ is the Matsubara frequency and μ the chemical potential. In the usual low energy approximation where only regions in the vicinity of each K point contribute, the real space Green's function is given by the finite temperature analogue to Eq. (3.1.8) with the Fourier transform of $\mathcal{G}_m^0(\mathbf{k}, i\omega_n)$ obtained as

$$\mathcal{G}_m^0(\mathbf{R}, i\omega_n) = -\operatorname{sgn}(\omega_n) \frac{2\pi i (\hbar \omega_n - i\mu)}{\hbar v_F^2 \Omega_{BZ}}$$

$$\times \begin{pmatrix} \operatorname{sign}(\omega_n) K_0 \left(\operatorname{sign}(\omega_n) \frac{\hbar \omega_n - i\mu}{\hbar v_F} R \right) & \Phi_m(\mathbf{R}) K_1 \left(\operatorname{sign}(\omega_n) \frac{\hbar \omega_n - i\mu}{\hbar v_F} R \right) \\ \Phi_m^*(\mathbf{R}) K_1 \left(\operatorname{sign}(\omega_n) \frac{\hbar \omega_n - i\mu}{\hbar v_F} R \right) & \operatorname{sign}(\omega_n) K_0 \left(\operatorname{sign}(\omega_n) \frac{\hbar \omega_n - i\mu}{\hbar v_F} R \right) \end{pmatrix}$$
(3.1.11)

where $K_{\nu}(x)$ stands for the modified Bessel function of the second kind and ν^{th} -order. The temperature enters Eqs. (3.1.10) and (3.1.11) through parameter $\beta = 1/(k_B T)$ where k_B is the Boltzmann constant.

The RKKY Interaction in Monolayer Graphene at Zero Temperature

We now turn to the RKKY interaction between two magnetic impurities which is mediated by the low energy excitations in graphene. We assume that each impurity spin couples to the itinerant electron spin density via a single site that belongs either to sublattice A or B. The interaction energy for such a system is presented in Section 2.1 and it remains here to calculate the exchange integral $J(\mathbf{R})$. After substituting the appropriate matrix element of the zero temperature Green's function into Eq. (2.1.29) we obtain for two impurities on the same sublattice the result which can be similarly found in Refs. [1, 2]

$$J_{AA}(\mathbf{R}) = -4Cf_{AA}(\mathbf{R}) \int_{-\infty}^{E_F} dE \left(\frac{E}{\hbar v_F}\right)^2 \Im \left[H_0^1 \left(\frac{(E+i\eta)R}{\hbar v_F}\right)^2 \right]$$
(3.2.1)

with $C = -\lambda^2 \hbar^2 a^2/(64\pi t^2)$, the Fermi energy E_F and the separation vector $\mathbf{R} = \mathbf{r}' - \mathbf{r}$ where $\mathbf{r}' = \mathbf{r}' - \mathbf{r}'$ where $\mathbf{r}' = \mathbf{r}' - \mathbf{r}'$ is the position of the first (second) impurity. The function $f_{AA}(\mathbf{R}) = 1/2\sum_{m,n=1}^{2} \exp[-i(\mathbf{K}_m - \mathbf{K}_n) \cdot \mathbf{R}]$ is obtained from summing over the inequivalent K points and may be rewritten as follows

$$f_{AA}(\mathbf{R}) = 1 + \cos\left[\mathbf{K}_2.\mathbf{R}\right] \tag{3.2.2}$$

where the wave vector \mathbf{K}_2 must be taken from Table (3.1). In the case where the two moments reside on different sublattices the exchange integral in agreement with [1, 2] reads

$$J_{BA}(\mathbf{R}) = -4C f_{BA}(\mathbf{R}) \int_{-\infty}^{E_F} dE \left(\frac{E}{\hbar v_F} \right)^2 \Im \left[H_1^1 \left(\frac{(E+i\eta)R}{\hbar v_F} \right)^2 \right]$$
(3.2.3)

with the function $f_{BA}(\mathbf{R}) = 1/2 \sum_{m,n=1}^{2} \exp[-i(\mathbf{K}_m - \mathbf{K}_n) \cdot \mathbf{R}] \Phi_m^*(\mathbf{R}) \Phi_n(\mathbf{R})$ which can be brought with help of the identity $\Phi_m(-\mathbf{R}) = -\Phi_m(\mathbf{R})$ to the form

$$f_{BA}(\mathbf{R}) = 1 + \cos\left[\mathbf{K}_2 \cdot \mathbf{R} + \pi - 2\theta\right]$$
 (3.2.4)

In both cases the exchange integral separates into the product of an intervalley and an intravalley contribution: $J_{\alpha\alpha'}(\mathbf{R}) = 4Cf_{\alpha\alpha'}(\mathbf{R})I_{\alpha\alpha'}(R)$ where α (α') is the sublattice of the first (second) impurity. The intervalley scattering function $f_{\alpha\alpha'}(\mathbf{R})$ oscillates on the scale of the lattice constant between the value 0 and 2. This function obeys the identity $f_{\alpha\alpha'}(\mathbf{R}) = f_{\alpha'\alpha}(-\mathbf{R})$ and reflects the D_{3h} symmetry of the graphene lattice. The threefold rotational symmetry can be, for example, observed in zigzag or in armchair direction: in all three zigzag directions $f_{AA}(\mathbf{R})$ takes the values 2, 1/2, 1/2 which are repeated periodically while for $f_{BA}(\mathbf{R})$ the values are 3/2, 3/2, 0. In the armchair direction both functions take a constant value of 2. The intravalley scattering function $I_{\alpha\alpha'}(R)$ is a result of the graphene spectral properties. It depends

on the impurity separation R and on the Fermi energy E_F . The sign of the intravalley scattering function determines whether the coupling is ferro- or antiferromagnetic.

Undoped Monolayer Graphene

The effect of the linear energy spectrum in graphene on the RKKY interaction can be especially well seen when the Fermi energy is at the apex of the Dirac cone, as it is the case for the undoped monolayer. Despite the lack of the charge carriers in the conduction band there is, as we will see, an indirect exchange interaction through the virtual Dirac-Weyl excitations. It is convenient to rewrite the exchange integral for two spins on the same sublattice as follows

$$J_{AA}(\mathbf{R}) = \frac{8C\hbar v_F}{R^3} f_{AA}(\mathbf{R}) \lim_{s \to 0} \int_0^\infty dx \ x^2 J_0(x) Y_0(x) \ e^{-sx}$$
 (3.2.5)

with $x = ER/(\hbar v_F)$. Then we replace the Bessel function of the second kind by $Y_0(x) = 2/\pi \Re \left[\int_0^\infty dx' \ x' J_0(x')/(x'^2 - x^2) \right]$. For this identity it is important to stress that x as well as x' have a vanishing, positive imaginary part which is important near the singularity x = x' and comes from the retarded Green's function in Eqs. (3.2.1) and (3.2.3). This imaginary part ensures the convergence of all zero temperature exchange integrals. After replacing $Y_0(x)$ and after a subsequent partial fraction expansion the exchange integral takes the form

$$J_{AA}(\mathbf{R}) = \frac{8C\hbar v_F}{\pi R^3} f_{AA}(\mathbf{R})$$

$$\times \lim_{s \to 0} \int_0^\infty dx \int_0^\infty dx' \left(\frac{xx'}{x - x'} + \frac{xx'}{x + x'} \right) J_0(x) J_0(x') e^{-s(x + x')}$$
(3.2.6)

From an interchange of x and x' it can be seen that the integral over the first term with the minus sign in the denominator vanishes. There remains the integral over the second term with the plus sign in the denominator which has no more singularities that must be taken into account since the two-dimensional integral is taken over the first quadrant where x as well as x' are positive valued. In this way it can be seen that Eq. (3.2.6) is real valued and may be written as

$$J_{AA}(\mathbf{R}) = \frac{8\hbar v_F}{R^3} C f_{AA}(\mathbf{R}) \lim_{s \to 0} I(s)$$
(3.2.7)

where the integral I(s) is defined as follows:

$$I(s) = \int_0^\infty dx \int_0^\infty dx' \, \frac{xx' J_0(x) J_0(x')}{x + x'} \, e^{-s(x + x')}$$
 (3.2.8)

The derivative with respect to s yields an expression which is well known as the Laplace transform of $xJ_0(x)$:

$$\frac{dI(s)}{ds} = -\left(\int_0^\infty dx \ x e^{-sx} J_0(x)\right)^2
= -\frac{s^2}{(1+s^2)^3}$$
(3.2.9)

Performing the integration with the boundary condition $\lim_{s\to\infty} I(s) = 0$ yields

$$I(s) = -\frac{1}{8}\arctan(s) + \frac{s(1-s^2)}{8(1+s^2)^2} + \frac{\pi}{16}$$
(3.2.10)

Hence $J_{AA}(\mathbf{R})$ takes in analogy to Refs. [1, 3, 4, 5, 6, 7, 35] the form

$$J_{AA}(\mathbf{R}) = \frac{\hbar v_F}{2R^3} C f_{AA}(\mathbf{R}) \tag{3.2.11}$$

In a similar way we can treat the interaction between two moments which reside on different sublattices. In this case the exchange integral can be brought to the following form

$$J_{BA}(\mathbf{R}) = -\frac{8\hbar v_F}{R^3} C f_{BA}(\mathbf{R}) \lim_{s \to 0} \int_0^\infty dx \int_0^\infty dx' \, \frac{x x' J_1(x) J_1(x')}{x + x'} \, e^{-s(x+x')}$$
(3.2.12)

where the double integral can be explicitly calculated, which yields as shown in Refs. [1, 3, 4, 5, 6, 7, 35] the following result

$$J_{BA}(\mathbf{R}) = -\frac{3\hbar v_F}{2R^3} C f_{BA}(\mathbf{R})$$
(3.2.13)

We see that, in contrast to a usual two-dimensional electron gas, the RKKY interaction in graphene oscillates, due to the functions $f_{AA}(\mathbf{R})$ or $f_{BA}(\mathbf{R})$, on the scale of the lattice constant. It decays with a $1/R^3$ envelope function and it depends on the sublattice position of both impurities: for two moments on the same sublattice the coupling is ferromagnetic while for two moments on opposite sublattice the coupling is antiferromagnetic.

Doped Monolayer Graphene

At higher Fermi energies the particular form of the energy spectrum becomes less important and we obtain an RKKY interaction which highly resembles that in a usual two-dimensional electron gas. This can be seen as follows: when the Fermi energy is fixed at a value $E_F > 0$ the Hankel function can be replaced by its asymptotics for large arguments that is presented in Appendix B.3.4. Under these circumstances the exchange integrals can be taken analytically. In the case of impurity spins on the

same sublattice we get following Ref. [2] the result

$$J_{AA}(\mathbf{R}) = \frac{4\hbar v_F}{R^3} C f_{AA}(\mathbf{R}) \lim_{s \to 0} \int_{k_F R}^{\infty} dx \ x^2 \Im \left[-\frac{2i}{\pi x} e^{2ix} \left(1 - \frac{i}{4x} \right) \right] e^{-sx} =$$

$$= \frac{4}{\pi R^2} C f_{AA}(\mathbf{R}) \left[E_F \sin(2k_F R) + \frac{\hbar v_F}{4R} \cos(2k_F R) \right]$$
(3.2.14)

with $k_F = E_F/(\hbar v_F)$. For two impurities on different sublattices the same calculation yields in agreement with Ref. [2] the result

$$J_{BA}(\mathbf{R}) = \frac{4\hbar v_F}{R^3} C f_{BA}(\mathbf{R}) \lim_{s \to 0} \int_{k_F R}^{\infty} dx \ x^2 \Im \left[\frac{2i}{\pi x} e^{2ix} \left(1 + \frac{3i}{4x} \right) \right] e^{-sx} =$$

$$= -\frac{4}{\pi R^2} C f_{BA}(\mathbf{R}) \left[E_F \sin \left(2k_F R \right) + \frac{5\hbar v_F}{4R} \cos \left(2k_F R \right) \right]$$
(3.2.15)

The RKKY interaction decays with a $1/R^2$ envelope function and oscillates, as expected, with the wave number $2k_F$ changing sign between a ferro- and an antiferromagnetic coupling.

The RKKY Interaction in Monolayer Graphene at Finite Temperature

In the zero temperature formalism we found a non-vanishing RKKY interaction in the undoped monolayer where the number of free charge carriers is zero. When the temperature is increased electrons are excited into the conduction band leaving holes in the conduction band and this launches two countervailing processes. On the one hand more states become available which is expected to increase the strength of the interaction and on the other hand the smearing of the Fermi surface is known to cause an asymptotic damping of the interaction[39]. In the following sections we want to figure out which of these processes dominates and whether the unusual features of the RKKY interaction survive at finite temperature. To this end we consider, similar to the previous section, two magnetic impurities in the gas of Dirac-Weyl electrons and we want to describe the coupling of impurity spins as a function of the impurity position, the chemical potential μ and the temperature T. For two moments on the same sublattice we find the exchange integral given by

$$\mathcal{J}_{AA}(\mathbf{R}) = \frac{16}{\pi \beta} C f_{AA}(\mathbf{R}) \sum_{n=-\infty}^{+\infty} \left(\frac{\hbar \omega_n - i\mu}{\hbar v_F} \right)^2 K_0 \left(\text{sign} \left(\omega_n \right) \frac{\hbar \omega_n - i\mu}{\hbar v_F} R \right)^2$$
(3.3.1)

while for two moments on opposite sublattice we get

$$\mathcal{J}_{BA}(\mathbf{R}) = -\frac{16}{\pi\beta} C f_{BA}(\mathbf{R}) \sum_{n=-\infty}^{+\infty} \left(\frac{\hbar\omega_n - i\mu}{\hbar v_F} \right)^2 K_1 \left(\operatorname{sign}(\omega_n) \frac{\hbar\omega_n - i\mu}{\hbar v_F} R \right)^2 \quad (3.3.2)$$

with $C = -\lambda^2 \hbar^2 a^2/(64\pi t^2)$ and $\omega_n = \pi (2n+1)/(\hbar \beta)$. In both cases the exchange integral separates into the product of an intervalley and an intravalley function. The intervalley scattering functions $f_{AA}(\mathbf{R})$ and $f_{BA}(\mathbf{R})$ are independent of the temperature and defined in Eqs. (3.2.2) and (3.2.4).

Asymptotic Expansion

For large impurity separations we can replace the modified Bessel functions in Eqs. (3.3.1) and (3.3.2) by their asymptotics. We begin with the interaction between two moments on the same sublattice which has the asymptotic form

$$\mathcal{J}_{AA}(\mathbf{R}) = \frac{8}{\beta R} C f_{AA}(\mathbf{R}) \sum_{n=-\infty}^{+\infty} \left[\operatorname{sign}(\omega_n) \frac{\hbar \omega_n - i\mu}{\hbar v_F} - \frac{1}{4R} \right] e^{-2\operatorname{sign}(\omega_n) \frac{\hbar \omega_n - i\mu}{\hbar v_F} R} \quad (3.3.3)$$

In order to evaluate the Matsubara sum analytically we proceed as follows: first we introduce the differential operator [d/(dR) + 1/(2R)] and get

$$\mathcal{J}_{AA}(\mathbf{R}) = -\frac{4Cf_{AA}(\mathbf{R})}{R} \left(\frac{d}{dR} + \frac{1}{2R}\right) k_B T \sum_{n=-\infty}^{+\infty} e^{-2\operatorname{sign}(\omega_n) \frac{\hbar \omega_n - i\mu}{\hbar v_F} R}$$
(3.3.4)

Then we split the sum into two parts that are both taken over positive values of n. Both parts correspond to a geometric series which can be taken and lead to the expression

$$k_B T \sum_{n=-\infty}^{+\infty} e^{-2\operatorname{sign}(\omega_n) \frac{\hbar \omega_n - i\mu}{\hbar v_F} R} = \cos\left(\frac{2\mu}{\hbar v_F} R\right) F_1 \tag{3.3.5}$$

where we defined

$$F_1 = \frac{k_B T}{\sinh\left(\frac{2\pi k_B TR}{\hbar v_F}\right)} \tag{3.3.6}$$

Finally we insert Equation 3.3.5 into 3.3.4, take the derivative with respect to R and obtain the following result

$$\mathcal{J}_{AA}(\mathbf{R}) = \frac{8Cf_{AA}(\mathbf{R})}{\hbar v_F R} F_1 \left[\mu \sin \left(\frac{2\mu}{\hbar v_F} R \right) + \pi F_2 \cos \left(\frac{2\mu}{\hbar v_F} R \right) - \frac{\hbar v_F}{4R} \cos \left(\frac{2\mu}{\hbar v_F} R \right) \right],$$
(3.3.7)

in which we have further defined

$$F_2 = \frac{k_B T}{\tanh\left(\frac{2\pi k_B T R}{\hbar v_F}\right)} \tag{3.3.8}$$

For two moments on different sublattices the same calculation yields

$$\mathcal{J}_{BA}(\mathbf{R}) = -\frac{8Cf_{BA}(\mathbf{R})}{\hbar v_F R} F_1 \left[\mu \sin \left(\frac{2\mu}{\hbar v_F} R \right) + \pi F_2 \cos \left(\frac{2\mu}{\hbar v_F} R \right) + \frac{3\hbar v_F}{4R} \cos \left(\frac{2\mu}{\hbar v_F} R \right) \right]. \tag{3.3.9}$$

Here it is important to stress that the $T \to 0$ and the $\mu \to 0$ limit of Eq. (3.3.7) and Eq. (3.3.9) cannot be taken at the same time since both expressions are obtained from the large argument asymptotics of the modified Bessel functions which is, for $\mu = 0$ and T = 0, no longer valid. The temperature dependence of the RKKY interaction can be seen in 3.2a) where the asymptotic form of $\mathcal{J}_{AA}(\mathbf{R})$ (red dashed line) and the exact exchange integral (black solid line) is plotted as a function of temperature for the undoped monolayer. Both curves, the asymptotic form and the exact exchange

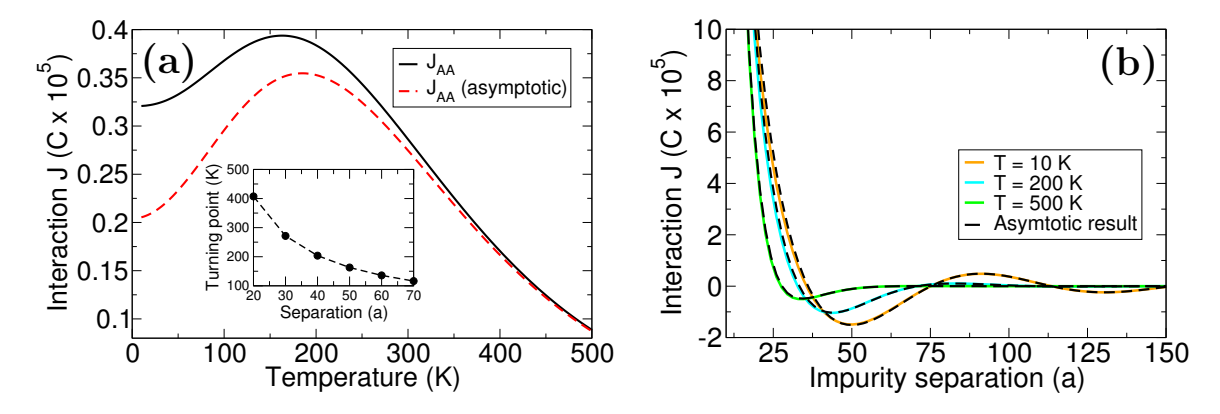


Figure 3.2: The RKKY interaction in pristine and doped graphene. In Fig. (3.2a) the exchange integral of pristine graphene $\mathcal{J}_{AA}(\mathbf{R})$ is plotted as a function of temperature at an impurity separation of 50a. The black solid line represents the exact result that is obtained from a numerical evaluation of Eq. (3.3.1) while the red dashed line represents the asymptotic form which is given by Eq. (3.3.7). The interaction is plotted in armchair direction where the function $f_{AA}(\mathbf{R})$ takes a constant value and is furthermore expressed in terms of the constant $C \times 10^5$. This means that the coupling is ferromagnetic for positive values of J(C) and negative for negative values of J(C). The inset of Fig. (3.2a) shows the temperature of the maximum for different impurity separations. In Fig. (3.2b) the chemical potential is increased to a value of 0.1eV and the interaction between two moments on the A sublattice is plotted versus the impurity separation for three different temperatures.

integral, are in particular at high temperature in good agreement and have a maximum at about 153K. At low temperature the interaction increases in both cases with increasing temperature and this is in fact the region where the increasing number of states that contribute to the RKKY interaction outweighs the exponential damping that comes from the smearing of the Fermi surface. At high temperature the RKKY interaction is governed by the exponential damping. This behaviour can be imme-

diately understood from Eq. (3.3.7): the temperature dependence is hidden in the two coefficients F_1 and F_2 . The product of both coefficients increases linearly for low temperature, has a maximum at some finite temperature and decreases exponentially with the coefficient $F_1 \propto \exp[-2\pi k_B T R/(\hbar v_F)]$ for large temperature. Since the latter coefficient is a function of the product TR at larger separation R the exponential decay gets stronger and reduces the temperature up to which the unusual increase of the RKKY interaction persists. The temperature of the maximum plotted as a function of the impurity separation is presented in the small inset of Fig. (3.2a). When the chemical potential is increased to a sufficiently large value the RKKY interaction of a normal metal is recovered. The interaction oscillates with the wave vector $2k_F$ and decreases at high temperature exponentially in the impurity separation. This can be seen in Fig. (3.2b) which shows the evolution of the exchange integral as a function of the impurity separation for different temperature.

Zero Temperature Limit

In the zero temperature limit we recover the results that we derived in Section 3.2. This can be seen easily for undoped monolayer graphene: the Matsubara sum in Eq. (3.3.1) and Eq. (3.3.2) turns into an integral which can be taken analytically. After the substitution $x = \omega R/v_F$ the exchange integral for two moments on the same sublattice reduces to the form

$$\mathcal{J}_{AA}(\mathbf{R}) = \frac{8\hbar v_F}{\pi^2 R^3} C f_{AA}(\mathbf{R}) \int_{-\infty}^{+\infty} dx \ x^2 K_0 (|x|)^2$$
$$= \frac{\hbar v_F}{2R^3} C f_{AA}(\mathbf{R})$$
(3.3.10)

and for two moments on opposite sublattice the exchange integral converges to the expression

$$\mathcal{J}_{BA}(\mathbf{R}) = -\frac{8\hbar v_F}{\pi^2 R^3} C f_{BA}(\mathbf{R}) \int_{-\infty}^{+\infty} dx \ x^2 K_1 \left(|x|\right)^2$$
$$= -\frac{3\hbar v_F}{2R^3} C f_{BA}(\mathbf{R}) \tag{3.3.11}$$

In the doped monolayer we can recover zero temperature results from an expansion of Eqs. (3.3.9) and (3.3.7) about T = 0. This procedure yields for $\mathcal{J}_{AA}(\mathbf{R})$ the following expression

$$\mathcal{J}_{AA}(\mathbf{R}) = \frac{4}{\pi R^2} C f_{AA}(\mathbf{R}) \left(\mu \sin \left(\frac{2\mu}{\hbar v_F} R \right) + \frac{\hbar v_F}{4R} \cos \left(\frac{2\mu}{\hbar v_F} R \right) - \frac{2\pi^2 k_B^2 R^2}{3\hbar^2 v_F^2} T^2 \left[\mu \sin \left(\frac{2\mu}{\hbar v_F} R \right) - \frac{3\hbar v_F}{4R} \cos \left(\frac{2\mu}{\hbar v_F} R \right) \right] \right)$$
(3.3.12)

and for $\mathcal{J}_{BA}(\mathbf{R})$ we get

$$\mathcal{J}_{BA}(\mathbf{R}) = -\frac{4}{\pi R^2} C f_{BA}(\mathbf{R}) \left(\mu \sin \left(\frac{2\mu}{\hbar v_F} R \right) + \frac{5\hbar v_F}{4R} \cos \left(\frac{2\mu}{\hbar v_F} R \right) - \frac{2\pi^2 k_B^2 R^2}{3\hbar^2 v_F^2} T^2 \left[\mu \sin \left(\frac{2\mu}{\hbar v_F} R \right) + \frac{\hbar v_F}{4R} \cos \left(\frac{2\mu}{\hbar v_F} R \right) \right] \right)$$
(3.3.13)

The RKKY Interaction between Plaquette Impurities

Up to this point we focused on the RKKY interaction between impurities that couple via a contact interaction to the electron spin density at a single site. This coupling scheme holds as long as the covalent radius of the impurity is significantly smaller than the lattice constant of graphene. However, practically any atom with a substantial magnetic moment, such as a lanthanide or a transition metal, has a covalent radius that is much greater than the graphene lattice constant. For this reason it is more realistic to assume that the impurity couples to a set of lattice sites and prefers a high symmetry position in the graphene lattice rather than the position directly on top of a carbon atom. In this section we study the RKKY interaction between two impurities that are each sitting in the center of a hexagonal plaquette. We begin with a very simple coupling model, the incoherent coupling scheme, where each impurity couples only via on-site spin-flip to the six surrounding carbon atoms. In such a model the exchange integral follows from a sum over all 36 site-to-site interactions

$$\mathcal{J}_{\text{plaq}}(\mathbf{R}) = \sum_{a_1=1}^{6} \sum_{a_2=1}^{6} \mathcal{J}_{\alpha_{a_2}\alpha_{a_1}}(\mathbf{r}_{a_2} - \mathbf{r}_{a_1})$$
(3.4.1)

where \mathbf{r}_{a_1} (\mathbf{r}_{a_2}) and α_{a_1} (α_{a_2}) represent the position vector and the sublattice of a carbon atom in the local environment of the first (second) impurity. As shown in Section 3.2 each site-to-site exchange integral $\mathcal{J}_{\alpha_{a_1}\alpha_{a_2}}(\mathbf{r}_{a_2} - \mathbf{r}_{a_1})$ is a product of an intervalley and an intravalley scattering function. For a further analytical evaluation of Eq. (3.4.1) we approximate the intravalley scattering function by $\mathcal{I}(|\mathbf{R}\pm\mathbf{v}|) \approx \mathcal{I}(R)$ and use the identity $f_{\alpha\alpha'}(\mathbf{R}) + f_{\alpha\alpha'}(\mathbf{R}-\mathbf{v}) + f_{\alpha\alpha'}(\mathbf{R}+\mathbf{v}) = 3$, where \mathbf{R} is the separation of the two plaquette centers and \mathbf{v} stands for a small lattice vector. This procedure yields an RKKY exchange integral that is isotropic in space:

$$\mathcal{J}_{\text{plaq}}(R) = 18C \left[\mathcal{I}_{AA}(R) + \mathcal{I}_{BA}(R) \right]$$
(3.4.2)

The exchange integral is here expressed in terms of the site-to-site intravalley scattering functions $\mathcal{I}_{AA}(R)$ and $\mathcal{I}_{BA}(R)$, which can be for $\mu = 0$ and T = 0 extracted from Eqs. (3.3.10) and (3.3.11). Substitution of these expressions into Eq. (3.4.2) leads in

agreement with Refs. [1, 5] to the following result:

$$\mathcal{J}_{\text{plaq}}(R) = -\frac{18\hbar v_F}{R^3}C\tag{3.4.3}$$

For $\mu > 0$ we use the leading order of the temperature expansion, Eq. (3.3.12) and Eq. (3.3.13), and find the RKKY interaction asymptotically given by:

$$\mathcal{J}_{\text{plaq}}(R) = -\frac{72\hbar v_F}{\pi R^3} C \cos\left(\frac{2\mu}{\hbar v_F}R\right)$$
(3.4.4)

In pristine graphene the interaction is antiferromagnetic and decays as $1/R^3$. From

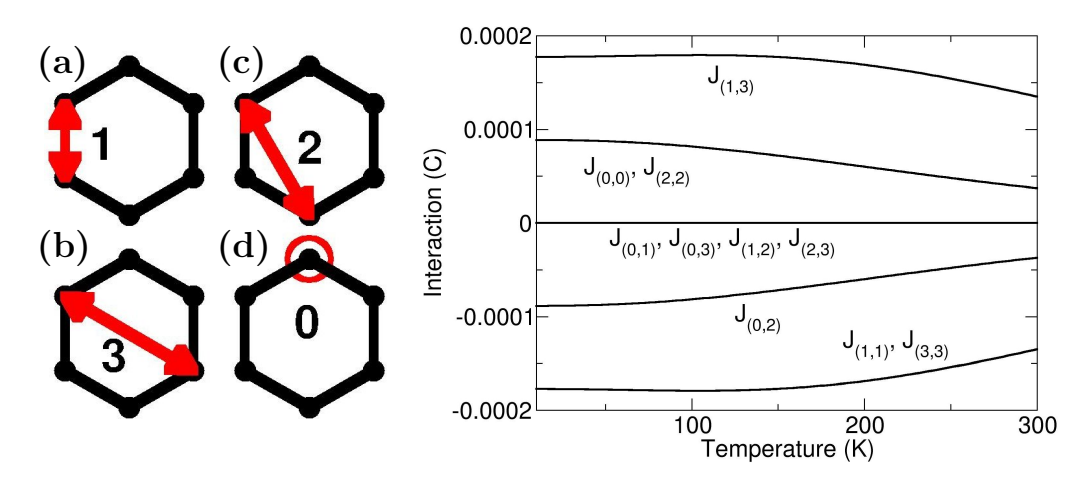


Figure 3.3: The RKKY interaction between two plaquette impurities in pristine monolayer graphene. From the geometry of the plaquette it can be seen that each impurity can couple to the six surrounding lattice sites via four distinct nearest-neighbor spin-flip processes. In the picture on the right hand side the ten distinct RKKY exchange integrals $\mathcal{J}_{(i,j)}$ are plotted as a function of temperature at an impurity separation of 20a. The notation $\mathcal{J}_{(i,j)}$ means that the first impurity spin couples to the gas of delocalized electrons via i^{th} and the second impurity couples via j^{th} nearest-neighbor spin-flip process. The interaction is expressed in terms of the constant C.

Eq. (3.4.4) it can be seen that the unusual $1/R^3$ decay holds even for doped monolayer graphene where surprisingly the $1/R^2$ -order of the site-to-site exchange integrals cancels and the interaction oscillates with the period which is determined by the chemical potential between ferro- and antiferromagnetic types.

Naturally there arises the question how robust the result is under a change of the local electron-impurity coupling scheme. In order to figure this out we now turn to the most general case where each impurity couples to the six surrounding carbon atom sites via on-site as well as inter-site spin-flip process, as introduced in Sec. 2.3.1. From the geometry of the plaquette, shown in Fig. (3.3), it is clear that there are four such processes: the on-site and the first, second, and third nearest-neighbor spin-flip process which are labeled by the numbers i = 0, 1, 2, 3. Accordingly, the RKKY interaction between two plaquette impurities may be written as a linear combination of

 4×4 exchange integrals of the type $\mathcal{J}_{(i,j)}$ that describe in each case the coupling of the first (second) impurity to the gas of delocalized electrons via a *i*th (*j*th) nearest-neighbor spin-flip process. Due to the symmetry $\mathcal{J}_{(i,j)} = \mathcal{J}_{(j,i)}$ there are only ten

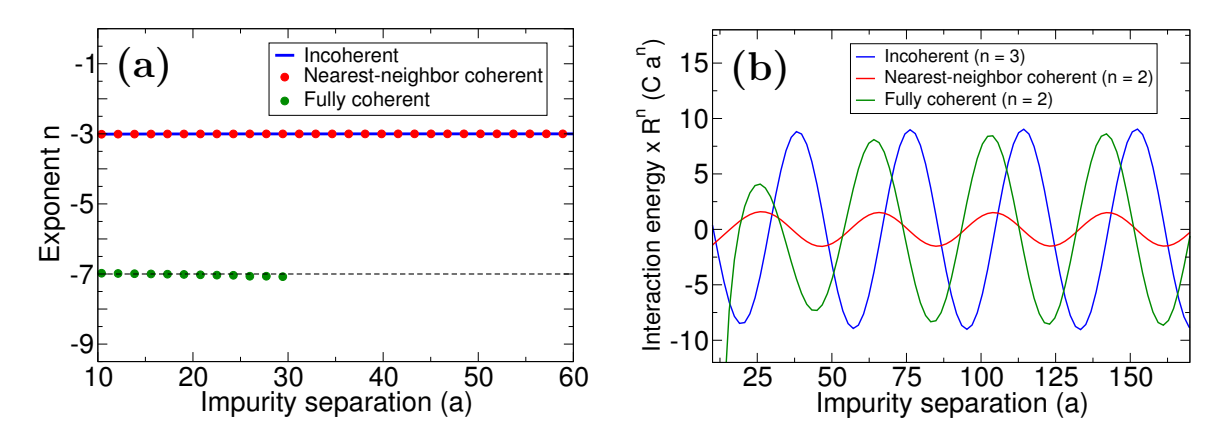


Figure 3.4: The RKKY interaction between two plaquette impurities in pristine and in doped monolayer graphene at zero temperature for three different coupling schemes: incoherent, nearest-neighbor coherent and fully coherent. In pristine monolayer graphene the RKKY interaction decays monotonically as R^{-n} with a power that depends significantly on the local coupling scheme. In Fig. (3.4a) the exponent $n = \log_{10} [J(R)/J(R_0)]$ is plotted as a function of the impurity separation, where R_0 is to the largest separation that can be calculated within floating point precision ($\approx 35a$). In Fig. (3.4b) the chemical potential is increased to 0.1eV. The RKKY interaction oscillates in armchair direction with the period of the chemical potential μ and decays as R^{-2} , in both coherent coupling schemes, and as R^{-3} , in the incoherent coupling scheme. For presentational reason the exchange integral of the fully coherent coupling scheme is multiplied by 10^5 .

distinct exchange integrals. These exchange integrals are plotted in Fig. (3.3) as a function of temperature at zero chemical potential and an impurity separation of 20a. It can be seen that the choice of the coupling scheme does have a serious impact on the form of the RKKY interaction: $\mathcal{J}_{(0,0)}$, $\mathcal{J}_{(0,2)}$ and $\mathcal{J}_{(2,2)}$ decrease monotonically while $\mathcal{J}_{(1,1)}$, $\mathcal{J}_{(1,3)}$ and $\mathcal{J}_{(3,3)}$ increase monotonically with temperature. In all other cases the exchange integral is zero. For the total exchange integral of the plaquette impurity which corresponds to the linear combination of the individual $\mathcal{J}_{(i,j)}$'s it is essential to know how the different processes are weighted relative to each other. A reliable answer would require a detailed information about the orbital structure of the impurity which then allows to determine by ab initio calculation the precise electron-impurity coupling scheme. Rather than providing this specific information we present here exemplarily three possible coupling schemes: the incoherent coupling scheme, the nearest-neighbor coherent coupling scheme and the fully coherent coupling scheme. The incoherent coupling scheme takes only on-site spin-flip processes into account and was discussed in an analytical approach earlier in this section. In the nearest-neighbor coherent coupling scheme only on-site and inter-site spin-flip processes between nearest-neighbor carbon atoms contribute and in the fully coherent coupling scheme all possible scattering processes are taken into account. These three coupling schemes are compared in Fig. (3.4) at T=0 and under the assumption that all spin-flip processes are weighted by the same coupling constant. From the picture on the left, where the chemical potential is set to zero, it can be clearly seen that the RKKY interaction shows an unusual $1/R^7$ decay rate in the fully coherent coupling scheme. This decay rate holds as long as all coupling constants are the same. When different coupling constants are used the fully coherent coupling scheme is dominated by the usual $1/R^3$ decay which is also found in the other two coupling schemes. In the doped monolayer the RKKY interaction decays in the incoherent coupling scheme as $1/R^3$ and in both coherent coupling schemes as $1/R^2$. From these results we have to conclude that the RKKY interaction is very sensitive to the local coupling scheme. This is an important difference to a common electron gas which arises from the multivalley structure of the graphene spectrum.

The RKKY Interaction in Bilayer Graphene

Bilayer graphene is a compound of two graphene layers that is held together by vander-Waals forces. Since these forces are weak compared to the in-plane covalent bonding the distance between the two layers is much greater than the lattice constant of graphene. Another consequence of the weakness of the interlayer coupling is that various stacking configurations are possible. In this work we shall consider two of them: the AA stacking and the most common AB stacking (known as Bernal stacking, which is realized in graphite). The interlayer bonding, albeit weak, has a serious effect on the electronic properties of the bilayer. This can be seen, for example, at the band structure close to the Dirac point where the dispersion is parabolic for AB-stacked bilayer graphene and linear for AA-stacked bilayer graphene. The interesting form of the spectrum manifests in an unusual RKKY interaction which is the subject of the current chapter. We start with the RKKY interaction in AA-stacked bilayer graphene

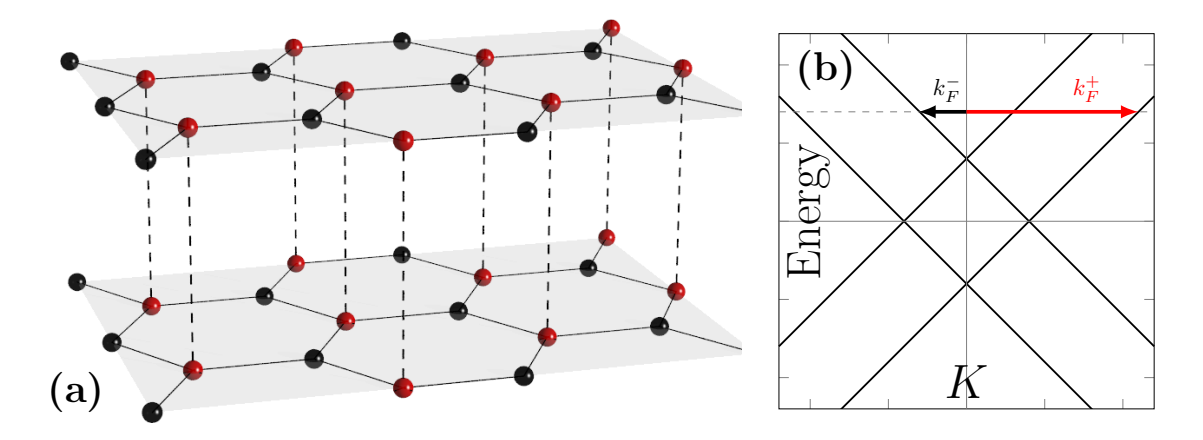


Figure 4.1: Illustration of AA-stacked bilayer graphene. The crystal structure [Fig. (4.1a)] and the band structure in vicinity of the K point [Fig. (4.1b)].

which is less common in nature. It serves here mainly as an introductory model that allows us to study the interference effects that arise from the interlayer coupling. Next we come to AB-stacked bilayer graphene which is indeed a stable configuration that is realized in nature and we shall study in this system the effect of temperature on the RKKY interaction. Finally we conclude the chapter with the RKKY interaction

in an AB-stacked bilayer to which an external layer-symmetry breaking electric field is applied.

AA-stacked Bilayer Graphene

The AA-stacked bilayer is, perhaps, the simplest example of a few layer graphene. In that stacking configuration the two graphene layers are sitting directly on top of each other so that all carbon atoms in the top and in the bottom layer are vertically aligned. The Brillouin zone is the same as for the graphene monolayer with two inequivalent K points. The low energy excitations in the vicinity of each K point can be described by a Hamiltonian that takes into account, in addition to the usual nearest-neighbor in-plane hopping of electrons, also the vertical interlayer hopping. In the basis of the four Bloch sums $|\Psi_{A_1}^{\bf k}\rangle$, $|\Psi_{B_1}^{\bf k}\rangle$, $|\Psi_{A_2}^{\bf k}\rangle$ and $|\Psi_{B_2}^{\bf k}\rangle$ the Hamiltonian reads [90, 92]

$$H_m^0(\mathbf{k}) = \begin{pmatrix} 0 & \tilde{\Phi}_m(\mathbf{k}) & -t_{\perp} & 0\\ \tilde{\Phi}_m^*(\mathbf{k}) & 0 & 0 & -t_{\perp}\\ -t_{\perp} & 0 & 0 & \tilde{\Phi}_m(\mathbf{k})\\ 0 & -t_{\perp} & \tilde{\Phi}_m^*(\mathbf{k}) & 0 \end{pmatrix}$$
(4.1.1)

where $m \in \{1, \dots, 6\}$ labels the position of the K point in the Brillouin zone, t_{\perp} stands for the interlayer hopping constant and $\tilde{\Phi}_m(\mathbf{k})$ is defined according to Eq. (3.1.4). It may be easily seen that the spectrum of the Hamiltonian consists of two Dirac cones which are shifted relative to each other by $2t_{\perp} \simeq 0.8eV$

$$\epsilon_{\sigma\sigma'}(k) = \sigma \left[\hbar v_F k + \sigma' t_\perp\right] \tag{4.1.2}$$

with $\sigma, \sigma' \in \{\pm\}$ and the Fermi velocity $v_F = \sqrt{3}at/(2\hbar)$. In the latter expression $a \approx 2.46\text{Å}$ is the lattice constant and $t \approx 2.8eV$ the nearest-neighbor hopping ampli-

	AA-stacked BLG		AB-stacked BLG	
	$ E < t_{\perp}$	$ E > t_{\perp}$	$ E < t_{\perp}$	$ E > t_{\perp}$
$\rho_{A_{1,2}}(E)$	$2t_{\perp}$	2 E	E	2 E
$\rho_{B_{1,2}}(E)$	$2t_{\perp}$	2 E	$ E + t_{\perp}$	2 E
$\rho(E)$	$8t_{\perp}$	8 E	$2(2 E +t_{\perp})$	8 E

Table 4.1: The DOS of AA- and AB-stacked bilayer graphene [90, 91]. For each system the DOS can be brought to the form $D_{\alpha_l}(E) = 2D_0 \ \rho_{\alpha_l}(E)$ with $D_0 = \pi/(2\hbar^2 v_F^2 \Omega_{BZ})$. The first two rows of this table define the function $\rho_{\alpha_l}(E)$ with $\alpha \in \{A, B\}$ and $l \in \{1, 2\}$. The last row defines the function $\rho(E)$ which is obtained from the sum over all four sites.

tude. The corresponding DOS is presented in Table (4.1). In contrast to the DOS of monolayer graphene the DOS of AA-stacked bilayer graphene takes a constant value at low energies and has a kink, i.e. a discontinuity in the derivative, at the apex of the upper and lower Dirac cone.

The RKKY Interaction at Zero Temperature

The emergence of a second Dirac cone in the spectrum opens an additional scattering channel and results in a DOS that is, at low energies, constant. This should have a great impact on the RKKY interaction and the goal of this section is to show how the form of the interaction changes when the additional channel is switched on. To this end we consider two magnetic impurities that both couple via the site of a carbon atom to the gas of delocalized electrons. The interaction energy can be obtained from the standard Green's function approach that was introduced in Section 2.1.2. This approach requires the Green's functions of AA-stacked bilayer graphene which is in the low energy approximation given by

$$\mathbf{G}^{0R}(\mathbf{R}, E) = \sum_{m=1}^{2} \mathbf{G}_{m}^{0R}(\mathbf{R}, E) \exp(i\mathbf{K}_{m}.\mathbf{R})$$

where $\mathbf{G}_{m}^{0R}(\mathbf{R},E)$ is the real space Fourier transform of the retarded momentum space Green's function $G_{m}^{0}(\mathbf{k},E)=[E+i\eta-H_{m}^{0}(\mathbf{k})]^{-1}$ which is tabulated in Appendix C.1. Using this result, we can calculate the exchange integral in each of the four distinct cases where the two impurities reside either on the same or on opposite sublattice in the same or in the opposite layer

$$J_{A_l A_{l'}}(\mathbf{R}) = C f_{A_1 A_1}(\mathbf{R}) \int_{E_F}^{\infty} dE \,\Im\left(\left[z^+ H_0^1 \left(z^+ R\right) + (-1)^{l-l'} z^- H_0^1 \left(z^- R\right)\right]^2\right) \,(4.1.3)$$

$$J_{B_l A_{l'}}(\mathbf{R}) = C f_{B_1 A_1}(\mathbf{R}) \int_{E_F}^{\infty} dE \,\Im\left(\left[z^+ H_1^1 \left(z^+ R\right) + (-1)^{l-l'} z^- H_1^1 \left(z^- R\right)\right]^2\right) \,(4.1.4)$$

with $C = -\lambda^2 \hbar^2 a^2/(256\pi t^2)$, $z^+ = (E + i\eta + t_\perp)/(\hbar v_F)$ and $z^- = (E + i\eta - t_\perp)/(\hbar v_F)$. The function $H^1_{\nu}(x)$ stands for the Hankel function of the first kind and ν th order and \mathbf{R} is the impurity separation vector which is in polar coordinates given by the radius R and the polar angle θ . Each exchange integral is the product of an intravalley contribution $I_{\alpha\alpha'}(R)$ and an intervalley scattering function $f_{\alpha\alpha'}(\mathbf{R})$. The intravalley functions may be directly read off from Eqs. (4.1.3) and (4.1.4) and the two intervalley scattering functions are defined as

$$f_{A_1A_1}(\mathbf{R}) = f_{AA}(\mathbf{R}) \tag{4.1.5}$$

$$f_{B_1A_1}(\mathbf{R}) = f_{BA}(\mathbf{R}) \tag{4.1.6}$$

with $f_{AA}(\mathbf{R})$ and $f_{BA}(\mathbf{R})$ given by Eqs. (3.2.2) and (3.2.4). The exchange integrals can be evaluated numerically at any distance and at any Fermi energy E_F . However,

for an analytical investigation it is convenient to consider the case of large impurity separations where Eqs. (4.1.3) and (4.1.4) can be written as

$$J_{\alpha_{l}\alpha'_{l'}}(\mathbf{R}) = (-1)^{\nu_{\alpha\alpha'}+1} \frac{2C}{\pi R} f_{\alpha_{l}\alpha'_{l'}}(\mathbf{R})$$

$$\times \lim_{s \to 0} \int_{E_F}^{\infty} dE \,\Re\left(\left[\sqrt{z^{+}} e^{iz^{+}R} + (-1)^{l'-l} \sqrt{z^{-}} e^{iz^{-}R}\right]^{2}\right) e^{-sE}$$
(4.1.7)

with $\nu_{\alpha\alpha'} = 1 - \delta_{\alpha\alpha'}$, $\alpha \in \{A, B\}$ taken for the sublattice and $l \in \{1, 2\}$ for the layer of each impurity. The Kronecker Delta $\delta_{\alpha\alpha'}$ is 1 if both impurities are on the same sublattice and 0 if both impurities are on opposite sublattice. Furthermore it is important to stress that the energy has always a small, positive imaginary part which is important near the singularities of the Green's function and which ensures via an exponential damping factor the convergence of the exchange integrals. The integral can be taken by integration by parts. This procedure yields in the leading order the following result

$$J_{\alpha_{l}\alpha'_{l'}}(\mathbf{R}) = (-1)^{\nu_{\alpha\alpha'}} \frac{C\hbar v_{F}}{\pi R^{2}} f_{\alpha_{l}\alpha'_{l'}}(\mathbf{R}) \left[k_{F}^{+} \sin\left(2k_{F}^{+}R\right) + k_{F}^{-} \sin\left(2k_{F}^{-}R\right) + 2(-1)^{l'-l} \sqrt{|k_{F}^{+}k_{F}^{-}|} \sin\left(\left[k_{F}^{+} + k_{F}^{-}\right]R + \frac{\pi}{2}\Theta\left[t_{\perp} - E_{F}\right]\right) \right]$$
(4.1.8)

with $k_F^+ = (E_F + t_\perp)/(\hbar v_F)$ and $k_F^- = (E_F - t_\perp)/(\hbar v_F)$. A further simplification of this expression is possible in the limit of very high or very low Fermi energy and in the case where the Fermi energy lies exactly at the apex of the upper or the lower Dirac cone. We start with the limit $E_F \ll t_\perp$ where Eq. (4.1.8) can be brought to the form

$$J_{\alpha_{l}\alpha'_{l'}}(\mathbf{R}) = (-1)^{l'-l+\nu_{\alpha\alpha'}} \frac{4Ct_{\perp}}{\pi R^{2}} f_{\alpha_{l}\alpha'_{l'}}(\mathbf{R})$$

$$\times \cos\left(2\frac{E_{F}}{\hbar v_{F}}R\right) \cos^{2}\left(\frac{t_{\perp}}{\hbar v_{F}}R + \frac{\pi}{2}\left[l' - l\right] - \frac{\pi}{4}\right)$$
(4.1.9)

The exchange integral factorizes into the product of two oscillatory parts. On the one hand there is an oscillation with the wavelength $\lambda_{\perp} = \pi \hbar v_F/t_{\perp}$ which arises from the interlayer scattering of electrons. On the other hand there occurs the usual Fermi energy dependent oscillation with the wave length $\lambda_F = \pi \hbar v_F/E_F$ that was already found for the interaction in monolayer graphene. In the limit $E_F \to 0$ the wave length of the latter type of oscillation continuously increases. Remarkably, Eq. (4.1.9) is valid for the case $E_F = 0$ where solely one type of oscillation with finite wave length $\lambda_{\perp} = \pi \hbar v_F/(2t_{\perp})$ remains. This case is particularly interesting since the interaction is now exclusively determined by sublattice and layer position of both impurities. The interaction is antiferromagnetic for even values of $l - l' + \nu_{\alpha\alpha'}$, which is for example the case when the two moments reside on the same sublattice of the same layer, and ferromagnetic for odd values of $l - l' + \nu_{\alpha\alpha'}$. The low energy approximation,

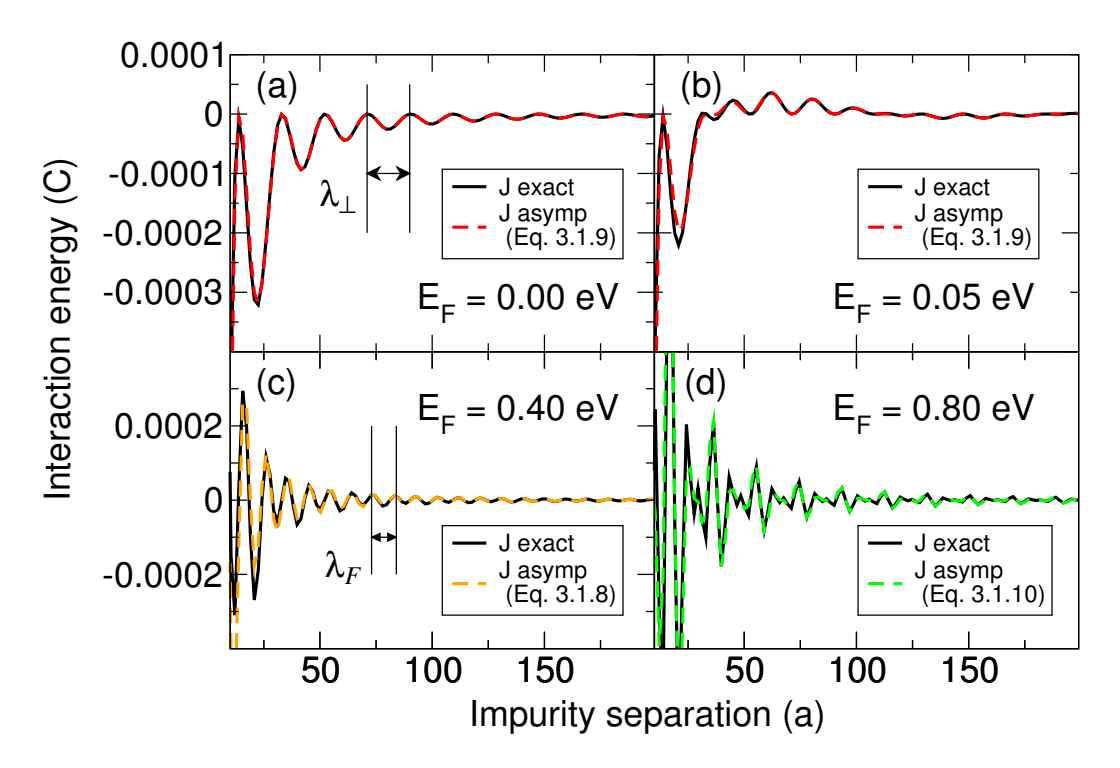


Figure 4.2: The RKKY interaction in AA-stacked bilayer graphene at a Fermi energy of 0eV, 0.05eV, 0.4eV and 0.8eV. Plotted is the exact exchange integral and the asymptotic form of the interaction as a function of the impurity separation for two moments that reside on sublattice A of the same layer. The interaction is always plotted in armchair direction and measured in terms of the constant C. Negative values of J(C) correspond to antiferromagnetic coupling.

Eq. (4.1.9), becomes less and less accurate for higher Fermi energy and we have to go back to Eq. (4.1.8). Especially, at $E_F = t_{\perp}$ we obtain the asymptotic form from a substitution of $k_F^- = 0$ and $k_F^+ = 2t_{\perp}/(\hbar v_F)$. In this way we find an interaction that oscillates with the period $\lambda_{\perp} = \pi \hbar v_F/(2t_{\perp})$. It is interesting to note that this is exactly half of the wavelength which is found for the case $E_F = 0$. Finally in the limit $E_F >> t_{\perp}$ the Eq. (4.1.8) can be approximated as

$$J_{\alpha_{l}\alpha'_{l'}}(\mathbf{R}) = (-1)^{l'-l+\nu_{\alpha\alpha'}} \frac{4CE_F}{\pi R^2} f_{\alpha_{l}\alpha'_{l'}}(\mathbf{R})$$

$$\times \sin\left(2\frac{E_F}{\hbar v_F}R\right) \cos^2\left(\frac{t_{\perp}}{\hbar v_F}R + \frac{\pi}{2}\left[l' - l\right]\right)$$
(4.1.10)

This expression consists of a short wavelength oscillation with the period $\lambda_F = \pi \hbar v_F/E_F$ which is modulated by another oscillation with the period $\lambda_{\perp} = \pi \hbar v_F/t_{\perp}$. The modulation with the long wave length is responsible for the beats which are seen in Fig. (4.2d). In the pictures we depicted the exact exchange integral which is obtained by numerical integration of Eq. (4.1.3) as well as the asymptotic form, Eq. (4.1.10). The Fermi energy is set to 0.8eV. The other three cases of doping can

be seen in Figs. (4.2a)-(4.2c). In all four cases the asymptotic form agrees for R > 10a very well with the exact exchange integral.

AB-stacked Bilayer Graphene

The most common realization of a graphene bilayer is the AB-stacked bilayer. In this stacking, the A-sites of both layers are vertically aligned while the B-sites of one layer are directly below or above of the center of the hexagonal plaquette of the other layer. In a model where only nearest neighbor in-plane and only the vertical interlayer hopping of electrons is taken into account the low energy physics at the K point is determined by the Hamiltonian [45, 47, 48, 91]

$$H_m^0(\mathbf{k}) = \begin{pmatrix} 0 & \tilde{\Phi}_m(\mathbf{k}) & -t_{\perp} & 0\\ \tilde{\Phi}_m^*(\mathbf{k}) & 0 & 0 & 0\\ -t_{\perp} & 0 & 0 & \tilde{\Phi}_m^*(\mathbf{k})\\ 0 & 0 & \tilde{\Phi}_m(\mathbf{k}) & 0 \end{pmatrix}$$
(4.2.1)

with $\tilde{\Phi}_m(\mathbf{k})$ taken from Eq. (3.1.4) and the interlayer hopping amplitude $t_{\perp} \approx 0.4 eV$. The spectrum of the Hamiltonian is given by

$$\epsilon_{\sigma\sigma'} = \sigma \left[\frac{t_{\perp}}{2} + \sigma' \sqrt{\hbar^2 v_F^2 k^2 + \frac{t_{\perp}^2}{4}} \right]$$
 (4.2.2)

with $\sigma, \sigma' \in \{\pm\}$. As may be seen in Fig. (4.3b) all four bands follow at low energies a parabolic dispersion. The two lowest bands touch at the Dirac point while the two

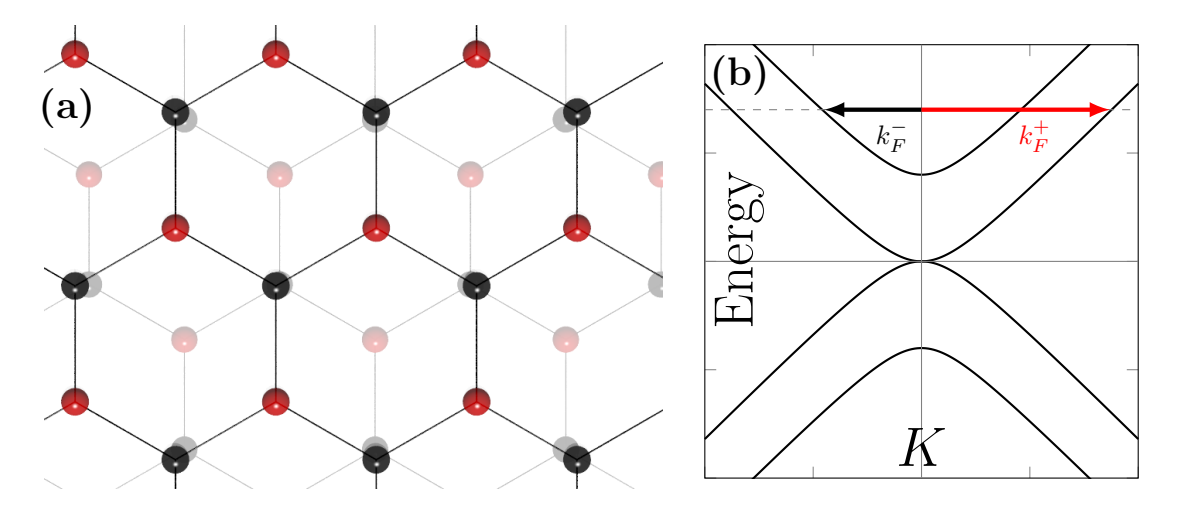


Figure 4.3: Illustration of AB-stacked bilayer graphene. The crystal structure [Fig. 4.3a)] and the spectrum in vicinity of each K point [Fig. 4.3b)]. At high doping the Fermi energy (dashed line) lies in the two band region of the spectrum. The two Fermi wave vectors k_F^+ and k_F^- are highlighted as a red and a black arrow.

outer ones, the bonding and antibonding bands, are separated by the gap of $2t_{\perp}$. An analytical expression for the DOS is presented in the right hand column of Table (4.1). Evidently, the DOS is particularly interesting inside the bonding-antibonding band gap where it takes different forms on sublattice A and B: on the A-sites the DOS starts at zero and grows with the absolute value of E. On the B-sites the DOS starts at a finite value and is significantly enhanced inside the bad gap. At the edge of the bonding-antibonding gap there is a discontinuity in the DOS on the A-sites and a kink in the DOS on the B-sites. Finally, in the two band region, the disparity between A-and B-sites disappears.

The RKKY Interaction at Zero Temperature

The electronic properties of AB-stacked bilayer graphene are quite different from those of monolayer and of the AA-stacked bilayer. The AB bilayer has two non-equivalent sites in the unit cell and at each K point a parabolic band structure with two distinct regions, the bonding-antibonding band gap and the two band region. The intention of

$$\frac{\alpha_{l}\alpha'_{l'}}{A_{1}A_{1}} = \frac{\int_{E_{F}}^{\infty} dE \, \frac{E^{2}}{\hbar^{2}v_{F}^{2}} \, \Im\left(\left[H_{0}^{1}\left(z^{+}R\right) + H_{0}^{1}\left(z^{-}R\right)\right]^{2}\right)}{\int_{E_{F}}^{\infty} dE \, \frac{E^{2}}{\hbar^{2}v_{F}^{2}} \, \Im\left(\left[H_{0}^{1}\left(z^{+}R\right) - H_{0}^{1}\left(z^{-}R\right)\right]^{2}\right)}$$

$$B_{1}B_{1} = \int_{E_{F}}^{\infty} dE \, \frac{\hbar^{2}v_{F}^{2}}{E^{2}} \, \Im\left(\left[(z^{+})^{2}H_{0}^{1}\left(z^{+}R\right) + (z^{-})^{2}H_{0}^{1}\left(z^{-}R\right)\right]^{2}\right)}$$

$$B_{2}B_{1} = \int_{E_{F}}^{\infty} dE \, \frac{\hbar^{2}v_{F}^{2}}{E^{2}} \, \Im\left(\left[(z^{+})^{2}H_{0}^{1}\left(z^{+}R\right) - (z^{-})^{2}H_{0}^{1}\left(z^{-}R\right)\right]^{2}\right)$$

$$B_{1}A_{1} = \int_{E_{F}}^{\infty} dE \, \Im\left(\left[z^{+}H_{1}^{1}\left(z^{+}R\right) + z^{-}H_{1}^{1}\left(z^{-}R\right)\right]^{2}\right)$$

$$B_{2}A_{1} = \int_{E_{F}}^{\infty} dE \, \Im\left(\left[z^{+}H_{1}^{1}\left(z^{+}R\right) - z^{-}H_{1}^{1}\left(z^{-}R\right)\right]^{2}\right)$$

Table 4.2: The six distinct intravalley scattering functions $I_{\alpha_l\alpha'_{l'}}(R)$ for AB-stacked bilayer graphene [54]. In this table $H_{\nu}(z^{\pm}R)$ stands for the Hankel function of the first kind and ν th order. The convergence is ensured by the positive real part of $z^{\pm}R = [(E+i\eta)(E+i\eta\pm t_{\perp})]^{1/2} R/(\hbar v_F)$ where R denotes the impurity separation.

this section is to study the effect of these features on the RKKY interaction. To this end we consider similar to Refs. [52, 53, 54] two magnetic moments that couple on a single carbon atom to the gas of delocalized electrons. In order to determine the nature of the impurity spin coupling. We take the zero temperature Green's function which is given in Appendix C.2 and calculate according to Eq. (2.1.29) the RKKY exchange integral for a given Fermi energy and given impurity positions. The symmetry of the lattice implies that there are six impurity configurations to distinguish: two sites

on the same sublattice, either A or B, and two places on opposite sublattice which are located either on the same or on opposite layer. In all these cases the exchange integral separates into the product of two functions

$$J_{\alpha_{l}\alpha'_{l'}}(\mathbf{R}) = Cf_{\alpha_{l}\alpha'_{l'}}(\mathbf{R})I_{\alpha_{l}\alpha'_{l'}}(R) \tag{4.2.3}$$

with $C = -\lambda^2 \hbar^2 a^2/(64\pi t^2)$ and where α (α') stands for the sublattice and l (l') for the layer of the first (second) impurity. The scattering in the vicinity of each K point is described by six distinct intravalley scattering functions $I_{\alpha_l \alpha'_{l'}}(R)$ which are presented in Table (4.2) while the scattering between the K points is encoded in the three fast oscillation functions which are given by

$$f_{A_1A_1}(\mathbf{R}) = f_{AA}(\mathbf{R}) \tag{4.2.4}$$

$$f_{B_1A_1}(\mathbf{R}) = f_{BA}(\mathbf{R}) \tag{4.2.5}$$

$$f_{B_2B_1}(\mathbf{R}) = 1 + \cos\left[\mathbf{K}_2.\mathbf{R} + 4\theta\right] \tag{4.2.6}$$

with $f_{AA}(\mathbf{R})$ and $f_{BA}(\mathbf{R})$ defined according to Eqs. (3.2.2) and (3.2.4). The relation between these three functions and the six distinct impurity configurations can be read off from the Table (4.3).

	A_1	B_1	A_2	B_2
A_1	$f_{A_1A_1}(\mathbf{R})$	$f_{B_1A_1}(-\mathbf{R})$	$f_{A_1A_1}(\mathbf{R})$	$f_{B_1A_1}(\mathbf{R})$
B_1	$f_{B_1A_1}(\mathbf{R})$	$f_{A_1A_1}(\mathbf{R})$	$f_{B_1A_1}(\mathbf{R})$	$f_{B_2B_1}(-\mathbf{R})$
$\overline{A_2}$	$f_{A_1A_1}(\mathbf{R})$	$f_{B_1A_1}(-\mathbf{R})$	$f_{A_1A_1}(\mathbf{R})$	$f_{B_1A_1}(\mathbf{R})$
B_2	$f_{B_1A_1}(-\mathbf{R})$	$f_{B_2B_1}(\mathbf{R})$	$f_{B_1A_1}(-\mathbf{R})$	$f_{A_1A_1}(\mathbf{R})$

Table 4.3: The relation between the three distinct fast oscillation functions $f_{A_1A_1}$, $f_{B_1A_1}$, and $f_{B_2B_1}$ and the 16 impurity configurations.

Zero Doping

The disparity between the A- and B-sites is particularly evident at zero doping, where the Fermi energy lies at the apex of the low energy bands. On the A-sites there are no states in the conduction band which could contribute to the RKKY interaction while on the B-sites a finite number of states is available. This is the reason why the exchange integrals that are presented in Table (4.2) have, not only in its strength but also in its decay rate, an extraordinary strong dependence on the sublattice position of both impurities. The unusual behavior at zero doping can be understood in a simplified model where only two low energy bands of the bilayer are included. This model has the advantage that it is analytically tractable and it is based on the observation that the exchange integrals are dominated by the contribution of the stationary point

at E=0 while the oscillations at higher energies average out. The model preserves the data of Table (4.2) and requires solely to redefine the two arguments of the Hankel functions. In such an approximation the interaction between two moments on sublattice A may be written as

$$J_{A_l A_{l'}}(\mathbf{R}) = \frac{4C\hbar^4 v_F^4}{t_\perp^3 R^2} \lim_{s \to 0} \int_0^\infty dx \ x^5 \left[J_0(x) Y_0(x) - (-1)^{l+l'} \frac{2}{\pi} J_0(x) K_0(x) \right] e^{-sx^2}$$

$$(4.2.7)$$

with $x = z^+R$ and $z^+ = \sqrt{(E + i\eta)t_{\perp}}/(\hbar v_F)$. For a further analytical evaluation of Eq. (4.2.7) we replace the Bessel functions $Y_0(x)$ and $K_0(x)$ by their integral representation which is displayed in Appendix B [Eqs. (B.2.1) and (B.4.1)].

$$J_{A_l A_{l'}}(\mathbf{R}) = \frac{8C\hbar^4 v_F^4}{\pi t_\perp^3 R^6} f_{A_1 A_1}(\mathbf{R}) \lim_{s \to 0} \left[\int_0^\infty dx \int_0^\infty dx' \, \frac{x^5 x' J_0(x) J_0(x')}{x^2 - x'^2} e^{-s(x^2 + x'^2)} \right]$$

$$-(-1)^{l+l'} \int_0^\infty dx \int_0^\infty dx' \, \frac{x^5 x' J_0(x) J_0(x')}{x'^2 + x^2} e^{-s(x^2 + x'^2)} \right]$$

$$(4.2.8)$$

It can be easily shown that the double integral in the first line gives zero so that there remains only the contribution of the double integral in the second line

$$J_{A_l A_{l'}}(\mathbf{R}) = (-1)^{l+l'} \frac{8C\hbar^4 v_F^4}{\pi t_1^3 R^6} f_{A_1 A_1}(\mathbf{R}) \lim_{s \to 0} I(s)$$
 (4.2.9)

with the function I(s) defined as follows

$$I(s) = \int_0^\infty dx \int_0^\infty dx' \, \frac{x^3 x'^3 J_0(x) J_0(x')}{x'^2 + x^2} \, e^{-s(x^2 + x'^2)} \tag{4.2.10}$$

Since there is no more singularity in the integrand, both variables x and x' can be, from now on, considered as purely real. This allows us to apply the usual trick: first we take the derivative with respect to s and obtain a product of two Laplace transforms which are both of the form $\int_0^\infty dx \ x^3 J_0(x) e^{-sx}$. The Laplace transform of $x^3 J_0(x)$ is a well known expression and it is given in Eq. (B.5.3). A subsequent integration over s with the boundary condition $\lim_{s\to\infty} I(s) = 0$ then yields the function I(s):

$$I(s) = -\frac{1}{64}e^{-\frac{1}{2s}}\left(\frac{2}{s^4} + \frac{32}{s^2} + \frac{128}{s} + 256\right) + 4 \tag{4.2.11}$$

Finally we take the $s \to 0$ limit of Eq. (4.2.11) and insert the result into Eq. (4.2.7) obtaining the following RKKY interaction [52]

$$J_{A_l A_{l'}}(\mathbf{R}) = (-1)^{l'-l} \frac{32C(\hbar v_F)^4}{\pi t_A^3 R^6} f_{A_l A_{l'}}(\mathbf{R})$$
 (4.2.12)

The other four impurity configurations are treated in the same way and the results are presented in Table (4.4). Using this model we find the RKKY interaction that is layer antisymmetric and in its strength and its decay rate very sensitive to the sub-

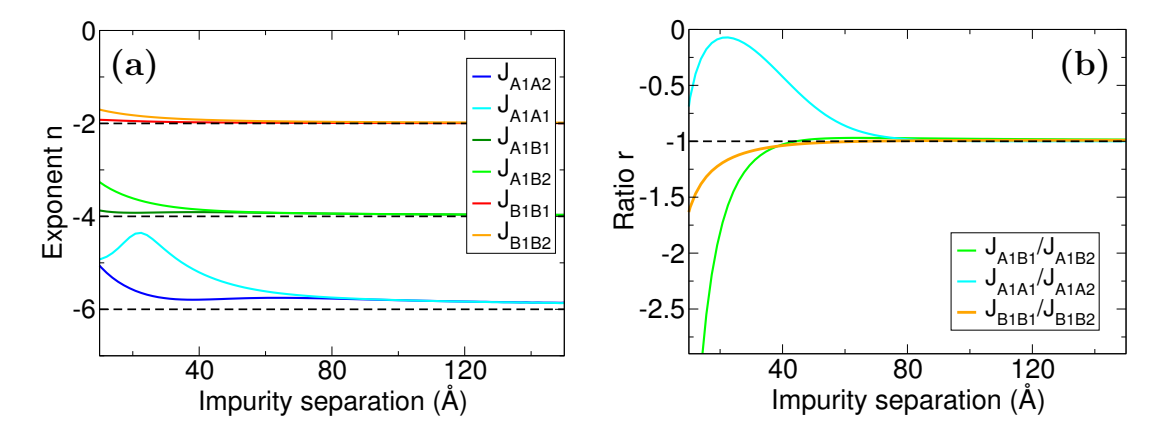


Figure 4.4: The RKKY interaction in pristine AB-stacked bilayer graphene. Fig. (4.4a) shows the power of the algebraic decay $n = \log_{10} \left(J_{\alpha_l \alpha'_{l'}}(R)/J_{\alpha_l \alpha'_{l'}}(R_0)\right)/\log_{10}(R/R_0)$ where $R_0 = 173.2\text{Å}$ is a reference distance at which the interaction is assumed to be well described by the power law R^{-n} . Fig. (4.4b) shows the ratio of the intralayer and the interlayer exchange integrals. Both quantities are obtained from numerical evaluation of Table (4.4). It can be seen that the RKKY interaction is for impurity separations greater than 60a layer antisymmetric and decays as R^{-6} for two moments on sublattice A, R^{-4} for two moments on different sublattice and R^{-2} for to moments on sublattice R.

lattice position of both impurities: for two moments on sublattice A the interaction decays as R^{-6} , for two moments on opposite sublattice as R^{-4} , and for two moments on sublattice B as R^{-2} .

In order to figure out how accurate the two-band model provides the RKKY interaction we compare in Fig 4.4 the analytical result to a numerical calculation which includes the full four-band structure. This figure shows the two quantities of main interest, the power of the algebraic decay and the ratio of the intralayer and the interlayer exchange integral, plotted as a function of the impurity separation. It can be seen that for low impurity separations the power and the ratio deviates significantly from the analytically predicted values. But for impurity separations greater than 60a we find a very good agreement: the exponent converges to -6 for two moments on sublattice A, -4 for two moments on different sublattice and -2 for two moments on sublattice B. The ratio of the intralayer and the interlayer exchange integrals limits to -1 which confirms the layer antisymmetry of the system. Interestingly, the convergence to the expected value is very fast for two moments on sublattice B and particularly slow for two moments on opposite sublattice.

We conclude that the RKKY interaction in the undoped AB bilayer is for large impurity separations well described by the two band model. But for small impurity separations the contribution of the high energy bands must be included. Taking these

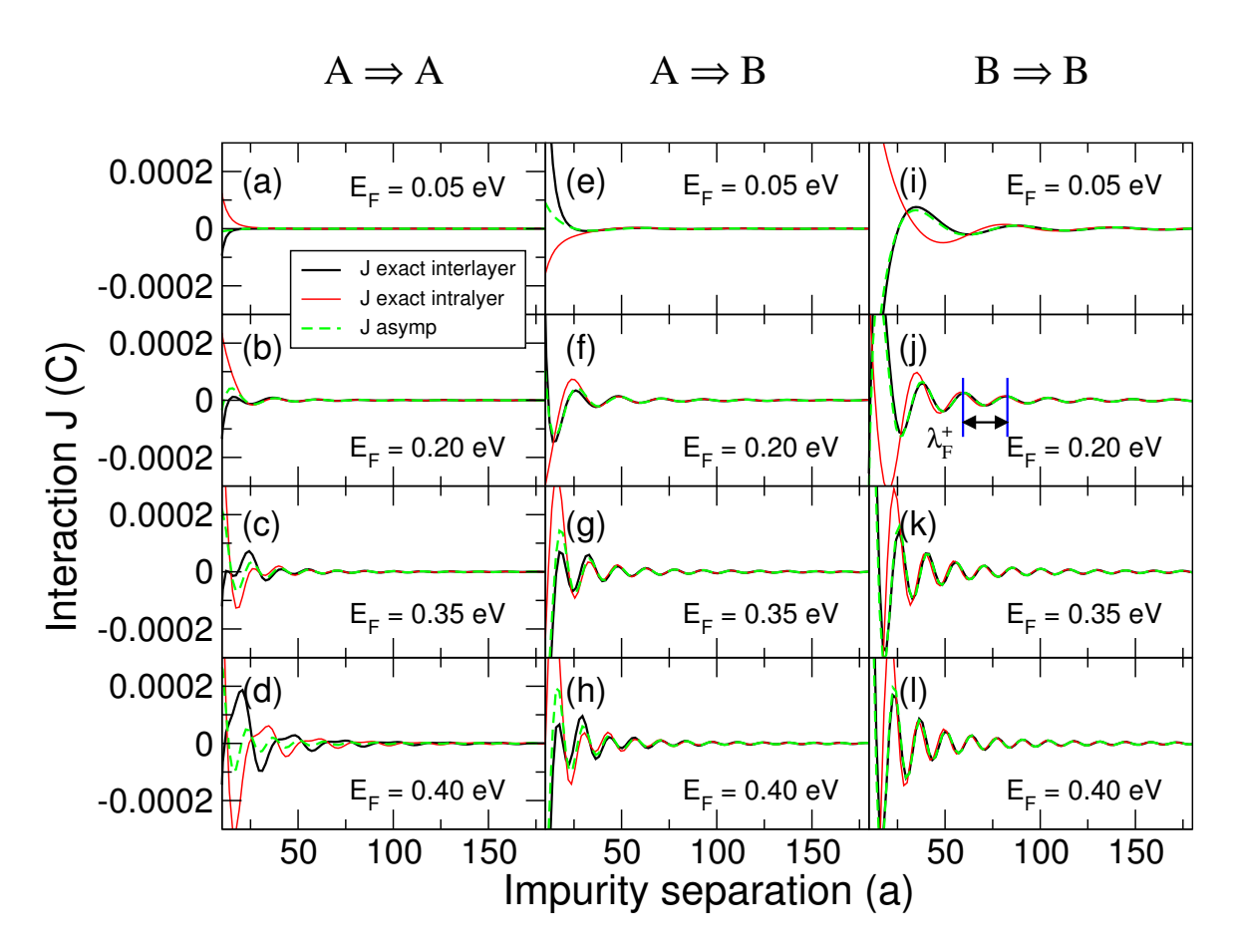


Figure 4.5: The RKKY interaction in AB-stacked bilayer graphene plotted in arm-chair direction as a function of the impurity separation. The Fermi energy is increased from 0.05eV in the first row to 0.4eV in the last row. Each column represents a different sublattice configuration: the first column shows two moments on sublattice A, the second column two moments are on opposite sublattice and the third column two moments on sublattice B. The exchange integral is measured in terms of the coupling constant C.

bands into account breaks the layer antisymmetry of the two band model and has an impact on the decay rate.

In the Bonding-Antibonding Band Gap

When the Fermi energy lies in the bonding-antibonding band gap the RKKY interaction can be treated analytically in an asymptotic expansion for large impurity separations: each exchange integral consists, according to Table (4.2), of two Hankel functions and in the band gap one of these Hankel functions has a purely imaginary argument. The contribution of this Hankel function is, for large impurity separations, damped exponentially and the form of the RKKY interaction is hence governed by the oscillatory character of the remaining Hankel function with purely real argument

$$J_{A_l A_{l'}}(\mathbf{R}) = -\frac{2}{\pi \hbar^2 v_F^2 R} C f_{A_1 A_1}(\mathbf{R}) \lim_{s \to 0} \int_{E_F}^{\infty} dE \ E^2 \ \Re\left(\frac{e^{2iz^+ R}}{z^+}\right) e^{-sE^2}$$
(4.2.13)

with $z^+ = \sqrt{(E + i\eta)(E + i\eta + t_{\perp})}/(\hbar v_F)$. Integration by parts leads for the exchange integral $J_{A_lA_{l'}}(\mathbf{R})$ to the result [54]

$$J_{A_l A_{l'}}(\mathbf{R}) = 2C \frac{2E_F + t_{\perp}}{\pi R^2} n_A(E_F) n_A(E_F) f_{A_l A_{l'}}(\mathbf{R}) \sin(2k_F^+ R)$$
(4.2.14)

with $n_A(E_F) = |E_F|/(2|E_F| + t_\perp)$. The results for all other impurity configurations may be seen in Table (4.4) and are plotted in Fig. (4.5) together with the exact exchange integral. The picture reveals that the RKKY interaction is, at low Fermi energy and small impurity separation, layer antisymmetric and still described by the R^{-n} power law from Section 4.2.1. When the Fermi energy is increased the interaction starts to oscillate with the Fermi wave vector of the low energy band $k_F^+ = \sqrt{E_F(E_F + t_\perp)}/(\hbar v_F)$. In addition to that the interaction changes its decay rate to $1/R^2$ and becomes layer symmetric. Under these circumstances the asymptotic form that we derived in the current section is applicable for large impurity separations and in the limit $E_F \to t_{\perp}$ where it agrees especially well with the exact exchange integral. However, there is one exception: for $J_{A_lA_{l'}}(\mathbf{R})$ the asymptotic form becomes less and less accurate as the Fermi energy approaches the point $E_F = t_{\perp}$. In contrast to what one would expect from Eq. (4.2.14), the RKKY interaction is at $E_F = t_{\perp}$ layer antisymmetric and the strength of the RKKY interaction is suddenly comparable to the strength of the interaction between two moments on site B. This behavior can be understood from the fact that the Hankel function $H_{\nu}(z^{-}R)$ diverges logarithmically in the limit $E_F \to t_{\perp}$. For two moments on opposite sublattices and for two moments on sublattice B the logarithmic divergence is ruled out by the algebraic coefficient in front of the Hankel functions. However, for two moments on sublattice A the whole integrand divergences and for this reason it is necessary to perform the exact integral which takes the irregular behavior of the divergent Hankel function into account.

At the Gap Edge

At the edge of the bonding-antibonding band gap the real space Green's function that describes the propagation between two A-sites diverges logarithmically. In this case the usual stationary phase approximation from the previous section does no longer hold and it is necessary to go back to the exact exchange integral. As a first step towards an analytical evaluation we write $J_{A_lA_{l'}}$ as follows

$$J_{A_l A_{l'}} = C f_{A_l A_{l'}} \left[I_{AA}^{(1)} + I_{A_l A_{l'}}^{(2)} + I_{AA}^{(3)} + I_{A_l A_{l'}}^{(4)} \right]$$
(4.2.15)

with the four integrals $I_{AA}^{(1)}$, $I_{A_lA_{l'}}^{(2)}$, $I_{AA}^{(3)}$ and $I_{A_lA_{l'}}^{(4)}$ given by

$$I_{AA}^{(1)} = \int_{t_{\perp}}^{\infty} dE \, \frac{2E^2}{(\hbar v_F)^2} J_0(z^+ R) Y_0(z^+ R) \tag{4.2.16}$$

$$I_{A_l A_{l'}}^{(2)} = (-1)^{l-l'} \int_{t_{\perp}}^{\infty} dE \, \frac{2E^2}{(\hbar v_F)^2} J_0(z^- R) Y_0(z^+ R) \tag{4.2.17}$$

$$I_{AA}^{(3)} = \int_{t_{\perp}}^{\infty} dE \, \frac{2E^2}{(\hbar v_F)^2} J_0(z^- R) Y_0(z^- R) \tag{4.2.18}$$

$$I_{A_l A_{l'}}^{(4)} = (-1)^{l-l'} \int_t^{\infty} dE \, \frac{2E^2}{(\hbar v_F)^2} J_0(z^+ R) Y_0(z^- R) \tag{4.2.19}$$

where $J_0(x)$ and $Y_0(x)$ stand for the Bessel function of the first and second kind. This form is particularly convenient since it consists of two groups of integrals that exhibit completely different behaviour at the gap edge: the first two integrals are regular in the domain of integration since the argument of the Bessel function of the second kind $Y_0(z^+R)$ is always finite (for R > 0). However, the last two integrals are irregular due to the divergence of the function $Y_0(z^-R)$ at the point $E = t_{\perp}$. Accordingly, the first integral, $I_{AA}^{(1)}$, may be taken within the stationary phase approximation. This procedure leads in the lowest order to the result

$$I_{AA}^{(1)} = \frac{2t_{\perp}}{3\pi R^2} \sin(2k_F^{\perp}R) \tag{4.2.20}$$

where k_F^{\perp} is the Fermi wave vector of the low energy band evaluated at the energy $E = t_{\perp}$. We continue with $I_{A_l A_{l'}}^{(2)}$ where we replace the Bessel function of the first and the second kind by its integral representation, Eqs. (B.1.3) and (B.2.2).

$$I_{A_{l}A_{l'}}^{(2)} = (-1)^{l-l'} \int_{0}^{\infty} dt \int_{0}^{\infty} dt' \int_{t_{\perp}}^{\infty} dE \, \frac{E^{2}}{(\hbar v_{F})^{2}} \Big(\sin \left[(z^{+} \cosh t + z^{-} \cosh t') R \right] - \sin \left[(z^{+} \cosh t - z^{-} \cosh t') R \right] \Big)$$

Using integration by parts it can be shown that the integral vanishes. Then we come to the last two integrals, Eqs. (4.2.18) and (4.2.19), which are dominated by the contribution of the divergence at the gap edge. Here we linearize both variables z^+ and z^- around the point $E = t_{\perp}$ which yields $z^- = \sqrt{t_{\perp}\delta}/(\hbar v_F)$ and $z^+ = \sqrt{2}t_{\perp}/(\hbar v_F)$ with $\delta = E - t_{\perp}$. After the substitution $x = z^- R$ we can bring the integral $I^{(3)}$ to the form

$$I_{AA}^{(3)} = \frac{4t_{\perp}}{R^2} \int_0^{\infty} dx \, x J_0(x) Y_0(x)$$
 (4.2.21)

This integral can be taken with help of Eq. (B.5.5) and yields (evaluated at the upper and lower bound of integration) the result $I_{AA}^{(3)} = 0$. Finally, there remains the integral

 $I^{(4)}$ which may be, after a linearization of z^+ and z^- , written as

$$I_{A_l A_{l'}}^{(4)} = \frac{4}{R^2} J_0(k_F^{\perp} R) \int_0^{\infty} dx \ x Y_0(x)$$
 (4.2.22)

The latter integral is known in literature: $\int_0^\infty dx \ x Y_0(x) = 2/\pi$. All in all we find that the exchange integral at the gap edge has the following asymptotic form

$$J_{A_{l}A_{l'}} = C f_{A_{l}A_{l'}} \left[\frac{2t_{\perp}}{3\pi R^{2}} \sin(2k_{F}^{\perp}R) + (-1)^{l-l'} \frac{8t_{\perp}}{\pi R^{5/2}} \sqrt{\frac{2}{\pi k_{F}^{\perp}}} \cos(k_{F}^{\perp}R - \pi/4) \right].$$
(4.2.23)

Interestingly, Eq. (4.2.23) consists of two parts: the first part is the usual $1/R^2$ -term which is obtained from a stationary phase approximation. This term oscillates with the wave vector $2k_F^+$ and is layer symmetric. The second term of Eq. (4.2.23) comes from the irregular part of the exchange integral and has completely different features: it oscillates with the wave vector k_F^+ , decays as $1/R^{5/2}$ and is layer anti symmetric. Although the second term may seem negligible from the mathematical point of view,

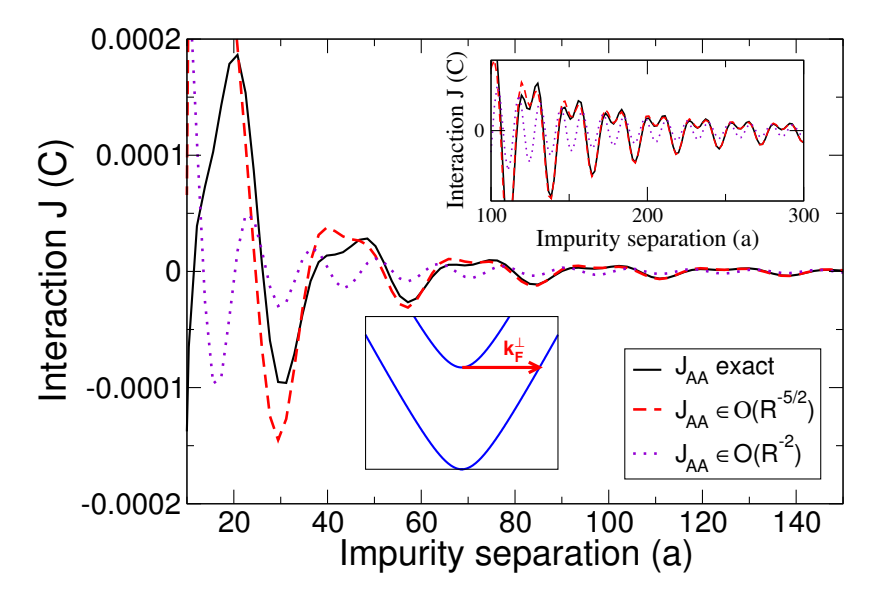


Figure 4.6: The RKKY interaction in AB-stacked bilayer graphene at a Fermi energy of 0.4eV. Plotted is the exact exchange integral for two moments on sublattice A and two different types of asymptotic forms versus the impurity separation. The exchange integral is always taken in armchair direction and expressed in terms of the coupling constant C. While the $O(R^2)$ asymptotic form is in pronounced disagreement with the exact exchange integral the $O(R^{-3/2})$ asymptotic form agrees very well, in particular for large impurity separations.

it is necessary in order to describe the RKKY interaction in the physically relevant range. This can be seen in Fig. (4.6) where the exact exchange integral obtained from numerical integration is compared to the $O(R^2)$ and $O(R^{5/2})$ asymptotic form. While the $O(R^2)$ asymptotics reveals a rather poor agreement, it can be seen that the $O(R^{5/2})$ asymptotics agrees very well with the numerical result.

In the Two Band Region

Another feature which makes the AB bilayer interesting with respect to the RKKY interaction is the existence of a two band region. When the Fermi energy lies in the two band region the arguments of both Hankel functions, z^+ and z^- , are real valued and greater than zero. Under these circumstances it is convenient to replace

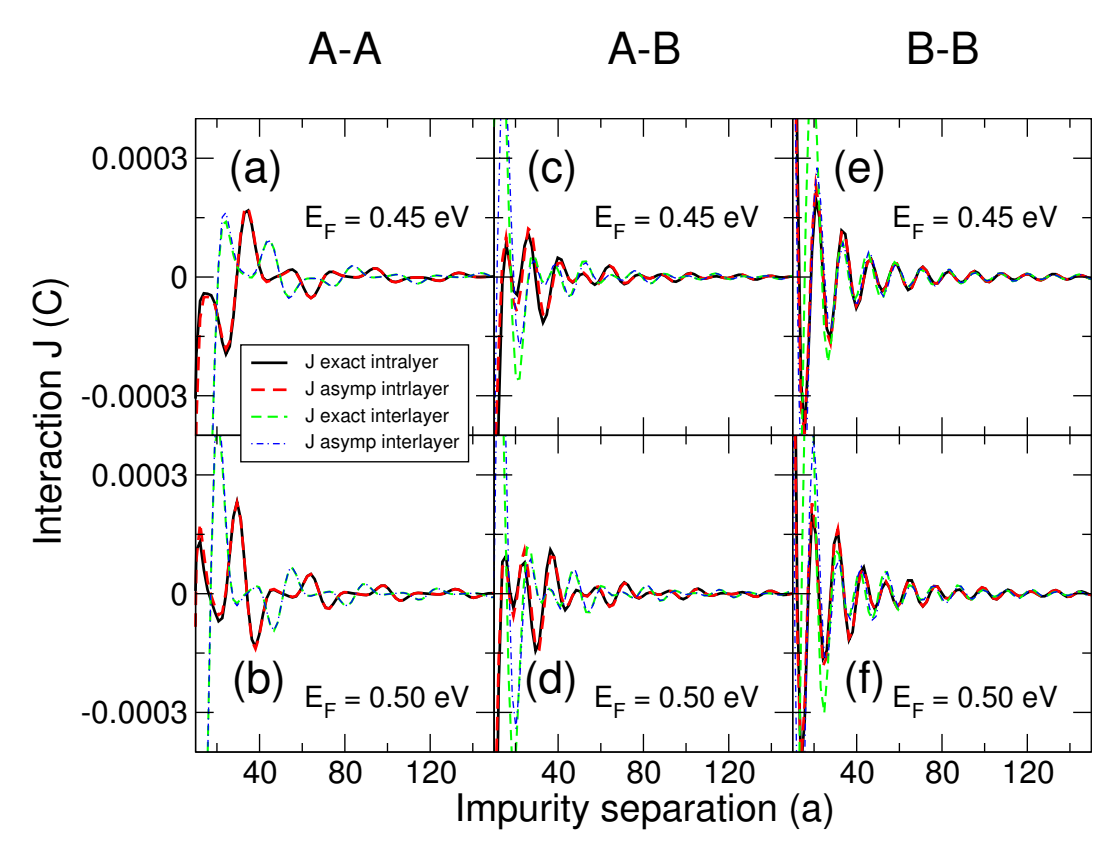


Figure 4.7: The RKKY interaction in AB-stacked bilayer graphene plotted in arm-chair direction as a function of the impurity separation. The Fermi energy is increased from 0.45eV in the first row to 0.5eV in the second row. Each column represents another impurity configuration: the first column represents the case where two moments reside on sublattice A, the second column the case where the two moments reside on different sublattice and the last column the case where the two moments reside on sublattice B.

both Hankel functions by their asymptotic forms for large arguments and to treat the exchange integrals within a stationary phase approximation. In this way the exchange

E_F	$\alpha_l \alpha'_{l'}$	$I_{\alpha_l \alpha'_{l'}}(R)$	Layer symmetry
$E_F = 0$	$A_l A_{l'}$	$(-1)^{l'-l} \frac{32\hbar^4 v_F^4}{\pi t_\perp^3 R^6}$	AS
	$B_lB_{l'}$	$(-1)^{l'-l} rac{4t_\perp}{\pi R^2}$	AS
	$B_lA_{l'}$	$(-1)^{l'-l+1} rac{8\hbar^2 v_F^2}{\pi t_\perp R^4}$	AS
$0 < E_F < t_{\perp}$	$A_l A_{l'}$	$2 \frac{2E_F + t_{\perp}}{\pi R^2} n_A(E_F) n_A(E_F) \sin(2k_F^+ R)$	S
	$B_lB_{l'}$	$2 \frac{2E_F + t_\perp}{\pi R^2} n_B(E_F) n_B(E_F) \sin(2k_F^+ R)$	S
	$B_lA_{l'}$	$-2 \frac{2E_F + t_{\perp}}{\pi R^2} n_A(E_F) n_B(E_F) \sin(2k_F^+ R)$	S
$E_F = t_{\perp}$	$A_l A_{l'}$	$\frac{2t_{\perp}}{3\pi R^2}\sin(2k_F^{\perp}R) + (-1)^{l-l'}\frac{8t_{\perp}}{\pi R^{5/2}}\sqrt{\frac{2}{\pi k_F^{\perp}}}\cos(k_F^{\perp}R - \pi/4)$	mixed
	$B_lB_{l'}$	$\frac{8t_{\perp}}{3\pi R^2} \sin\left(2k_F^{\perp}R\right)$	S
	$B_lA_{l'}$	$-rac{4t_{\perp}}{3\pi R^2}~\sin\left(2k_F^{\perp}R ight)$	S
$E_F > t_{\perp}$	$A_lA_{l'}$	$\frac{2E_F^2}{\pi R^2} \left[\frac{1}{2E_F + t_\perp} \sin(2k_F^+ R) + \frac{1}{2E_F - t_\perp} \sin(2k_F^- R) + 4(-1)^{l-l'} \frac{1}{f} \sin(k_F^+ + k_F^-) R \right]$	mixed
	$B_lB_{l'}$	$\frac{2}{\pi R^2} \left[\frac{(E_F + t_\perp)^2}{2E_F + t_\perp} \sin(2k_F^+ R) + \frac{(E_F - t_\perp)^2}{2E_F - t_\perp} \sin(2k_F^- R) + 4(-1)^{l-l'} \frac{E_F^2 - t_\perp^2}{f} \sin(k_F^+ + k_F^-) R \right]$	mixed
	$B_lA_{l'}$	$-\frac{2E_F}{\pi R^2} \left[\frac{(E_F + t_\perp)}{2E_F + t_\perp} \sin(2k_F^+ R) + \frac{(E_F - t_\perp)}{2E_F - t_\perp} \sin(2k_F^- R) + 4(-1)^{l-l'} \frac{\sqrt{E_F^2 - t_\perp^2}}{f} \sin(k_F^+ + k_F^-) R \right]$	mixed
		Def: $f = (2E_F + t_\perp) \sqrt[4]{\frac{(E_F - t_\perp)}{(E_F + t_\perp)}} + (2E_F - t_\perp) \sqrt[4]{\frac{(E_F + t_\perp)}{(E_F - t_\perp)}}$	
$E_F >> t_{\perp}$	$\alpha_l \alpha'_{l'}$	$(-1)^{l'-l}(-1)^{1-\delta_{\alpha\alpha'}} \frac{4E_F}{\pi R^2} \sin\left(2\frac{E_F}{\hbar v_F}R\right)$	AS
		$ imes \cos^2\left(\frac{t_{\perp}}{2\hbar v_F}R + \frac{\pi}{2}\left[l' - l\right]\right)$	

Table 4.4: The asymptotic form of the RKKY interaction in AB-stacked bilayer graphene. The exchange integral separates in each of the six distinct cases into the product $J_{\alpha_l\alpha'_{l'}}(\mathbf{R}) = CI_{\alpha_l\alpha'_{l'}}(R)f_{\alpha_l\alpha'_{l'}}(\mathbf{R})$ and this table defines the asymptotic form of the intervalley scattering function $I_{\alpha_l\alpha'_{l'}}(R)$. The intervalley scattering function $f_{\alpha_l\alpha'_{l'}}(\mathbf{R})$ may be taken from Table (4.3). In the expressions above l refers to a layer index, α to a sublattice index and $k_F^{\pm} = \sqrt{E_F(E_F \pm t_{\perp})}/(\hbar v_F)$ to the Fermi wave vector of the AB bilayer. In addition to that we have introduced here the functions $n_A(E_F) = |E_F|/(2|E_F| + t_{\perp})$ and $n_B(E_F) = (|E_F| + t_{\perp})/(2|E_F| + t_{\perp})$ which stand for the site projected density at the Fermi level. The last column gives the layer symmetry of the asymptotic form; 'S' stands for layer symmetric and 'AS' for layer antisymmetric.

integral can be brought for each of the six distinct impurity configurations to the form

$$J_{\alpha_{l}\alpha'_{l'}}(\mathbf{R}) = \frac{2C}{\pi R^2} \Big[W_{\alpha\alpha'}^{+} \sin 2k_F^{+} R + W_{\alpha\alpha'}^{-} \sin 2k_F^{-} R + (-1)^{l-l'} W_{\alpha\alpha'}^{+-} \sin(k_F^{+} + k_F^{-}) R \Big], \qquad (4.2.24)$$

with the three functions $W^+_{\alpha\alpha'}$, $W^-_{\alpha\alpha'}$ and $W^{+-}_{\alpha\alpha'}$ defined in Table (4.4). These functions weight the contribution of the three different scattering processes that occur at the Fermi surface: (i) scattering with the Fermi wave vector of the low energy band k_F^+ which is weighted by the function $W^+_{\alpha\alpha'}$, (ii) scattering with the Fermi wave vector of the high energy band k_F^- which is weighted by the function $W^-_{\alpha\alpha'}$ and (iii) scattering with $k_F^+ + k_F^-$ which is weighted by $W^{+-}_{\alpha\alpha'}$. Interestingly, all three weight functions are layer symmetric and it is solely the prefactor $(-1)^{l-l'}$ that makes the interband scattering term in the second line of Eq. (4.2.29) layer antisymmetric. The ratios

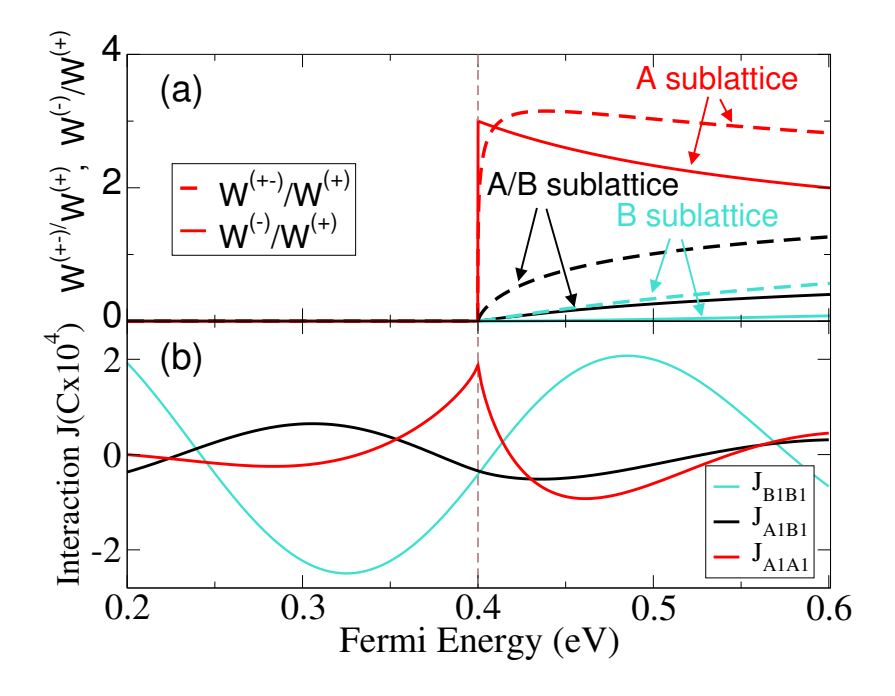


Figure 4.8: The relative weight functions of the three Fermi surface spanning vectors k_F^+ , k_F^- and k_F^+ + k_F^- and the exchange integrals $J_{A_1A_1}$, $J_{A_1B_1}$ and $J_{B_1B_1}$ plotted as a function of the Fermi energy. As may be seen from Fig. (4.8a) the transition from the bonding-antibonding band gap to the two band region is accompanied by a sharp change of the relative weight function W_{AA}^{+-}/W_{AA}^{+} and a discontinuous change of W_{AA}^{-}/W_{AA}^{+} . This unusual behavior at the gap edge is responsible for the discontinuity in the derivative of $J_{A_1A_1}$ that can be seen in Fig. (4.8b). The weight functions are taken from Table (4.4). The exchange integrals presented in Fig. (4.8b) are obtained from numerical integration of Table (4.2) and expressed in terms of the coupling constant C.

of the weight functions $W^-_{\alpha\alpha'}/W^+_{\alpha\alpha'}$ and $W^{+-}_{\alpha\alpha'}/W^-_{\alpha\alpha'}$ are plotted in Fig. (4.8a) for two

moments on sublattice A, two moments on sublattice B and two moments on opposite sublattice. It can be clearly seen that the relative weight functions grow in the latter two cases as a continuous function of the Fermi energy. That behavior manifests in an RKKY interaction that is in the bonding-antibonding band gap governed by oscillations with the period of the low energy band k_F^+ and in the two band region by oscillations with the period of all three Fermi surface spanning vectors. The transition between the two regions is smooth and this is the reason why no abrupt change can be observed in Fig. (4.8b) where the exchange integrals are plotted as a function of the Fermi energy. However, for two moments on sublattice A there is at the gap edge a sudden, and in case of W_{AA}^-/W_{AA}^+ even a discontinuous increase of the relative weight function from zero to a finite value of about three. From the relevant expression in Table (4.4) it may be seen that the weight function W_{AA}^+ is continuous in energy and for this reason the discontinuity must arise from W_{AA}^- . But it is necessary to stress that the discontinuity in the weight function W_{AA}^- does not mean that the RKKY interaction itself is discontinuous. Since the function $\sin(2k_F^-R)$ goes to zero at the gap edge we find solely a discontinuity in the derivative of the RKKY interaction. In order to figure out how accurate Eq. (4.2.29) describes the RKKY interaction we plot in Fig. (4.7) the asymptotic form and the exact exchange integral as a function of the impurity separation for the six distinct impurity configurations. Exemplarily we choose two different Fermi energies in the two band region: 0.45eV and 0.5eV. One immediately notes that the asymptotic form and the numerical calculation agree very well already at a Fermi energy of 0.45eV. An increase of the Fermi energy to 0.5eV improves the agreement and leaves the form of the RKKY interaction between spins on sublattice B almost unchanged but has a dramatic effect on the interaction between two spins on sublattice A. The latter observation and also the unusual behavior directly at the gap edge are a consequence of the divergence of the real space propagator that we identified in the previous section.

For highly doped AB-stacked bilayer graphene the expressions of Table (4.4) can be expanded around $E_F/t_{\perp} >> 1$. In the leading order of this expansion we find an exchange integral that oscillates with the period E_F and has a beat structure which arises from the modulation with the interlayer hopping constant t_{\perp} :

$$J_{\alpha_{l}\alpha'_{l'}}(\mathbf{R}) = (-1)^{l'-l}(-1)^{1-\delta_{\alpha\alpha'}} \frac{4E_{F}}{\pi R^{2}} f_{\alpha_{l}\alpha'_{l'}}(\mathbf{R})$$

$$\times \sin\left(2\frac{E_{F}}{\hbar v_{F}}R\right) \cos^{2}\left(\frac{t_{\perp}}{2\hbar v_{F}}R + \frac{\pi}{2}\left[l' - l\right]\right)$$
(4.2.25)

This equation is valid for all six distinct impurity configurations. From a comparison to the exact exchange integral we find that the asymptotic form holds for Fermi energies greater than 1eV. Yet, such a high doping is probably unrealistic.

The RKKY Interaction at Finite Temperature

At zero temperature we uncovered an unusual RKKY interaction which is, at zero doping, extraordinarily sensitive to the impurity position and has at the edge of

the band gap a remarkable $1/R^{3/2}$ term in its asymptotic form. Now we want to figure out whether the unusual behaviour persists for higher temperature. We use the finite temperature Green's function (given in in Appendix C.2) and insert it into the finite temperature exchange integral, Eq. (2.1.29). This procedure yields the following separable form

$$\mathcal{J}_{\alpha_{l}\alpha'_{l'}}(\mathbf{R}) = C\mathcal{I}_{\alpha_{l}\alpha'_{l'}}(R)f_{\alpha_{l}\alpha'_{l'}}(\mathbf{R})$$
(4.2.26)

with $C = -\lambda^2 \hbar^2 a^2/(64\pi t^2)$. The fast oscillation function $f_{\alpha_l \alpha'_{l'}}(\mathbf{R})$ turns out to be temperature independent and for this reason we use the same definition and also the same connection to the six distinct impurity configurations than above. The temper-

$\alpha_l \alpha'_{l'}$	$\mathcal{I}_{lpha_{l}lpha_{l'}'}(R)$
A_1A_1	$\frac{4}{\pi\beta} \sum_{n} \left(\frac{\hbar\omega_{n} - i\mu}{\hbar v_{F}} \right)^{2} \left[K_{0} \left(z^{+} R \right) + K_{0} \left(z^{-} R \right) \right]^{2}$
A_2A_1	$\frac{4}{\pi\beta} \sum_{n} \left(\frac{\hbar\omega_{n} - i\mu}{\hbar v_{F}} \right)^{2} \left[K_{0} \left(z^{+} R \right) - K_{0} \left(z^{-} R \right) \right]^{2}$
B_1B_1	$\frac{4}{\pi\beta} \sum_{n} \left(\frac{\hbar v_F}{\hbar \omega_n - i\mu} \right)^2 \left[z^{+2} K_0 \left(z^+ R \right) + z^{-2} K_0 \left(z^- R \right) \right]^2$
B_2B_1	$\frac{4}{\pi\beta} \sum_{n} \left(\frac{\hbar v_F}{\hbar \omega_n - i\mu} \right)^2 \left[z^{+2} K_2 \left(z^+ R \right) - z^{-2} K_2 \left(z^- R \right) \right]^2$
B_1A_1	$-\frac{4}{\pi\beta}\sum_{n} \left[z^{+}K_{1}\left(z^{+}R\right) + z^{-}K_{1}\left(z^{-}R\right)\right]^{2}$
B_2A_1	$-\frac{4}{\pi\beta}\sum_{n}\left[z^{+}K_{1}\left(z^{+}R\right)-z^{-}K_{1}\left(z^{-}R\right)\right]^{2}$

Table 4.5: The six distinct intravalley scattering functions $\mathcal{I}_{\alpha_l\alpha'_{l'}}(R)$ for AB-stacked bilayer graphene at finite temperature. Each $\mathcal{I}_{\alpha_l\alpha'_{l'}}(R)$ is the linear combination of two modified Bessel functions $K_{\nu}(z^{\pm}R)$ of the second kind and ν th order with $z^{\pm} = [(\hbar\omega_n - i\mu)(\hbar\omega_n - i\mu \mp it_{\perp})]^{1/2}/(\hbar v_F)$ and the impurity separation R. By definition the real part of the square root is positive valued.

ature dependence enters through the intravalley scattering function $\mathcal{I}_{\alpha_l\alpha'_{l'}}(R)$ which is (for each impurity configuration) presented in Table (4.5). The Matsubara sum, in exchange integrals, has a very small convergence radius since all items of the infinite series decay rapidly as the frequency increases. This makes the finite temperature formalism much more efficient compared to the zero temperature formalism where the exchange integrals are highly oscillatory and must be integrated over a wide range until they converge. But unfortunately, it is very hard to treat the finite temperature exchange integrals analytically. Even in the case of an asymptotic expansion for large impurity separations the attempt to take the Matsubara sums analytically fails due to the square root function of the two variables z^+ and z^- . For this reason we proceed with a numerical evaluation of the exchange integrals. In order to make the situation as realistic as possible we focus on the RKKY interaction between two

intercalated impurities, that means impurities which reside on high symmetry points midway between the two layers and couple to a local environment that consists of a set of surrounding lattice sites.

The RKKY Interaction between Intercalated Impurities

The covalent radius of a typical magnetic atom is much greater than that of carbon and for this reason we expect that a realistic impurity couples to a set of surrounding lattice sites and resides at a high symmetry position. The most open position in

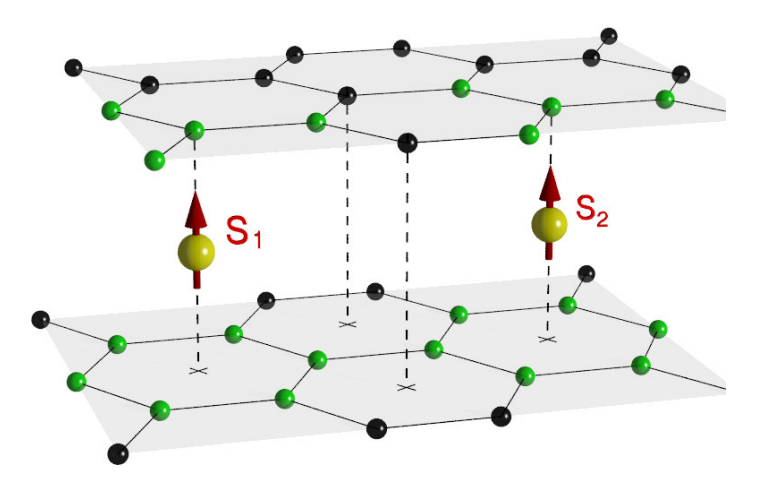


Figure 4.9: Two intercalated impurities in AB-stacked bilayer graphene. Each impurity spin (red) is assumed to couple to an environment of ten carbon atoms which are highlighted in green.

the AB-stacked bilayer graphene is where the impurity sits midway between the two layers, below the center of a hexagonal plaquette in the top layer and above a B-site carbon atom in the bottom layer. This configuration is shown in Fig. (4.9). As a model, we assume that each impurity couples to the gas of delocalized electrons via ten surrounding sites which are in Fig. (4.9) highlighted in green. Furthermore we assume that the coupling constant depends only on the distance to the respective lattice site. Under these circumstances the Hamiltonian for the electron-impurity coupling reads

$$H' = -\lambda_1 \sum_{a_1} \mathbf{S}_1 \cdot \mathbf{s}_{a_1} - \lambda_2 \mathbf{S}_1 \cdot \mathbf{s}_{B2} - \lambda_1 \sum_{a_2} \mathbf{S}_2 \cdot \mathbf{s}_{a_2} - \lambda_2 \mathbf{S}_2 \cdot \mathbf{s}_{B2'}$$
(4.2.27)

where \mathbf{S}_i stands for impurity spin and \mathbf{s}_{a_i} is the operator for electron spin density. Each sum is taken over nine sites of carbon atoms, i.e. the six carbon atoms in the top layer and the three A-site carbon atoms in the bottom layer. These nine sites have the same distance to the impurity and for this reason enter with the same coupling constant λ_1 . The coupling to the B-site, directly below the impurity, is stronger since the distance is shorter and therefore we use here another coupling constant which is denoted as λ_2 . In the incoherent coupling scheme the interaction energy between

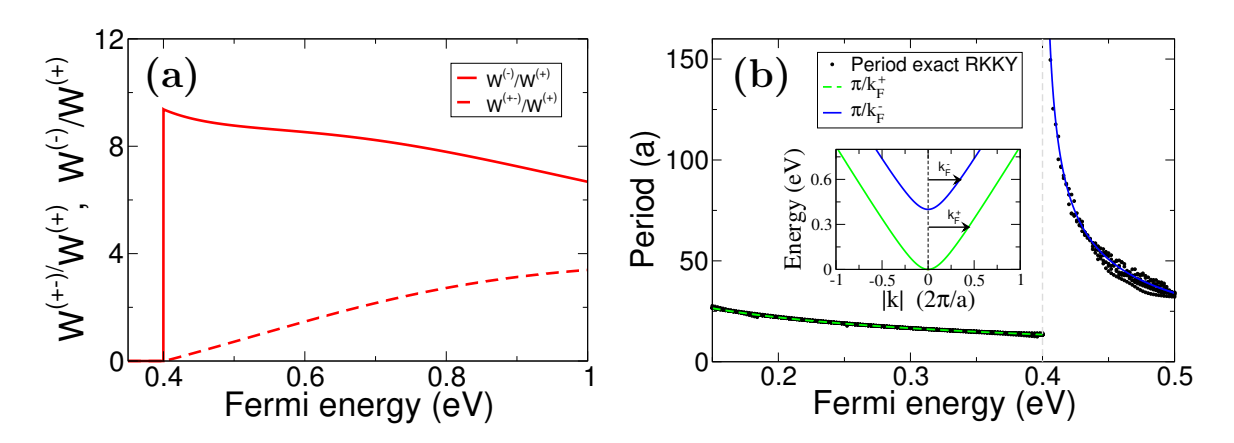


Figure 4.10: The relative weight functions W^-/W^+ and W^{+-}/W^+ and the period of the RKKY interaction plotted as a function of the Fermi energy. The figure shows the interaction between intercalated impurities separated in armchair direction. At the gap edge the relative weight function W^-/W^+ switches discontinuously from zero to a value of about ten while the relative weight function W^{+-}/W^+ increases continuously on a lower level. This behavior indicates that the RKKY interaction oscillates in the band gap with the period π/k_F^- and in the two band region with the period π/k_F^+ . The weight functions W^+ , W^- and W^{+-} are taken from Eqs. (4.2.30) - (4.2.32). The period of the exact interaction is obtained from numerical evaluation at some discrete points and in Fig. (4.9b) compared to the period of the low and the high energy band.

the two impurities can be obtained from the sum over all $10 \times 10 = 100$ site-to-site interactions. Each individual exchange integral is according to Eq. (4.2.26) given by a product of an intravalley scattering function $\mathcal{I}_{\alpha_l\alpha'_{l'}}(R)$ and a fast oscillation function $f_{\alpha_l\alpha'_{l'}}(\mathbf{R})$ that oscillates on the scale of the lattice constant. Since the former function changes very slowly on the scale of the lattice constant it is convenient to adopt the approximation $\mathcal{I}_{\alpha_l\alpha'_{l'}}(|\mathbf{R}+\mathbf{v}|) \approx \mathcal{I}_{\alpha_l\alpha'_{l'}}(R)$. Under these circumstances the sum can be taken analytically and yields the following result

$$\mathcal{J}_{intercal}(\mathbf{R}) = 9C \left[2\mathcal{I}_{A_{1}A_{1}}(R) + 2\mathcal{I}_{A_{2}A_{1}}(R) + \mathcal{I}_{B_{1}B_{1}}(R) + 2\mathcal{I}_{B_{2}A_{1}}(R) + 2\mathcal{I}_{B_{1}A_{1}}(R) \right] + 6C \left(\frac{\lambda_{2}}{\lambda_{1}} \right) \left[\mathcal{I}_{B_{2}B_{1}}(R) + \mathcal{I}_{B_{1}A_{1}}(R) + \mathcal{I}_{B_{2}A_{1}}(R) \right] + C \left(\frac{\lambda_{2}}{\lambda_{1}} \right)^{2} \mathcal{I}_{B_{1}B_{1}}(R) f_{A_{1}A_{1}}(\mathbf{R})$$
(4.2.28)

It should be noted that the \mathbf{R} dependence of the fast oscillation functions has been treated exactly. Due to the particular position of the impurity almost all fast oscillation functions sum up to a constant value and there remains only the function

 $f_{A_1A_1}(\mathbf{R})$ in the last line of Eq. (4.2.28).

At zero temperature, the asymptotic form can be obtained from a substitution of Table (4.4) into Eq. (4.2.28). For small Fermi energies the procedure yields a Fermi energy dependent prefactor that comes in product with a term that oscillates with the wave vector k_F^+ and decays as $1/R^2$. This asymptotic form holds even at the gap edge since the unusual, layer anti-symmetric $1/R^{3/2}$ contributions from the asymptotic form of $\mathcal{I}_{A_1A_1}(R)$ and $\mathcal{I}_{A_2A_1}(R)$ cancel each other. When the Fermi energy is further increased and lies finally in the two band region the exchange integral can be brought to the form

$$J_{\text{intercal}}(\mathbf{R}) = \frac{2C}{\pi R^2} \Big[W^+ \sin 2k_F^+ R + W^- \sin 2k_F^- R + (-1)^{l-l'} W^{+-} \sin(k_F^+ + k_F^-) R \Big], \qquad (4.2.29)$$

with the weight prefactors W^+ , W^- and W^{+-} defined as follows:

$$W^{+} = \frac{1}{2E_{F} + t_{\perp}} \left(9(E_{F} - t_{\perp})^{2} - 6 \left(\frac{\lambda_{2}}{\lambda_{1}} \right) (E_{F}^{2} - t_{\perp}^{2}) \right)$$

$$+ f_{A_{1}A_{1}}(\mathbf{R}) \left(\frac{\lambda_{2}}{\lambda_{1}} \right)^{2} (E_{F} + t_{\perp})^{2} \right)$$

$$W^{-} = \frac{1}{2E_{F} - t_{\perp}} \left(9(E_{F} + t_{\perp})^{2} - 6 \left(\frac{\lambda_{2}}{\lambda_{1}} \right) (E_{F}^{2} - t_{\perp}^{2}) \right)$$

$$+ f_{A_{1}A_{1}}(\mathbf{R}) \left(\frac{\lambda_{2}}{\lambda_{1}} \right)^{2} (E_{F} - t_{\perp})^{2} \right)$$

$$W^{+-} = \frac{4}{f} \left(9(E_{F} - t_{\perp})^{2} - 6 \left(\frac{\lambda_{2}}{\lambda_{1}} \right) (E_{F}^{2} - t_{\perp}^{2}) \right)$$

$$+ f_{A_{1}A_{1}}(\mathbf{R}) \left(\frac{\lambda_{2}}{\lambda_{1}} \right)^{2} (E_{F}^{2} - t_{\perp}^{2})$$

$$(4.2.32)$$

These expressions are plotted in form of the relative weight functions W^-/W^+ and W^{+-}/W^+ in Fig. (4.10) as a function of the Fermi energy. It can be clearly seen that both relative weight functions are zero in the band gap. At the edge of the band gap W^- jumps suddenly to a finite value which is about ten times greater than W^+ while the function W^{+-} increases as a continuous function of the energy and is much smaller than W^+ . From these findings we conclude that the RKKY interaction oscillates in the bonding-antibonding band gap with the period of the low energy band and switches at the edge of the band gap suddenly to the period of the high energy band. The discontinuous change of the period of the RKKY interaction at the gap edge can be seen in Fig. (4.10b) where one finds the numerically calculated period of the exact interaction compared to the period of the low and the high energy band. The numerical values agree very well with the asymptotic form and reflect in particular at the gap edge the expected behavior: the period limits to the value $\lambda = \pi \hbar v_F/(\sqrt{2}t_\perp) \approx 15a$ as the gap edge is approached from smaller Fermi energies

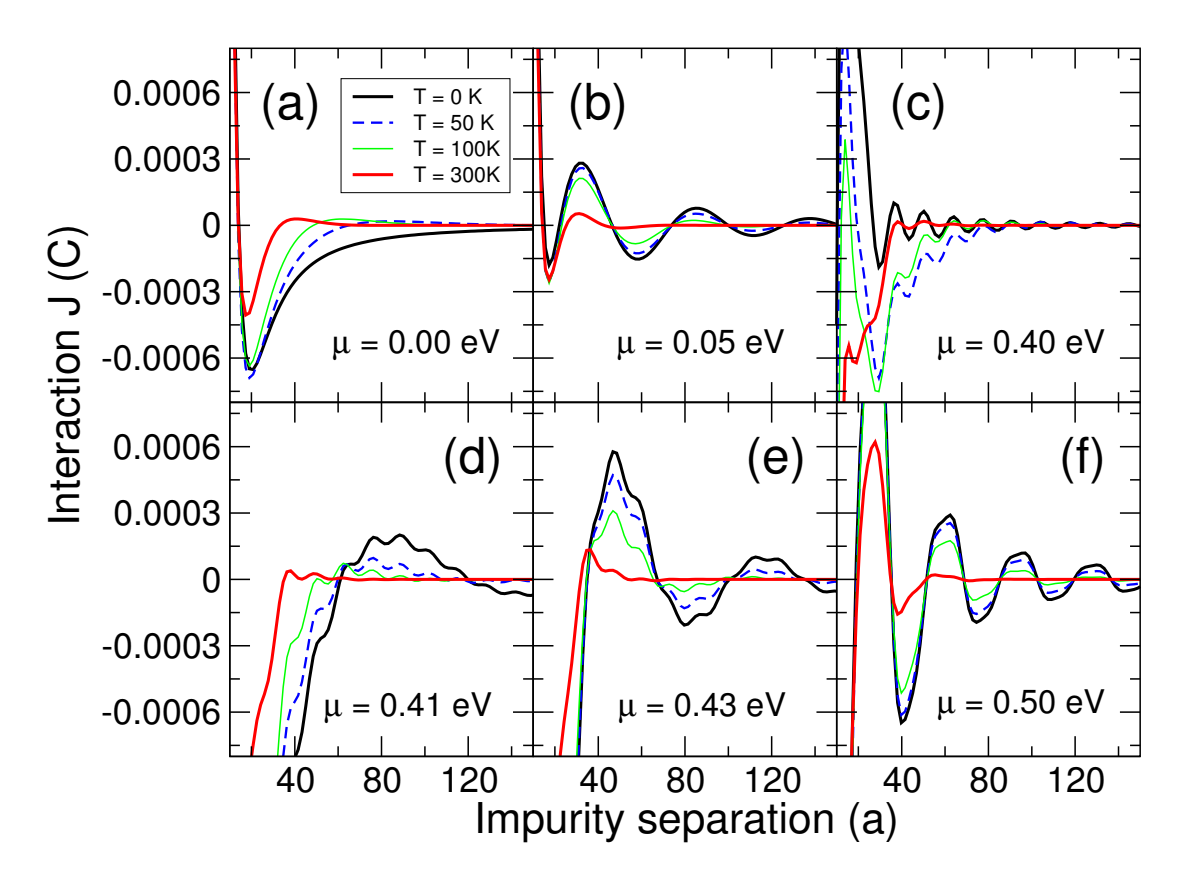


Figure 4.11: The RKKY interaction between two intercalated impurities plotted as a function of the impurity separation for different chemical potentials. Shown is the exchange integral expressed in terms of the coupling constant C in armchair direction. At the gap edge the RKKY interaction changes its form as a function of the temperature. Away from the gap edge the form is conserved while the amplitude is damped exponentially.

and diverges due to the vanishing Fermi wave vector of the high energy band as the gap edge is approached from higher Fermi energies. When the Fermi energy is further raised into the two band region we observe a broadening of the distribution of the oscillation period which can be attributed to the increasing importance of the relative weight functions W^{+-} . Besides the oscillations with the period k_F^- the RKKY interaction shows now oscillations with the period k_F^+ and $k_F^+ + k_F^-$.

In Fig. (4.11) the RKKY exchange integral is plotted as a function of the impurity separation for different temperatures. At zero temperature the RKKY interaction shows at the gap edge, when the chemical potential is increased from 0.4eV to 0.41eV, the discontinuous change of the period that we uncovered above, and in addition to that, at low impurity separation, a transition from oscillatory to antiferromagnetic behaviour. Such a transition can be also observed when the chemical potential is held fixed at 0.4eV and the temperature is increased to 50K or 100K. The temperature-dependent transition arises from the smearing of the Fermi surface, which allows all states in a certain temperature-dependent window around the chemi-

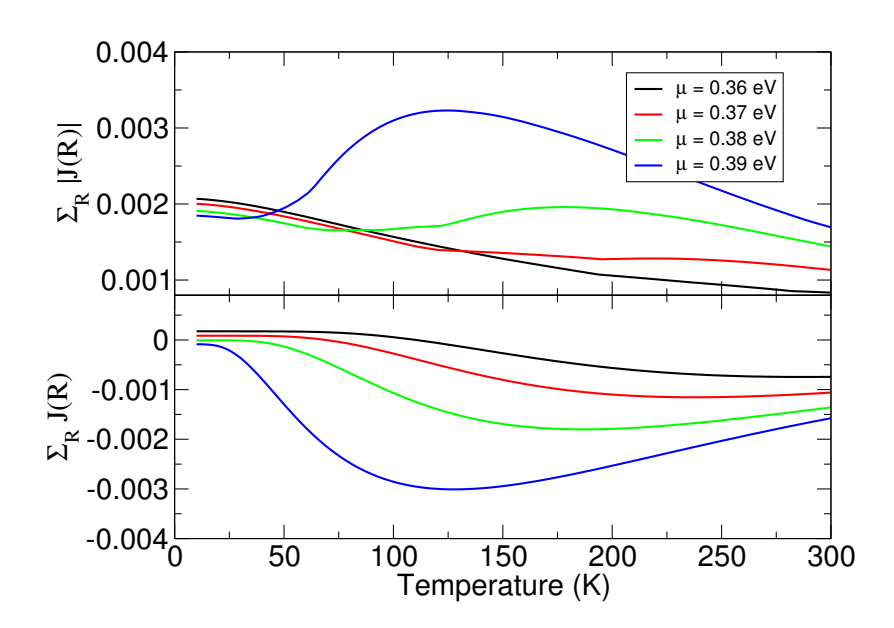


Figure 4.12: The two quantities $\sum_{R>R_c} \mathcal{J}(\mathbf{R})$ and $\sum_{R>R_c} |\mathcal{J}(\mathbf{R})|$ plotted as a function of temperature for different chemical potentials. In the lower panel it may be seen that the blue curve undergoes a transition from a small negative value to a pronounced negative value which means that the RKKY interaction evolves from oscillatory to antiferromagnetic. This transition is accompanied by an overall increase in strength that should be noticed in the upper panel where the quantity $\sum_{R>R_c} |\mathcal{J}(\mathbf{R})|$ is presented. When the chemical potential is placed further away from the gap edge the transition occurs at higher temperature, before, far away from the gap edge there is no transition anymore.

cal potential to contribute to the RKKY interaction. In particular, when the chemical potential lies near the gap edge, the RKKY interaction becomes the superposition of the short-wavelength oscillations with small amplitude from below the gap edge and the long-wavelength oscillations with large amplitude from above the gap edge. This leads to an RKKY interaction that changes its form with temperature and is significantly enhanced in magnitude. But it should be stressed that such a transition can be observed only at low impurity separation and when the chemical potential lies in a certain window around the gap edge. Away from the gap edge and at high temperature the usual behavior of a metal is recovered: the form of the interaction is conserved while the amplitude is exponentially damped as a function of T and R. These observations can be also made in Fig. (4.13) where we plot the exchange integral as a function of the impurity separation and the chemical potential for different temperature. At zero temperature and low impurity separation there are two distinct regions with oscillatory RKKY interaction below the gap edge and antiferromagnetic interaction above the gap edge. The transition between the two regions is associated with a discontinuous change of the RKKY period and with an increase in magnitude. When the temperature is raised, at fixed impurity separation and fixed chemical potential, the discontinuity disappears.

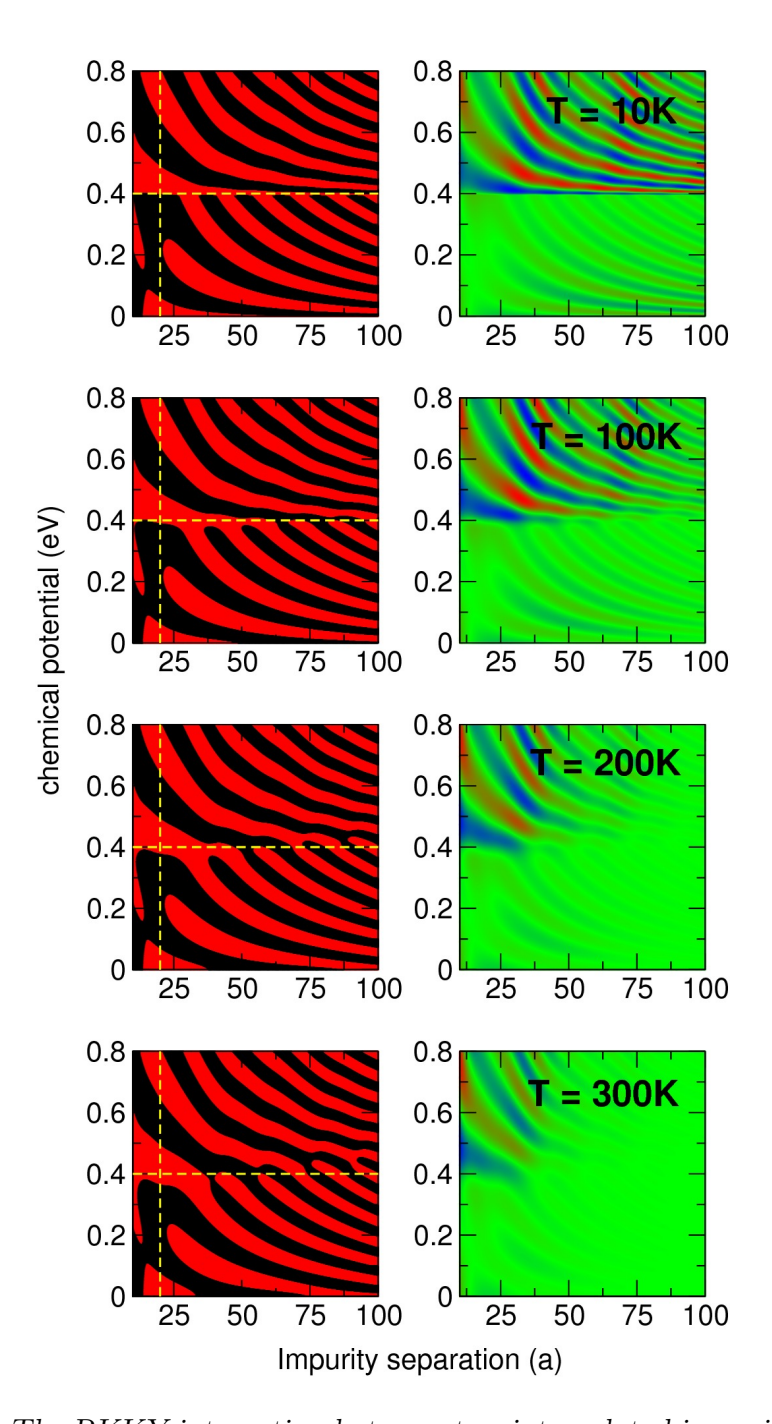


Figure 4.13: The RKKY interaction between two intercalated impurities plotted as a function of the impurity separation and the chemical potential. The temperature is increased from 10K in the first row to 300K in the last row. The right-hand column shows the RKKY interaction multiplied by the factor R^2/μ in the color scheme that is presented in the upper right corner. The left-hand column displays the sign of the interaction; black is taken for ferromagnetic coupling and red for antiferromagnetic coupling. At a temperature of 10K there are two distinct regions that are separated by a discontinuity at the gap edge. When the temperature is increased the discontinuity smoothes out.

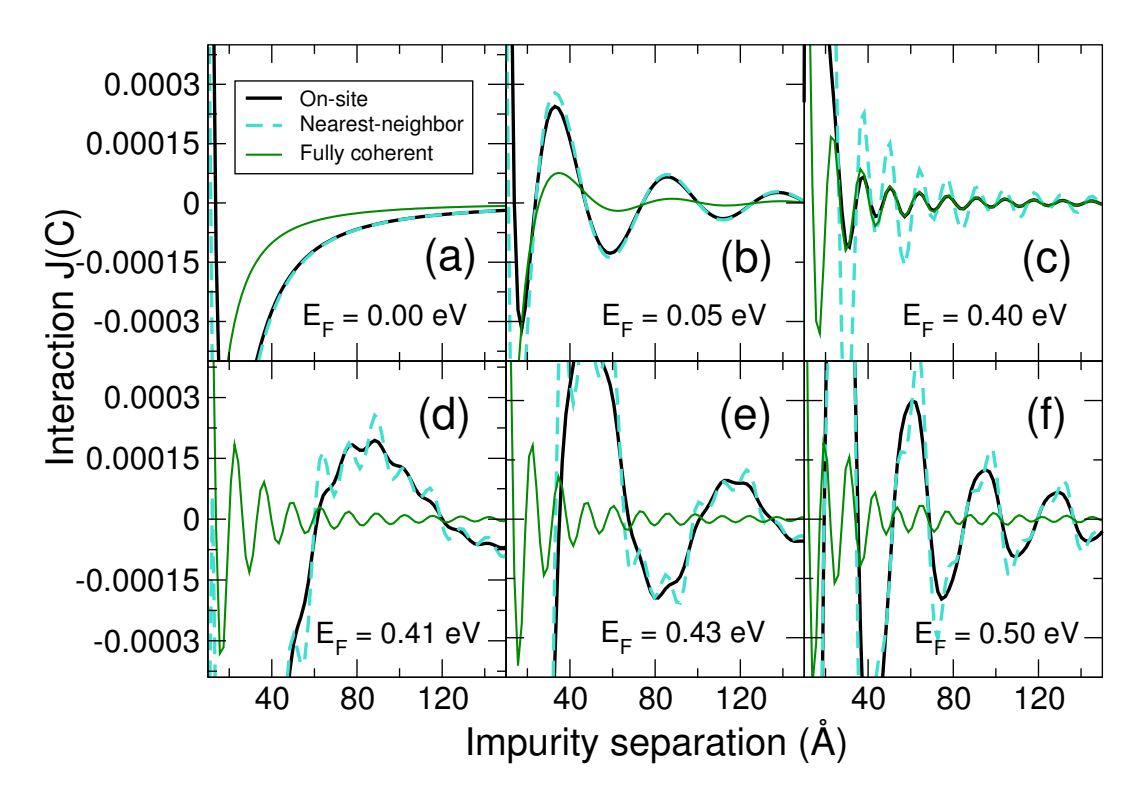


Figure 4.14: The RKKY interaction between two intercalated impurities in armchair direction for three different coupling schemes: incoherent, nearest-neighbor coherent and fully coherent. The picture shows the exchange integral expressed in terms of the coupling constant C. The temperature is set to 10K. While the incoherent and the nearest-neighbor coherent coupling scheme have at the gap edge a discontinuity in their period the fully coherent coupling scheme does not show such distinctive behaviour.

In order to figure out at which point, that means at which temperature and at which chemical potential, the crossover from oscillatory to antiferromagnetic occurs we plot in Fig. (4.12) the quantities $\sum_{R>R_c} \mathcal{J}(\mathbf{R})$ and $\sum_{R>R_c} |\mathcal{J}(\mathbf{R})|$. At a chemical potential of 0.39eV the quantity $\sum_{R>R_c} \mathcal{J}(\mathbf{R})$ stays only in a very small temperature range close to zero and after that increases rapidly. That means that the crossover from oscillatory to antiferromagnetic occurs at that chemical potential already at very low temperature. From the corresponding plot of the quantity $\sum_{R>R_c} |\mathcal{J}(\mathbf{R})|$ it can be seen that the crossover is associated with an increase of the magnitude of the interaction. When the chemical potential is placed further away from the band edge the oscillatory RKKY interaction persists up to higher temperature and finally, far away from the edge, the antiferromagnetic region cannot be accessed anymore.

Naturally there arises the question whether the unusual sharp change of the RKKY period at the gap edge is a particularity of the incoherent coupling scheme. In order to answer this question we consider the most general case where each impurity induces apart from on-site spin-flip processes also inter-site spin-flip processes between the ten carbon atoms in its environment. Each spin-flip process is weighted by an

individual coupling constant and accordingly there is a remarkably high number of different coupling schemes. From an analysis of a wide range of coupling schemes we find that the discontinuity is present in a large number of coupling schemes but not in all. Exemplarily we present here three coupling schemes, the incoherent, the nearest-neighbor coherent and the fully coherent coupling scheme, and plot the RKKY exchange integrals as a function of the impurity separation. In Fig. (4.14) it can be clearly seen that the discontinuity at the gap edge is present in the incoherent and nearest-neighbor coherent coupling scheme but disappears in the fully coherent coupling scheme. Above the gap edge the RKKY interaction takes in the fully coherent coupling scheme a completely new form: the interaction is for low impurity separations oscillatory instead of antiferromagnetic. The sensitiveness to the local coupling scheme comes from the particularity that the graphene spectrum has two valleys at the two inequivalent K points. A choice of a particular coupling scheme requires a detailed information about the orbital structure of the impurity and can be made only on the grounds of an ab initio calculation.

Biased AB-stacked Bilayer Graphene

In the previous section we found that the form and the strength of the RKKY interaction in AB-stacked bilayer graphene can be controlled by three parameters: the impurity separation, the Fermi energy and the temperature. Depending on experimental situation, these parameters may be hard to control or this may be impracticable in technical applications. The external electric field applied normally to the layers

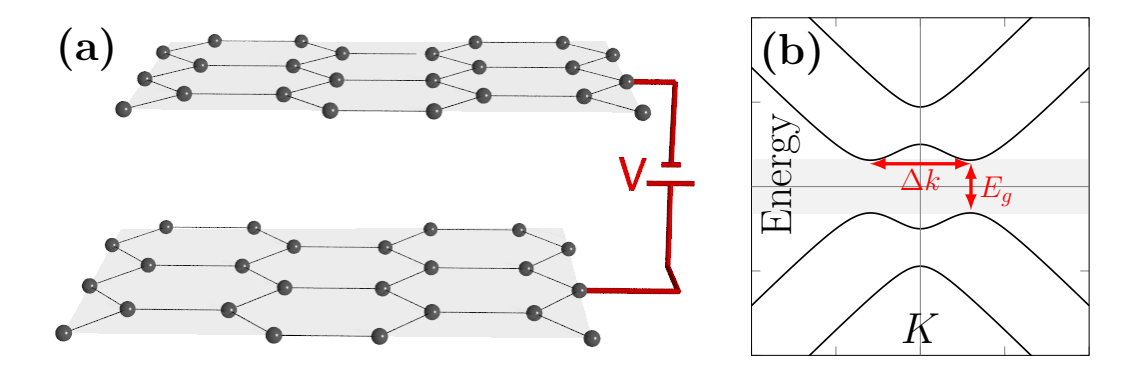


Figure 4.15: Illustration of biased AB-stacked bilayer graphene. The electric field opens around the K point a band gap and distorts the low energy band structure to a form which resembles that of a Mexican hat. The height of the band gap E_g and the width of the Mexican hat Δk are defined according to Eq. (4.3.3).

may provide a more convenient way to tune the RKKY coupling. In the literature it is well known that such electric field converts the low energy band structure into a Mexican-hat-type configuration and opens a band gap at the K point. This behaviour gives rise to the hope that the application of an electric field provides a practicable and powerful way to control the coupling of impurity spins. On these grounds we

want to discuss in this section the RKKY interaction in biased AB-stacked bilayer graphene. In our model the interaction is mediated by the low energy excitations of the biased bilayer which are, in the basis of the four Bloch states $|\Psi_{A_1}^{\mathbf{k}}\rangle$, $|\Psi_{B_1}^{\mathbf{k}}\rangle$, $|\Psi_{A_2}^{\mathbf{k}}\rangle$ and $|\Psi_{B_2}^{\mathbf{k}}\rangle$, described by the following Hamiltonian [93, 94]

$$H_m^0(\mathbf{k}) = \begin{pmatrix} \frac{V}{2} & \tilde{\Phi}_m(\mathbf{k}) & -t_{\perp} & 0\\ \tilde{\Phi}_m^*(\mathbf{k}) & \frac{V}{2} & 0 & 0\\ -t_{\perp} & 0 & -\frac{V}{2} & \tilde{\Phi}_m^*(\mathbf{k})\\ 0 & 0 & \tilde{\Phi}_m(\mathbf{k}) & -\frac{V}{2} \end{pmatrix}$$
(4.3.1)

where V stands for the electrostatic potential between the two layers, t_{\perp} for the interlayer hopping constant of the AB bilayer and $\tilde{\Phi}_{m}(\mathbf{k})$ is defined according to Eq. (3.1.4). The corresponding band structure is given by

$$\epsilon_{\sigma\sigma'}(\mathbf{k}) = \sigma \left[\hbar^2 v_F^2 k^2 + \frac{t_\perp^2}{2} + \frac{V^2}{4} + \sigma' \sqrt{\frac{t_\perp^2}{4} + \hbar^2 v_F^2 k^2 (t_\perp^2 + V^2)} \right]^{1/2}$$
(4.3.2)

with $\sigma, \sigma' \in \{\pm\}$. This expression is plotted in Fig. (4.15b) and one immediately notes that there are four distinct regions: the band gap around the K point, the Mexican hat region, the gap between the low and the high energy band and the two band region. Of particular importance for is the fact that the band structure and in particular the two characteristic parameters, the height of the band gap E_g and the width of the Mexican hat Δk , can be controlled by the electric field:

$$E_g = \frac{Vt_{\perp}}{\sqrt{V^2 + t_{\perp}^2}} \qquad \Delta k = \frac{V}{2\hbar v_F} \sqrt{\frac{V^2 + 2t_{\perp}^2}{V^2 + t_{\perp}^2}}$$
(4.3.3)

These low energy excitations lead to a DOS which takes in the low energy regime the following form

$$D_{\alpha_l}(E) = D_0 \operatorname{sgn}(E) \frac{\rho_{\alpha_l}(E)}{u(E)}$$
(4.3.4)

with $\rho_{\alpha_l}(E)$ defined in Table (4.6), $D_0 = \pi/(2\hbar^2 v_F^2 \Omega_{BZ})$ and u(E) given by

$$u(E) = \operatorname{sgn}\left(E + Vt_{\perp}/(2\sqrt{V^2 + t_{\perp}^2})\right)\sqrt{E^2(V^2 + t_{\perp}^2) - \frac{V^2t_{\perp}^2}{4}}$$
(4.3.5)

The DOS is obtained in an analytical calculation from the imaginary part of the zero temperature Green's function. The Green's function is given in Appendix C.3 and it can be clearly seen that each matrix element is a linear combination of two Hankel functions. Depending on the energy these Hankel functions enter into the formula $D_{\alpha_l}(E) = -1/\pi \lim_{R\to 0} \Im \left[G_{\alpha_l\alpha_l}(\mathbf{R}, E)\right]$ as purely real, purely imaginary or complex and this leads after taking the imaginary part to the results that are presented in Table (C.3). A detailed derivation of the DOS is shown in Appendix C.4. From a

	$ E < \frac{Vt_{\perp}}{2\sqrt{V^2 + t_{\perp}^2}}$	$\frac{Vt_{\perp}}{2\sqrt{V^2+t_{\perp}^2}} \le E \le \frac{V}{2}$	$\frac{V}{2} < E < \sqrt{\frac{V^2}{4} + t_\perp^2}$	$ E \ge \sqrt{\frac{V^2}{4} + t_\perp^2}$
$\rho_{A_1}(E)$	0	$-2 E V\left(2E-V\right)$	$(2E - V) \left(u(E) - E V\right)$	$2u(E)\left(2E-V\right)$
$ \rho_{B_1}(E) $	0	$-2\operatorname{sgn}(E)\left[\left(2E-V\right)EV\right.$ $-\left(2E+V\right)t_{\perp}^{2}\right]$	$(2E - V) (u(E) - E V)$ $+t_{\perp}^{2} \operatorname{sgn}(E) (2E + V)$	2u(E)(2E-V)
$\rho_{A_2}(E)$	0	$2 E V\left(2E+V\right)$	(2E+V)(u(E)+ E V)	$2u(E)\left(2E+V\right)$
$ \rho_{B_2}(E) $	0	$2\operatorname{sgn}(E)\left[\left(2E+V\right)EV\right. \\ \left.+\left(2E-V\right)t_{\perp}^{2}\right]$	$(2E+V)(u(E)+ E V)$ $+t_{\perp}^{2}\operatorname{sgn}(E)(2E-V)$	2u(E)(2E+V)
$\rho(E)$	0	$8 E \left(V^2+t_\perp^2\right)$	$4E\left(2u + \operatorname{sgn}(E)(V^2 + t_{\perp}^2)\right)$	16u(E)E

Table 4.6: The DOS of biased AB-stacked bilayer graphene. The DOS takes the form $D_{\alpha_l}(E) = D_0 \operatorname{sgn}(E) \rho_{\alpha_l}(E)/u(E)$ and the first four rows of this table define the function $\rho_{\alpha_l}(E)$ with $\alpha \in \{A, B\}$, $l \in \{1, 2\}$ and u(E) taken from Eq. (4.3.5). The sum over all four sites yields the function $\rho(E)$ which is presented in the last row.

comparison of the different sublattices it may be seen that the DOS is different on site A and B in each layer. This may be equally found in the unbiased bilayer and can be attributed to the particular stacking of the two layers. A particular effect of the bias voltage is the broken layer inversion symmetry, which can be seen from a comparison of site A_1 and A_2 (or alternatively B_1 and B_2).

The RKKY Interaction at Finite Temperature

We now turn to the RKKY interaction in biased AB-stacked bilayer graphene. As a model we consider a system with two magnetic impurities that couple each via a single site to the gas of delocalized electrons. There are four distinct sites of localized charge and accordingly ten distinct impurity configurations to discuss. With help of the Green's function that is shown in Appendix C.4 we find the ten distinct exchange integrals given by the following separable form

$$\mathcal{J}_{\alpha_{l}\alpha'_{l'}}(\mathbf{R}) = C\mathcal{I}_{\alpha_{l}\alpha'_{l'}}(R)f_{\alpha_{l}\alpha'_{l'}}(\mathbf{R})$$
(4.3.6)

with the intervalley scattering function $f_{\alpha_l\alpha'_{l'}}(\mathbf{R})$ taken from Table (4.3) and the intravalley scattering function defined in Table (4.7). Instead of discussing the effect of the electric field on the ten distinct site-to-site interactions we proceed immediately with the RKKY interaction between intercalated impurities. Here we use the finite

$\alpha_l \alpha'_{l'}$	${\cal I}_{lpha_llpha_{l'}'}(R)$	Definitions
A_1A_1	$\frac{\pi}{4\hbar^2 v_F^2 \beta} \sum_n \frac{\mathcal{B}(-V)^2}{\mathcal{U}^2} \left[\mathcal{A}(-V) H_0^1(z^+ R) + \mathcal{A}(V) H_0^1(z^- R) \right]^2$	
A_2A_2	$\tfrac{\pi}{4\hbar^2 v_F^2 \beta} {\sum}_n \tfrac{\mathcal{B}(V)^2}{\mathcal{U}^2} \left[\mathcal{A}(V) H_0^1(z^+ R) + \mathcal{A}(-V) H_0^1(z^- R) \right]^2$	$z^{+} = \frac{1}{\hbar v_F} \sqrt{(i\hbar\omega_n + \mu)^2 + \frac{V^2}{4} + \mathcal{U}}$
B_1B_1	$\frac{\pi}{4\hbar^2 v_F^2 \beta} \sum_n \frac{\mathcal{B}(-V)^2}{\mathcal{U}^2} \left[\mathcal{F}_+(V) H_0^1(z^+ R) + \mathcal{F}(V) H_0^1(z^- R) \right]^2$	$z^- = rac{1}{\hbar v_F} \sqrt{(i\hbar\omega_n + \mu)^2 + rac{V^2}{4} - \mathcal{U}}$
B_2B_2	$\frac{\pi}{4\hbar^2 v_F^2 \beta} \sum_n \frac{\mathcal{B}(V)^2}{\mathcal{U}^2} \left[\mathcal{F}_+(-V) H_0^1(z^+ R) + \mathcal{F}(-V) H_0^1(z^- R) \right]^2$	$\mathcal{U} = \sqrt{(i\hbar\omega_n + \mu)^2 \left(V^2 + t_\perp^2\right) - \frac{V^2 t_\perp^2}{4}}$
B_1A_1	$\frac{\pi}{\beta} \sum_{n} \frac{1}{\mathcal{U}^2} \left[\mathcal{A}(-V) z^+ H_1^1(z^+ R) + \mathcal{A}(V) z^- H_1^1(z^- R) \right]^2$	
A_2B_2	$\frac{\pi}{\beta} \sum_{n} \frac{1}{\mathcal{U}^2} \left[\mathcal{A}(V) z^+ H_1^1(z^+ R) + \mathcal{A}(-V) z^- H_1^1(z^- R) \right]^2$	$\mathcal{A}(V) = \mathcal{U} + \left[i\hbar\omega_n + \mu\right]V$
B_2A_1	$\frac{\pi t_{\perp}^2}{4\beta} \sum_n \frac{\mathcal{B}(-V)^2}{\mathcal{U}^2} \left[z^+ H_1^1(z^+ R) - z^- H_1^1(z^- R) \right]^2$	$\mathcal{B}(V) = 2i\hbar\omega_n + 2\mu + V$
A_2B_1	$\frac{\pi t_{\perp}^2}{4\beta} \sum\nolimits_n \frac{\mathcal{B}(V)^2}{\mathcal{U}^2} \left[z^+ H_1^1(z^+ R) - z^- H_1^1(z^- R) \right]^2$	$\mathcal{F}_s(V) = \mathcal{U} - s \left[i\hbar \omega_n + \mu \right] V$
A_2A_1	$\frac{\pi t_{\perp}^2}{16\hbar^2 v_F^2 \beta} {\sum}_n \frac{\mathcal{B}(V)^2 \mathcal{B}(-V)^2}{\mathcal{U}^2} \left[H_0^1(z^+ R) - H_0^1(z^- R) \right]^2$	$+ s \frac{2i\hbar\omega_n + 2\mu + V}{2i\hbar\omega_n + 2\mu - V} t_\perp^2$
B_2B_1	$\frac{\pi \hbar^2 v_F^2 t_\perp^2}{\beta} \sum\nolimits_n \frac{1}{\mathcal{U}^2} \left[z^{+2} H_2^1(z^+ R) - z^{-2} H_2^1(z^- R) \right]^2$	

Table 4.7: The ten distinct intravalley scattering functions $\mathcal{I}_{\alpha_l\alpha'_{l'}}(R)$ of biased AB-stacked bilayer graphene. The interaction is always expressed in terms of the six functions that are defined on the right hand side of this table; V stands for the interlayer bias, μ for the chemical potential and $\omega_n = \pi(2n+1)/(\hbar\beta)$ for the Matsubara frequency.

temperature formalism since it provides a much more efficient and powerful way for the numerical implementation. For completeness the ten distinct zero temperature site-to-site exchange integrals are presented in Appendix C.5.

The RKKY Interaction between Intercalated Impurities

The most open position for the intercalation of the AB bilayer is, as described in Section 4.2.3, the position midway in-between the two layers, on top of a B-site carbon atom in the bottom layer and below the hexagon of carbon atoms of the top layer. In a model where each impurity couples via ten nearest carbon atoms to the Dirac-Weyl electron gas there are ten on-site spin-flip processes, four nearest-neighbor spin-flip processes in the top layer, three nearest-neighbor spin-flip processes in the bottom layer and two distinct inter-site spin-flip processes between the two layers. Accordingly there is a remarkably high number of coupling schemes. However, as we have seen above, a wide range of coupling schemes reproduce the basic features of the simplest one, the incoherent coupling scheme. For this reason we restrict the following discussion to this coupling scheme and assume that there are only two different coupling constants that depend solely on the distance to the respective carbon atom: the coupling to the hexagon of carbon atoms in the top layer and the coupling to the three A-site carbon atoms in the bottom layer is described by the constant λ_1 while the coupling to the B-site carbon atom in the bottom layer is described by λ_2 . In this coupling scheme the exchange integral of the intercalated impurity follows from the linear combination of the 10×10 site-to-site interactions. The linear combination is taken in a numerical calculation using the analytical results from Table (4.7). When we discuss the RKKY interaction as a function of the interlayer bias we have to remember that the interlayer bias has impact on the number of the low energy states. Depending on whether or not the system has the possibility to exchange electrons with its surroundings, either the chemical potential or the particle number is fixed when the interlayer bias is applied.

The RKKY interaction with a fixed chemical Potential

First we consider the RKKY interaction in a system with a fixed chemical potential. This situation is, for example, found in epitaxial AB-stacked bilayer graphene grown on SiC where the dangling bonds of the substrate donate conduction electrons and ensure in this way that the chemical potential is pinned. The chemical potential is set, in our model, to a value of 0.1eV. The fixed chemical potential requires that the number of states becomes a function of the interlayer bias. From integration of the DOS which is defined in the last row of Table (4.6) we obtain, at zero temperature, the following expression for the number of electrons in the conduction band

$$N_c(E_F) = 4D_0 \operatorname{sgn}(E_F) \xi(E_F)$$
 (4.3.7)

with $D_0 = \pi/(2\hbar^2 v_F^2 \Omega_{BZ})$ and the function $\xi(E_F)$ defined in Table (4.8). It should be noted that this formula can be also used for other systems with $E_F < 0$ where it gives the number of states in the valence band. The above expression clearly shows that the interlayer bias provides a way to tune the number of electrons in the conduction

	$ E_F < \frac{Vt_{\perp}}{2\sqrt{V^2 + t_{\perp}^2}}$	$\frac{Vt_{\perp}}{2\sqrt{V^2 + t_{\perp}^2}} \le E_F \le \frac{V}{2}$	$\frac{V}{2} < E_F < \sqrt{\frac{V^2}{4} + t_\perp^2}$	$ E_F \ge \sqrt{\frac{V^2}{4} + t_\perp^2}$
$\xi(E_F)$	0	$2 u(E_F) $	$E_F^2 + \frac{V^2}{4} + u(E_F) $	$2\left(E_F^2 + \frac{V^2}{4}\right)$

Table 4.8: The function $\xi(E_F)$ which determines according to Eq. (4.3.7) the particle number in the low energy bands of AB-stacked bilayer graphene for a given Fermi energy E_F and a given interlayer bias V. The function u(E) must be taken from Eq. (4.3.5).

(valence) band so that the chemical potential crosses a certain band structure region and in the following we use this effect to control the RKKY interaction.

In order to get an overview of the RKKY interaction we plot in Fig. (4.16) the exchange integral as a function of the impurity separation and the interlayer bias at a chemical potential of 0.1eV and a temperature of 10K. The density plot on the left shows solely the sign of interaction while the density plot on the right displays the full magnitude of the interaction, multiplied by the factor R^2/E_F . One immediately notes

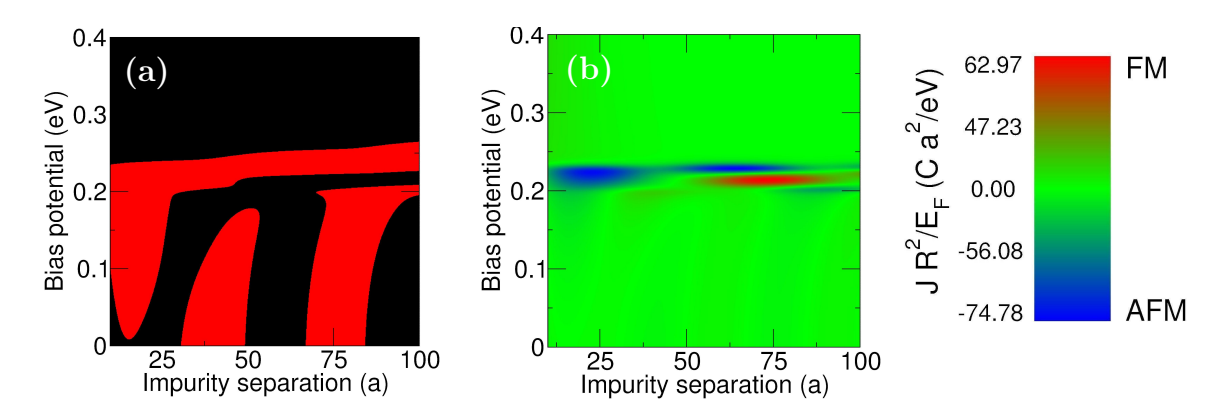


Figure 4.16: The RKKY interaction in biased AB-stacked bilayer graphene at a fixed chemical potential of 0.1eV. The temperature is set to 10K. The density plot on the left shows the sign of the interaction plotted as a function of the impurity separation and the interlayer bias voltage; black stands for ferromagnetic and red for antiferromagnetic coupling. The density plot on the right shows the full strength of the interaction represented in the color scheme which is shown on the right. For presentational reason the exchange integral is in Fig. (4.16b) multiplied by a factor of R^2/E_F .

that there are three distinct regions where the RKKY interaction differs qualitatively. The existence of these three regions can be understood from the different position of the chemical potential within the band structure: for a small bias the chemical potential lies in the gap between the low and the high energy band and the RKKY

interaction oscillates with the period of the Fermi wave vector between ferro- and antiferromagnetic coupling. When the bias is increased so that the chemical potential crosses the Mexican hat region we find an RKKY interaction that oscillates with the different k-vectors that span the Fermi surface. The relative weight of these oscillations as well as the oscillation period can be controlled by the electric field. Here we can achieve for a special interlayer bias the situation that the interaction is antiferromagnetic over the whole range from 10a < R < 100a. Apart from that it is important to note that the magnitude of the interaction is significantly enhanced in the whole Mexican hat region. The latter effect is comparable to the increase in strength that we found in the unbiased bilayer at the edge of the bonding-antibonding band gap and can be seen in Fig. (4.13). The increase in strength follows from a divergence

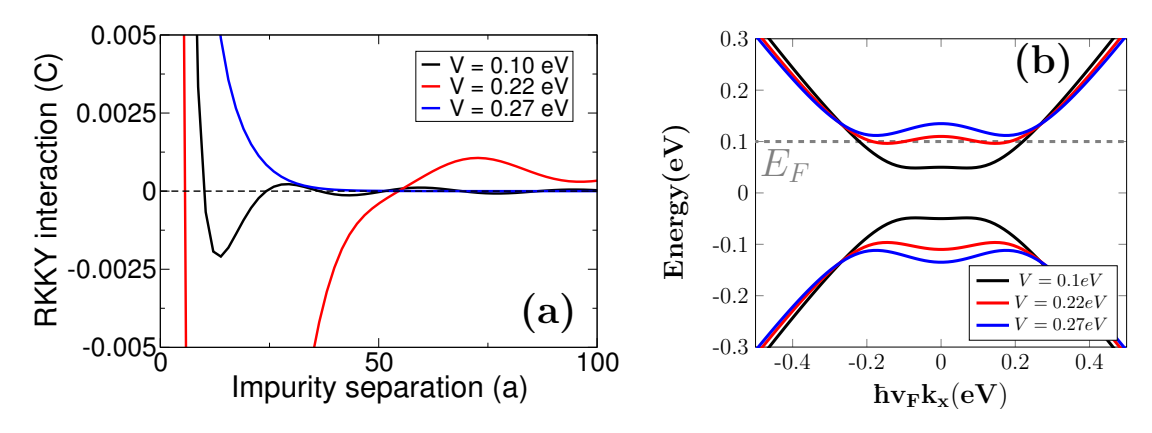


Figure 4.17: The RKKY interaction plotted in armchair direction [Fig. (4.17a)] and the band structure [Fig. 4.17b)] for different interlayer bias voltages. The chemical potential is always held fixed at 0.1eV and the temperature is set to 10K.

of the real space propagator at zero temperature and is partly washed out at higher temperatures. For the bias greater than 0.26eV we access the third region where the chemical potential is in the band gap. For such a high bias the RKKY interaction is always ferromagnetic and decays rapidly as a function of impurity separation.

A more detailed understanding of the RKKY interaction in biased bilayer graphene may be obtained from Fig. (4.17) where the exchange integral is plotted as a function of the impurity separation for different bias voltage. The chemical potential is set to 0.1eV and the temperature to 10K. One immediately notes that the interaction is significantly enhanced in the case V=0.2eV and decays exponentially for V=0.25eV. From comparison of the three curves in the range 10a < R < 30a it gets particularly evident that the interaction changes its form dramatically with interlayer bias, in particular when (as it is the case here) the chemical potential falls in a different band structure region. The sensitivity to the position of the chemical potential gives rise to the question whether the transition from ferro- to antiferromagnetic interaction can be also observed as a function of temperature. To answer this question we plot in Fig. (4.18) the RKKY interaction for a Fermi energy of 0.1eV and different temperature. For the interlayer bias voltage we choose 0.26eV, a value which places the chemical potential into the band gap but close to the band edge. Indeed, we find

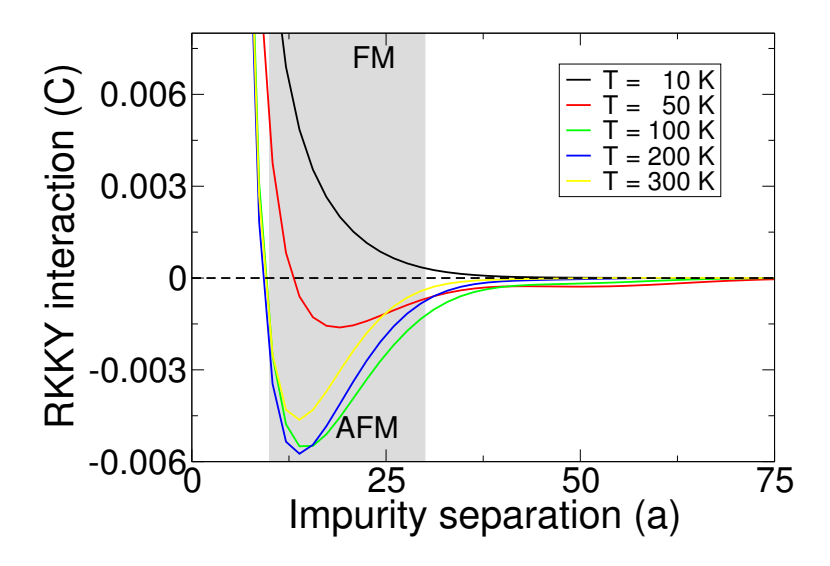


Figure 4.18: The RKKY interaction plotted as a function of the impurity separation for different temperature at a chemical potential of 0.1eV and an interlayer bias of 0.26eV. The picture shows the interaction in armchair direction expressed in terms of the coupling constant C.

that the interaction evolves in the gray shaded region from ferromagnetic to antiferromagnetic as the temperature is increased. Furthermore we find that - instead of the usual temperature dependent damping - the RKKY interaction is massively enhanced in the gray-shaded region. This unusual behaviour can be understood from the fact that for a sufficiently large temperature also the states from the Mexican hat region contribute to the interaction. These states dominate the RKKY interaction when the chemical potential is close to the edge of the Mexican hat region.

The RKKY Interaction with a fixed Particle Number

Now we come to the RKKY interaction in biased AB-stacked bilayer graphene with a fixed particle number, which can be realized in experiment for a graphene bilayer which is deposited on an insulating, nonpolar substrate. In such a system we can directly control the position of the chemical potential by raising or lowering the interlayer bias voltage. For a given particle number and a given interlayer bias the position of the Fermi energy may be read off from Table (4.9). As an approximation, we use this formula also to calculate the position of the Fermi level at low temperature.

The effect of the interlayer bias on the RKKY interaction may be seen in Fig. (4.19) where the exchange integral is shown as a function of impurity separation at different bias voltages. The temperature is fixed at 10K and the particle number is held at its value for zero bias. The initial chemical potential at zero bias is 0.1eV. In the range 10a < R < 30a we find for zero bias an oscillatory interaction that develops into an antiferromagnetic interaction at finite bias. The strength of the interaction increases with increasing interlayer bias. This behaviour can be understood as follows: increasing the interlayer bias we shift the chemical potential into the Mexican hat

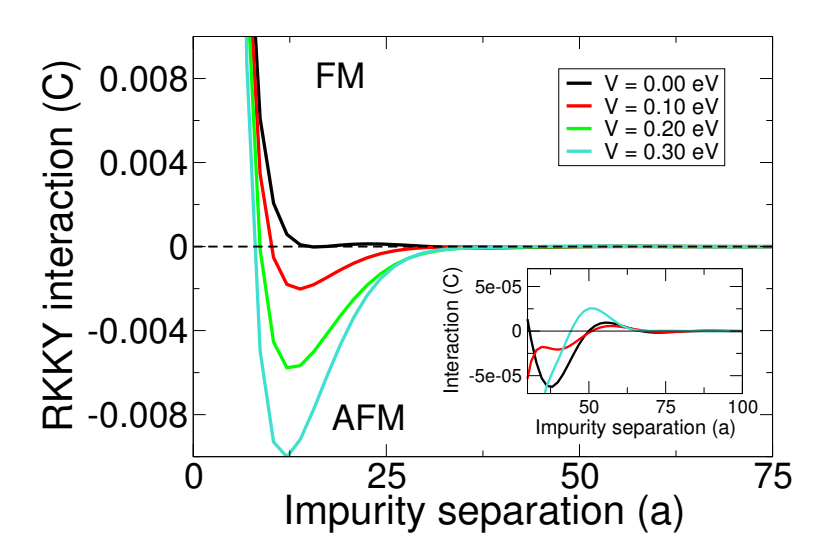


Figure 4.19: The RKKY interaction in biased AB-stacked bilayer graphene at a fixed particle number. Plotted is the exchange integral in armchair direction for different values of the interlayer bias voltage. The particle density is fixed to $n = 1.8 \times 10^{10}/cm^2$ and the temperature is set to 10K. As may be seen from the inset, the interaction starts to oscillate at higher impurity separations.

region where the interaction is, as may be seen in Fig. (4.19), significantly enhanced and antiferromagnetic in the range from 10a to 30a.

	$0 < \xi(N_c) \le V^2$	$V^2 < \xi(N_c) < V^2 + 2t_{\perp}^2$	$\xi(N_c) \ge V^2 + 2t_\perp^2$
$ E_F(N_c) $	$\sqrt{\frac{\xi(N_c)^2 + V^2 t_\perp^2}{4\left(V^2 + t_\perp^2\right)}}$	$\sqrt{\frac{V^2}{4} + \frac{t_{\perp}^2}{2} + \xi(N_c) - \sqrt{\frac{t_{\perp}^4}{4} + \xi(N_c) (V^2 + t_{\perp}^2)}}$	$\sqrt{\frac{ \xi(N_c) }{2} - \frac{V^2}{4}}$

Table 4.9: The Fermi energy E_F as a function of the particle number. In this table we have introduced the function $\xi(N_c) = N_c/(4D_0)$ where N_c is the number of electrons in the conduction band.

The Bulk Band Structure of a IV-VI Semiconductor

IV-VI semiconductors are compounds of a metal from the fourth group and a semimetal from the sixth group of the periodic table. They crystallize, similar to sodium chloride, in a face-centered cubic (fcc) lattice with two atoms per unit cell. It has been discovered, quite recently, that some IV-VI materials, e.g. SnTe, belong to the class of topological insulators [63, 75, 95], i.e. materials that feature topologically protected surface states. The existence of these topological surface states is bound to a non-trivial topology of the bulk but unfortunately (due to a complicated crystal and electronic structure) it is normally very difficult to trace how the surface state derives from the bulk. In this respect, the IV-VI materials offer a unique opportunity for such analysis due to their simple bulk band structure. We recapitulate in this chapter

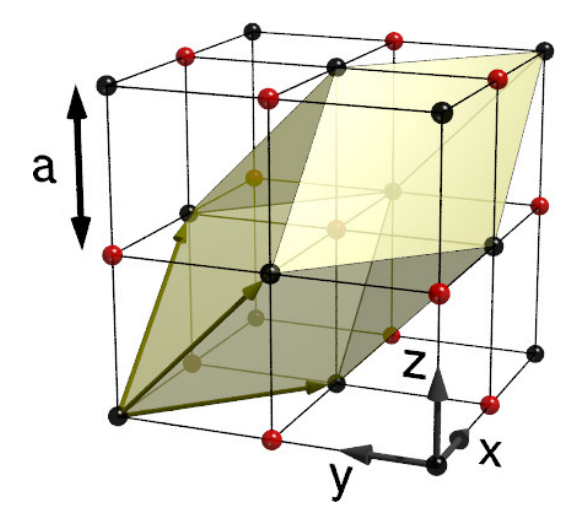


Figure 5.1: Illustration of the crystal structure of a IV-VI semiconductor. The IV-VI semiconductor crystallizes in a face centered cubic (fcc) lattice with two atoms per unit cell. The unit cell is highlighted in yellow.

a model that allows to derive the L point bulk band structure of the IV-VI semiconductor from the microscopic degrees of freedom. Following Ref [73, 74, 84] we start with a tight binding scheme for a simple cubic lattice which serves as a 'parent phase' of the NaCl-type lattice. Later, we turn on the difference of the constituent atoms via adding the different ionization energy of group IV and group VI elements. In this

way we find near the Fermi surface two sixfold degenerate energy levels (including spin degree of freedom) which derive from atomic p-states and split under the effect of the crystal field and the spin-orbit interaction.

Tight Binding Approach for the Parent Phase

Before we come to the IV-VI semiconductor we consider a solid that crystallizes in a simple cubic lattice with one atom per unit cell. We assume that each atom has three valence electrons that occupy three p-orbitals and contribute to the interatomic bonding. The electronic motion in the crystal is described by the Schrödinger equation $H^0\Phi = E\Phi$ with the Hamiltonian $H^0 = -\hbar^2/(2m)\Delta + V(\mathbf{r})$ and the periodic potential $V(\mathbf{r})$. For the solution of the Schrödinger equation we make the tight binding ansatz

$$\Phi_{n\mathbf{k}}(\mathbf{r}) = \frac{1}{\sqrt{N}} \sum_{\mathbf{R} \in \{\text{sc lattice}\}} e^{i\mathbf{k}.\mathbf{R}} p_n(\mathbf{r} - \mathbf{R})$$
 (5.1.1)

where **R** is a position vector of the simple cubic lattice sites, $p_n(\mathbf{r})$ the wave function of the p-orbital in direction $n \in \{x, y, z\}$ and N the number of unit cells. This wave function is an eigenfunction of H^0 on the condition that only the lowest coordination sphere contributes and that the matrix elements between different values of n can be neglected. The first assumption is justified since the wave function decays rapidly with the distance R for remote sites. The second assumption is a good approximation for all k-points on the initial Fermi surface which are non-degenerate in n. Under

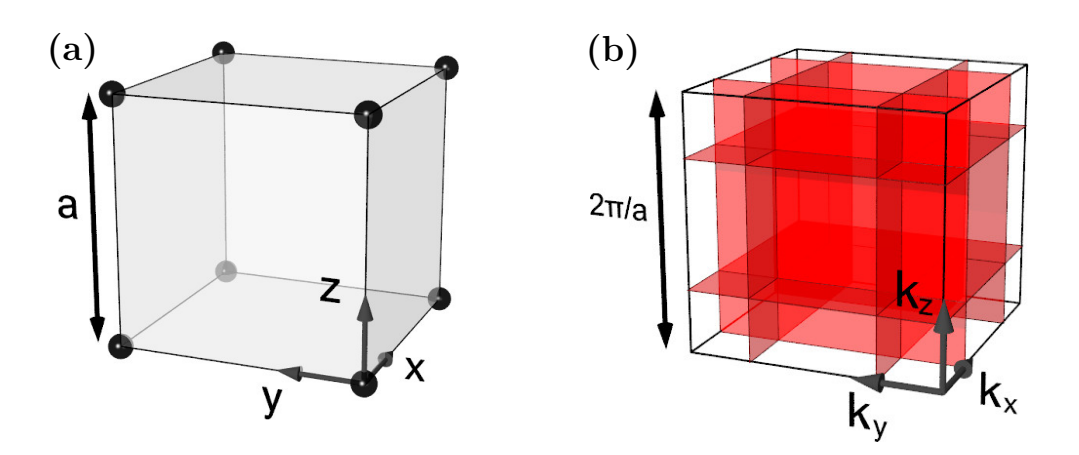


Figure 5.2: The primitive cell of the parent phase in real [Fig. (5.2a)] and reciprocal space [Fig. (5.2b)]. The parent phase crystallizes in a simple cubic lattice with one atom per unit cell. The corresponding Brillouin zone can be seen on the left with the Fermi surface drawn in its inside. The Fermi surface consists, under the assumption of one dimensional orbitals, of six mutually perpendicular planes that intersect in the six points $\mathbf{k}_L = \pi/(2a)(1,1,1)$ (Adapted from [84]).

CHAPTER 5. THE BULK BAND STRUCTURE OF A IV-VI SEMICONDUCTOR

these circumstances the spectrum is given by

$$E_n(\mathbf{k}) = \xi_n(\mathbf{k}) + \eta_n(\mathbf{k}) \tag{5.1.2}$$

with the lattice constant a and the functions ξ_x and η_x defined as

$$\xi_x(\mathbf{k}) = \xi_0 \cos(k_x a) + \xi_1 \left[\cos(k_y a) + \cos(k_z a) \right]$$
(5.1.3)

$$\eta_x(\mathbf{k}) = \eta_1 \cos(k_y a) \cos(k_z a) + \eta_2 \cos(k_x a) \left[\cos(k_y a) + \cos(k_z a)\right]$$
(5.1.4)

The other functions, i.e. $\xi_y(\mathbf{k})$, $\xi_z(\mathbf{k})$, $\eta_y(\mathbf{k})$ and $\eta_z(\mathbf{k})$, can be obtained from Equation 5.1.3 and 5.1.4 by cyclic permutation of the indices. Due to the cubic symmetry there remain no more than four material dependent parameters ξ_0 , ξ_1 , η_1 and η_2 to calculate which can be brought to the form

$$\xi_0 = 2\langle p_x(0,0,0) \mid H_0 \mid p_x(a,0,0) \rangle \tag{5.1.5}$$

$$\xi_1 = 2\langle p_x(0,0,0) \mid H_0 \mid p_x(0,a,0) \rangle \tag{5.1.6}$$

$$\eta_1 = 4\langle p_x(0,0,0) \mid H_0 \mid p_x(0,a,a) \rangle$$
(5.1.7)

$$\eta_2 = 4\langle p_x(0,0,0) \mid H_0 \mid p_x(a,a,0) \rangle$$
(5.1.8)

If we treat the orbitals as if they were one dimensional, that means as if p_x was only finite along the x-axis and zero everywhere else, the spectrum reduces to the form:

$$E_n(\mathbf{k}) = \xi_0 \cos(k_n a) \tag{5.1.9}$$

Each band is half filled so that the hypothetical crystal is a metal. The Fermi surface

	Δ_{ion}	ξ_0	ξ_1	$\hbar\Lambda^-$	$\hbar\Lambda^+$	W_{xy}^-	W_{xy}^+	Θ^-	Θ^+	$\hbar v_{\parallel}$	$\hbar v_{\perp}$
PbTe	0.876	3.41	-0.9	0.424	0.28	-0.09	0.29	1.70	2.54	1.92	5.22
SnTe	0.47	3.5	-0.9	0.158	0.28	-0.075	0.38	1.42	2.63	2.69	4.65
PbSe	1.243	3.65	-0.9	0.424	0.14	-0.315	0.65	1.16	2.95	3.78	3.54
SnSe	0.77	3.7	-0.9	0.158	0.14	-0.5	0.8	0.67	2.99	4.52	2.29

Table 5.1: Material parameters for several IV-VI semiconductors. The crystal field parameter W^{\pm} , the spin-orbit parameter Λ^{\pm} and the matrix elements ξ_0 and ξ_1 are given in units of eV. The two velocities $\hbar v_{\parallel}$ and $\hbar v_{\perp}$ are given in eVÅ. The superscript '–' is taken for group IV atoms whereas the superscript '+' is taken for group VI atoms. It should be noted that SnSe crystallizes normally in a orthorhombic lattice. The rock salt structure must be stabilized through alloying the SnSe crystal with lead (Adapted from [74, 84]).

consists, as illustrated in Fig. (5.2b), of six mutually perpendicular planes.

Formation of the Semiconductor: Dielectrization of the Parent Phase

The model of the parent phase is extraordinary useful for understanding the electronic structure of IV-VI semiconductors: the NaCl-type lattice can be obtained from a simple cubic lattice by filling the (111) planes with group IV and group VI elements alternately. This transformation yields in reciprocal space a body centered cubic (bcc) lattice with a Brillouin zone that is, as may be seen in Fig. (5.3), represented by a truncated octahedron. Folding back the parent phase Fermi surface into the truncated octahedron Brillouin zone clearly shows that a general point on the Fermi surface is twofold degenerate. This degeneracy is lifted by the crystal potential (the one that differentiates between group IV and group VI elements). As a result, the whole Fermi surface of the parent phase gets covered by the band gap and the material transforms into an insulator. However, there are points on the initial Fermi surface which feature a higher degeneracy: these are the crossing lines and points in Fig. (5.2b). The highest degeneracy occurs at the L points where all three planes intersect. As we shall see below, these are the points where the band extrema of a IV-VI semiconductor occur. First, we turn on the ionicity $V_{\text{ion}}(\mathbf{r})$ in the degenerate subspace which is spanned by two states on the initial Fermi surface $|\Phi_{n\mathbf{k}-\mathbf{q}/2}\rangle$ and $|\Phi_{n\mathbf{k}+\mathbf{q}/2}\rangle$ where \mathbf{q} is a bcc basis vector. When we take only the first and the second coordination sphere into account we obtain the following Hamiltonian

$$H_n(\mathbf{k}) = \begin{pmatrix} E_n(\mathbf{k}) & \Delta_{\text{ion}} \\ \Delta_{\text{ion}} & -E_n(\mathbf{k}) \end{pmatrix}$$
 (5.2.1)

with $\Delta_{ion} = \langle p_x(0,0,0) \mid V_{ion}(\mathbf{r}) \mid p_x(0,0,0) \rangle$ and $E_n(\mathbf{k})$ given by Eq. (5.1.9). From a diagonalization of the Hamiltonian it can be seen that the ionization potential splits the degenerate energy band $E_n(\mathbf{k})$ into a separate valence and a separate conduction band

$$\epsilon_n^{\pm}(\mathbf{k}) = \mp \sqrt{E_n(\mathbf{k})^2 + \Delta_{\text{ion}}^2}$$
 (5.2.2)

The initial Fermi surface is now covered by a band gap of $2\Delta_{ion}$ and hence the above transformation turns the crystal into an insulator. The material dependent parameters of the model ξ_0 and Δ_{ion} can be determined by ab initio calculation or experiment and are for a range of IV-VI semiconductors given in Table (5.1).

The Band Structure at the L Point

The maximum degeneracy on the initial Fermi surface occurs at the L points, the points where the cube diagonals intersect with the hexagonal faces of the Brillouin

zone. These eight L points can be connected pairwise by a bcc reciprocal lattice vector so that there remain only four inequivalent ones. At all these L points, the

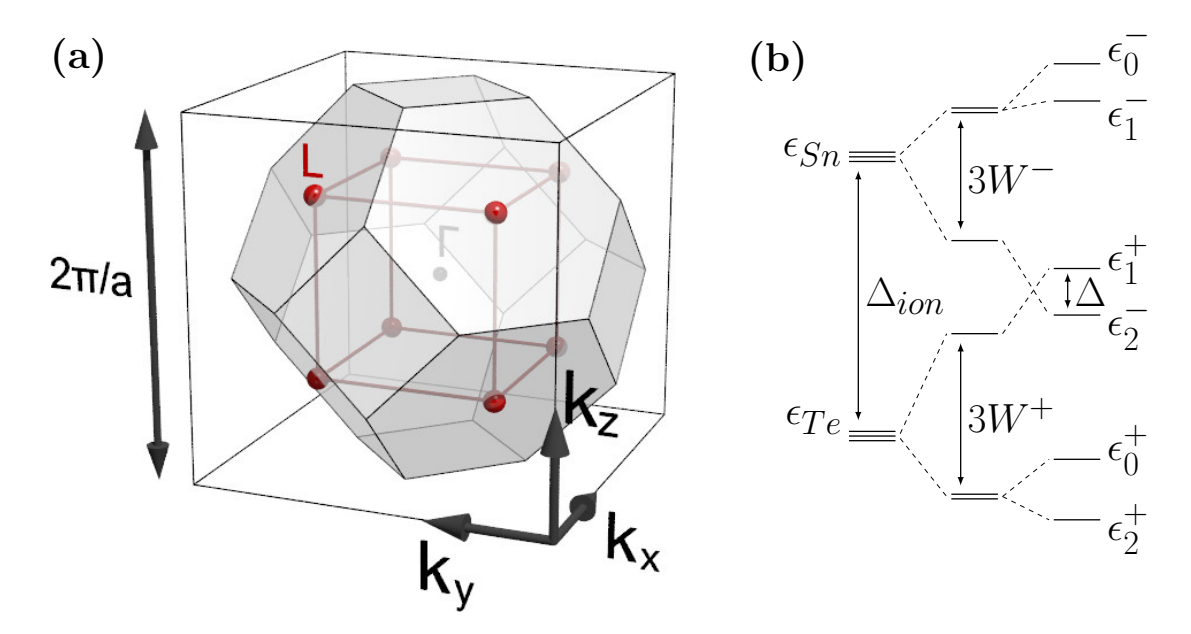


Figure 5.3: The Brillouin zone of a IV-VI semiconductor [Fig. (5.3a)] and the splitting of the band structure at the L points [Fig. 5.3b)]. The Brillouin zone of the fcc lattice is represented by a truncated octahedron. The eight L points coincide with the points where three planes of the initial Fermi surface intersect [see Fig. (5.2)] and are characterized by a sixfold fold degeneracy of the band structure (without spin degree of freedom). The degeneracy is removed, as illustrated in Fig. (5.3b), under the effect of the ionization potential, the crystal field and the spin-orbit interaction (Adapted from [84]). It should be noted that the two band edge states ϵ_1^+ and ϵ_2^- are in this picture inverted, a situation which is for example found in SnTe.

ionization potential $V_{\text{ion}}(\mathbf{r})$ splits the sixfold degeneracy on the initial Fermi surface into two threefold degenerate energy levels $\epsilon^{\pm} = \mp \Delta_{ion}$ which are separated by a gap of $2\Delta_{\text{ion}}$. The corresponding eigenstates are given by

$$\Phi_n^{\pm}(\mathbf{r}) = \sqrt{\frac{2}{N}} \sum_{\mathbf{R} \in \{\text{sc lattice}\}} p_n(\mathbf{r} - \mathbf{R}) \begin{cases} i \sin(\mathbf{k}_L \cdot \mathbf{R}) \\ \cos(\mathbf{k}_L \cdot \mathbf{R}) \end{cases}$$
(5.3.1)

with $\mathbf{k}_L = \pi/(2a)(1,1,1)$. There are two important points to highlight about Eq. (5.3.1): (i) the wave functions, $\Phi_n^+(\mathbf{r})$ and $\Phi_n^-(\mathbf{r})$, have opposite parities and (ii) each wave function includes only one type of p-orbitals either from the atom of the fourth or of the sixth group of the periodic table. The first point is apparent from the transformation $\mathbf{r} \to -\mathbf{r}$. The superscript '+' is taken for even and '-' for odd parity. The second point can be understood as follows: the simple cubic lattice is spanned by the position vectors $\mathbf{R} = \sum_{i=1}^3 m_i \mathbf{a}_i$ with $m_i \in \mathbb{Z}$ and the basis vectors \mathbf{a}_i . An evaluation of the dot product in the argument of the sine or cosine of Eq. (5.3.1) yields $\mathbf{k}_L \cdot \mathbf{R} = \pi/2 \sum_{i=1}^3 m_i$

and hence even multiples of $\pi/2$ at group IV sites and odd multiples of $\pi/2$ on group VI sites. These considerations illustrate the effect of the ionization potential on the L point band structure. However, in order to obtain a realistic spectrum it is necessary to take into account the hybridization of the p-orbitals by the crystal field and the spin-orbit interaction. These interactions remove the threefold degeneracies of even and odd triplets completely and generate the narrow semiconductor band gap.

The Crystal Field

The crystal field operator is in a representation in the degenerate subspace $|\Phi_x^{\pm}\rangle$, $|\Phi_y^{\pm}\rangle$ and $|\Phi_z^{\pm}\rangle$ given by $W_{mn}^{\pm} = \langle \Phi_m^{\pm} | H^0 | \Phi_n^{\pm} \rangle$ with $m \neq n \in \{x,y,z\}$. The particular form of the basis wave functions and the inversion symmetry of H^0 is the reason why the crystal field operator separates into the direct product of two parts, W^+ and W^- , which are defined on the group IV and the group VI subspace, respectively. Using the threefold rotational symmetry around the (111) axis each part may be written as

$$W^{\pm} = W_{xy}^{\pm} \left(C_3 + C_3^{-1} \right) \tag{5.3.2}$$

with $W_{xy}^{\pm} = \sum_{\mathbf{R}} \exp(i\mathbf{k}.\mathbf{R}) \langle p_{x0} \mid H^0 \mid p_{y\mathbf{R}} \rangle$. Under the assumption that only the two lowest coordination spheres contribute, the matrix element W_{xy}^{\pm} reduces to the form

$$W_{xy}^{\pm} = -4\langle p_x(0,0,0) \mid H^0 \mid p_y(a,a,0)\rangle \sin(k_x a) \sin(k_y a)$$
 (5.3.3)

For the definition of the symmetry operator C_3 , which describes a threefold rotation around the (111) axis, it is most convenient to choose a coordinate system where the z'-axis is parallel to the (111)-direction. In this coordinate system the symmetry operator reads

$$C_3 = \exp(2\pi i/3L_z') \tag{5.3.4}$$

with the z' projection of the angular momentum operator L'_z . Now, we write the Hamiltonian that describes the effect of the ionization potential and the crystal field as:

$$H^{\pm} = \mp \Delta_{ion} + 2W_{xy}^{\pm} \cos\left(\frac{2\pi}{3}L_z'\right)$$
 (5.3.5)

From this representation it is clear that the crystal field splits the threefold degenerate level $\epsilon_n^{\pm} = \mp \Delta_{ion}$ into the nondegenerate level $\epsilon_0^{\pm} = \mp \Delta_{ion} + 2W_{xy}^{\pm}$ and the twofold degenerate level $\epsilon_1^{\pm} = \mp \Delta_{ion} - W_{xy}^{\pm}$. The corresponding wave functions coincide with the eigenstates of L_z'

$$|\Phi_0^{\pm}\rangle = |\Phi_{z'}^{\pm}\rangle \tag{5.3.6}$$

$$|\Phi_{\pm}^{\pm}\rangle = \mp \frac{1}{\sqrt{2}} \left(|\Phi_{x'}^{\pm}\rangle \pm i |\Phi_{y'}^{\pm}\rangle \right)$$
 (5.3.7)

with $|\Phi_{x'}^{\pm}\rangle$, $|\Phi_{y'}^{\pm}\rangle$ and $|\Phi_{z'}^{\pm}\rangle$ obtained from the transformation

$$\begin{pmatrix} \begin{vmatrix} \Phi_{x'}^{\pm} \rangle \\ | \Phi_{y'}^{\pm} \rangle \\ | \Phi_{z'}^{\pm} \rangle \end{pmatrix} = \begin{pmatrix} -\frac{1}{\sqrt{6}} & -\frac{1}{\sqrt{6}} & \sqrt{\frac{2}{3}} \\ \frac{1}{\sqrt{2}} & -\frac{1}{\sqrt{2}} & 0 \\ \frac{1}{\sqrt{3}} & \frac{1}{\sqrt{3}} & \frac{1}{\sqrt{3}} \end{pmatrix} \begin{pmatrix} | \Phi_{x}^{\pm} \rangle \\ | \Phi_{y}^{\pm} \rangle \\ | \Phi_{z}^{\pm} \rangle \end{pmatrix}$$
(5.3.8)

The right hand side of Eq. (5.3.8) is a column of the three Bloch sums $|\Phi_n^{\pm}\rangle$ with $n \in \{x, y, z\}$ which are defined according to Eq. (5.3.1).

The Spin-Orbit Interaction

The spin-orbit interaction is given by the operator $H_{SO}^{\pm} = \Lambda^{\pm}(\mathbf{L}.\boldsymbol{\sigma})$ with the coupling constant Λ^{\pm} , the spin operator $\boldsymbol{\sigma}$ and the angular momentum operator \mathbf{L} . Since the parity is a good quantum number at the L point, the Schrödinger equation for the electronic motion in the crystal separates into an equation on the group IV and another equation on the group VI subspace with the Hamiltonian in each case given by

$$H^{\pm} = \mp \Delta_{\text{ion}} + 2W_{xy}^{\pm} \cos\left(\frac{2\pi}{3}L_z'\right) + \Lambda^{\pm} (\mathbf{L}.\boldsymbol{\sigma})$$
 (5.3.9)

To get an explicit representation of the Hamiltonian in the six-dimensional space (including spin degree of freedom) which is spanned by the basis wave functions $|\Phi_0^{\pm\uparrow\downarrow}\rangle$, $|\Phi_+^{\pm\uparrow\downarrow}\rangle$ and $|\Phi_-^{\pm\uparrow\downarrow}\rangle$ we rewrite the dot product as $\mathbf{L}.\boldsymbol{\sigma}=L'_+\sigma'_-+L'_-\sigma'_++L'_z\sigma'_z$. Then we use the well known effect of the ladder operators $L'_{\pm}=L'_x\pm iL'_y$ and $\sigma'_{\pm}=1/2\left(\sigma'_x\pm i\sigma'_y\right)$ on the basis wave functions. We arrange the basis wave functions so that they are sorted by a descending total angular momentum which is, besides the parity, a good quantum number. In this way we can bring the Hamiltonian to the following block diagonal form:

following block diagonal form:
$$H^{\pm} = \mp \Delta_{ion} + \begin{pmatrix} \hbar \Lambda^{\pm} - W_{xy}^{\pm} & 0 & 0 & 0 & 0 & 0 \\ 0 & \hbar \Lambda^{\pm} - W_{xy}^{\pm} & 0 & 0 & 0 & 0 & 0 \\ 0 & 0 & -\hbar \Lambda^{\pm} - W_{xy}^{\pm} & \sqrt{2}\hbar \Lambda^{\pm} & 0 & 0 \\ 0 & 0 & \sqrt{2}\hbar \Lambda^{\pm} & 2W_{xy}^{\pm} & 0 & 0 \\ 0 & 0 & 0 & 0 & -\hbar \Lambda^{\pm} - W_{xy}^{\pm} & \sqrt{2}\hbar \Lambda^{\pm} \\ 0 & 0 & 0 & 0 & \sqrt{2}\hbar \Lambda^{\pm} & 2W_{xy}^{\pm} \end{pmatrix}$$
 (5.3.10)

The solution of the Schrödinger equation is presented in Table (5.2). The results are expressed in terms of the six material dependent parameters Δ_{ion} , ξ_0 , Λ^+ , Λ^- , W_{xy}^+ and W_{xy}^- which are for a range of the IV-VI semiconductors given in Table (5.1). It can be clearly seen that the ionization potential, the crystal field and the spin-orbit

interaction split the twelvefold degenerate level (including the spin degree of freedom) into six levels ϵ_n^{\pm} with $n \in \{0,1,2\}$ which are twofold Kramers-degenerate. Due to W and $H_{\rm SO}$ interactions the band gap covering the parent phase Fermi surface reduces to a minimum at the L points and it is formed by the energy levels ϵ_2^- and ϵ_1^+ . The eigenfunctions that correspond to the upper and the lower edge of the band gap take a particularly interesting form since the crystal field and the spin-orbit interaction mix two basis wave functions with different angular momentum and opposite spin. The mixing is controlled by the spin mixing parameter Θ^{\pm} which is defined as

$$\sin \Theta^{\pm} = \sqrt{2} \frac{\hbar \Lambda^{\pm}}{A^{\pm}} \qquad \cos \Theta^{\pm} = -\frac{\hbar \Lambda^{\pm} + 3W_{xy}^{\pm}}{2A^{\pm}} \qquad (5.3.11)$$

with

$$A^{\pm} = \left[2\hbar^2 \lambda^{\pm 2} + \left(\hbar \Lambda^{\pm} + 3W_{xy}^{\pm} \right)^2 / 4 \right]^{1/2}$$
 (5.3.12)

From a comparison of the different IV-VI semiconductors it can be seen that there are some materials where the ordering of the gap edge states can be inverted compared to vacuum, that means the even state gets into the conduction band whereas the odd state into the valence band. As an example of a material with such a strong crystal field and spin-orbit interaction we present in Fig. (5.3b) the L point energy bands in SnTe. This band inversion makes the material topologically non-trivial [63, 75, 79] because such level ordering is the opposite to what one expects in 'vacuum', e.g. for separated atoms (where W=0).

The k.p Hamiltonian

In the previous section, we have presented an analytical derivation of the L point band structure of a IV-VI semiconductor. We started with a simple cubic lattice and then included subsequently the difference of the ionization energies of the group IV and group VI atoms, the crystal field and the spin-orbit interaction. In this way we found that the former twelvefold degenerate energy level (including spin degree of freedom) splits into six separate energy levels which are each twofold degenerate. However, an understanding of the low energy physics including the topological surface states requires the momentum-dependent Hamiltonian close to the L point, which can be, for example, obtained from $\mathbf{k}.\mathbf{p}$ theory. The standard $\mathbf{k}.\mathbf{p}$ procedure is to express the solution of the Schrödinger equation $H \mid \Psi \rangle = \epsilon \mid \Psi \rangle$ in the basis of an expansion point $\exp(i\mathbf{k}.\mathbf{r}) \mid \Phi_i \rangle$. The coefficients of this expansion $\psi_{jl}(\mathbf{r})$ have to satisfy the eigenvalue equation $\sum_j H_{ij} \psi_{jl} = \epsilon_{lk} \psi_{il}$ with the $\mathbf{k}.\mathbf{p}$ Hamiltonian H_{ij} given by

$$H_{ij} = \epsilon_i \delta_{ij} + \frac{\hbar}{m} \langle \Phi_i \mid \mathbf{k}.\mathbf{p} \mid \Phi_j \rangle$$
 (5.4.1)

where $\mathbf{p} = -i\hbar\nabla$ stands for the momentum operator and m for the electron mass. As a basis we choose the four band edge states $|\Phi_2^-\rangle$, $K|\Phi_2^-\rangle$, $|\Phi_1^+\rangle$ and $K|\Phi_1^+\rangle$ which

$\overline{\epsilon_0^{\pm} = \mp \Delta_{ion} + \hbar \Lambda^{\pm} - W_{xy}^{\pm}}$	$ \Phi_0^{\pm}\rangle = \Phi_+^{\pm\uparrow}\rangle$ $K \Phi_0^{\pm}\rangle = - \Phi^{\pm\downarrow}\rangle$
$\epsilon_1^{\pm} = \mp \Delta_{ion} + \frac{W_{xy}^{\pm} - \hbar \Lambda^{\pm}}{2} + A^{\pm}$	$ \Phi_{1}^{\pm}\rangle = \cos\frac{\Theta^{\pm}}{2} \Phi_{+}^{\pm\downarrow}\rangle + \sin\frac{\Theta^{\pm}}{2} \Phi_{0}^{\pm\uparrow}\rangle$ $K \Phi_{1}^{\pm}\rangle = \cos\frac{\Theta_{\pm}}{2} \Phi_{-}^{\pm\uparrow}\rangle + \sin\frac{\Theta^{\pm}}{2} \Phi_{0}^{\pm\downarrow}\rangle$
$\epsilon_2^{\pm} = \mp \Delta_{ion} + \frac{W_{xy}^{\pm} - \hbar \Lambda^{\pm}}{2} - A^{\pm}$	$ \Phi_{2}^{\pm}\rangle = -\sin\frac{\Theta^{\pm}}{2} \Phi_{+}^{\pm\downarrow}\rangle + \cos\frac{\Theta^{\pm}}{2} \Phi_{0}^{\pm\uparrow}\rangle$ $K \Phi_{2}^{\pm}\rangle = -\sin\frac{\Theta^{\pm}}{2} \Phi_{-}^{\pm\uparrow}\rangle + \cos\frac{\Theta^{\pm}}{2} \Phi_{0}^{\pm\downarrow}\rangle$

Table 5.2: The L point band structure of a IV-VI semiconductor. The band structure is obtained from diagonalization of the Hamiltonian, Eq. (5.3.10), with A^{\pm} defined according to Eq. (5.3.12). The spectrum is expressed in terms of the six material dependent parameters $\Delta_{\rm ion}$, ξ_0 , Λ^+ , Λ^- , W^+_{xy} and W^-_{xy} which are for a range of IV-VI semiconductors given in Table (5.1). To each eigenvalue belongs a pair of eigenstates that is always presented in the column on the right; K stands for the Kramers operator, the superscript ' \pm ' for the parity of the wave function and the basis wave functions $|\Phi_0^{\pm\uparrow}\rangle$, $|\Phi_+^{\pm\uparrow}\rangle$ and $|\Phi_-^{\pm\uparrow}\rangle$ are defined according to Eqs. (5.3.6) and (5.3.7).

are pairwise connected by the time reversal symmetry and which have, as indicated by the superscript ' \pm ', opposite parity. A consequence of the particular structure of the basis wave functions is that the complexity of the calculation reduces dramatically: the different parity of the two wave functions and the inversion symmetry of the dot product $\mathbf{k}.\mathbf{p}$ imply that both 2×2 blocks on the diagonal of the $\mathbf{k}.\mathbf{p}$ matrix are zero

$$\langle \Phi_{2}^{-} \mid \mathbf{k}.\mathbf{p} \mid \Phi_{2}^{-} \rangle = \langle I\Phi_{2}^{-} \mid \mathbf{k}.\mathbf{p} \mid I\Phi_{2}^{-} \rangle$$

$$= \langle \Phi_{2}^{-} \mid I^{\dagger}\mathbf{k}.\mathbf{p}I \mid \Phi_{2}^{-} \rangle$$

$$= -\langle \Phi_{2}^{-} \mid \mathbf{k}.\mathbf{p} \mid \Phi_{2}^{-} \rangle$$

$$= 0$$
(5.4.2)

where I stands for the inversion operator. The time reversal symmetry imposes furthermore relations between the matrix elements in the off-diagonal blocks so that the problem reduces to two matrix elements only:

$$\langle K\Phi_2^- \mid \mathbf{k}.\mathbf{p} \mid K\Phi_1^+ \rangle = \langle \Phi_2^- \mid K^{\dagger}\mathbf{k}.\mathbf{p}K \mid \Phi_1^+ \rangle^*$$
$$= -\langle \Phi_2^- \mid \mathbf{k}.\mathbf{p} \mid \Phi_1^+ \rangle^*$$
(5.4.3)

$$\langle \Phi_2^- \mid \mathbf{k}.\mathbf{p} \mid K\Phi_1^+ \rangle = \langle K\Phi_2^- \mid K\mathbf{k}.\mathbf{p}K \mid \Phi_1^+ \rangle^*$$
$$= \langle K\Phi_2^- \mid \mathbf{k}.\mathbf{p} \mid \Phi_1^+ \rangle^*$$
(5.4.4)

For a further simplification of these matrix elements we rewrite the dot product $\mathbf{k}.\mathbf{p}$ with help of the operator $p'_{\pm} = p'_x \pm i p'_y$ and the wave vector $k'_{\pm} = k'_x \pm i k'_y$. In order to use the symmetry of the system it is here convenient to choose a coordinate system where the z'-axis is parallel to the (111)-direction. After replacing the band edge states $|\Phi_1^+\rangle$ and $|\Phi_2^-\rangle$ by the expressions from Table (5.2) we can bring the first matrix element, Eq. (5.4.3), to the form:

$$\langle \Phi_{2}^{-} \mid \mathbf{k}.\mathbf{p} \mid \Phi_{1}^{+} \rangle = -\frac{1}{2} \sin \frac{\Theta^{-}}{2} \cos \frac{\Theta^{+}}{2} \langle \Phi_{+}^{-\downarrow} \mid k'_{+} p'_{-} + k'_{-} p'_{+} \mid \Phi_{+}^{+\downarrow} \rangle$$

$$+ \frac{1}{2} \cos \frac{\Theta^{-}}{2} \sin \frac{\Theta^{+}}{2} \langle \Phi_{0}^{-\uparrow} \mid k'_{+} p'_{-} + k'_{-} p'_{+} \mid \Phi_{0}^{+\uparrow} \rangle$$

$$- \sin \frac{\Theta^{-}}{2} \cos \frac{\Theta^{+}}{2} \langle \Phi_{+}^{-\downarrow} \mid k'_{z} p'_{z} \mid \Phi_{+}^{+\downarrow} \rangle$$

$$+ \cos \frac{\Theta^{-}}{2} \sin \frac{\Theta^{+}}{2} \langle \Phi_{0}^{-\uparrow} \mid k'_{z} p'_{z} \mid \Phi_{0}^{+\uparrow} \rangle$$
(5.4.5)

Then we use the identity $[L'_z, p_{\pm}] = \pm \hbar p_{\pm}$ in order to show that the first two lines of Eq. (5.4.5) vanish:

$$0 = \langle \Phi_{+}^{-\downarrow} \mid [L'_{z}, p'_{\pm}] \mid \Phi_{+}^{+\downarrow} \rangle = \pm \hbar \langle \Phi_{+}^{-\downarrow} \mid p'_{\pm} \mid \Phi_{+}^{+\downarrow} \rangle$$
 (5.4.6)

$$0 = \langle \Phi_0^{-\uparrow} \mid [L'_z, p'_{\pm}] \mid \Phi_0^{+\uparrow} \rangle = \pm \hbar \langle \Phi_0^{-\uparrow} \mid p'_{\pm} \mid \Phi_0^{+\uparrow} \rangle$$
 (5.4.7)

On these grounds Eq. (5.4.5) reduces to the form $\langle \Phi_2^- | \mathbf{k}.\mathbf{p} | \Phi_1^+ \rangle = mv_{\parallel}k_z'$ with the velocity v_{\parallel} defined as follows:

$$v_{\parallel} = \frac{1}{m} \cos \frac{\Theta^{-}}{2} \sin \frac{\Theta^{+}}{2} \langle \Phi_{0}^{-\uparrow} \mid p'_{z} \mid \Phi_{0}^{+\uparrow} \rangle$$
$$-\frac{1}{m} \sin \frac{\Theta^{-}}{2} \cos \frac{\Theta^{+}}{2} \langle \Phi_{+}^{-\downarrow} \mid p'_{z} \mid \Phi_{+}^{+\downarrow} \rangle$$
(5.4.8)

Similarly we replace the dot product and the basis wave functions in the second matrix element, Eq. (5.4.4), which gives the following expression

$$\langle \Phi_{2}^{-} \mid \mathbf{k}.\mathbf{p} \mid K\Phi_{1}^{+} \rangle = -\frac{1}{2} \sin \frac{\Theta^{-}}{2} \sin \frac{\Theta^{+}}{2} \langle \Phi_{+}^{-\downarrow} \mid k'_{+}p'_{-} + k'_{-}p'_{+} \mid \Phi_{0}^{+\downarrow} \rangle$$

$$+ \frac{1}{2} \cos \frac{\Theta^{-}}{2} \cos \frac{\Theta^{+}}{2} \langle \Phi_{0}^{-\uparrow} \mid k'_{+}p'_{-} + k'_{-}p'_{+} \mid \Phi_{-}^{+\uparrow} \rangle$$

$$- \sin \frac{\Theta^{-}}{2} \sin \frac{\Theta^{+}}{2} \langle \Phi_{+}^{-\downarrow} \mid k'_{z}p'_{z} \mid \Phi_{0}^{+\downarrow} \rangle$$

$$+ \cos \frac{\Theta^{-}}{2} \cos \frac{\Theta^{+}}{2} \langle \Phi_{0}^{-\uparrow} \mid k'_{z}p'_{z} \mid \Phi_{-}^{+\uparrow} \rangle$$
(5.4.9)

With help of the two commutators $[L'_z, p_{\pm}] = \pm \hbar p_{\pm}$ and $[L'_z, p'_z] = 0$ it can be shown easily that parts of this matrix element evaluate to zero

$$\langle \Phi_{+}^{-\downarrow} \mid [L'_{z}, p'_{-}] \mid \Phi_{0}^{+\downarrow} \rangle = \hbar \langle \Phi_{+}^{-\downarrow} \mid p'_{-} \mid \Phi_{0}^{+\downarrow} \rangle = -\hbar \langle \Phi_{+}^{-\downarrow} \mid p'_{-} \mid \Phi_{0}^{+\downarrow} \rangle = 0$$
 (5.4.10)

$$\langle \Phi_0^{-\uparrow} \mid [L'_z, p'_-] \mid \Phi_-^{+\uparrow} \rangle = \hbar \langle \Phi_0^{-\uparrow} \mid p'_- \mid \Phi_-^{+\uparrow} \rangle = -\hbar \langle \Phi_0^{-\uparrow} \mid p'_- \mid \Phi_-^{+\uparrow} \rangle = 0 \tag{5.4.11}$$

$$\langle \Phi_{+}^{-\downarrow} \mid [L'_z, p'_z] \mid \Phi_{0}^{+\downarrow} \rangle = \hbar \langle \Phi_{+}^{-\downarrow} \mid p'_z \mid \Phi_{0}^{+\downarrow} \rangle = 0 \tag{5.4.12}$$

$$\langle \Phi_0^{-\uparrow} \mid [L_z', p_z'] \mid \Phi_-^{+\uparrow} \rangle = \hbar \langle \Phi_0^{-\uparrow} \mid p_z' \mid \Phi_-^{+\uparrow} \rangle = 0$$
 (5.4.13)

so that Eq. (5.4.9) may be written as $\langle \Phi_2^- | \mathbf{k}.\mathbf{p} | K\Phi_1^+ \rangle = mv_{\perp}k'_{\perp}$ with the velocity v_{\perp} given by:

$$v_{\perp} = \frac{1}{2m} \cos \frac{\Theta^{-}}{2} \cos \frac{\Theta^{+}}{2} \langle \Phi_{0}^{-\uparrow} \mid p'_{+} \mid \Phi_{-}^{+\uparrow} \rangle$$
$$-\frac{1}{2m} \sin \frac{\Theta^{-}}{2} \sin \frac{\Theta^{+}}{2} \langle \Phi_{+}^{-\downarrow} \mid p'_{+} \mid \Phi_{0}^{+\downarrow} \rangle$$
(5.4.14)

Overall, we conclude that the $\mathbf{k}.\mathbf{p}$ Hamiltonian takes the form

$$H = \begin{pmatrix} \Delta & 0 & \hbar v_{\parallel} k_z' & \hbar v_{\perp} k_{-}' \\ 0 & \Delta & \hbar v_{\perp} k_{+}' & -\hbar v_{\parallel} k_z' \\ \hbar v_{\parallel} k_z' & \hbar v_{\perp} k_{-}' & -\Delta & 0 \\ \hbar v_{\perp} k_{+}' & -\hbar v_{\parallel} k_z' & 0 & -\Delta \end{pmatrix}$$
(5.4.15)

with $\Delta = (\epsilon_2^- - \epsilon_1^+)/2$. The two velocities v_{\parallel} and v_{\perp} are for a range of IV-VI semiconductors given in Table (5.1). These two velocities were obtained in Ref. [84] from a tight binding approach that allows to express them through parameters of the band structure.

The Band Structure in Vicinity of the L Point

The low energy excitations in the vicinity of the L point are given by the $\mathbf{k}.\mathbf{p}$ Hamiltonian [Eq. (5.4.15)]. With this Hamiltonian we get the following Dirac-type equation

$$\begin{pmatrix} \Delta & \hbar \, \boldsymbol{\tau}' . V \mathbf{k}' \\ \hbar \, \boldsymbol{\tau}' . V \mathbf{k}'_{\perp} & -\Delta \end{pmatrix} \psi = \epsilon \psi \tag{5.5.1}$$

where $V = \text{Diag}(v_{\perp}, v_{\perp}, v_{\parallel})$, $\mathbf{k}' = -i\nabla$ and $\boldsymbol{\tau}' = \left(\tau_x', \tau_y', \tau_z'\right)$ is the vector of Pauli matrices. Solving this equation yields the results which are displayed in Table (5.3). Each of the two bands is twofold degenerate and the bands are separated by a band gap of 2Δ . Close to the L point the band structure can be approximated by an elliptic paraboloid with the eccentricity controlled by the two velocities v_{\parallel} and v_{\perp} .

$\epsilon_{\mathbf{k}'+} = +\sqrt{\Delta^2 + \hbar^2 \left(v_{\parallel}^2 k_z'^2 + v_{\perp}^2 k_{\perp}'^2\right)}$	$ \Psi_{\mathbf{k}'+}^{(1)}\rangle = N\left(\Phi_{2}^{-}\rangle + \gamma_{1}(\mathbf{k}') \Phi_{1}^{+}\rangle + \gamma_{2}(\mathbf{k}')K \Phi_{1}^{+}\rangle\right)$ $ \Psi_{\mathbf{k}'+}^{(2)}\rangle = N\left(K \Phi_{2}^{-}\rangle + \gamma_{2}^{*}(\mathbf{k}') \Phi_{1}^{+}\rangle - \gamma_{1}(\mathbf{k}') K \Phi_{1}^{+}\rangle\right)$
$\epsilon_{\mathbf{k}'-} = -\sqrt{\Delta^2 + \hbar^2 \left(v_{\parallel}^2 k_z'^2 + v_{\perp}^2 k_{\perp}'^2\right)}$	$ \Psi_{\mathbf{k}'-}^{(1)}\rangle = N\left(-\gamma_1(\mathbf{k}') \mid \Phi_2^-\rangle - \gamma_2(\mathbf{k}') K \mid \Phi_2^-\rangle + \Phi_1^+\rangle\right)$
	$ \Psi_{\mathbf{k}'-}^{(2)}\rangle = N\left(-\gamma_2^*(\mathbf{k}') \mid \Phi_2^-\rangle - \gamma_1(\mathbf{k}') K \mid \Phi_2^-\rangle + K \mid \Phi_1^+\rangle\right)$

Table 5.3: The band structure in vicinity of the L points. The band structure is expressed in terms of the material dependent parameters shown in Table (5.1). Each eigenvalue $\epsilon_{\mathbf{k}'l}$ with $l \in \{\pm\}$ is twofold degenerate. The corresponding eigenfunctions $|\Psi_{\mathbf{k}'l}^{(1)}\rangle$ and $|\Psi_{\mathbf{k}'l}^{(2)}\rangle$ are displayed in the column on the right represented in the basis of the bulk band edge states $|\Phi_2^-\rangle$, $K|\Phi_2^-\rangle$, $|\Phi_1^+\rangle$ and $K|\Phi_1^+\rangle$ which are defined in Table (5.2). The components of each eigenvector are given in terms of $\gamma_1(\mathbf{k}') = \hbar v_{\parallel} k'_{z}/(\Delta + |\epsilon|)$ and $\gamma_2(\mathbf{k}') = \hbar v_{\perp} k'_{+}/(\Delta + |\epsilon|)$. The normalization N ensures that $\langle \Psi_{\mathbf{k}'l}^{i} | \Psi_{\mathbf{k}'l}^{i} \rangle = 1$ with $i \in \{1, 2\}$.

The Topological Surface States of a Topological Insulator of the SnTe Class

The IV-VI semiconductors feature, as we have seen in the previous chapter, a direct band gap in the bulk spectrum at the L points of the Brillouin zone [73, 74]. The band gap separates two Kramers doublets - at the upper and the lower band edge - which have opposite parities. In the 'normal' order, which is for example found in lead telluride (PbTe), the odd states belong to the conduction band and the even states to the valence band of the crystal. This order is called 'normal' since such level ordering

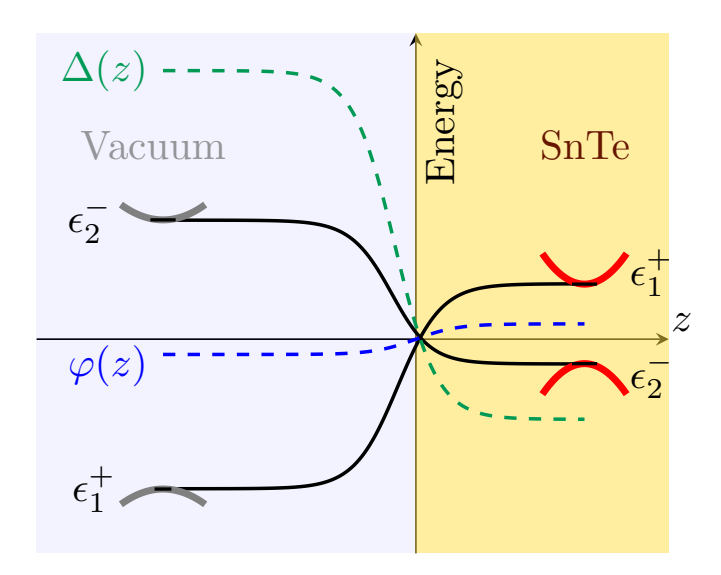


Figure 6.1: Illustration of the band structure at surface. The valence and the conduction band are separated by a band gap which takes negative sign on the SnTe side and positive sign on the vacuum side. Both bands are bend downwards as the surface is approached. The band gap is modeled by the function $\Delta(z)$ and the band bending by the function $\varphi(z)$.

can be adiabatically connected to the level ordering in a free atom limit with the odd states stemming from the group IV atom and the even states stemming from the

group VI atom. However, in some materials such as tin telluride (SnTe) the band edge states are inverted compared to the 'normal' order. These materials are referred to as crystalline topological insulators [57, 58, 59, 60, 61, 62] and they host at the interface to a 'normal' material [75, 76, 77, 78, 95], or to vacuum [63, 64, 79, 80, 81, 82, 83], linear dispersing surface states. These surface states obey a Dirac-Weyl equation and are a consequence of the particular topology of the bulk band structure. They are protected by the specific mirror symmetry plane of the crystal [64]. Although the Dirac-Weyl character of the topological surface states is universal, their spin properties (i.e. the spin texture) are not. Understanding these properties requires a direct link of the surface states to the bulk band structure. The model which we described in the previous chapter offers a unique opportunity to explicitly trace this connection. In the following we derive the topological surface states from the microscopic model of the bulk and present their spin texture for the Γ and the M points of the hexagonal Brillouin zone of the (111) surface. We find that the spin texture is represented by a vector field which is always tangential to a conic section. At the M points, the conic section can be efficiently tuned by raising or lowering the band bending at the surface and in this way it is even possible to drive the spin texture from the usual elliptic to a hyperbolic form.

The Topological Surface States

There are two most common low-indexed surface planes which are available experimentally in the IV-VI semiconductors: the (100) and (111) surfaces. The (001) surface is the common cleavage plane. For this facet the two bulk L points project on the same X point of the surface Brillouin zone. In this situation the scattering between the two L points must be included. Yet the scattering matrix element is unknown, and to avoid this uncertainty we shall focus in this work on the (111) surface. The (111) surface is covered by one single type of atom. At the projections of the four bulk L points, the Γ and the three M points, there occur topological surface states. These states are the consequence of the inverted bulk band structure that is found for some IV-VI semiconductors, which are here referred to as the topological insulators of the SnTe class. The present section addresses the derivation of these topological surface states starting from the low energy spectrum of the bulk. To this end we take the k.p Hamiltonian that we derived in the previous section and replace the band gap Δ by a gap function $\Delta(z) = \Delta_0 f(z)$. This function models the inversion of the band gap across a contact which connects vacuum on the one side with the topological insulator on the other side [75, 81]. The inversion takes place along the z direction which coincides in our choice of the coordinate system with the (111) direction. We model the material-vacuum border assuming that the gap is of infinite height on the vacuum side, takes the zero value on the surface and limits to $\Delta_0 < 0$ on the SnTe side. Henceforth, the function f(z) is subject to the following boundary conditions: $f(-\infty) = -\infty$, f(0) = 0 and $f(\infty) = 1$. Also there is a band bending of the valence and the conduction bands close to the surface [Fig. (6.1)]. This effect is included in our model via the function $\varphi(z) = \varphi_0 f(z)$ which we assume to have the same z dependence than the gap function. After substituting the gap and the band bending function into the \mathbf{k} . \mathbf{p} Hamiltonian we find the low energy excitations of the surface described by the following Dirac-type equation

$$\begin{pmatrix} \Delta(z) & \lambda \\ \lambda & -\Delta(z) \end{pmatrix} \psi = (\epsilon - \varphi(z)) \psi \tag{6.1.1}$$

with $\lambda = \boldsymbol{\tau}.RVR^{\dagger}\mathbf{k},\ V = \mathrm{Diag}\left(v_{\perp},v_{\perp},v_{\parallel}\right),\ \mathbf{k} = -i\nabla$, the vector of Pauli matrices $\boldsymbol{\tau} = (\tau_x, \tau_y, \tau_z)$, and the two velocities v_{\parallel} and v_{\perp} defined according to Eqs. (5.4.8) and (5.4.14). The rotation matrix $R = R_u(\beta)R_z(\alpha)$ allows to describe with the formalism not only the surface states in vicinity of the Γ point but also the surface states in vicinity of the three M points of the surface Brillouin zone. The Γ point is captured by the case $\alpha = \beta = 0$. For the three M points the rotation matrix ensures the rotation from the local coordinate system at each bulk L point, where the operator λ takes the form $\lambda = \tau' \cdot V \mathbf{k}'$, to a coordinate system which has the z-axis parallel to the (111) direction. This transformation can be achieved by a rotation around the (111) axis which is represented by the elementary rotation matrix $R_z(\alpha)$ and a subsequent rotation around the new y-axis which is represented by $R_y(\beta)$. The rotation angles for the three different M points, which may be seen in Fig. (6.2a), are given by $\alpha_i = (-1)^{i+1}\pi/6$ and $\beta_i = \arccos(1/3)$ with $i \in \{1,2,3\}$. The rotation angles are chosen so that the Γ and the three M points have a common z-axis. But it should be noted that each of these high symmetry points has its own coordinate system in the (111) plane. Furthermore it is necessary to stress that the rotation of the coordinate system also implies a transformation to a new set of basis wave functions. While the k.p Hamiltonian of the bulk is defined in the basis of the four band edge states $|\Phi_2^-\rangle$, $K|\Phi_2^-\rangle$, $|\Phi_1^+\rangle$ and $K|\Phi_1^+\rangle$ the Hamiltonian of the band inversion contact, Eq. (6.1.1), is represented in the basis $|\Phi_a\rangle$, $K |\Phi_a\rangle$, $|\Phi_b\rangle$ and $K |\Phi_b\rangle$ which are obtained as

$$\left|\Phi_{a}^{-}\right\rangle = e^{-i\frac{\alpha}{2}}\cos\frac{\beta}{2}\left|\Phi_{2}^{-}\right\rangle + e^{i\frac{\alpha}{2}}\sin\frac{\beta}{2}K\left|\Phi_{2}^{-}\right\rangle \tag{6.1.2}$$

$$K\left|\Phi_{a}^{-}\right\rangle = -e^{-i\frac{\alpha}{2}}\sin\frac{\beta}{2}\left|\Phi_{2}^{-}\right\rangle + e^{i\frac{\alpha}{2}}\cos\frac{\beta}{2}K\left|\Phi_{2}^{-}\right\rangle \tag{6.1.3}$$

$$\left|\Phi_{b}^{+}\right\rangle = e^{-i\frac{\alpha}{2}}\cos\frac{\beta}{2}\left|\Phi_{1}^{+}\right\rangle + e^{i\frac{\alpha}{2}}\sin\frac{\beta}{2}K\left|\Phi_{1}^{+}\right\rangle \tag{6.1.4}$$

$$K\left|\Phi_{b}^{+}\right\rangle = -e^{-i\frac{\alpha}{2}}\sin\frac{\beta}{2}\left|\Phi_{1}^{+}\right\rangle + e^{i\frac{\alpha}{2}}\cos\frac{\beta}{2}K\left|\Phi_{1}^{+}\right\rangle \tag{6.1.5}$$

The relations from Table (5.2) can be basically taken in order to express the bulk band edge states in the basis of the twelve Bloch wave functions $|\Phi_0^{\pm\uparrow\downarrow}\rangle$, $|\Phi_+^{\pm\uparrow\downarrow}\rangle$ and $|\Phi_-^{\pm\uparrow\downarrow}\rangle$. But it is necessary to keep in mind that the spin wave function $|\uparrow\rangle$ and $|\downarrow\rangle$ must be replaced by its representation in the rotated coordinate system

$$|\uparrow\rangle = e^{i\frac{\alpha}{2}}\cos\frac{\beta}{2}|\uparrow_M\rangle - e^{i\frac{\alpha}{2}}\sin\frac{\beta}{2}|\downarrow_M\rangle$$
 (6.1.6)

$$|\downarrow\rangle = e^{-i\frac{\alpha}{2}}\sin\frac{\beta}{2}|\uparrow_M\rangle + e^{-i\frac{\alpha}{2}}\cos\frac{\beta}{2}|\downarrow_M\rangle$$
 (6.1.7)

where $|\uparrow_M\rangle$ and $|\downarrow_M\rangle$ stands for the spin up and spin down wave function in the local coordinate system of each M point.

In order to solve the eigenvalue problem, Eq. (6.1.1), we use a similar strategy as deployed in Refs. [76, 95]: first we make a plane wave ansatz $\exp(i\mathbf{k}_{\perp}.\mathbf{r}_{\perp})$ and then we multiply Eq. (6.1.1) with the operator on its left hand side. This procedure yields the following equation

$$\begin{bmatrix} B^2 k_z^2 + A^2 + \{A, B\} k_z - (\epsilon - \varphi(z))^2 + \Delta(z)^2 \\ -i \begin{pmatrix} 0 & \varphi'(z) - \Delta'(z) \\ \varphi'(z) + \Delta'(z) & 0 \end{pmatrix} \otimes B \end{bmatrix} \psi = 0$$
 (6.1.8)

with $A = \hbar \left(\boldsymbol{\tau}.RVR^{\dagger}\mathbf{k}_{\perp} \right)$, $B = \hbar \left(\boldsymbol{\tau}.RVR^{\dagger}\mathbf{e}_{z} \right)$ and $k_{z} = -i\partial_{z}$. The first derivative of the gap function $\Delta(z)$ and the work function $\varphi(z)$ are in this expression denoted as $\Delta'(z)$ and $\varphi'(z)$. Furthermore we have introduced here the wave vector \mathbf{k}_{\perp} as a standard notation for the projection of \mathbf{k} into the (111) plane and \mathbf{e}_{z} as a unit vector in z direction. It can be easily seen that Eq. (6.1.8) represents a system of four differential equations in z which can be decoupled using under the basis transformation $\zeta = S\psi$. The transformation is given by the matrix S

$$S = \sqrt{\frac{\Delta_0}{2(\varphi_0^2 - \Delta_0^2)}} \begin{pmatrix} \sqrt{\varphi_0 + \Delta_0} & \sqrt{\varphi_0 - \Delta_0} \\ -\sqrt{\varphi_0 + \Delta_0} & \sqrt{\varphi - \Delta_0} \end{pmatrix} \otimes U$$
 (6.1.9)

with the unitary operator $U=e^{i\kappa z}\left[a_{+}\left(1-i\tau_{z}\right)+ia_{-}\left(\tau_{y}-\tau_{x}\right)\right]/2$, the coefficient $a_{\pm}=\sqrt{1\pm\left[v_{\perp}\sin^{2}\beta+v_{\parallel}\cos^{2}\beta\right]/v_{1}}$ and the velocity $v_{1}=\sqrt{v_{\perp}^{2}\sin^{2}\beta+v_{\parallel}^{2}\cos^{2}\beta}$. After the transformation of Eq. (6.1.8) we obtain for each spinor ζ_{+} and ζ_{-} in the wave function $\zeta=(\zeta_{+},\zeta_{-})$ a separate system of differential equations

$$[B^{2}(\kappa + k_{z})^{2} + W(z)^{2} \mp \hbar v_{1} \sigma_{z} W(z)
+ \{A, B\}(\kappa + k_{z})] \zeta_{\pm} = \left[\frac{\epsilon^{2} \varphi_{0}^{2}}{\Delta_{0}^{2} - \varphi_{0}^{2}} - A^{2} + \epsilon^{2}\right] \zeta_{\pm}$$
(6.1.10)

with $W(z) = \sqrt{\Delta_0^2 - \varphi_0^2} [f(z) + \epsilon \varphi_0/(\Delta_0^2 - \varphi_0^2)]$. In order to eliminate the term linear in k_z which occurs on the left hand side we use the possibility to set the parameter κ to the value $-\text{Tr}\{A,B\}/(2\hbar\text{Tr}B^2)$. In this way the eigenvalue problem can be brought to the form of a supersymmetric equation [96]:

$$\left[-i\hbar v_1 \sigma_z k_z \pm W(z)\right] \left[i\hbar v_1 \sigma_z k_z \pm W(z)\right] \zeta_{\pm}$$

$$= \left[\epsilon^2 - A^2 + \frac{\{A, B\}^2}{4B^2} + \frac{\epsilon^2 \varphi_0^2}{\Delta_0^2 - \varphi_0^2} \right] \zeta_{\pm}$$
 (6.1.11)

This form is particularly convenient since it has a product of two adjoint operators on the left and a scalar matrix on the right. The low energy excitations are given by the ground state of the supersymmetric equation and due to its particular structure the condition for the ground state is simply $[\hbar v_1 \sigma_z \partial_z \pm W(z)] \zeta_{\pm} = 0$. This latter equation has two normalizable solutions which are of the form

$$\zeta_{+} = c_{+} \begin{pmatrix} 1 \\ 0 \end{pmatrix} g(z) \qquad \zeta_{-} = c_{-} \begin{pmatrix} 0 \\ 1 \end{pmatrix} g(z)$$
(6.1.12)

Each of the solutions displayed in Eq. (6.1.12) is the product of a two component

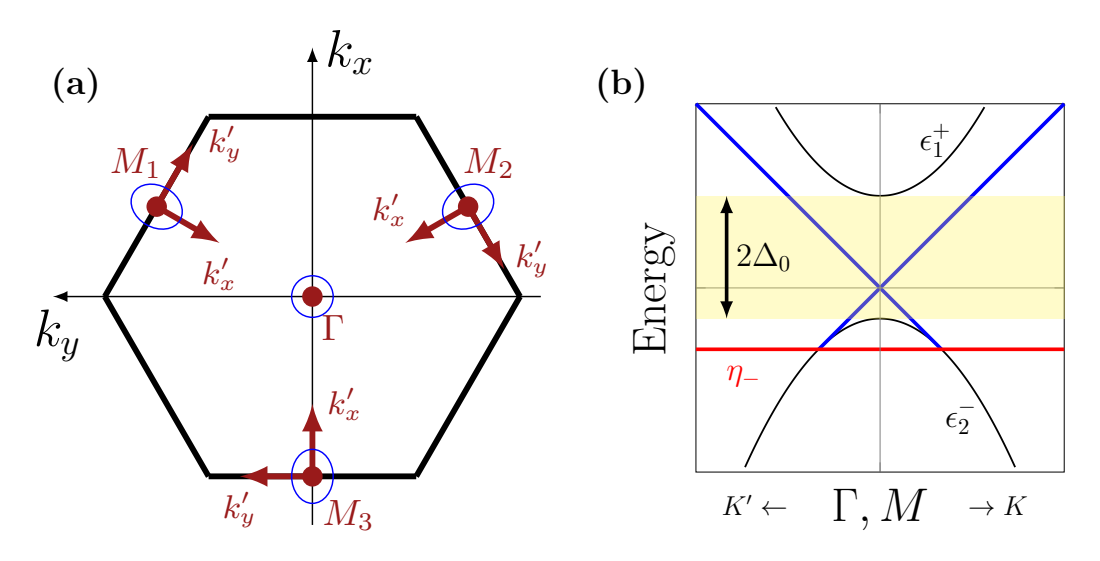


Figure 6.2: The Brillouin zone of the (111) surface [Fig. (6.2a)] and the spectrum of the topological surface state [Fig. (6.2b)]. The Brillouin zone has four high symmetry points where Dirac cone surface states exist: the Γ point and the three M points. The derivation of the topological surface states that is presented in the current chapter is for each of these high symmetry points carried out in an own coordinate system which is in Fig. (6.2a) highlighted in red. Due to band bending at the surface the apex of the Dirac cone is shifted, as may be seen in Fig. (6.2b), downwards away from the center of the two bulk bands ϵ_1^+ and ϵ_2^- . When the energy approaches the value η_- the surface states merge with the valence band of the bulk.

vector, a coefficient $c_{\pm} \in \mathbb{C}$ and an envelope function g(z). The envelope function g(z) defines the asymptotic decay of the surface state into the bulk and must satisfy the differential equation $[\hbar v_1 \partial_z + W(z)] g(z) = 0$. Its solution is evidently given by

$$g(z) = N \exp\left[-\frac{1}{\hbar v_1} \int_0^z dz \ W(z)\right]$$
 (6.1.13)

with the normalization chosen so that $\int_{-\infty}^{\infty} dz \ g(z)^2 = 1$. The fact that the wave function must be normalizable over the whole z range implies that the superpotential must change its sign asymptotically. This requirement manifests in the topological boundary condition which requires (asymptotically) the band inversion. However, the presence of the work function makes the situation more complicated and brings up two supplementary conditions: the work function of the material must be smaller than the gap function which can be expressed as $|\varphi_0| < |\Delta_0|$ and additionally the energy of the surface state ϵ is limited to the range $\eta_s < \epsilon < \eta_{-s}$ with $\eta_s = \varphi(s\infty) \left(1 - \Delta_0^2/\varphi_0^2\right)$ and $s = \text{sgn}(\varphi_0)$. For downwards band bending $(\varphi_0 > 0)$, which has been found for the tin terminated surface of SnTe [97], the latter condition means that the surface state exists only above a minimum energy η_+ and below that energy merges with the bulk valence band. This is shown in Fig. (6.2b).

In order to determine the full surface state wave function it remains to calculate the two coefficients c_+ and c_- . These coefficients encode the coupling of the two spinors in the full wave function $\psi = S^{-1}(\zeta_+, \zeta_-)^T$ and must be determined from a substitution of ψ into Eq. (6.1.1). This procedure yields a system of four equations of which only two are independent and may be brought to the form of a Dirac-Weyl equation

$$\hbar \gamma \begin{pmatrix} 0 & v_x k_x - i v_\perp k_y \\ v_x k_x + i v_\perp k_y & 0 \end{pmatrix} \begin{pmatrix} c_+ \\ c_- \end{pmatrix} = \epsilon \begin{pmatrix} c_+ \\ c_- \end{pmatrix}$$
 (6.1.14)

with $\gamma = \sqrt{1 - \varphi_0^2/\Delta_0^2}$. The Dirac-Weyl equation has been similarly presented in recent publications [63, 80, 82, 98] where the topological surface states have been derived in a model which is based on symmetry considerations. However, a connection to a realistic material is in these works entirely missing. This connection is in our model given by the two Kramer conjugate basis wave functions X and KX which relate the pseudospin degree of freedom of Eq. (6.1.14) to the microscopic variables of the bulk. For upwards band bending the wave function X can be obtained from the transformation $S^{-1}(1,0,0,0)^T$ and for downwards band bending we have to use $S^{-1}(0,0,1,0)^T$. Both cases may be summarized in one formula

$$|X\rangle = a_{+}F_{-} |\Phi_{a}^{-}\rangle + a_{-}F_{-}K |\Phi_{a}^{-}\rangle + a_{+}F_{+} |\Phi_{b}^{+}\rangle + a_{-}F_{+}K |\Phi_{b}^{+}\rangle$$
 (6.1.15)

where we have introduced $F_{\pm}=1/2\sqrt{1\pm\varphi_0/\Delta_0}e^{\pm i\pi/4}$. From the full expansion of the wave function it can be seen that the above expression depends on the physical spin. The physical spin enters through the bulk band edge states and is already at this stage entangled with the p-orbital. This intrinsic spin dependence is a feature which is missing in graphene where the low energy excitations also obey a Dirac-Weyl equation but are completely spin unpolarized.

The spectrum of the Dirac-Weyl equation is represented by an elliptic cone

$$\epsilon_{\mathbf{k}_{\perp}l} = l\hbar\gamma\sqrt{v_x^2k_x^2 + v_{\perp}^2k_y^2} \tag{6.1.16}$$

with $l \in \{\pm\}$ and $v_x = (v_{\parallel}v_{\perp})/v_1$. The semi-axes of the ellipse are for any rotation angle β aligned with the axes of the coordinate system. This is ensured by the

particular choice of coordinate system that we made at the beginning of the chapter. The semi-axis in k_x direction is (through v_x) a function of the rotation angle β and this is the reason why the spectrum takes different form at the Γ and the M point of the surface Brillouin zone: at the Γ point the two velocities v_x and v_{\perp} are equal which means that the points of constant energy lie on a circle. However, at the M point the two velocities are different and this results in a spectrum which is represented by an elliptic cone. The surface Brillouin zone together with the local coordinate system for each Dirac point is illustrated in Fig. (6.2a) and the low energy spectrum which is found in vicinity of the Γ and the M point may be seen in Fig. (6.2b).

The eigenstates of Eq. (6.1.14) are given by Dirac-Weyl spinors

$$\begin{pmatrix} c_+ \\ c_- \end{pmatrix} = \frac{1}{\sqrt{2}} \begin{pmatrix} 1 \\ le^{i\phi} \end{pmatrix} \tag{6.1.17}$$

with $\phi = \tan^{-1}[v_{\perp}k_y/(v_xk_x)]$. Expressed in terms of the two basis wave functions X and KX the full surface state finally reads

$$|\Psi_{\mathbf{k}_{\perp}l}\rangle = \left(c_{+} |X\rangle + c_{-}K |X\rangle\right)e^{i\mathbf{k}_{\perp}\cdot\mathbf{r}_{\perp}}e^{i\kappa z}g(z)$$
(6.1.18)

This equation represents one of the main results of this work. It describes the topological surface states on the (111) surface of the topological insulator of the SnTe class expressed in terms of the microscopic degrees of freedom of the bulk. The two rotation angles α and β which enter through the basis wave functions X and KX allow to access the four inequivalent Dirac points. These surface states, with their conical spectrum and the anisotropy at the M points, are in agreement with recent works [79, 81, 82] but provide, in contrast to these works, a link to the parameters of the bulk. However, our model does not reflect the energetic disparity between the Γ and the M point Dirac cone which has been reported in Ref. [79]. The shift comes from an acoustic deformation at the surface and must be included in the derivation of the bulk band edge states. The acoustic deformation leaves the wave functions unchanged but shifts the energy of the three oblique bulk L points in the surface region which results then in a shift of the energy of the M point and the Γ point Dirac cone [99]. Finally it is interesting to note that the formalism that is presented here can also be used to describe other facets of the crystal and other materials which are described by the Hamiltonian, Eq. (5.5.1). However, for topological insulators that do not belong to the class of IV-VI semiconductors, the basis wave functions $|\Phi_2^-\rangle$, $K|\Phi_2^-\rangle$, $|\Phi_1^+\rangle$ and $K\mid\Phi_1^+\rangle$ must be replaced by appropriate expressions.

The Spin Texture

The nontrivial topology of the bulk band structure of some of the IV-VI semiconductors such as SnTe manifests, as shown in the previous section, in Dirac-Weyl surface states at the Γ and the three M points of the hexagonal Brillouin zone of the (111) surface. A particular achievement of our formalism is that it links the topological

surface states in an analytical way with the bulk L-point wave functions. These band edge states are spin-polarized and from the given structure of these states one can easily determine the spin texture on the surface. According to the definition of the surface state, Eq. (6.1.18), the spin texture follows from the expression

$$\langle \Psi_{\mathbf{k}_{\perp}l} \mid \boldsymbol{\sigma} \mid \Psi_{\mathbf{k}_{\perp}l} \rangle = l \Re \left[e^{i\phi} \langle X \mid \boldsymbol{\sigma}K \mid X \rangle \right]$$
 (6.2.1)

where σ is the spin operator. For a further analytical evaluation we use the connection to the basis wave functions $|\Phi_2^-\rangle$, $K |\Phi_2^-\rangle$, $|\Phi_1^+\rangle$ and $K |\Phi_1^+\rangle$ and write the matrix element $\langle X | \sigma K | X \rangle$ as a linear combination of the twelve matrix elements which are shown in Appendix D.1. This calculation yields the following result

$$\langle \Psi_{\mathbf{k}_{\perp}l} \mid \boldsymbol{\sigma} \mid \Psi_{\mathbf{k}_{\perp}l} \rangle = l \begin{pmatrix} -a \sin \phi \\ b \cos \phi \\ -m_z \sin \phi \end{pmatrix}$$
 (6.2.2)

with $a=\rho_1\frac{v_x}{v_\parallel}\sin^2\beta+\rho_2\frac{v_x}{v_\perp}\cos^2\beta,\ b=\rho_2$ and $m_z=\frac{1}{2}\sin(2\beta)\left[\frac{v_x}{v_\perp}\rho_2-\frac{v_x}{v_\parallel}\rho_1\right]$ and where we have furthermore introduced $\rho_1=\frac{1}{2}(1+\frac{\varphi_0}{\Delta_0})\cos\Theta^++\frac{1}{2}(1-\frac{\varphi_0}{\Delta_0})\cos\Theta^-$ and $\rho_2=-\frac{1}{2}(1+\frac{\varphi_0}{\Delta_0})\sin^2\frac{\Theta^+}{2}+\frac{1}{2}(1-\frac{\varphi_0}{\Delta_0})\cos^2\frac{\Theta^-}{2}$. One immediately notes that the in-plane part of the spin texture is a vector field which is tangential to a conic section of the implicit form $k_x^2/a^2+\mathrm{sgn}(ab)k_y^2/b^2=1$ while the out-of-plane component is governed by the parameter m_z . The absolute value of the spin does not necessarily equal to one. This can be proven as shown in Appendix D.2 with help of the Cauchy-Schwarz inequality and comes from the fact that the spin space is in the basis wave function X entangled with the p-orbital. The spin texture is controlled by the parameters of the bulk: the spin mixing parameters Θ^+ and Θ^- , the two velocities v_\parallel and v_\perp as well as the band bending parameter φ_0/Δ_0 . In addition to that it may be seen that the spin texture is a function of the rotation angles α and β and this results in a different spin texture at the Γ and the M point of the (111) surface.

At the Γ point, where $\beta=0$, the spin is polarized exactly in the surface plane. The two parameters a and b are equal and for this reason the spin is tangential to a circle. For the conduction band of SnTe, where downwards band bending $(\varphi_0>0)$ is reported for the tin terminated surface [97], we find, in agreement with recent works [81, 100], a helical spin texture with the winding number -1. Via a manipulation of the band bending at the surface, which can be tuned by the gate voltage or by doping of the the surface, it is possible to tune the absolute value and the winding number of the spin texture. The spin texture vanishes altogether at $\varphi_0/\Delta_0 = -\left(\sin^2\frac{\Theta^+}{2} - \cos^2\frac{\Theta^-}{2}\right)/\left(\sin^2\frac{\Theta^+}{2} + \cos^2\frac{\Theta^-}{2}\right)$ and, for smaller band bending, it changes the winding number to +1.

At the M points, where $\beta = \arccos(1/3)$, we find for downwards band bending $(\varphi_0 > 0)$ a spin texture which is tangential to an ellipse and has a winding number -1. Lowering the band bending offers the possibility to control the two parameters of the conic section, a and b, in sign and in magnitude. This effect can be seen in Fig. (6.3) where the texture number $\tanh(a/b)$ is plotted as a function of Θ^+ and Θ^-

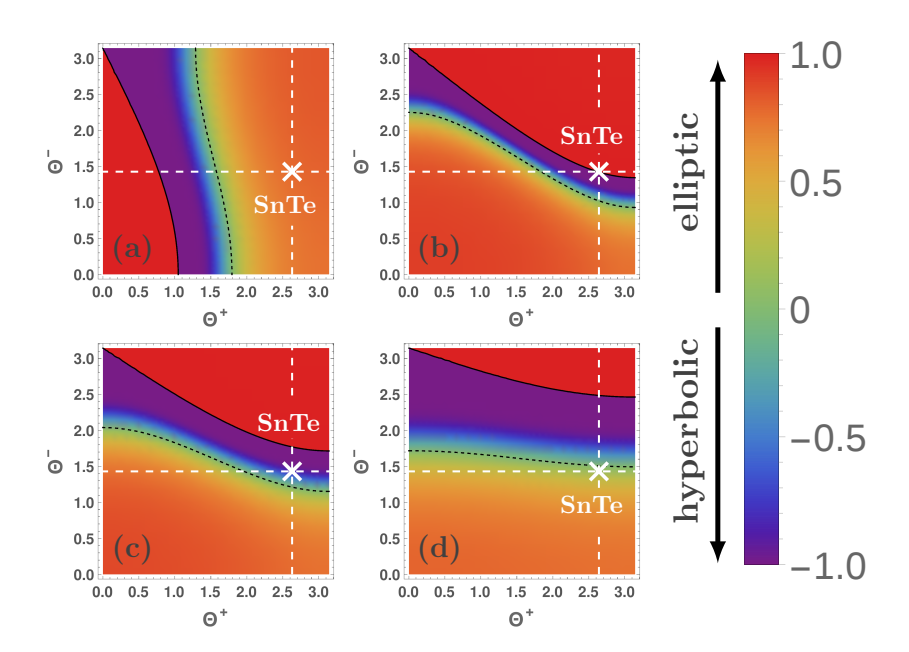


Figure 6.3: The texture number $\tanh(a/b)$ plotted as a function of the spin mixing parameters Θ^+ and Θ^- at the M point of the (111) surface Brillouin zone. From the top left to the bottom right picture the band bending is lowered from 0.6, through -0.24 and -0.4, to -0.8. The position of the material SnTe is always highlighted in white.

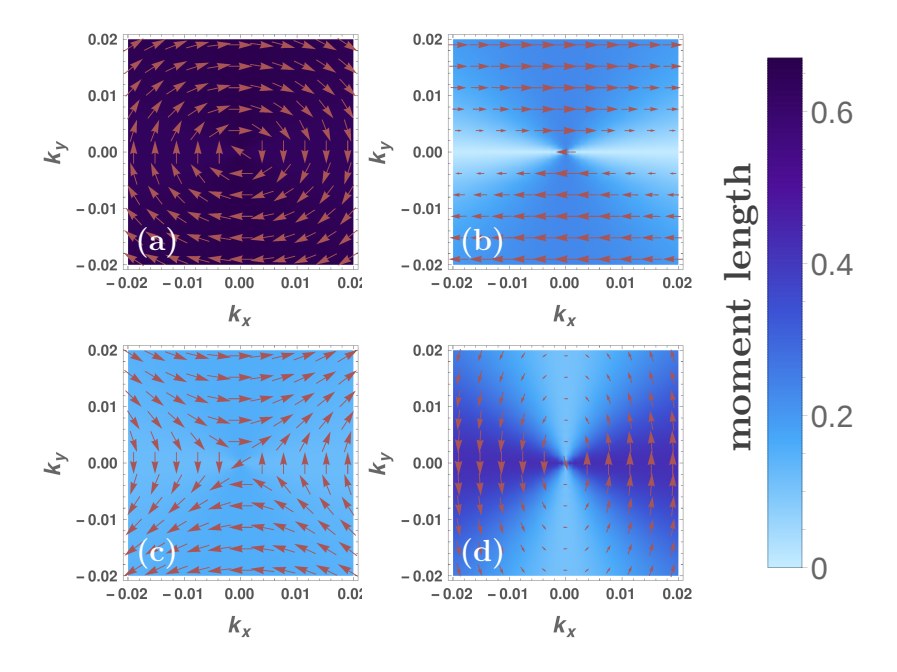


Figure 6.4: The spin texture at the M point of the (111) surface of SnTe. From the top left to the bottom right picture the band bending is lowered from 0.6, through -0.24 and -0.4, to -0.8 and the spin polarization changes accordingly from elliptic with winding number -1, through linear and hyperbolic to elliptic with winding number +1. The density plot in the background illustrates the absolute value of the spin.

for different values of the band bending parameter. From a comparison of the different density plots one immediately notes that the blue region, where the two parameters a and b have opposite signs, shifts in the plane and changes its spatial extent. The point in the parameter space which corresponds SnTe is highlighted in white and the corresponding M point spin texture is shown in Fig. (6.4). Most striking is the observation of a hyperbolic spin texture in the region where the texture number is negative. At the border of this region which is indicated by a black solid and black dashed line in Fig. (6.3) either a or b is zero and this results in a linear spin polarization along the y- or x-axis. Finally, in the region where the texture parameter is positive the

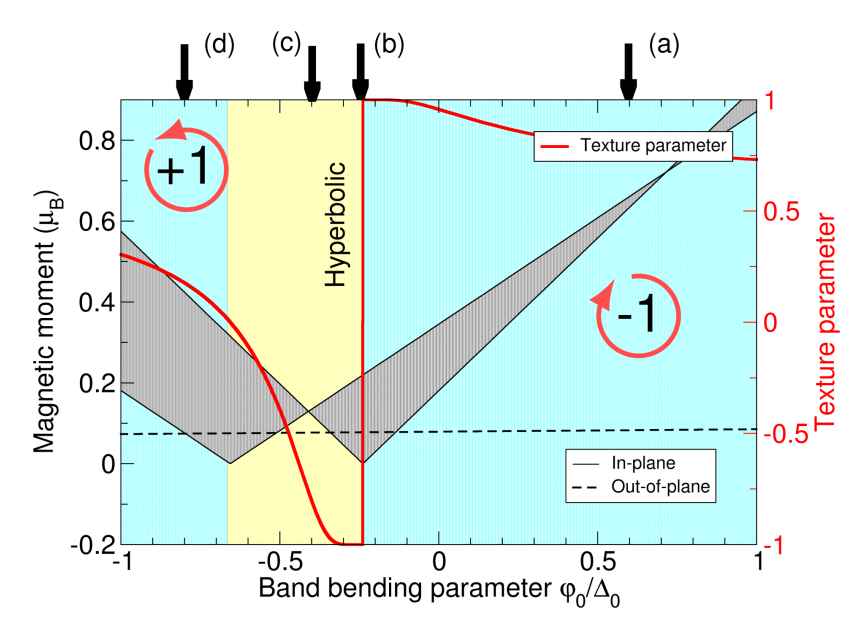


Figure 6.5: The texture parameter $\tanh(a/b)$, the in-plane absolute value of the spin and the parameter m_z plotted as a function of the band bending parameter at the M point of the (111) surface of SnTe. The form of the spin texture can be read off from the texture parameter: it changes from elliptic with winding number -1 through linear and hyperbolic to elliptic with winding number +1 as the band bending is lowered from +1 to -1. The absolute value of the spin is anisotropic in the surface plane and takes a value in the gray shaded region. The four arrows at the upper edge of the picture tag the band bending which is taken for the spin texture plots in Figs. (6.3) and (6.4).

usual elliptic spin texture is found, with winding number -1 for $a \wedge b > 0$ and +1 for $a \wedge b < 0$. The density plot in the background of Fig. (6.4) represents the absolute value of the spin. It can be clearly seen that the absolute value of the spin changes dramatically as a function of the band bending and is in some cases highly anisotropic in the surface plane. The latter behaviour reflects the fact that the spin polarization is a periodic function in $\phi = \tan[v_{\perp}k_y/(v_xk_x)]$. According to Eq. (6.2.2) the in-plane absolute value lies in the range between |a| and |b| while the out-of-plane component takes a value between 0 and m_z . A deeper insight into the evolution of the spin polarization as a function of the band bending may be obtained from Fig. (6.5) where the

CHAPTER 6. THE TOPOLOGICAL SURFACE STATES OF A TOPOLOGICAL INSULATOR OF THE SnTe CLASS

spin texture parameter $\tan(a/b)$, the range of the in-plane spin absolute value and the parameter m_z are plotted. At a band bending of +1 the spin is mainly polarized in the surface plane. When the band bending is lowered the in-plane absolute value reduces dramatically, while the parameter m_z stays, in contrast to that, constant at about $0.08\mu_B$. The evolution of the spin texture number confirms the observation that the spin momentum locking at the M points is highly non-universal and it can be tuned as a function of the band bending.

The RKKY Interaction on the Surface of a Topological Insulator of the SnTe Class

In the second and the third chapter of this thesis we discussed the RKKY interaction mediated by a gas of spin unpolarized electrons such as, for example, in graphene or in bilayer graphene. A general feature of these spin unpolarized systems is that they allow only two possibilities for impurity-spin interaction, either ferro or antiferromagnetic. The situation gets much more interesting on the surface of a topological insulator of the SnTe class where the presence of spin-polarized surface states gives way to a much richer variety of spin coupling schemes. Whereas the RKKY interaction is, due to the band gap, strongly suppressed in the bulk semiconductor, studying this interaction on the surface opens the possibility to probe the existence of topological states. The topological surface states are, similar to the low energy excitations of graphene, described by Dirac-Weyl spinors which are characterized by a pseudospin. The real spin dependence enters through the basis wave functions which are linked to the microscopic variables of the bulk. In that respect, the topological insulator of the SnTe class is exceptional, since such a connection in analytical form is not available for other known topological insulators. The route connecting the surface state to the bulk spectrum was presented in the previous chapter and here we use this relation in order to derive an analytical expression for the RKKY interaction. We find an interaction energy which has, apart from the usual Heisenberg term, also an XY-type, an Ising-type and a Dzyaloshinskii-Moriya-type term. This results in an RKKY interaction which allows, apart from the usual ferro- or antiferromagnetic coupling, much more complex spin interactions.

The Interaction Energy

In the following we consider two substitutional impurities on the (111) surface of a topological insulator of the SnTe class which is terminated either by elements of the IVth or VIth group of the periodic table. Both moments couple via a single lattice site to the gas of spin-polarized Dirac-Weyl electrons and in this way there arises an interaction between the two moments. As a model we assume that only the topological surface state at Γ contributes to the RKKY interaction. This may be justified by the

energy shift between the Γ point and the M point Dirac cone which amounts 170meV [79]. Due to this shift, the contribution of the M point Dirac cone is on the undoped or weakly doped surface is much weaker. In addition to that, we set for simplicity of the calculation the band bending at the surface to zero. The energy of the impurity spin-spin coupling can be determined from the minimization of the interaction energy which we derived in the first chapter of the thesis. Expressed in the basis of the topological surface states X and KX the interaction energy reads

$$E_{\alpha}^{int}(\mathbf{R}_{\perp}) = -\frac{1}{\pi} \left(\frac{\hbar\lambda}{2}\right)^{2} \int_{-\infty}^{E_{F}} dE$$

$$\times \Im\left(\operatorname{Tr}\left[\left(\boldsymbol{\sigma}.\mathbf{S}_{1}\right)_{\alpha} G^{0R}(-\mathbf{R}_{\perp}, E) \left(\boldsymbol{\sigma}.\mathbf{S}_{2}\right)_{\alpha} G^{0R}(\mathbf{R}_{\perp}, E)\right]\right)$$
(7.1.1)

where \mathbf{R}_{\perp} is the impurity separation vector and λ describes the strength of the electron-impurity coupling. The index α takes the value '-' on the group IV and '+' on the group VI terminated surface. In order to determine the interaction energy we need the real space propagator $G^{0R}(\mathbf{R}_{\perp}, E)$ and the scattering matrix $(\boldsymbol{\sigma}.\mathbf{S})_{\alpha}$ in the tin or in the tellurium subspace. The momentum space Green's function can be obtained from the analytical form of topological surface state and its spectrum, Eqs. (6.1.17) and (6.1.16). A subsequent Fourier transform yields the following real space propagator

$$G^{0R}(\mathbf{R}_{\perp}, E) = -i \frac{\pi^2 \left(E + i\eta\right)}{\hbar^2 v_{\perp}^2 \Omega_{SBZ}} \begin{pmatrix} H_0^1 \left(\frac{(E + i\eta)}{\hbar v_{\perp}} R_{\perp}\right) & ie^{-i\theta} H_1^1 \left(\frac{(E + i\eta)}{\hbar v_{\perp}} R_{\perp}\right) \\ ie^{i\theta} H_1^1 \left(\frac{(E + i\eta)}{\hbar v_{\perp}} R_{\perp}\right) & H_0^1 \left(\frac{(E + i\eta)}{\hbar v_{\perp}} R_{\perp}\right) \end{pmatrix}$$
(7.1.2)

where $H^1_{\nu}(x)$ stands for the Hankel function, Ω_{SBZ} for the area of the surface Brillouin zone and where we have expressed the impurity separation vector in polar coordinates with the radius R_{\perp} and the polar angle θ . It remains to determine the $(\boldsymbol{\sigma}.\mathbf{S}_i)_{\alpha}$ -matrix which can be easily done with help of the matrix elements of the spin operator that are presented in Appendix D.1. In the group IV subspace we obtain the following matrix

$$(\boldsymbol{\sigma}.\mathbf{S}_i)_{-} = \frac{1}{2} \begin{pmatrix} S_i^z \cos \Theta^- & iS_i^- \cos^2 \frac{\Theta^-}{2} \\ -iS_i^+ \cos^2 \frac{\Theta^-}{2} & -S_i^z \cos \Theta^- \end{pmatrix}$$
(7.1.3)

while in the group VI subspace we have

$$(\boldsymbol{\sigma}.\mathbf{S}_{i})_{+} = \frac{1}{2} \begin{pmatrix} -S_{i}^{z} \cos \Theta^{+} & -iS_{i}^{-} \sin^{2} \frac{\Theta^{+}}{2} \\ iS_{i}^{+} \sin^{2} \frac{\Theta^{+}}{2} & S_{i}^{z} \cos \Theta^{+} \end{pmatrix}$$
(7.1.4)

with $S_i^{\pm} = S_i^x \pm i S_i^y$ and $i \in \{1, 2\}$. These two matrices describe, depending on the termination of the surface, the scattering at a tin or tellurium site. Substitution of the appropriate $(\boldsymbol{\sigma}.\mathbf{S}_i)_{\alpha}$ -matrix and the Green's function $G^{0R}(\mathbf{R}_{\perp}, E)$ into Eq. (7.1.1)

leads to the following interaction energy

$$E_{\alpha}^{int}(\mathbf{R}_{\perp}) = -\frac{2\pi^{2}\hbar\lambda^{2}}{\Omega_{SBZ}^{2}v_{\perp}} \Big([A_{k_{F}}(R_{\perp}) - B_{k_{F}}(R_{\perp})] [a_{\alpha}S_{1}^{x}S_{2}^{x} + b_{\alpha}S_{1}^{z}S_{2}^{z}]$$

$$+ [A_{k_{F}}(R_{\perp}) + B_{k_{F}}(R_{\perp})] a_{\alpha}S_{1}^{y}S_{2}^{y}$$

$$+ [C_{k_{F}}(R_{\perp}) + D_{k_{F}}(R_{\perp})] c_{\alpha} [S_{1}^{x}S_{2}^{z} - S_{1}^{z}S_{2}^{x}] \Big)$$

$$(7.1.5)$$

with $C=\pi^2\hbar\lambda^2/(v_\perp\Omega_{SBZ}^2)$. It can be clearly seen that the interaction energy consists of three qualitatively distinct terms that support each taken on its own a rather different spin coupling schemes: firstly, there is an Ising-type term which has the form $S_1^zS_2^z$ and favors ferro- or antiferromagnetic coupling along the z-axis. Secondly, there occur two XY-type terms which are of the form $S_1^xS_2^x$ or $S_1^yS_2^y$ and support ferro (FM)- or antiferromagnetic (AFM) coupling along the x- or y-axis. Finally, there is a Dzyaloshinskii-Moriya-type (DM-type) term which has the form $(S_1^xS_2^z-S_1^zS_2^x)$ and which favors the two spins in the xz-plane in a configuration where both spins have a relative angle of 90 degrees. The contributions of these three individual terms are in Eq. (7.1.5) weighted by a linear combination of the functions $A_{k_F}(R_\perp)$, $B_{k_F}(R_\perp)$, $C_{k_F}(R_\perp)$ and $D_{k_F}(R_\perp)$ and the coefficients a_α , b_α and c_α . The coefficients a_α , b_α and

a_{lpha}	b_{lpha}	c_{lpha}
$\frac{1}{4}\cos^4\left(\frac{2\Theta^\alpha + \pi(1+\alpha)}{4}\right)$	$\frac{1}{4}\cos^2\Theta^{\alpha}$	$\frac{1}{4}\cos\Theta^{\alpha}\cos^{2}\left(\frac{2\Theta^{\alpha}+\pi(1+\alpha)}{4}\right)$

Table 7.1: The coefficients for the RKKY interaction on the surface of a topological insulator of the SnTe class. The spin mixing parameter Θ^{α} is for a range of IV-VI semiconductors given in Table (5.1). The parameter α takes the value '+' on the tellurium terminated surface and '-' on the tin terminated surface.

 c_{α} are given in Table (7.1). They depend through the spin mixing parameters Θ^{α} on the material and on the termination of the surface. By definition, a_{α} and b_{α} are positive while c_{α} can change its sign over the full Θ^{α} -range. The functions $A_{k_F}(R_{\perp})$, $B_{k_F}(R_{\perp})$, $C_{k_F}(R_{\perp})$ and $D_{k_F}(R_{\perp})$ are

$$A_{k_F}(R_{\perp}) = \frac{\pi}{2} \lim_{s \to 0} \int_{k_F}^{\infty} dk_{\perp} \ k_{\perp}^2 J_0(k_{\perp} R_{\perp}) Y_0(k_{\perp} R_{\perp}) e^{-sk_{\perp}}$$
 (7.1.6)

$$B_{k_F}(R_{\perp}) = \frac{\pi}{2} \lim_{s \to 0} \int_{k_F}^{\infty} dk_{\perp} \ k_{\perp}^2 J_1(k_{\perp} R_{\perp}) Y_1(k_{\perp} R_{\perp}) e^{-sk_{\perp}}$$
 (7.1.7)

$$C_{k_F}(R_{\perp}) = \frac{\pi}{2} \lim_{s \to 0} \int_{k_F}^{\infty} dk_{\perp} \ k_{\perp}^2 J_1(k_{\perp} R_{\perp}) Y_0(k_{\perp} R_{\perp}) e^{-sk_{\perp}}$$
 (7.1.8)

$$D_{k_F}(R_{\perp}) = \frac{\pi}{2} \lim_{s \to 0} \int_{k_F}^{\infty} dk_{\perp} \ k_{\perp}^2 J_0(k_{\perp} R_{\perp}) Y_1(k_{\perp} R_{\perp}) e^{-sk_{\perp}}$$
 (7.1.9)

with $k_{\perp} = E/(\hbar v_{\perp})$. The fact that Eqs. (7.1.6) - (7.1.9) as well as the interaction energy, Eq. (7.1.5), depend solely on the impurity separation R_{\perp} and not on the polar angle θ comes from the special choice of the coordinate system. In Eq. (7.1.5) we rotated the coordinate system so that the x-axis is aligned with the impurity separation vector.

The RKKY Interaction on the Pristine Surface

The profound impact of the bulk parameters on the RKKY interaction can be seen well for a pristine surface, where the Fermi energy lies at the apex of the Dirac cone. The pristine surface is a special case where no free particles are available. In graphene this leads, to an unusual monotonic $1/R^3$ decay of the RKKY interaction and a coupling which is, depending on the sublattice configuration, purely ferro- or antiferromagnetic. Now we want to figure out what happens on the surface of the topological insulator which has a similar spectrum but, in contrast to graphene, spin-polarized surface states. To this end it is convenient to bring Eqs. (7.1.6) - (7.1.9) with the help of Appendix B to the form of a double integral

$$A_0(R_{\perp}) = \lim_{s \to 0} \int_0^{\infty} dk_{\perp} \int_0^{\infty} dk'_{\perp} \frac{k'_{\perp}^2 k_{\perp}}{k'_{\parallel}^2 - k_{\parallel}^2} J_0(k'_{\perp} R_{\perp}) J_0(k_{\perp} R_{\perp}) e^{-s(k_{\perp} + k'_{\perp})}$$
 (7.2.1)

$$B_0(R_{\perp}) = \lim_{s \to 0} \int_0^{\infty} dk_{\perp} \int_0^{\infty} dk'_{\perp} \frac{k'_{\perp} k_{\perp}^2}{k'_{\perp}^2 - k_{\perp}^2} J_1(k'_{\perp} R_{\perp}) J_1(k_{\perp} R_{\perp}) e^{-s(k_{\perp} + k'_{\perp})}$$
 (7.2.2)

$$C_0(R_{\perp}) = \lim_{s \to 0} \int_0^{\infty} dk_{\perp} \int_0^{\infty} dk'_{\perp} \, \frac{k'_{\perp}^2 k_{\perp}}{k'_{\parallel}^2 - k_{\parallel}^2} \, J_1(k'_{\perp} R_{\perp}) \, J_0(k_{\perp} R_{\perp}) \, e^{-s(k_{\perp} + k'_{\perp})}$$
 (7.2.3)

$$D_0(R_{\perp}) = \lim_{s \to 0} \int_0^{\infty} dk_{\perp} \int_0^{\infty} dk'_{\perp} \frac{k'_{\perp} k_{\perp}^2}{k'_{\perp}^2 - k_{\perp}^2} J_0(k'_{\perp} R_{\perp}) J_1(k_{\perp} R_{\perp}) e^{-s(k_{\perp} + k'_{\perp})}$$
 (7.2.4)

A comparison of Eq. (7.2.3) and Eq. (7.2.4) makes evident that $C_0(R_\perp) + D_0(R_\perp) = 0$. The remaining two integrals $A_0(R_\perp)$ and $B_0(R_\perp)$ can be taken with help of the usual Laplace trick that we have introduced in Chapter 3 of the thesis. In this way we obtain $A_0(R_\perp) = \pi/(32R_\perp^3)$ and $B_0(R_\perp) = -3\pi/(32R_\perp^3)$ which then allows us to write the interaction energy as follows

$$E_{\alpha}^{int}(\mathbf{R}_{\perp}) = -\frac{\pi^3 \hbar \lambda^2}{8\Omega_{SBZ}^2 v_{\perp} R_{\perp}^3} \left[a_{\alpha} \left(2S_1^x S_2^x - S_1^y S_2^y \right) + 2b_{\alpha} S_1^z S_2^z \right]$$
 (7.2.5)

One immediately notes that the DM-type term is absent in the interaction on the undoped surface. From a minimization of Eq. (7.2.5) we find that there are depending on a_{α} and b_{α} two fundamentally different cases. For $a_{\alpha} < b_{\alpha}$ the two spins favor a ferromagnetic coupling in the direction normal to the surface while for $a_{\alpha} > b_{\alpha}$ both spins couple ferromagnetically in the surface plane, parallel to the connection vector. The case $a_{\alpha} = b_{\alpha}$ is a special one since the minimum of the interaction energy becomes degenerate with all possibilities for ferromagnetic coupling in the xz-plane. In Fig. (7.1) the in-plane coefficient a_{α} and the out-of-plane coefficient b_{α} are plotted

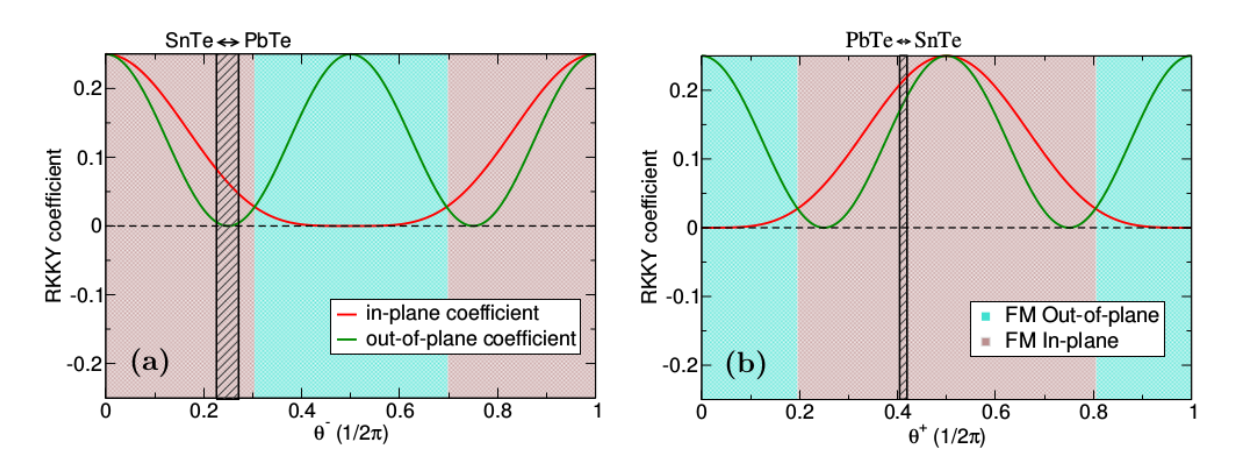


Figure 7.1: The evolution of the the in-plane coefficient a_{α} and the out-of-plane coefficient b_{α} as a function of Θ^{α} for the group IV and the group VI terminated surface of a topological insulator of the SnTe class. The color scheme in the background highlights the two distinct RKKY regions that feature ferromagnetic (FM) coupling either in the surface plane or normal to the surface plane. The alloy $Pb_xSn_{1-x}Te$ lies in the black shaded area.

as a function of the material dependent parameter Θ^{α} for the group IV $(\alpha = -)$ and the group VI $(\alpha = +)$ terminated surface. The corresponding spin coupling scheme is given as a background color and the position of SnTe $(\Theta^+ = 2.63 \text{ and } \Theta^- = 1.42)$ is indicated by a black solid line. By alloying the SnTe crystal with lead we can slightly impact the parameter Θ^+ and Θ^- and hence access the region which is in both pictures shaded in black. The corresponding Θ^+ -range $(\Theta^-$ -range) lies in the brown region where we expect ferromagnetic coupling in the surface plane. However it should be noted that topological surface states exist in $Pb_xSn_{1-x}Te$ only up to a certain lead concentration. In previous experimental works the topological phase has been observed up to a concentration of x = 0.25 [77]. With help of Table (5.1) we can do a similar analysis for SnSe and its alloy $Pb_xSn_{1-x}Se$. We find the same in-plane ferromagnetic coupling.

The RKKY Interaction on the Doped Surface

Depending on the termination of the surface either donors or acceptors may prevail on the surface, and this shifts the position of the Fermi energy either up or down. An analytical evaluation of the interaction energy is in this case possible only for large impurity separations. To this end we take the interaction energy, Eq. (7.1.5), make the substitution $x = ER_{\perp}/(\hbar v_{\perp})$ and replace the Bessel functions by its asymptotics for large arguments. In this way we can bring the function $A_{k_F}(R)$ to the form

$$A_{k_F}(R_\perp) = -\frac{1}{R_\perp^3} \lim_{s \to 0} \int_{x_E}^\infty dx \ x \left[\cos(2x) + \frac{1}{4x} \sin(2x) \right] e^{-sx}$$
 (7.3.1)

A subsequent integration leads to the result:

$$A_{k_F}(R_{\perp}) = \frac{1}{4R_{\perp}^2} \left[k_F \sin(2k_F R_{\perp}) + \frac{1}{4R_{\perp}} \cos(2k_F R_{\perp}) \right]$$
 (7.3.2)

Similarly we proceed with the functions $B_{k_F}(R_\perp)$, $C_{k_F}(R_\perp)$ and $D_{k_F}(R_\perp)$ and find the interaction energy in the lowest two orders given by

$$E_{\alpha}^{int}(\mathbf{R}_{\perp}) = -\frac{\pi^{2}k_{F}\hbar\lambda^{2}}{\Omega_{SBZ}^{2}v_{\perp}R_{\perp}^{2}} \left[\sin\left(2k_{F}R_{\perp}\right) \left(a_{\alpha}S_{1}^{x}S_{2}^{x} + b_{\alpha}S_{1}^{z}S_{2}^{z}\right) - c_{\alpha}\cos\left(2k_{F}R_{\perp}\right) \left(S_{1}^{x}S_{2}^{z} - S_{1}^{z}S_{2}^{x}\right) \right] - \frac{\pi^{2}\hbar\lambda^{2}}{4\Omega_{SBZ}^{2}v_{\perp}R_{\perp}^{3}} \left[\cos\left(2k_{F}R_{\perp}\right) \left(3a_{\alpha}S_{1}^{x}S_{2}^{x} - 2a_{\alpha}S_{1}^{y}S_{2}^{y} + 3b_{\alpha}S_{1}^{z}S_{2}^{z}\right) + 3c_{\alpha}\sin\left(2k_{F}R_{\perp}\right) \left(S_{1}^{x}S_{2}^{z} - S_{1}^{z}S_{2}^{x}\right) \right]$$

$$(7.3.3)$$

In the leading order of this expression (which decays as $1/R^2$) we have a contribution from all three distinct terms - the Ising-type, the XY-type and the DM-type term - which are weighted by the periodic function $\sin(2k_FR)$ or $\cos(2k_FR)$ and the coefficients a_{α} , b_{α} or c_{α} . In order to figure out which impurity spin configuration is energetically favored it is convenient to consider first the case where $\cos(2k_F R) \approx 0$. Under these circumstances the DM term vanishes and we find that the two spins couple for $a_{\alpha} < b_{\alpha}$ ferro- or antiferromagnetically parallel to the surface normal and for $a_{\alpha} > b_{\alpha}$ either ferro- or antiferromagnetically parallel to the connection vector. When the $\cos(2k_F R)$ increases, the DM term gets more and more important and causes a canting of both spins with respect to the in-plane or out-of-plane reference state. These two regions are highlighted in Fig. (7.2) in brown and turquoise. In addition to that there occurs a third region which is highlighted in yellow: when the out-of-plane coefficient b_{α} and the DM coefficient c_{α} are small and $a_{\alpha}\sin(2k_FR)\approx 0$, the leading order goes to zero and the next order of Eq. (7.3.3) (which decays as $1/R^3$) must be taken into account. The second order is for $\cos(k_F R) \approx -1$ dominated by the $S_1^y S_2^y$ term and there hence occurs in a certain window around the point $2k_FR \approx \pi$ a new type of interaction where a ferro- or antiferromagnetic coupling parallel to the y-axis is preferred. The tellurium terminated surface of the alloy Pb_xSn_{1-x} Te lies, depending on the lead concentration, somewhere in the brown region which means that the two impurity spins cant with respect to the in-plane FM or AFM reference state. But interestingly, on the tin terminated surface it is possible to access the yellow region where the axis of the spin coupling flips in a small window to the direction normal to the xz-plane.

The evolution of the impurity spin coupling as a function of the impurity separation is illustrated in Fig. (7.3): on the tin terminated surface of SnTe both impurity spins

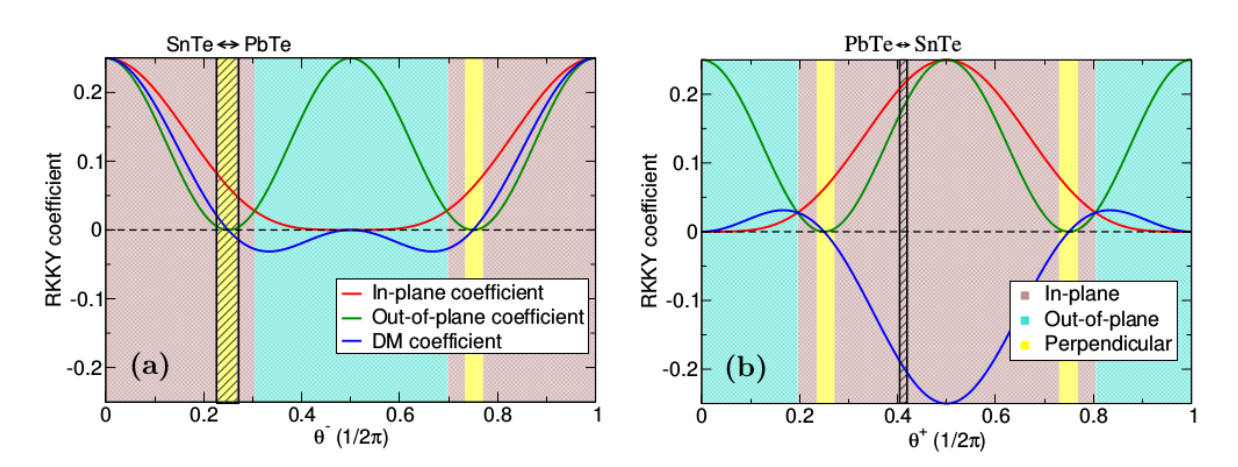


Figure 7.2: The evolution of the coefficients a_{α} , b_{α} and c_{α} as a function of Θ^{α} on the doped surface of a topological insulator of the SnTe class. There are three distinct regions for the RKKY interaction that are highlighted in different background color: in the brown and in the turquoise region both spins cant with respect to a ferro- or antiferromagnetic reference state parallel to the x- or z-axis. When the out-of-plane coefficient b_{α} and the DM coefficient c_{α} are small there exists a narrow window for the impurity separation where a collinear coupling parallel to the y-axis is preferred. The corresponding Θ^{α} range is highlighted in yellow.

couple at an impurity separation of 20Å in Fig. (7.3a) ferromagnetic parallel to the connection vector. At higher impurity separations the two spins start to cant. This leads, as may be for example seen at at 40Å, to an increasing out-of-plane component. At an impurity separation of about 61Å the canting angle reaches its maximum before finally at 80Å the canting angle decreases and is now measured with respect to the new AFM reference state. In the further course of the evolution the two spins oscillate between the two types of interaction. The period of this oscillation is given by the Fermi energy which is here set to 0.1eV. The corresponding behaviour on the tin terminated surface of Pb_{0.25}Sn_{0.75}Te is shown in Fig. (7.3b): in large parts the interaction resembles that on the surface of SnTe but in small window from 59Å and 67Å a coupling in the direction parallel to the y-axis can be observed. As shown in Fig. (7.3d) the canting angle is in that region quite small so that the coupling can considered to be, as a good approximation, ferromagnetic.

It should be noted that the Fig. (7.3) is obtained from a numerical minimization of the exact interaction energy and shows at low impurity separation some features which cannot be understood from the asymptotic form: from the DM-type term one would expect strong canting at $R_{\perp} = 0$ and zero canting at $R_{\perp} = \pi/(4k_F)$ but in contrast to that it can be observed that the canting angle goes in the interval from 61Å to 0Å continuously to zero. This is just a manifestation of the fact that the asymptotic form is not valid for small argument. Since solely the product $k_F R_{\perp}$ enters the Bessel functions in the exact interaction, a similar problem occurs in the limit $E_F \to 0$. In particular at $E_F = 0$ the integral must be taken exactly as presented in Section 7.2. Under these circumstances the DM-type term vanishes, the canting angle is always

zero and the yellow shaded region, which may be seen in Fig. (7.2), cannot be accessed anymore.

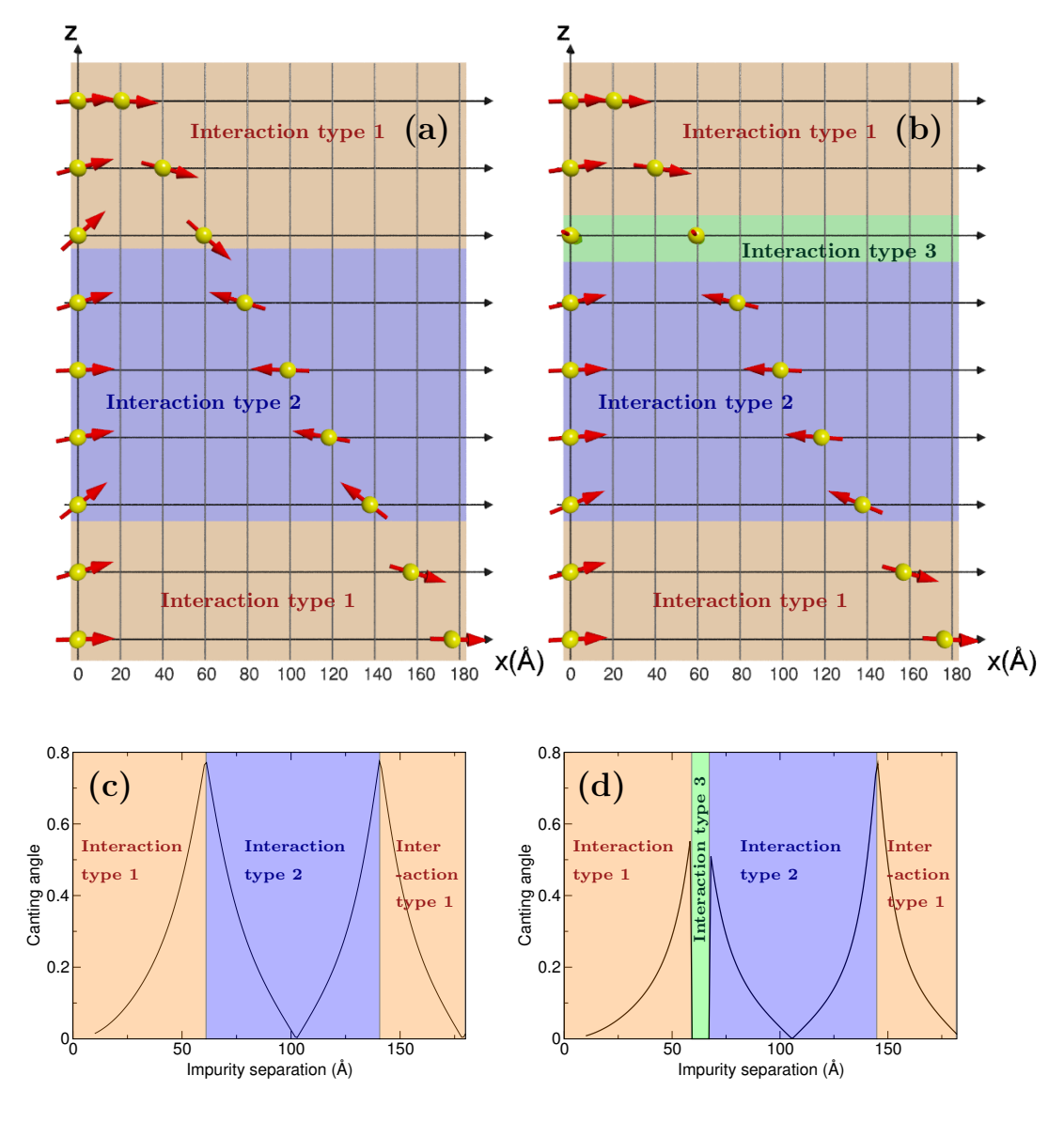


Figure 7.3: The RKKY interaction on the tin terminated surface of SnTe [Figs. (7.3a) and (7.3c)] and $Pb_{0.25}Sn_{0.75}Te$ [Figs. (7.3b) and (7.3d)] at a Fermi energy of 0.1eV. The SnTe crystal features two distinct types of interaction: canting with respect to the ferromagnetic coupling parallel to the x-axis (interaction type 1) and canting with respect to the antiferromagnetic reference state parallel to the x-axis (interaction type 2). The canting angle is given in Fig. (7.3c). By alloying the SnTe crystal with lead it is possible to open a small window where ferromagnetic coupling parallel to the y-axis is preferred (interaction type 3).

Conclusions

This work addresses the magnetic structure and magnetic interactions in two classes of materials that host chiral low energy excitations. In the first part of the thesis we focus on graphene and few layer graphenes for which the spin degree of freedom can be considered, to an excellent approximation, as decoupled from the position space wave function. The low energy physics in graphene and bilayer graphene is described by massless and massive chiral quasiparticles, respectively. In Chapters 3 and 4 we investigate the RKKY interaction and consider the effect of an electric bias applied across the bilayer. The out-of-plane electric field opens a gap in the bilayer spectrum and we demonstrate that this qualitatively alters the RKKY interaction. The second part of the thesis is dedicated to the spin physics in a topological insulator (TI) which features - similar to the graphene monolayer - a gas of Dirac-Weyl electrons on its surface. In contrast to graphene, however, spin and coordinate wave functions are fundamentally entangled in a TI surface state. In previous analytical works the spin physics has been treated in a generic Dirac-Weyl model based on symmetry considerations. Such phenomenological model is essentially unconnected to the bulk band structure although the very existence of the Dirac-Weyl surface states is due to the topology of the bulk spectrum. Hence it cannot reveal the relation between the properties of the TI surface state (such as the spin texture and RKKY coupling) and the parameters that govern the bulk band structure. In Chapters 5-7 we describe a realistic model of the topological insulators of the tin telluride class that, as we show, allows a fully microscopic theory of the TI surface state.

Graphene is particularly interesting for the RKKY interaction since it has, in contrast to the usual electron gas, a linear spectrum with two valleys and a density of states that vanishes at the apex of the Dirac cone. The specific form of the spectrum leads, as reported in earlier works, at zero doping, to a monotonic $1/R^3$ decay and at finite doping to an oscillatory interaction that decays as $1/R^2$. The multivalley nature of the spectrum is responsible for additional oscillations on the scale of the lattice constant which make the interaction extraordinarily sensitive to the local electron-impurity coupling scheme. This can be particularly well seen in case of the RKKY interaction in AB-stacked bilayer graphene which is addressed in Chapter 4 of the thesis. We focus on the most realistic case of an intercalated impurity, which is situated between the two layers of the bilayer. We find that in various coupling schemes the impurities show an asymptotically discontinuous RKKY interaction (as a function of the Fermi energy) at the edge of the antibonding (or bonding) band. For a Fermi energy just below the antibonding band one has an oscillatory RKKY interaction which abruptly

changes to antiferromagnetic once the Fermi energy crosses the gap. This reflects an underlying topological transition from a single- to a double-sheet Fermi surface. This unusual T=0 behaviour leads to a qualitative change of the RKKY interaction with increasing temperature in which, for Fermi energies close to the antibonding band edge, one finds that a low temperature oscillatory RKKY goes over to a high temperature antiferromagnetic RKKY interaction. We also find that one of the most effective and practical ways to tailor the form of the RKKY interaction is to apply an interlayer bias. The resulting "Mexican hat" spectrum leads to a complex RKKY in which the form of the interaction depends on whether the Fermi energy is "below the hat" (i.e., in the band gap), "on the brim of the hat", or "above the hat". The RKKY interaction due to spin-polarized surface states can be studied on the surface of a topological insulator. It is well known that some IV-VI semiconductors such as SnTe host linear dispersing, spin-polarized states on their (111) surface which are protected by the mirror symmetry of the crystal. These states exist not only at the Γ but also at the three M points of the surface Brillouin zone. In Chapter 6 we derive these topological surface states and their spin texture in an analytical model that is linked with the microscopic parameters of the bulk. We find that the spin texture is in the surface plane tangential to the curve of a conic section and determined by three fundamental parameters: the crystal field, the spin-orbit coupling and the band bending at the surface. The dependence on the latter can be well seen at the M point spin texture. At these points the in-plane spin texture can be tuned as a function of the band bending from elliptic with winding number -1, through linear and hyperbolic to elliptic with winding number +1. As may be seen in Chapter 7 of the thesis the fact that the surface states are spin-polarized has interesting consequences for the RKKY interaction. In a model where the RKKY interaction is solely mediated by the Γ point surface states we find an interaction which comprises the XY-type term, the Ising-type and the Dzyaloshinskii-Moriya-type term. The linear combination of these qualitatively distinct terms is governed by coefficients that depend on the microscopic parameters of the bulk and on the termination of the surface. On the Sn-terminated surface (of SnTe and SnSe) we find at zero doping a ferromagnetic coupling parallel to the connection vector. At finite doping this behaviour goes over to a canting of both impurity spins which is driven by the Dzyaloshinskii-Moriya term. This canting takes place in the xz-plane (where the x-axis is the axis parallel to the connection vector of both impurities and the z-axis is parallel to the (111) direction), depends on the Fermi energy and is a function of the impurity separation. Finally we consider the possibility to tune the parameters of the bulk through alloying the SnTe crystal with lead. We show that the alloying opens a small window with ferromagnetic coupling in the direction perpendicular to the xz-plane.

Zusammenfassung

Diese Arbeit untersucht die magnetische Struktur und magnetische Wechselwirkungen in zwei Klassen von Materialien, die beide über niederenergetische chirale Zustände verfügen. Der erste Teil befasst sich mit ein- bzw. zweilagigen graphenartigen Systemen, deren Anregungen sich bei tiefen Energien durch masselose bzw. massive chirale Quasiteilchen beschreiben lassen. Für diese Systeme kann in guter Näherung angenommen werden, dass die Spin- und die Ortswellenfunktion entkoppelt sind. Wir untersuchen in Kapitel 3 und 4 die RKKY-Wechselwirkung und diskutieren die Auswirkungen eines elektrischen Feldes, welches zwischen zwei in AB-Folge gestapelten Graphenlagen angelegt wird. Das elektrische Feld öffnet eine Bandlücke und diese Veränderung hat, wie in Kapitel 4 dieser Arbeit gezeigt, qualitative Auswirkungen auf die RKKY-Wechselwirkung. Der zweite Teil dieser Arbeit befasst sich mit der Spinphysik auf der Oberfläche eines topologischen Isolators, der ebenso wie Graphen Dirac-Weyl-Oberflächenzustände aufweist. Im Gegensatz zu Graphen sind die Spin- und die Ortswellenfunktion allerdings miteinander verschränkt. In vorherigen analytischen Arbeiten wurde die Spinphysik in einem phänomenologischen Dirac-Weyl-Modell behandelt, welches einzig und allein auf Symmetrieüberlegungen basiert und keine Verbindung zu der Bandstruktur des Volumenkristalls aufweist. Wir hingegen beschreiben in Kapitel 5-7 dieser Arbeit den topologischen Isolator der Zinntellurid-Klasse und die Eigenschaften des Oberflächenzustandes (wie die RKKY-Wechselwirkung und die Spinstruktur) in einem mikroskopischen Modell, welches auf grundlegende Art und Weise mit den Parametern des Volumenkristalls verknüpft ist.

Das Kohlenstoffallotrop Graphen verfügt, im Gegensatz zu einem normalen zweidimensionalen Elektronengas, über eine lineare Bandstruktur mit zwei unterschiedlichen Dirac-Punkten und hat eine Zustandsdichte, die am Scheitelpunkt des Dirac-Kegels verschwindet. Diese ungewöhnliche Bandstruktur führt, wie in früheren Arbeiten berichtet, zu einer RKKY-Wechselwirkung, die in "Armchair"-Richtung mit dem Abstand als monotone $1/R^3$ -Funktion abklingt. Wenn die Fermi-Energie nicht am Scheitelpunkt des Dirac-Kegels liegt, was durch Dotieren von Graphen erreicht werden kann, findet man allerdings eine Wechselwirkung, die zwischen ferromagnetisch und antiferromagnetisch oszilliert und mit $1/R^2$ fällt. Aufgrund der Besonderheit, dass das Spektrum zwei Minima an zwei unterschiedlichen K-Punkten aufweist, hängt die Wechselwirkung außerordentlich stark von dem Kopplungsschema zwischen dem Elektronengas und dem magnetischen Fremdatom ab. Dies wird vor allem, wie in Kapitel 4 beschrieben, am Beispiel der RKKY-Wechselwirkung in zweilagigem AB-gestapeltem Graphen deutlich. Wir betrachten in dieser Arbeit den äußert realistischen Fall eines interkalierten magnetischen Fremdatoms, welches mittig zwischen den beiden Graphenlagen sitzt und untersuchen eine ganze Reihe von unterschiedlichen Elektron-Fremdatom-Kopplungsschemen. Einige Kopplungsschemen zeigen einen komplett unauffälligen Verlauf. Bei anderen finden wir hingegen eine Wechselwirkung, die dramatisch an Stärke zunimmt und ihre Wellenlänge unstetig am Rande der virtuellen Bandlücke (d.h. an der Grenze zwischen den beiden unterschiedlichen Bandstrukturbereichen) als Funktion der Fermi-Energie verändert: innerhalb dieser virtuellen Bandlücke oszilliert die Wechselwirkung mit dem Wellenzahlvektor, der zu den niederenergetischen Bändern gehört. Am Rand der Bandlücke verändert die Wechselwirkung schlagartig ihre Periode und oszilliert, für höhere Fermi-Energie, mit dem Wellenzahlvektor der äußeren, hochenergetischen Bänder. Zusätzlich nimmt die Wechselwirkung in diesem Bandstrukturbereich außerordentlich an Stärke zu und ist für kurze Abstände zwischen den beiden Fremdatomen antiferromagnetisch. Ein ähnlicher Übergang kann auch erreicht werden, wenn die Temperatur des Systems erhöht wird: bei endlicher Temperatur tragen alle Zustände in einem Bereich von k_BT um das chemische Potential bei und wenn das chemische Potential ausreichend nahe an dem Rande der virtuellen Bandlücke liegt, bestimmt das Verhalten der Zustände oberhalb der Bandlücke die RKKY-Wechselwirkung. Eine der effektivsten Methoden um die RKKY-Wechselwirkung zu beeinflussen ist allerdings das Anlegen eines elektrischen Feldes zwischen den beiden Graphenlagen. Das elektrischen Feldes verändert die Bandstruktur und die RKKY-Wechselwirkung hängt unter diesen Umständen maßgeblich davon ab, ob die Fermi-Energie in der Bandlücke um den K-Punkt, in dem Bandstrukturbereich der einem "mexikanischen Hut" ähnelt oder oberhalb dieses Bandstrukturbereichs liegt.

Die Oberfläche eines topologischen Isolators bietet die besondere Möglichkeit die RKKY-Wechselwirkung in einem Gas von spinpolarisierten Leitungselektronen zu untersuchen. Es ist aus vorherigen Arbeiten bekannt, dass einige IV-VI Halbleiter wie beispielsweise Zinntellurid (SnTe) auf der (111)-Oberfläche lineare, spinpolarisierte Zustände aufweisen die durch die Inversionssymmetrie des Kristalls geschützt sind. Diese Zustände existieren nicht nur am Γ -Punkt sondern auch an den drei M-Punkten der hexagonalen Oberflächen-Brillouin-Zone. In Kapitel 6 leiten wir diese Oberflächenzustände und die dazugehörige Spintextur in einem analytischen Modell her. Das Modell ist auf fundamentale Art und Weise mit den mikroskopischen Parametern des Volumenkristalls, wie dem Kristallfeld, der Spin-Bahn-Kopplung und der Bandverbiegung an der Oberfläche, verknüpft. Wir finden eine Spintextur, die in der Oberflächenebene durch ein Vektorfeld gegeben ist, das immer tangential zu der Kurve eines Kegelschnitts verläuft. An den M-Punkten ist es möglich dieses Vektorfeld in Abhängigkeit von der Bandverbiegung von elliptisch mit Windungszahl -1, über linear und hyperbolisch nach elliptische mit Windungszahl +1 zu verformen. Wie in Kapitel 7 dieser Arbeit zu sehen ist, hat die Tatsache, dass die Oberflächenzustände spinpolarisiert sind interessante Auswirkungen auf die RKKY-Wechselwirkung. In einem Modell, indem die RKKY-Wechselwirkung lediglich über die Oberflächenzustände in der Nähe des Γ-Punktes vermittelt wird, finden wir eine Wechselwirkungsenergie, die aus einem XY-Term, einem Ising-Term und einem Dzyaloshinskii-Moriya-Term besteht. Die Linearkombination der unterschiedlichen Beiträge wird durch die mikroskopischen Parameter des Volumenkristalls und die Wahl der Oberfläche bestimmt. Auf der Snterminierten Oberfläche von SnTe und SnSe finden wir eine ferromagnetische Kopplung, parallel zu dem Verbindungsvektor von beiden Fremdatomen. Dies gilt allerdings nur solange die Fermi-Energie am Scheitelpunkt des Dirac-Kegels liegt. Auf der dotierten, Sn-terminierten Oberfläche finden wir eine Verkantung von den Spins der beiden Fremdatome in Bezug auf den ferromagnetischen oder antiferromagnetischen Referenzzustand parallel zu dem Verbindungsvektor. Diese Verkantung wird durch den Dzyaloshinskii-Moriya-Term hervorgerufen und findet in der xz-Ebene statt (wobei die x-Achse die Verbindungsachse zwischen den beiden magnetischen Fremdatomen ist und die z-Achse parallel zu der (111)-Richtung liegt). Das Ausmaß der Verkantung hängt von der Position der Fermi-Energie und dem Abstand der beiden Fremdatome ab. Schließlich betrachten wir eine weitere Möglichkeit um die RKKY-Wechselwirkung auf der Oberfläche eines topologischen Isolators der Zinntellurid-Klasse zu beeinflussen, nämlich das Legieren des SnTe-Kristalls mit Blei. Es stellt sich in dieser Arbeit heraus, dass man auf diese Weise eine Situation erreichen kann, in der die Spins von beiden Fremdatomen, in einem kleinen Bereich, zu einer ferromagnetischen Ausrichtung senkrecht zu der xz-Ebene neigen.

The Indirect Exchange Interaction

The Spin Product
$$(S_i.\boldsymbol{\sigma})(S_{i_1}.\boldsymbol{\sigma})\cdots(S_{i_m}.\boldsymbol{\sigma})$$

Lemma:

Let m be a positive integer, let \mathbf{S}_i , \mathbf{S}_{i_1} , ..., \mathbf{S}_{i_m} be a vector in \mathbb{R}^3 and let $\boldsymbol{\sigma}$ be the vector of Pauli matrices.

Then, for odd m, the product $(\mathbf{S}_{i}.\boldsymbol{\sigma})(\mathbf{S}_{i_{1}}.\boldsymbol{\sigma})\cdots(\mathbf{S}_{i_{m}}.\boldsymbol{\sigma})$ takes the form

$$(\mathbf{S}_{i}.\boldsymbol{\sigma}) (\mathbf{S}_{i_{1}}.\boldsymbol{\sigma}) \cdots (\mathbf{S}_{i_{m}}.\boldsymbol{\sigma})$$

$$= \sum_{\gamma} \operatorname{sgn}(\gamma) \left(\mathbf{S}_{i_{\gamma(0)}}.\mathbf{S}_{i_{\gamma(1)}} \right) \cdots \left(\mathbf{S}_{i_{\gamma(m-1)}}.\mathbf{S}_{i_{\gamma(m)}} \right)$$

$$+ i \sum_{\gamma} \operatorname{sgn}(\gamma) \left(\mathbf{S}_{i_{\gamma(0)}}.\mathbf{S}_{i_{\gamma(1)}} \right) \cdots \left(\mathbf{S}_{i_{\gamma(m-3)}}.\mathbf{S}_{i_{\gamma(m-2)}} \right) \left[\left(\mathbf{S}_{i_{\gamma(m-1)}} \times \mathbf{S}_{i_{\gamma(m)}} \right) .\boldsymbol{\sigma} \right]$$
(A.1.1)

with $i = i_0$ and the trace given by

$$\operatorname{Tr}\left[\left(\mathbf{S}_{i}.\boldsymbol{\sigma}\right)\left(\mathbf{S}_{i_{1}}.\boldsymbol{\sigma}\right)\cdots\left(\mathbf{S}_{i_{m}}.\boldsymbol{\sigma}\right)\right]$$

$$=2\sum_{\gamma}\operatorname{sgn}(\gamma)\left(\mathbf{S}_{i_{\gamma(0)}}.\mathbf{S}_{i_{\gamma(1)}}\right)\cdots\left(\mathbf{S}_{i_{\gamma(m-1)}}.\mathbf{S}_{i_{\gamma(m)}}\right)$$
(A.1.2)

For even m the spin product takes the form

$$(\mathbf{S}_{i}.\boldsymbol{\sigma}) (\mathbf{S}_{i_{1}}.\boldsymbol{\sigma}) \cdots (\mathbf{S}_{i_{m}}.\boldsymbol{\sigma})$$

$$= \sum_{\gamma} \operatorname{sgn}(\gamma) \left(\mathbf{S}_{i_{\gamma(0)}}.\mathbf{S}_{i_{\gamma(1)}} \right) \cdots \left(\mathbf{S}_{i_{\gamma(m-2)}}.\mathbf{S}_{i_{\gamma(m-1)}} \right) (\mathbf{S}_{i_{m}}.\boldsymbol{\sigma})$$

$$- \sum_{\gamma} \operatorname{sgn}(\gamma) \left(\mathbf{S}_{i_{\gamma(0)}}.\mathbf{S}_{i_{\gamma(1)}} \right) \cdots \left(\mathbf{S}_{i_{\gamma(m-4)}}.\mathbf{S}_{i_{\gamma(m-3)}} \right) \left(\left[\left(\mathbf{S}_{i_{\gamma(m-2)}} \times \mathbf{S}_{i_{\gamma(m-1)}} \right) \times \mathbf{S}_{i_{m}} \right] .\boldsymbol{\sigma} \right)$$

$$+ i \sum_{\gamma} \operatorname{sgn}(\gamma) \left(\mathbf{S}_{i_{\gamma(0)}}.\mathbf{S}_{i_{\gamma(1)}} \right) \cdots \left(\mathbf{S}_{i_{\gamma(m-3)}}.\mathbf{S}_{i_{\gamma(m-2)}} \right) \left[\left(\mathbf{S}_{i_{\gamma(m-1)}} \times \mathbf{S}_{i_{\gamma(m)}} \right) .\mathbf{S}_{i_{m}} \right]$$
(A.1.3)

with the trace given by

$$\operatorname{Tr}\left[\left(\mathbf{S}_{i}.\boldsymbol{\sigma}\right)\left(\mathbf{S}_{i_{1}}.\boldsymbol{\sigma}\right)\cdots\left(\mathbf{S}_{i_{m}}.\boldsymbol{\sigma}\right)\right]$$

$$=2i\sum_{\gamma}\operatorname{sgn}(\gamma)\left(\mathbf{S}_{i_{\gamma(0)}}.\mathbf{S}_{i_{\gamma(1)}}\right)\cdots\left(\mathbf{S}_{i_{\gamma(m-4)}}.\mathbf{S}_{i_{\gamma(m-3)}}\right)\left[\left(\mathbf{S}_{i_{\gamma(m-2)}}\times\mathbf{S}_{i_{\gamma(m-1)}}\right).\mathbf{S}_{i_{m}}\right] \quad (A.1.4)$$

In these expressions the sum \sum_{γ} is taken over all possibilities to make inequivalent pairs from the set of vectors $\{\mathbf{S}_i, \mathbf{S}_{i_1}, \cdots, \mathbf{S}_{i_m}\}$. Provided that each pair is sorted by its indices in ascending order, the sign of each sequence is determined from the total number of interchanges.

Proof:

- The Base Case
 - m = 1

$$\left(\mathbf{S}_{i_0}.\boldsymbol{\sigma}\right)\left(\mathbf{S}_{i_1}.\boldsymbol{\sigma}\right) = \left(\mathbf{S}_{i_0}.\mathbf{S}_{i_1}\right) + i\left[\left(\mathbf{S}_{i_0} \times \mathbf{S}_{i_1}\right).\boldsymbol{\sigma}\right]$$
$$\operatorname{Tr}\left[\left(\mathbf{S}_{i_0}.\boldsymbol{\sigma}\right)\left(\mathbf{S}_{i_1}.\boldsymbol{\sigma}\right)\right] = 2\left(\mathbf{S}_{i_0}.\mathbf{S}_{i_1}\right)$$

• m = 2

$$(\mathbf{S}_{i_0}.\boldsymbol{\sigma}) (\mathbf{S}_{i_1}.\boldsymbol{\sigma}) (\mathbf{S}_{i_2}.\boldsymbol{\sigma})$$

$$= (\mathbf{S}_{i_0}.\mathbf{S}_{i_1}) (\mathbf{S}_{i_2}.\boldsymbol{\sigma}) + (\mathbf{S}_{i_1}.\mathbf{S}_{i_2}) (\mathbf{S}_{i_0}.\boldsymbol{\sigma})$$

$$- (\mathbf{S}_{i_0}.\mathbf{S}_{i_2}) (\mathbf{S}_{i_1}.\boldsymbol{\sigma}) + i [(\mathbf{S}_{i_0} \times \mathbf{S}_{i_1}) .\mathbf{S}_{i_2}]$$

$$\operatorname{Tr}\left[\left(\mathbf{S}_{i_{0}}.\boldsymbol{\sigma}\right)\left(\mathbf{S}_{i_{1}}.\boldsymbol{\sigma}\right)\left(\mathbf{S}_{i_{2}}.\boldsymbol{\sigma}\right)\right]=2i\left[\left(\mathbf{S}_{i_{0}}\times\mathbf{S}_{i_{1}}\right).\mathbf{S}_{i_{2}}\right]$$

- The Inductive Step
 - m+1, even

$$\begin{split} &\left(\mathbf{S}_{i_{0}}.\boldsymbol{\sigma}\right)\left(\mathbf{S}_{i_{1}}.\boldsymbol{\sigma}\right)\cdots\left(\mathbf{S}_{i_{m}}.\boldsymbol{\sigma}\right)\left(\mathbf{S}_{i_{m+1}}.\boldsymbol{\sigma}\right) \\ &=\sum_{\gamma}\operatorname{sgn}(\gamma)\left(\mathbf{S}_{i_{\gamma(0)}}.\mathbf{S}_{i_{\gamma(1)}}\right)\cdots\left(\mathbf{S}_{i_{\gamma(m-1)}}.\mathbf{S}_{i_{\gamma(m)}}\right)\left(\mathbf{S}_{i_{m+1}}.\boldsymbol{\sigma}\right) \\ &-\sum_{\gamma}\operatorname{sgn}(\gamma)\left(\mathbf{S}_{i_{\gamma(0)}}.\mathbf{S}_{i_{\gamma(1)}}\right)\cdots\left(\mathbf{S}_{i_{\gamma(m-3)}}.\mathbf{S}_{i_{\gamma(m-2)}}\right)\left(\left[\left(\mathbf{S}_{i_{\gamma(m-1)}}\times\mathbf{S}_{i_{\gamma(m)}}\right)\times\mathbf{S}_{i_{m+1}}\right].\boldsymbol{\sigma}\right) \\ &+i\sum_{\gamma}\operatorname{sgn}(\gamma)\left(\mathbf{S}_{i_{\gamma(0)}}.\mathbf{S}_{i_{\gamma(1)}}\right)\cdots\left(\mathbf{S}_{i_{\gamma(m-3)}}.\mathbf{S}_{i_{\gamma(m-2)}}\right)\left[\left(\mathbf{S}_{i_{\gamma(m-1)}}\times\mathbf{S}_{i_{\gamma(m)}}\right).\mathbf{S}_{i_{m+1}}\right] \end{split}$$

$$\operatorname{Tr}\left[\left(\mathbf{S}_{i_{0}}.\boldsymbol{\sigma}\right)\left(\mathbf{S}_{i_{1}}.\boldsymbol{\sigma}\right)\cdots\left(\mathbf{S}_{i_{m}}.\boldsymbol{\sigma}\right)\left(\mathbf{S}_{i_{m+1}}.\boldsymbol{\sigma}\right)\right]$$

$$=2i\sum_{\gamma}\operatorname{sgn}(\gamma)\left(\mathbf{S}_{i_{\gamma(0)}}.\mathbf{S}_{i_{\gamma(1)}}\right)\cdots\left(\mathbf{S}_{i_{\gamma(m-3)}}.\mathbf{S}_{i_{\gamma(m-2)}}\right)\left[\left(\mathbf{S}_{i_{\gamma(m-1)}}\times\mathbf{S}_{i_{\gamma(m)}}\right).\mathbf{S}_{i_{m+1}}\right]$$

• m+1, odd

$$\begin{split} &(\mathbf{S}_{i_0}.\boldsymbol{\sigma})\left(\mathbf{S}_{i_1}.\boldsymbol{\sigma}\right)\cdots\left(\mathbf{S}_{i_m}.\boldsymbol{\sigma}\right)\left(\mathbf{S}_{i_{m+1}}.\boldsymbol{\sigma}\right) = \\ &= \sum_{\gamma}\operatorname{sgn}(\gamma)\left(\mathbf{S}_{i_{\gamma(0)}}.\mathbf{S}_{i_{\gamma(1)}}\right)\cdots\left(\mathbf{S}_{i_{\gamma(m-2)}}.\mathbf{S}_{i_{\gamma(m-1)}}\right)\left(\mathbf{S}_{i_m}.\mathbf{S}_{i_{m+1}}\right) \\ &+ \sum_{\gamma}\operatorname{sgn}(\gamma)\left(\mathbf{S}_{i_{\gamma(0)}}.\mathbf{S}_{i_{\gamma(1)}}\right)\cdots\left(\mathbf{S}_{i_{\gamma(m-4)}}.\mathbf{S}_{i_{\gamma(m-3)}}\right)\left(\mathbf{S}_{i_{\gamma(m-1)}}.\mathbf{S}_{i_m}\right)\left(\mathbf{S}_{i_{\gamma(m-2)}}.\mathbf{S}_{i_{m+1}}\right) \\ &- \sum_{\gamma}\operatorname{sgn}(\gamma)\left(\mathbf{S}_{i_{\gamma(0)}}.\mathbf{S}_{i_{\gamma(1)}}\right)\cdots\left(\mathbf{S}_{i_{\gamma(m-4)}}.\mathbf{S}_{i_{\gamma(m-3)}}\right)\left(\mathbf{S}_{i_{\gamma(m-2)}}.\mathbf{S}_{i_m}\right)\left(\mathbf{S}_{i_{\gamma(m-1)}}.\mathbf{S}_{i_{m+1}}\right) \\ &+ i\sum_{\gamma}\operatorname{sgn}(\gamma)\left(\mathbf{S}_{i_{\gamma(0)}}.\mathbf{S}_{i_{\gamma(1)}}\right)\cdots\left(\mathbf{S}_{i_{\gamma(m-2)}}.\mathbf{S}_{i_{\gamma(m-1)}}\right)\left(\left(\mathbf{S}_{i_m}\times\mathbf{S}_{i_{m+1}}\right).\boldsymbol{\sigma}\right) \\ &+ i\sum_{\gamma}\operatorname{sgn}(\gamma)\left(\mathbf{S}_{i_{\gamma(0)}}.\mathbf{S}_{i_{\gamma(1)}}\right)\cdots\left(\mathbf{S}_{i_{\gamma(m-4)}}.\mathbf{S}_{i_{\gamma(m-3)}}\right)\left(\mathbf{S}_{i_{\gamma(m-1)}}.\mathbf{S}_{i_m}\right)\left(\left(\mathbf{S}_{i_{\gamma(m-2)}}\times\mathbf{S}_{i_{m+1}}\right).\boldsymbol{\sigma}\right) \\ &- i\sum_{\gamma}\operatorname{sgn}(\gamma)\left(\mathbf{S}_{i_{\gamma(0)}}.\mathbf{S}_{i_{\gamma(1)}}\right)\cdots\left(\mathbf{S}_{i_{\gamma(m-4)}}.\mathbf{S}_{i_{\gamma(m-3)}}\right)\left(\mathbf{S}_{i_{\gamma(m-2)}}.\mathbf{S}_{i_m}\right)\left(\left(\mathbf{S}_{i_{\gamma(m-1)}}\times\mathbf{S}_{i_{m+1}}\right).\boldsymbol{\sigma}\right) \\ &+ i\sum_{\gamma}\operatorname{sgn}(\gamma)\left(\mathbf{S}_{i_{\gamma(0)}}.\mathbf{S}_{i_{\gamma(1)}}\right)\cdots\left(\mathbf{S}_{i_{\gamma(m-4)}}.\mathbf{S}_{i_{\gamma(m-3)}}\right)\left(\left(\mathbf{S}_{i_{\gamma(m-2)}}\times\mathbf{S}_{i_{\gamma(m-1)}}\right).\mathbf{S}_{i_m}\right)\left(\mathbf{S}_{i_{m+1}}.\boldsymbol{\sigma}\right) \\ &\rightarrow \qquad (\mathbf{S}_{i_0}.\boldsymbol{\sigma})\left(\mathbf{S}_{i_{\gamma(0)}}.\mathbf{S}_{i_{\gamma(1)}}\right)\cdots\left(\mathbf{S}_{i_{m}}.\boldsymbol{\sigma}\right)\left(\mathbf{S}_{i_{\gamma(m-2)}}.\mathbf{S}_{i_{\gamma(m-1)}}\right)\left(\mathbf{S}_{i_{\gamma(m)}}.\mathbf{S}_{i_{\gamma(m+1)}}\right) \\ &+ i\sum_{\gamma}\operatorname{sgn}(\gamma)\left(\mathbf{S}_{i_{\gamma(0)}}.\mathbf{S}_{i_{\gamma(1)}}\right)\cdots\left(\mathbf{S}_{i_{\gamma(m-2)}}.\mathbf{S}_{i_{\gamma(m-1)}}\right)\left(\left(\mathbf{S}_{i_{\gamma(m)}}.\mathbf{S}_{i_{\gamma(m+1)}}\right) \\ &+ i\sum_{\gamma}\operatorname{sgn}(\gamma)\left(\mathbf{S}_{i_{\gamma(0)}}.\mathbf{S}_{i_{\gamma(1)}}\right)\cdots\left(\mathbf{S}_{i_{\gamma(m-2)}}.\mathbf{S}_{i_{\gamma(m-1)}}\right)\left(\left(\mathbf{S}_{i_{\gamma(m)}}.\mathbf{S}_{i_{\gamma(m+1)}}\right).\boldsymbol{\sigma}\right] \end{aligned}$$

 $\operatorname{Tr}\left[\left(\mathbf{S}_{i_0}.\boldsymbol{\sigma}\right)\left(\mathbf{S}_{i_1}.\boldsymbol{\sigma}\right)\cdots\left(\mathbf{S}_{i_m}.\boldsymbol{\sigma}\right)\left(\mathbf{S}_{i_{m+1}}.\boldsymbol{\sigma}\right)\right]$

 $=2\sum_{\gamma}\operatorname{sgn}(\gamma)\left(\mathbf{S}_{i_{\gamma(0)}}.\mathbf{S}_{i_{\gamma(1)}}\right)\cdots\left(\mathbf{S}_{i_{\gamma(m)}}.\mathbf{S}_{i_{\gamma(m+1)}}\right)$

Bessel Functions

In the following we present some standard identities involving Bessel functions that are used throughout the thesis and can be for example found in Ref. [101].

Bessel Functions of the First Kind $J_{\nu}(z)$

Integral Representations

$$J_{\nu}(z) = \frac{1}{2\pi i^{\nu}} \int_{0}^{2\pi} d\varphi \ e^{iz\cos\varphi} e^{i\nu\varphi} \qquad \forall \nu \in \mathbb{Z}$$
 (B.1.1)

$$J_{\nu}(z) = \frac{1}{\pi} \int_{0}^{\pi} d\varphi \cos(z \sin \varphi - \nu \varphi)$$
$$-\frac{\sin \nu \pi}{\pi} \int_{0}^{\infty} dt \ e^{-z \sinh t - \nu t} \qquad \forall |\text{ph}(z)| < \frac{1}{2}\pi$$
(B.1.2)

$$J_{\nu}(z) = \frac{2}{\pi} \int_{0}^{\infty} dt \sin\left(z \cosh t - \frac{1}{2}\nu\pi\right) \cosh(\nu t)$$

$$\forall |\Re\nu| < 1 \land x > 0$$
(B.1.3)

Derivatives

$$\frac{d}{dz}J_0(z) = -J_1(z) \tag{B.1.4}$$

$$\left(\frac{1}{z}\frac{d}{dz}\right)^{k} z^{-\nu} J_{\nu}(z) = (-1)^{k} z^{-\nu-k} J_{\nu+k}(z) \qquad \forall \ k \in \mathbb{N}_{0}$$
 (B.1.5)

Negative Order

$$J_{-\nu}(z) = (-1)^{\nu} J_{\nu}(z) \qquad \forall \nu \in \mathbb{Z}$$
 (B.1.6)

Analytic Continuation

$$J_{\nu}(e^{im\pi}z) = e^{im\nu\pi} J_{\nu}(z) \qquad \forall m \in \mathbb{Z}$$
 (B.1.7)

Asymtptotics

Small Argument

$$J_{\nu}(z) = \frac{1}{\Gamma(\nu)} \left(\frac{z}{2}\right)^{\nu} \tag{B.1.8}$$

Large Argument

$$J_{\nu}(z) = \sqrt{\frac{2}{\pi z}} \left\{ \cos \left[z - \left(\nu + \frac{1}{2} \right) \frac{\pi}{2} \right] - \frac{4\nu^2 - 1}{8z} \sin \left[z - \left(\nu + \frac{1}{2} \right) \frac{\pi}{2} \right] \right\}$$
(B.1.9)

Bessel Functions of the Second Kind $Y_{\nu}(z)$

Integral Representations

$$Y_{\nu}(z) = \frac{1}{\pi} \int_{0}^{\pi} d\varphi \sin(z \sin \varphi - \nu \varphi)$$
$$-\frac{1}{\pi} \int_{0}^{\infty} dt \left(e^{\nu t} + e^{-\nu t} \cos(\nu \pi) \right) e^{-z \sinh t} \qquad \forall |\operatorname{ph}(z)| < \frac{1}{2}\pi \qquad (B.2.1)$$

$$Y_{\nu}(z) = -\frac{2}{\pi} \int_0^\infty dt \, \cos\left(z \cosh t - \frac{1}{2}\nu\pi\right) \cosh(\nu t) \qquad \forall \, |\Re\nu| < 1 \land x > 0 \quad (B.2.2)$$

Derivatives

$$\frac{d}{dz}Y_0(z) = -Y_1(z) \tag{B.2.3}$$

$$\left(\frac{1}{z}\frac{d}{dz}\right)^{k} z^{-\nu} Y_{\nu}(z) = (-1)^{k} z^{-\nu - k} Y_{\nu + k}(z) \qquad \forall \ k \in \mathbb{N}_{0}$$
 (B.2.4)

Negative Order

$$Y_{-\nu}(z) = (-1)^{\nu} Y_{\nu}(z) \qquad \forall \nu \in \mathbb{Z}$$
 (B.2.5)

Analytic Continuation

$$Y_{\nu}(e^{im\pi}z) = e^{-im\nu\pi} Y_{\nu}(z) + 2i\sin(m\nu\pi)\cot(\nu\pi)J_{\nu}(z) \qquad \forall m \in \mathbb{Z}$$
 (B.2.6)

Asymtptotics

Samll Argument

$$Y_{\nu}(z) = \begin{cases} \frac{2}{\pi} \left[\ln \left(\frac{1}{2} z \right) + \gamma \right] & \nu = 0 \\ -\frac{\Gamma(\nu)}{\pi} \left(\frac{2}{z} \right)^{\nu} & \nu \neq 0 \end{cases}$$
 (B.2.7)

Large Argument

$$Y_{\nu}(z) = \sqrt{\frac{2}{\pi z}} \left\{ \cos \left[z - \left(\nu + \frac{1}{2} \right) \frac{\pi}{2} \right] + \frac{4\nu^2 - 1}{8z} \sin \left[z - \left(\nu + \frac{1}{2} \right) \frac{\pi}{2} \right] \right\}$$
(B.2.8)

Hankel Functions

Definition

$$H_{\nu}^{1}(z) = J_{\nu}(z) + iY_{\nu}(z) \tag{B.3.1}$$

$$H_{\nu}^{2}(z) = J_{\nu}(z) - iY_{\nu}(z) \tag{B.3.2}$$

Recurrence Relation

$$\frac{d}{dz}H_0^1(z) = -H_1^1(z) \tag{B.3.3}$$

$$\left(\frac{1}{z}\frac{d}{dz}\right)^k z^{-\nu} H_{\nu}^1(z) = (-1)^k z^{-\nu-k} H_{\nu+k}^1(z) \qquad \forall \ k \in \mathbb{N}_0$$
 (B.3.4)

Analytic Continuation

$$\sin(\nu\pi) \ H_{\nu}^{1}(ze^{im\pi}) = -\sin([m-1]\nu\pi) \ H_{\nu}^{1}(z) - \sin(m\nu\pi) \ e^{-i\nu\pi} \ H_{\nu}^{2}(z)$$
 (B.3.5)

$$\sin(\nu\pi) \ H_{\nu}^{2}(ze^{im\pi}) = \sin(m\nu\pi) \ e^{i\nu\pi} \ H_{\nu}^{1}(z) + \sin([m+1]\nu\pi) \ H_{\nu}^{2}(z)$$
 (B.3.6)

Asymptotics

Small Argument

$$H_{\nu}^{1}(z) = \begin{cases} \frac{2i}{\pi} \ln(z) & \nu = 0\\ -\frac{i\Gamma(\nu)}{\pi} \left(\frac{2}{z}\right)^{\nu} & \nu \neq 0 \end{cases}$$
 (B.3.7)

$$H_{\nu}^{2}(z) = \begin{cases} -\frac{2i}{\pi} \ln(z) & \nu = 0\\ \frac{i\Gamma(\nu)}{\pi} \left(\frac{2}{z}\right)^{\nu} & \nu \neq 0 \end{cases}$$
(B.3.8)

Large Argument

$$H_{\nu}^{1}(z) = \sqrt{\frac{2}{\pi z}} \left(1 + i \frac{4\nu^{2} - 1}{8z} \right) e^{i\left(z - \frac{1}{2}\nu\pi - \frac{1}{4}\pi\right)}$$
 (B.3.9)

$$H_{\nu}^{2}(z) = \sqrt{\frac{2}{\pi z}} \left(1 - i \frac{4\nu^{2} - 1}{8z} \right) e^{i\left(z - \frac{1}{2}\nu\pi - \frac{1}{4}\pi\right)}$$
 (B.3.10)

$R \to 0$ Limit

$$\lim_{R \to 0} \Im \left(iH_0^1(xR) \right) = \lim_{R \to 0} \begin{cases} \Im \left(iJ_0(|x|R) - Y_0(|x|R) \right) & x \ge 0 \\ \Im \left(iJ_0(-|x|R) - Y_0(-|x|R) \right) & x < 0 \end{cases}$$

$$= \lim_{R \to 0} \begin{cases} \Im \left(iJ_0(|x|R) - Y_0(|x|R) \right) & x \ge 0 \\ -\Im \left(iJ_0(|x|R) + Y_0(|x|R) \right) & x < 0 \end{cases}$$

$$= \operatorname{sign}(E) \qquad \forall x \in \mathbb{R} \quad (B.3.11)$$

$$\lim_{R \to 0} \Im \left(H_0^1(xR) \right) = \lim_{R \to 0} \begin{cases} \Im \left(J_0(|x|R) + iY_0(|x|R) \right) & x \ge 0 \\ \Im \left(J_0(-|x|R) + iY_0(-|x|R) \right) & x < 0 \end{cases}$$

$$= \lim_{R \to 0} \begin{cases} \Im \left(J_0(|x|R) + iY_0(|x|R) \right) & x \ge 0 \\ \Im \left(-J_0(|x|R) + iY_0(|x|R) \right) & x < 0 \end{cases}$$

$$= \lim_{R \to 0} Y_0(|x|R) \qquad \forall x \in \mathbb{R}$$
(B.3.12)

Sum of Hankel Functions

$$H_0^1(z) + H_0^1(-z^*) = H_0^1(z) - H_0^2(z^*)$$

$$= H_0^1(z) - H_0^1(z)^*$$

$$= 2iY_0(z)$$
(B.3.13)

$$H_0^1(z) - H_0^1(-z^*) = H_0^1(z) + H_0^2(z)$$

$$= H_0^1(z) + H_0^1(z)^*$$

$$= 2J_0(z)$$
(B.3.14)

Modified Bessel Function of the Second Kind

Integral Representation

$$K_0(zR) = \int_0^\infty dk \; \frac{kJ_0(kR)}{k^2 + z^2} \qquad \forall \; \Re(z) > 0$$
 (B.4.1)

Connection to Hankel Functions

$$K_{\nu}(z) = \frac{1}{2}\pi i^{\nu+1} H_{\nu}^{1}(iz)$$
 (B.4.2)

Asymptotics

Small Argument

$$K_{\nu}(z) = \begin{cases} -\ln(z) & \nu = 0\\ \frac{\Gamma(\nu)}{2} \left(\frac{2}{z}\right)^{\nu} & \nu \neq 0 \end{cases}$$
 (B.4.3)

Large Argument

$$K_{\nu}(z) = \sqrt{\frac{2}{\pi z}} e^{-z} \left(1 + \frac{4\nu^2 - 1}{8z} \right)$$
 (B.4.4)

Integrals of Bessel functions

Laplace Transform

$$\int_0^\infty dx \ x^{\nu} J_{\nu}(ax) e^{-sx} = \frac{2^{\nu} a^{\nu} \Gamma(\nu + \frac{1}{2})}{\sqrt{\pi} (s^2 + a^2)^{\nu + \frac{1}{2}}} \qquad \forall \nu > -\frac{1}{2}$$
 (B.5.1)

$$\int_0^\infty dx \ x^{\nu+1} J_{\nu}(ax) e^{-sx} = \frac{2^{\nu+1} a^{\nu} s \Gamma(\nu + \frac{3}{2})}{\sqrt{\pi} (s^2 + a^2)^{\nu + \frac{3}{2}}} \qquad \forall \nu > -1$$
 (B.5.2)

$$\int_{0}^{\infty} dx \ x^{\frac{\nu}{2}} J_{\nu}(2\sqrt{ax}) e^{-sx} = \frac{a^{\frac{\nu}{2}}}{s^{\nu+1}} e^{-\frac{a}{s}} \qquad \forall \nu > -1$$
 (B.5.3)

Various Integrals

$$\int_0^x dx' \ x' J_0(x') Y_0(x') = \frac{1}{2} x^2 \left[J_0(x) Y_0(x) + J_1(x) Y_1(x) \right] \qquad \forall x > 0$$
 (B.5.4)

B.5. INTEGRALS OF BESSEL FUNCTIONS

$$\int_0^x dx' \ x'^{\nu} Y_{\nu-1}(x') = x^{\nu} Y_{\nu}(x) + \frac{2^{\nu} \Gamma(\nu)}{\pi}$$
 $\forall x > 0$ (B.5.5)

$$\int_0^\infty dx' \ x'^{\mu} K_{\nu}(x') = 2^{\mu - 1} \Gamma\left(\frac{\mu + \nu + 1}{2}\right) \Gamma\left(\frac{\mu - \nu + 1}{2}\right)$$

$$\forall \Re(\mu \pm \nu) > -1 \qquad (B.5.6)$$

The RKKY Interaction in Bilayer Graphene

The Green's Function of AA-stacked Bilayer Graphene

	Zero Temperature	Finite Temperature
$G_{m,lpha_{l}}^{0R}$	$_{\alpha'_{l'}}(\mathbf{R}, E) = -\frac{i\pi^2}{2\hbar v_F \Omega_{BZ}} M_{\alpha_l \alpha'_{l'}}(\mathbf{R}, E)$	$\mathcal{G}_{m,\alpha_{l}\alpha'_{l'}}^{0}(\mathbf{R},i\omega_{n}) = -\frac{i\pi}{v_{F}\Omega_{BZ}}\mathcal{M}_{\alpha_{l}\alpha'_{l'}}(\mathbf{R},i\omega_{n})$
	$z^{+} = \frac{1}{\hbar v_F} \left(E + i\eta + t_{\perp} \right)$	$z^{+} = \frac{1}{\hbar v_F} \left(\hbar \omega_n - i\mu - it_{\perp} \right)$
	$z^{-} = \frac{1}{\hbar v_F} \left(E + i\eta - t_{\perp} \right)$	$z^{-} = \frac{1}{\hbar v_F} \left(\hbar \omega_n - i\mu + it_{\perp} \right)$
$\alpha_l \alpha'_{l'}$	$M_{lpha_{l}lpha'{}_{l'}}$	$\mathcal{M}_{lpha_{l}lpha'{}_{l'}}$
A_1A_1	$z^{+}H_{0}^{1}(z^{+}R) + z^{-}H_{0}^{1}(z^{-}R)$	$sign(\omega_n)[z^+K_0(z^+R) + z^-K_0(z^-R)]$
A_1B_1	$i\Phi_m(\mathbf{R})\left[z^+H_1^1(z^+R) + z^-H_1^1(z^-R)\right]$	$\Phi_m(\mathbf{R}) \left[z^+ K_1(z^+ R) + z^- K_1(z^- R) \right]$
A_1A_2	$z^{+}H_{0}^{1}(z^{+}R) - z^{-}H_{0}^{1}(z^{-}R)$	$sign(\omega_n) [z^+ K_0(z^+ R) - z^- K_0(z^- R)]$
A_1B_2	$i\Phi_m(\mathbf{R})\left[z^+H_1^1(z^+R) - z^-H_1^1(z^-R)\right]$	$\Phi_m(\mathbf{R}) \left[z^+ K_1(z^+ R) - z^- K_1(z^- R) \right]$

Table C.1: The Green's function of AA-stacked bilayer graphene at zero and at finite temperature. Shown are only the four fundamentally different matrix elements which are at zero temperature represented by a linear combination of two Hankel functions $H^1_{\nu}(x)$ and at finite temperature represented by a linear combination of two modified Bessel function $K_{\nu}(x)$.

The Green's Function of AB-stacked Bilayer Graphene

Zero Temperature		Finite Temperature		
G_{r}^{0}	$\Omega_{m,\alpha_{l}\alpha'_{l'}}^{R}(\mathbf{R},E) = -\frac{i\pi^{2}}{2\hbar^{2}v_{F}^{2}\Omega_{BZ}}M_{\alpha_{l}\alpha'_{l'}}(\mathbf{R},E)$	$\mathcal{G}_{m,\alpha_{l}\alpha'_{l'}}^{0}(\mathbf{R},i\omega_{n}) = -\frac{i\pi}{\hbar v_{F}^{2}\Omega_{BZ}}\mathcal{M}_{\alpha_{l}\alpha'_{l'}}(\mathbf{R},i\omega_{n})$		
	$z^{+} = \frac{1}{\hbar v_F} \sqrt{(E+i\eta)(E+i\eta+t_{\perp})}$	$z^{+} = \frac{1}{\hbar v_{F}} \sqrt{(\hbar \omega_{n} - i\mu) (\hbar \omega_{n} - i\mu - it_{\perp})}$		
	$z^- = rac{1}{\hbar v_F} \sqrt{(E+i\eta)(E+i\eta-t_\perp)}$	$z^{-} = \frac{1}{\hbar v_F} \sqrt{(\hbar \omega_n - i\mu) (\hbar \omega_n - i\mu + it_{\perp})}$		
$\alpha_l {\alpha'}_{l'}$	$M_{lpha_llpha'{}_{l'}}$	$\mathcal{M}_{lpha_{l}lpha'_{l'}}$		
A_1A_1	$E\left[H_0^1(z^+R) + H_0^1(z^-R)\right]$	$(\hbar\omega_n - i\mu) \left[K_0(z^+R) + K_0(z^-R) \right]$		
A_1B_1	$i\hbar v_F \Phi_m(\mathbf{R}) \left[z^+ H_1^1(z^+ R) + z^- H_1^1(z^- R) \right]$	$\hbar v_F \Phi_m(\mathbf{R}) \left[z^+ K_1(z^+ R) + z^- K_1(z^- R) \right]$		
A_1A_2	$E\left[H_0^1(z^+R) - H_0^1(z^-R)\right]$	$(\hbar\omega_n - i\mu) \left[K_0(z^+R) - K_0(z^-R) \right]$		
A_1B_2	$i\hbar v_F \Phi_m^*(\mathbf{R}) \left[z^+ H_1^1(z^+ R) - z^- H_1^1(z^- R) \right]$	$\hbar v_F \Phi_m^*(\mathbf{R}) \left[z^+ K_1(z^+ R) - z^- K_1(z^- R) \right]$		
B_1B_1	$(E + \tau_{\perp})H_0^1(z^+R) + (E - \tau_{\perp})H_0^1(z^-R)$	$(\hbar\omega_n - i\mu - it_\perp)K_0(z^+R)$ $+(i\omega_n - i\mu + it_\perp)K_0(z^-R)$		
B_1B_2	$-\frac{\hbar^2 v_F^2}{E} \Phi_m^{*2}(\mathbf{R}) \left[z^{+2} H_2^1(z^+ R) - z^{-2} H_2^1(z^- R) \right]$	$\frac{\hbar^2 v_F^2}{\hbar \omega_n - i\mu} \Phi_m^{*2}(\mathbf{R}) \left[z^{+2} K_2(z^+ R) - z^{-2} K_2(z^- R) \right]$		

Table C.2: The Green's function of AB-stacked bilayer graphene at zero [54, 91] and at finite temperature. Shown are only the six fundamentally different matrix elements. $K_{\nu}(x)$ stands for the modified Bessel function and $H^1_{\nu}(x)$ for the Hankel function of the first kind and ν th order. The square roots are taken so that the real part is positive valued.

The Green's Function of Biased AB-stacked Bilayer Graphene

Zero Temperature $\mathbf{G}_{m}^{0R}(\mathbf{R}, E) = -\frac{i\pi^{2}}{8\hbar^{2}v_{\scriptscriptstyle P}^{2}\Omega_{\scriptscriptstyle RZ}u}M(\mathbf{R}, E)$ $z^{+} = \frac{1}{\hbar v_{E}} \sqrt{(E + i\eta)^{2} + \frac{V^{2}}{4} + u}$ $A(V) = u + (E + i\eta)V$ $z^{-} = \frac{1}{\hbar v_F} \sqrt{(E + i\eta)^2 + \frac{V^2}{4} - u}$ $B(V) = 2(E + i\eta) + V$ $u = \sqrt{(E+i\eta)^2 (V^2 + t_{\perp}^2) - \frac{V^2 t_{\perp}^2}{4}} \qquad F_s(V) = u - s(E+i\eta)V + s\frac{2(E+i\eta)+V}{2(E+i\eta)-V}t_{\perp}^2$ $\alpha_l \alpha'_{l'}$ $M_{\alpha_l \alpha'_{l'}}$ $2B(-V) \left[A(-V)H_0^1(z^+R) + A(V)H_0^1(z^-R) \right]$ A_1A_1 A_1B_1 $4i\hbar v_F \Phi_m(\mathbf{R}) \left[A(-V)z^+ H_1^1(z^+R) + A(V)z^- H_1^1(z^-R) \right]$ $t_{\perp}B(V)B(-V)\left[H_{0}^{1}(z^{+}R)-H_{0}^{1}(z^{-}R)\right]$ A_1A_2 $2i\hbar v_F \Phi_m^* (\mathbf{R}) t_\perp B(-V) \left[z^+ H_1^1 (z^+ R) - z^- H_1^1 (z^- R) \right]$ A_1B_2 $2B(-V)\left[F_{+}(V)H_{0}^{1}(z^{+}R)+F_{-}(V)H_{0}^{1}(z^{-}R)\right]$ B_1B_1 $2i\hbar v_F \Phi_m^* (\mathbf{R}) t_\perp B(V) \left[z^+ H_1^1 (z^+ R) - z^- H_1^1 (z^- R) \right]$ B_1A_2 $-4\hbar^{2}v_{F}^{2}\Phi_{m}^{*2}\left(\mathbf{R}\right)t_{\perp}\left[z^{+2}H_{2}^{1}\left(z^{+}R\right)-z^{-2}H_{2}^{1}\left(z^{-}R\right)\right]$ B_1B_2 $2B(V) \left[A(V)H_0^1(z^+R) + A(-V)H_0^1(z^-R) \right]$ A_2A_2 $4i\hbar v_F \Phi_m^* (\mathbf{R}) \left[A(V) z^+ H_1^1 (z^+ R) + A(-V) z^- H_1^1 (z^- R) \right]$ A_2B_2 $2B(V)\left[F_{+}(-V)H_{0}^{1}(z^{+}R)+F_{-}(-V)H_{0}^{1}(z^{-}R)\right]$ B_2B_2

Table C.3: The Green's function of biased AB-stacked bilayer graphene at zero temperature. Each matrix element is a linear combination of two Hankel functions $H^1_{\nu}(x)$ of the first kind and ν th order. By convention, all square roots are taken so that the real part is positive valued.

Finite Temperature

$$\begin{split} \mathcal{G}_{m}^{0}(\mathbf{R},i\omega_{n}) &= -\frac{i\pi^{2}}{8\hbar v_{F}^{2}\Omega_{BZ}u}\mathcal{M}(\mathbf{R},i\omega_{n}) \\ z^{+} &= \frac{1}{\hbar v_{F}}\sqrt{(i\hbar\omega_{n}+\mu)^{2}+\frac{V^{2}}{4}+u} & \mathcal{A}(V) = u + [i\hbar\omega_{n}+\mu]\,V \\ z^{-} &= \frac{1}{\hbar v_{F}}\sqrt{(i\hbar\omega_{n}+\mu)^{2}+\frac{V^{2}}{4}-u} & \mathcal{B}(V) = 2i\hbar\omega_{n}+2\mu+V \\ u &= \sqrt{(i\hbar\omega_{n}+\mu)^{2}\left(V^{2}+t_{\perp}^{2}\right)-\frac{V^{2}t_{\perp}^{2}}{4}} & \mathcal{F}_{s}(V) = u - s\left[i\hbar\omega_{n}+\mu\right]V + s\frac{2i\hbar\omega_{n}+2\mu+V}{2i\hbar\omega_{n}+2\mu-V}t_{\perp}^{2} \\ \frac{\alpha_{l}\alpha'_{l'}}{A_{1}A_{1}} & 2\mathcal{B}(-V)\left[\mathcal{A}(-V)H_{0}^{1}\left(z^{+}R\right)+\mathcal{A}(V)H_{0}^{1}\left(z^{-}R\right)\right] \\ A_{1}B_{1} & 4i\hbar v_{F}\Phi_{m}\left(\mathbf{R}\right)\left[\mathcal{A}(-V)z^{+}H_{1}^{1}\left(z^{+}R\right)+\mathcal{A}(V)z^{-}H_{1}^{1}\left(z^{-}R\right)\right] \\ A_{1}B_{2} & t_{\perp}\mathcal{B}(V)\mathcal{B}(-V)\left[H_{0}^{1}\left(z^{+}R\right)-H_{0}^{1}\left(z^{-}R\right)\right] \\ B_{1}B_{1} & 2\mathcal{B}(-V)\left[\mathcal{F}_{+}(V)H_{0}^{1}\left(z^{+}R\right)+\mathcal{F}_{-}(V)H_{0}^{1}\left(z^{-}R\right)\right] \\ B_{1}B_{2} & 2i\hbar v_{F}\Phi_{m}^{*}\left(\mathbf{R}\right)t_{\perp}\mathcal{B}(V)\left[z^{+}H_{1}^{1}\left(z^{+}R\right)-z^{-}H_{1}^{1}\left(z^{-}R\right)\right] \\ A_{2}A_{2} & 2\mathcal{B}(V)\left[\mathcal{A}(V)H_{0}^{1}\left(z^{+}R\right)+\mathcal{A}(-V)H_{0}^{1}\left(z^{-}R\right)\right] \\ A_{2}B_{2} & 4i\hbar v_{F}\Phi_{m}^{*}\left(\mathbf{R}\right)\left[\mathcal{A}(V)z^{+}H_{1}^{1}\left(z^{+}R\right)+\mathcal{A}(-V)z^{-}H_{1}^{1}\left(z^{-}R\right)\right] \\ B_{2}B_{2} & 2\mathcal{B}(V)\left[\mathcal{F}_{+}(-V)H_{0}^{1}\left(z^{+}R\right)+\mathcal{F}_{-}(-V)H_{0}^{1}\left(z^{-}R\right)\right] \\ \end{array}$$

Table C.4: The Green's function of biased AB-stacked bilayer graphene at finite temperature. $K_{\nu}(x)$ stands for the modified Bessel function of the ν th order. By convention, all square roots are taken so that the real part is positive valued.

The DOS of Biased AB-stacked Bilayer Graphene

In this Appendix, we present an analytical derivation of the DOS of biased AB-stacked bilayer graphene. For the derivation we use the zero temperature Green's function which is given in Table (C.3). Exemplarily we focus on site A_1 where the DOS can be obtained from the following ansatz

$$D_{A_1}(E) = -\frac{1}{\pi} \lim_{R \to 0} \Im \left[G_{A_1 A_1}^{0R} \left(\mathbf{R}, E \right) \right]$$
 (C.4.1)

Substituting the appropriate matrix element of the Green's function into Eq. (C.4.1) leads to the expression

$$D_{A1}(E) = \frac{1}{2\hbar^2 v_F^2 \Omega_{BZ}} \lim_{R \to 0} \Re \left[\frac{A(-V)B(-V)}{u} H_0^1(z^+ R) + \frac{A(V)B(-V)}{u} H_0^1(z^- R) \right]$$
(C.4.2)

with z^+ , z^- and u defined according to Table (C.3). Here it is worth to mention that the Green's function, that we have substituted into Eq. (C.4.1), consists of two parts expanded in vicinity of the two inequivalent K points. These two parts contribute equally to the DOS and this manifests in Eq. (C.4.2) in a factor of two. Apart from that it is important to note that the energy comes in Eq. (C.4.2) with a small imaginary part η . When we take the $\eta \to 0$ limit and proceed with a further analytical evaluation we have to distinguish between the four distinct band structure regions: the gap around the K point, the Mexican hat region, the gap between the low and the high energy band and the two band region.

In the gap around the K point the variable u is purely imaginary which implies that z^+ and z^- are complex valued and connected by the identity $z^+ = -z^{-*}$. Under these circumstances Eq. (C.4.2) can be brought to the form

$$D_{A1}(E) = -\frac{1}{\hbar^2 v_F^2 \Omega_{BZ}} \lim_{R \to 0} \Re \left[\frac{B(-V)}{u} \left(|u| Y_0(z^+ R) + EV J_0(z^+ R) \right) \right]$$
(C.4.3)

with $|u|^2 = (\Re u)^2 + (\Im u)^2$. It can be seen that the special connection between z^+ and z^- together with the structure of the coefficients ensure that the linear combination inside the real part is, in the $\eta \to 0$ limit, purely real. As a consequence the DOS is zero.

In the Mexican hat and in the two band region the $\eta \to 0$ limit of the small imaginary part in the denominator of Eq. (C.4.2) must be taken with help of the Sokhotsky-Plemelj theorem

$$D_{A1}(E) = \frac{\pi B(-V)}{2\hbar^2 v_F^2 \Omega_{BZ} u} \lim_{R \to 0} \Re \left[A(-V) H_0^1(z^+ R) + A(V) H_0^1(z^- R) \right]$$

$$+\frac{\pi^2 B(-V)}{2\hbar^2 v_F^2 \Omega_{BZ}} \delta(u) \lim_{R \to 0} \Im \left[A(-V) H_0^1(z^+ R) + A(V) H_0^1(z^- R) \right]$$
 (C.4.4)

where the variables u, z^+ and z^- are now taken as purely real. The term in the second line does not contribute to the DOS since the function inside the imaginary part is zero when u = 0. For this reason there remains only the term in the first line which can be rewritten with help of Eq. (B.3.11) as follows

$$D_{A1}(\epsilon) = \frac{\pi B(-V)}{2\hbar^2 v_F^2 \Omega_{BZ} u} \left[A(-V) \operatorname{sgn}(z^+) + A(V) \operatorname{sgn}(z^-) \right]$$
 (C.4.5)

After that step we have to distinguish between the Mexican hat region and the two band region since the sign of the two variables z^+ and z^- is a function of the energy: in the Mexican hat region z^+ is positive while z^- is negative and, hence, the DOS can be brought to the form

$$D_{A1}(E) = -\text{sgn}(E) \frac{\pi E V (2E - V)}{\hbar^2 v_F^2 \Omega_{BZ} u}$$
 (C.4.6)

In the two band region the signs are connected by the identity $sign(z^+) = -sign(z^-) = sgn(E)$ which yields, substituted into Eq. (C.4.5), the following result

$$D_{A1}(E) = -\frac{\pi (2E - V)}{\hbar^2 v_F^2 \Omega_{BZ}}$$
 (C.4.7)

In the gap between the low and the high energy band we have an entirely new situation: either z^+ or z^- is now purely imaginary which implies that the respective Hankel function is purely imaginary and gives no contribution to the real part of Eq. (C.4.2). The contribution from the remaining Hankel function can be simplified, in the $R \to 0$ limit, with help of Eq. (B.3.11):

$$D_{A_1}(E) = \operatorname{sgn}(E) \frac{\pi (2E - V)(u - |E|V)}{2\hbar^2 v_F^2 \Omega_{BZ} u}$$
 (C.4.8)

All in all we find the DOS of biased AB-stacked bilayer graphene on site A_1 given by

$$D_{A1}(E) = \operatorname{sign}(E) \frac{\pi}{2\hbar^2 v_F^2 \Omega_{BZ} u} \rho_{A1}(E)$$
 (C.4.9)

with $\rho_{A1}(E)$ defined as follows:

$$\rho_{A1}(E) = \begin{cases}
2u (2E - V) & |E| \ge \sqrt{\frac{V^2}{4} + t_{\perp}^2} \\
(2E - V) (u - |E|V) & \sqrt{\frac{V^2}{4} + t_{\perp}^2} > |E| > \frac{V}{2} \\
-2|E|V (2E - V) & \frac{V}{2} \ge |E| \ge \frac{Vt_{\perp}}{2\sqrt{V^2 + t_{\perp}^2}} \\
0 & |E| < \frac{Vt_{\perp}}{2\sqrt{V^2 + t_{\perp}^2}}
\end{cases}$$
(C.4.10)

The RKKY Interaction in Biased AB-stacked Bilayer Graphene at Zero Temperature

$$\begin{split} & \alpha_{l}\alpha_{l'}' \\ & A_{1}A_{1} \quad \frac{1}{4\hbar^{2}v_{F}^{2}} \int_{E_{F}}^{\infty} dE \ \Im \left(\frac{B(-V)^{2}}{u^{2}} \left[A(-V) H_{0}^{1}(z^{+}R) + A(V) H_{0}^{1}(z^{-}R) \right]^{2} \right) \\ & A_{2}A_{2} \quad \frac{1}{4\hbar^{2}v_{F}^{2}} \int_{E_{F}}^{\infty} dE \ \Im \left(\frac{B(V)^{2}}{u^{2}} \left[A(V) H_{0}^{1}(z^{+}R) + A(-V) H_{0}^{1}(z^{-}R) \right]^{2} \right) \\ & B_{1}B_{1} \quad \frac{1}{4\hbar^{2}v_{F}^{2}} \int_{E_{F}}^{\infty} dE \ \Im \left(\frac{B(-V)^{2}}{u^{2}} \left[F_{+}(V) H_{0}^{1}(z^{+}R) + F_{-}(V) H_{0}^{1}(z^{-}R) \right]^{2} \right) \\ & B_{2}B_{2} \quad \frac{1}{4\hbar^{2}v_{F}^{2}} \int_{E_{F}}^{\infty} dE \ \Im \left(\frac{B(V)^{2}}{u^{2}} \left[F_{+}(-V) H_{0}^{1}(z^{+}R) + F_{-}(-V) H_{0}^{1}(z^{-}R) \right]^{2} \right) \\ & B_{1}A_{1} \quad \int_{E_{F}}^{\infty} dE \ \Im \left(\frac{1}{u^{2}} \left[A(-V) z^{+} H_{1}^{1}(z^{+}R) + A(V) z^{-} H_{1}^{1}(z^{-}R) \right]^{2} \right) \\ & A_{2}B_{2} \quad \int_{E_{F}}^{\infty} dE \ \Im \left(\frac{1}{u^{2}} \left[A(V) z^{+} H_{1}^{1}(z^{+}R) + A(-V) z^{-} H_{1}^{1}(z^{-}R) \right]^{2} \right) \\ & A_{2}B_{1} \quad \frac{t_{1}^{2}}{4} \int_{E_{F}}^{\infty} dE \ \Im \left(\frac{B(-V)^{2}}{u^{2}} \left[z^{+} H_{1}^{1}(z^{+}R) - z^{-} H_{1}^{1}(z^{-}R) \right]^{2} \right) \\ & A_{2}A_{1} \quad \frac{t_{1}^{2}}{16\hbar^{2}v_{F}^{2}} \int_{E_{F}}^{\infty} dE \ \Im \left(\frac{B(V)B(-V)}{u^{2}} \left[H_{0}^{1}(z^{+}R) - H_{0}^{1}(z^{-}R) \right]^{2} \right) \\ & B_{2}B_{1} \quad \hbar^{2}v_{F}^{2}t_{\perp}^{2} \int_{E_{F}}^{\infty} dE \ \Im \left(\frac{1}{u^{2}} \left[z^{+2} H_{1}^{1}(z^{+}R) - z^{-2} H_{1}^{1}(z^{-}R) \right]^{2} \right) \end{aligned}$$

Table C.5: The RKKY interaction in biased bilayer graphene. The ten distinct exchange integrals can be brought to the separable form $J_{\alpha_l\alpha'_{l'}}(\mathbf{R}) = CI_{\alpha_l\alpha'_{l'}}(R)f_{\alpha_l\alpha'_{l'}}(\mathbf{R})$ with $C = -\lambda^2\hbar^2a^2/(64\pi t^2)$. This table defines the intravalley scattering function $I_{\alpha_l\alpha'_{l'}}(R)$ with A(V), B(V), $F_{\pm}(V)$, u, z^+ and z^- taken from Appendix C.3. The fast oscillation function $f_{\alpha_l\alpha'_{l'}}(\mathbf{R})$ may be read of from Table (4.3).

The Topological Surface States of a Topological Insulator of the SnTe Class

The Spin Operator in the Basis of the Bulk Band Edge States

In Chapter 6, we have presented a derivation of the topological surface states of a topological insulator of the SnTe class in vicinity of the Γ point and in vicinity of the three inequivalent M points of the surface Brillouin zone. The topological surface states at the three M points are treated each in an own coordinate system. These coordinate systems are chosen so that the k_x and k_y axis are aligned with the semi-axes of the elliptic cone that is obtained as a spectrum. In these local coordinate systems the bulk band edge states take the form

$$|\Phi_{2}^{-}\rangle = -\sin\frac{\Theta^{-}}{2}e^{-i\frac{\alpha}{2}}\left(\sin\frac{\beta}{2} |\Phi_{+}^{-\uparrow_{M}}\rangle + \cos\frac{\beta}{2} |\Phi_{+}^{-\downarrow_{M}}\rangle\right) + \cos\frac{\Theta^{-}}{2}e^{i\frac{\alpha}{2}}\left(\cos\frac{\beta}{2} |\Phi_{0}^{-\uparrow_{M}}\rangle - \sin\frac{\beta}{2} |\Phi_{0}^{-\downarrow_{M}}\rangle\right)$$
(D.1.1)

$$K \mid \Phi_{2}^{-} \rangle = -\sin \frac{\Theta^{-}}{2} e^{i\frac{\alpha}{2}} \left(\cos \frac{\beta}{2} \mid \Phi_{-}^{-\uparrow_{M}} \rangle - \sin \frac{\beta}{2} \mid \Phi_{-}^{-\downarrow_{M}} \rangle \right)$$

$$+ \cos \frac{\Theta^{-}}{2} e^{-i\frac{\alpha}{2}} \left(\sin \frac{\beta}{2} \mid \Phi_{0}^{-\uparrow_{M}} \rangle + \cos \frac{\beta}{2} \mid \Phi_{0}^{-\downarrow_{M}} \rangle \right)$$
(D.1.2)

$$|\Phi_{1}^{+}\rangle = \cos\frac{\Theta^{+}}{2}e^{-i\frac{\alpha}{2}}\left(\sin\frac{\beta}{2} |\Phi_{+}^{+\uparrow_{M}}\rangle + \cos\frac{\beta}{2} |\Phi_{+}^{+\downarrow_{M}}\rangle\right) + \sin\frac{\Theta^{+}}{2}e^{i\frac{\alpha}{2}}\left(\cos\frac{\beta}{2} |\Phi_{0}^{+\uparrow_{M}}\rangle - \sin\frac{\beta}{2} |\Phi_{0}^{+\downarrow_{M}}\rangle\right)$$
(D.1.3)

$$K \mid \Phi_{1}^{+} \rangle = \cos \frac{\Theta^{+}}{2} e^{i\frac{\alpha}{2}} \left(\cos \frac{\beta}{2} \mid \Phi_{-}^{+\uparrow_{M}} \rangle - \sin \frac{\beta}{2} \mid \Phi_{-}^{+\downarrow_{M}} \rangle \right)$$

$$+ \sin \frac{\Theta^{+}}{2} e^{-i\frac{\alpha}{2}} \left(\sin \frac{\beta}{2} \mid \Phi_{0}^{+\uparrow_{M}} \rangle + \cos \frac{\beta}{2} \mid \Phi_{0}^{+\downarrow_{M}} \rangle \right)$$
(D.1.4)

with Θ^+ and Θ^- defined in Table (5.1) and where $|\uparrow_M\rangle$ and $|\downarrow_M\rangle$ stand for the spin up or spin down wave function represented in the coordinate system of each M point. The two

parameters α and β are given by

$$\alpha_i = (-1)^{i+1} \pi/6$$
 $\beta_i = \arccos(1/3)$ (D.1.5)

where $i \in \{1, 2, 3\}$ labels according to Fig. (6.2a) the position of the M point in the surface Brillouin zone. A representation of the spin operator σ in this basis yields the following matrix elements

$$\langle \Phi_2^- \mid \sigma_x \mid \Phi_2^- \rangle = -\sin\beta\cos\Theta^- \tag{D.1.6}$$

$$\langle \Phi_1^+ \mid \sigma_x \mid \Phi_1^+ \rangle = \sin \beta \cos \Theta^+ \tag{D.1.7}$$

$$\langle \Phi_2^- \mid \sigma_x \mid K\Phi_2^- \rangle = e^{-i\alpha} \cos\beta \cos^2 \frac{\Theta^-}{2}$$
 (D.1.8)

$$\langle \Phi_1^+ \mid \sigma_x \mid K\Phi_1^+ \rangle = e^{-i\alpha} \cos \beta \sin^2 \frac{\Theta^+}{2}$$
 (D.1.9)

$$\langle \Phi_2^- \mid \sigma_y \mid \Phi_2^- \rangle = 0 \tag{D.1.10}$$

$$\langle \Phi_1^+ \mid \sigma_y \mid \Phi_1^+ \rangle = 0 \tag{D.1.11}$$

$$\langle \Phi_2^- \mid \sigma_y \mid K\Phi_2^- \rangle = -ie^{-i\alpha} \cos^2 \frac{\Theta^-}{2}$$
 (D.1.12)

$$\langle \Phi_1^+ \mid \sigma_y \mid K\Phi_1^+ \rangle = -ie^{-i\alpha} \sin^2 \frac{\Theta^+}{2}$$
 (D.1.13)

$$\langle \Phi_2^- \mid \sigma_z \mid \Phi_2^- \rangle = \cos \beta \cos \Theta^- \tag{D.1.14}$$

$$\langle \Phi_1^+ \mid \sigma_z \mid \Phi_1^+ \rangle = -\cos\beta\cos\Theta^+ \tag{D.1.15}$$

$$\langle \Phi_2^- \mid \sigma_z \mid K\Phi_2^- \rangle = e^{-i\alpha} \sin\beta \cos^2 \frac{\Theta^-}{2}$$
 (D.1.16)

$$\langle \Phi_1^+ \mid \sigma_z \mid K\Phi_1^+ \rangle = e^{-i\alpha} \sin\beta \sin^2 \frac{\Theta^+}{2}$$
 (D.1.17)

It should be noted that these formulas can be also used to describe the spin polarization at the Γ point. In this case we have to set $\alpha = \beta = 0$.

The Absolute Value of the Spin

In this Appendix, we prove that the absolute value of the expectation value of the spin operator $\|\langle \Psi \mid \boldsymbol{\sigma} \mid \Psi \rangle\|$ in the topological surface state $|\Psi\rangle$ [Eq. (6.1.18)] is always less than or equal to one. To this end we take the topological surface state $|\Psi\rangle$, in which spin and position space are entangled, and rewrite the wave function as follows

$$|\Psi\rangle = |\chi_1\rangle |\uparrow\rangle + |\chi_2\rangle |\downarrow\rangle \tag{D.2.1}$$

where $|\uparrow\rangle$ ($|\downarrow\rangle$) is the spin up (spin down) wave function and where the position space dependence is hidden in $|\chi_1\rangle$ and $|\chi_2\rangle$. Using this expansion we find the spin polarization

given by

$$\langle \Psi \mid \boldsymbol{\sigma} \mid \Psi \rangle = \begin{pmatrix} 2 \Re \langle \chi_1 \mid \chi_2 \rangle \\ 2 \Im \langle \chi_1 \mid \chi_2 \rangle \\ \langle \chi_1 \mid \chi_1 \rangle - \langle \chi_2 \mid \chi_2 \rangle \end{pmatrix}$$
(D.2.2)

where σ stands for the spin operator. Hence, the absolute value takes the form

$$\|\langle \Psi \mid \boldsymbol{\sigma} \mid \Psi \rangle\|^2 = 4|\langle \chi_1 \mid \chi_2 \rangle|^2 + \left[\langle \chi_1 \mid \chi_1 \rangle - \langle \chi_2 \mid \chi_2 \rangle\right]^2$$
 (D.2.3)

According to the Cauchy-Schwarz inequality the first term on the right hand side of Eq. (D.2.3) can be approximated as $|\langle \chi_1 \mid \chi_2 \rangle|^2 \leq \langle \chi_1 \mid \chi_1 \rangle \langle \chi_2 \mid \chi_2 \rangle$. Finally, we make use of this inequality and conclude:

$$\|\langle \Psi \mid \boldsymbol{\sigma} \mid \Psi \rangle\|^2 \le 1 \tag{D.2.4}$$

Bibliography

- [1] M. Sherafati and S. Satpathy. Phys. Rev. B, 83:165425, 2011.
- [2] M. Sherafati and S. Satpathy. Phys. Rev. B, 84:125416, 2011.
- [3] S. Saremi. Phys. Rev. B, 76:184430, 2007.
- [4] A. M. Black-Schaffer. Phys. Rev. B, 82:073409, 2010.
- [5] A. M. Black-Schaffer. Phys. Rev. B, 81:205416, 2010.
- [6] E. Kogan. Phys. Rev. B, 84:115119, 2011.
- [7] E. Kogan. Phys. Rev. B, 2:8–12, 2013.
- [8] P. R. Wallace. Phys. Rev., 71:622-634, 1947.
- [9] J. W. McClure. Phys. Rev., 104:666–671, 1956.
- [10] G. W. Semenoff. Phys. Rev. Lett., 53:2449-2452, 1984.
- [11] F. D. M. Haldane. Phys. Rev. Lett., 61:2015–2018, 1988.
- [12] R. Peierls. Annales de l'institut Henri Poincaré, 5(3):177–222, 1935.
- [13] L. D. Landau. Phys. Z. Sowjetunion, 11:26–35, 1937.
- [14] A. Fasolino, J. H. Los, and M. I. Katsnelson. *Nature materials*, 6(11):858–861, 2007.
- [15] K. S. Novoselov, A. K. Geim, S. V. Morozov, D. Jiang, Y. Zhang, S. V. Dubonos, I. V. Grigorieva, and A. A. Firsov. Science, 306(5696):666-669, 2004.
- [16] B. Uchoa, C.-Y. Lin, and A. H. Castro Neto. Phys. Rev. B, 77:035420, 2008.
- [17] D. Li, M. B. Müller, S. Gilje, R. B. Kaner, and G. Wallace. *Nature nanotechnology*, 3(2):101–105, 2008.
- [18] Y. Si and E. T. Samulski. Nano Letters, 8(6):1679–1682, 2008.
- [19] C. Lee, X. Wei, J. W. Kysar, and J. Hone. Science, 321(5887):385–388, 2008.
- [20] K. P. Loh, Q. Bao, P. K. Ang, and J. Yang. J. Mater. Chem., 20:2277–2289, 2010.
- [21] K. S. Novoselov, A. K. Geim, S. V. Morozov, D. Jiang, M. I. Katsnelson, I. V. Grigorieva, S. V. Dubonos, and A. A. Firsov. *Nature*, 438(7065):197–200, 2005.
- [22] Y. Zhang, Y.-W. Tan, H. L. Stormer, and P. Kim. Nature, 438(7065):201–204, 2005.

- [23] M. I. Katsnelson, K. S. Novoselov, and A. K. Geim. *Nature physics*, 2(9):620–625, 2006.
- [24] A. F. Young and P. Kim. Nature Physics, 5(3):222–226, 2009.
- [25] K. v. Klitzing, G. Dorda, and M. Pepper. Phys. Rev. Lett., 45:494–497, 1980.
- [26] M. Stone. Quantum Hall Effect. World Scientific, 1992.
- [27] F. Schwierz. Nature nanotechnology, 5(7):487–496, 2010.
- [28] D. Reddy, L. F. Register, G. D. Carpenter, and S. K. Banerjee. Journal of Physics D: Applied Physics, 44(31):313001, 2011.
- [29] B. Zhan, C. Li, J. Yang, G. Jenkins, W. Huang, and X. Dong. Small, 10(20):4042–4065, 2014.
- [30] M. A. Ruderman and C. Kittel. Phys. Rev., 96:99–102, 1954.
- [31] T. Kasuya. Progress of Theoretical Physics, 16(1):45–57, 1956.
- [32] K. Yosida. Phys. Rev., 106:893–898, 1957.
- [33] V. M. Silkin, I. A. Nechaev, E. V. Chulkov, and P. M. Echenique. *Surface Science*, 588(1–3):L239 L245, 2005.
- [34] A. A. Khajetoorians, J. Wiebe, B. Chilian, S. Lounis, S. Blügel, and R. Wiesendanger. *Nature Physics*, 8(6):497–503, 2012.
- [35] M. Sherafati and S. Satpathy. AIP Conference Proceedings, 1461(1):24–33, 2012.
- [36] C. Kittel. Solid State Physics, 22:1 26, 1969.
- [37] B. Fischer and M. W. Klein. Phys. Rev. B, 11:2025–2029, 1975.
- [38] M. T. Béal-Monod. Phys. Rev. B, 36:8835–8836, 1987.
- [39] V. I. Litvinov and V. K. Dugaev. Phys. Rev. B, 58:3584–3585, 1998.
- [40] F. Parhizgar, R. Asgari, S. H. Abedinpour, and M. Zareyan. Phys. Rev. B, 87:125402, 2013.
- [41] H. Lee, J. Kim, E. R. Mucciolo, G. Bouzerar, and S. Kettemann. *Phys. Rev. B*, 85:075420, 2012.
- [42] H. Lee, E. R. Mucciolo, G. Bouzerar, and S. Kettemann. Phys. Rev. B, 86:205427, 2012.
- [43] P. D. Gorman, J. M. Duffy, M. S. Ferreira, and S. R. Power. Phys. Rev. B, 88:085405, 2013.
- [44] J.-C. Charlier, J.-P. Michenaud, and X. Gonze. Phys. Rev. B, 46:4531–4539, 1992.

- [45] J. Nilsson, A. H. Castro Neto, N. M. R. Peres, and F. Guinea. Phys. Rev. B, 73:214418, 2006.
- [46] S. Shallcross, S. Sharma, and O. Pankratov. Phys. Rev. B, 87:245403, 2013.
- [47] J. Nilsson, A. H. Castro Neto, F. Guinea, and N. M. R. Peres. Phys. Rev. B, 78:045405, 2008.
- [48] A. H. Castro Neto, F. Guinea, N. M. R. Peres, K. S. Novoselov, and A. K. Geim. Rev. Mod. Phys., 81:109–162, 2009.
- [49] E. V. Castro, K. S. Novoselov, S. V. Morozov, N. M. R. Peres, J. M. B. Lopes dos Santos, J. Nilsson, F. Guinea, A. K. Geim, and A. H. Castro Neto. *Phys. Rev. Lett.*, 99:216802, 2007.
- [50] H. Min, B. Sahu, S. K. Banerjee, and A. H. MacDonald. Phys. Rev. B, 75:155115, 2007
- [51] Y. Zhang, T.-T. Tang, C. Girit, Z. Hao, M. C. Martin, A. Zettl, M. F. Crommie, Y. R. Shen, and F. Wang. *Nature*, 459(7248):820–823, 2009.
- [52] L. Jiang, X. Lü, W. Gao, G. Yu, Z. Liu, and Y. Zheng. Journal of Physics: Condensed Matter, 24(20):206003, 2012.
- [53] E. H. Hwang and S. Das Sarma. Phys. Rev. Lett., 101:156802, 2008.
- [54] F. Parhizgar, M. Sherafati, R. Asgari, and S. Satpathy. Phys. Rev. B, 87:165429, 2013.
- [55] S. Tanabe, Y. Sekine, H. Kageshima, M. Nagase, and H. Hibino. *Phys. Rev. B*, 84:115458, 2011.
- [56] N. Ray, S. Shallcross, S. Hensel, and O. Pankratov. Phys. Rev. B, 86:125426, 2012.
- [57] C. L. Kane and E. J. Mele. Phys. Rev. Lett., 95:146802, 2005.
- [58] B. A. Bernevig, T. L. Hughes, and S.-C. Zhang. Science, 314(5806):1757–1761, 2006.
- [59] L. Fu, C. L. Kane, and E. J. Mele. Phys. Rev. Lett., 98:106803, 2007.
- [60] L. Fu and C. L. Kane. Phys. Rev. B, 76:045302, 2007.
- [61] J. C. Y. Teo, L. Fu, and C. L. Kane. Phys. Rev. B, 78:045426, 2008.
- [62] L. Fu. Phys. Rev. Lett., 106:106802, 2011.
- [63] T. H. Hsieh, J. Liu, W. Duan, H. Lin, A. Bansil, and L. Fu. Nat Commun, 3, 2012.
- [64] Y. Tanaka, Z. Ren, T. Sato, K. Nakayama, S. Souma, T. Takahashi, K. Segawa, and Y. Ando. Nat Phys, 8:800–803, 2012.
- [65] Y. Xia, D. Qian, D. Hsieh, L. Wray, A. Pal, H. Lin, A. Bansil, D. Grauer, Y. S. Hor, R. J. Cava, and M. Z. Hasan. Nat Phys, 5:398–402, 2009.

- [66] Z.-H. Pan, E. Vescovo, A. V. Fedorov, D. Gardner, Y. S. Lee, S. Chu, G. D. Gu, and T. Valla. Phys. Rev. Lett., 106:257004, 2011.
- [67] S. Souma, K. Kosaka, T. Sato, M. Komatsu, A. Takayama, T. Takahashi, M. Kriener, Kouji Segawa, and Yoichi Ando. Phys. Rev. Lett., 106:216803, 2011.
- [68] S. R. Park, J. Han, C. Kim, Y. Y. Koh, C. Kim, H. Lee, H. J. Choi, J. H. Han, K. D. Lee, N. J. Hur, M. Arita, K. Shimada, H. Namatame, and M. Taniguchi. *Phys. Rev. Lett.*, 108:046805, 2012.
- [69] Z. Xie, S. He, C. Chen, Y. Feng, H. Yi, A. Liang, L. Zhao, D. Mou, J. He, Y. Peng, X. Liu, Y. Liu, G. Liu, X. Dong, L. Yu, J. Zhang, S. Zhang, Z. Wang, F. Zhang, F. Yang, Q. Peng, X. Wang, C. Chen, Z. Xu, and X. J. Zhou. Nat Commun, 5, 2014.
- [70] F. Vidal, M. Eddrief, B. Rache Salles, I. Vobornik, E. Velez-Fort, G. Panaccione, and M. Marangolo. Phys. Rev. B, 88:241410, 2013.
- [71] S. Basak, H. Lin, L. A. Wray, S.-Y. Xu, L. Fu, M. Z. Hasan, and A. Bansil. Phys. Rev. B, 84:121401, 2011.
- [72] J. Henk, A. Ernst, S. V. Eremeev, E. V. Chulkov, I. V. Maznichenko, and I. Mertig. Phys. Rev. Lett., 108:206801, 2012.
- [73] B. A. Volkov and O. A. Pankratov. *JETP*, 48:687, 1978.
- [74] B. A. Volkov, O. A. Pankratov, and A. V. Sazonov. JETP, 58:809, 1983.
- [75] B. A. Volkov and O. A. Pankratov. JETP Letters, 42:178, 1985.
- [76] O. A. Pankratov, S. V. Pakhomov, and B. A. Volkov. *Solid State Communications*, 61(2):93 96, 1987.
- [77] Y. Tanaka, T. Sato, K. Nakayama, S. Souma, T. Takahashi, Z. Ren, M. Novak, K. Segawa, and Y. Ando. Phys. Rev. B, 87:155105, 2013.
- [78] C. Yan, J. Liu, Y. Zang, J. Wang, Z. Wang, P. Wang, Z.-D. Zhang, L. Wang, X. Ma, S. Ji, K. He, L. Fu, W. Duan, Q.-K. Xue, and X. Chen. *Phys. Rev. Lett.*, 112:186801, 2014.
- [79] Y. Tanaka, T. Shoman, K. Nakayama, S. Souma, T. Sato, T. Takahashi, M. Novak, Kouji Segawa, and Yoichi Ando. Phys. Rev. B, 88:235126, 2013.
- [80] J. Liu, W. Duan, and L. Fu. Phys. Rev. B, 88:241303, 2013.
- [81] F. Zhang, C. L. Kane, and E. J. Mele. *Phys. Rev. B*, 86:081303, 2012.
- [82] Y. Shi, M. Wu, F. Zhang, and J. Feng. Phys. Rev. B, 90:235114, 2014.
- [83] J. Liu, T. H. Hsieh, P. Wei, W. Duan, J. Moodera, and L. Fu. *Nature materials*, 13(2):178–183, 2014.
- [84] O. A. Pankratov and B. A. Volkov. Sov. Sci. Rev. A. Phys., 9:355–459, 1987.

- [85] J.-J. Zhu, D.-X. Yao, S.-C. Zhang, and K. Chang. Phys. Rev. Lett., 106:097201.
- [86] D. K. Efimkin and V. Galitski. Phys. Rev. B, 89:115431, 2014.
- [87] Q. Liu, C.-X. Liu, C. Xu, X.-L. Qi, and S.-C. Zhang. Phys. Rev. Lett., 102:156603, 2009.
- [88] Z. L. Li, J. H. Yang, G. H. Chen, M.-H. Whangbo, H. J. Xiang, and X. G. Gong. Phys. Rev. B, 85:054426, 2012.
- [89] C. Bena. Phys. Rev. Lett., 100:076601, Feb 2008.
- [90] C. L. Lu, C. P. Chang, Y. C. Huang, J. H. Ho, C. C. Hwang, and M. F. Lin. *Journal of the Physical Society of Japan*, 76(2):024701, 2007.
- [91] Z. F. Wang, Q. Li, H. Su, X. Wang, Q. W. Shi, J. Chen, J. Yang, and J. G. Hou. Phys. Rev. B, 75:085424, 2007.
- [92] A.V. Rozhkov, A.O. Sboychakov, A.L. Rakhmanov, and Franco Nori. *Physics Reports*, 648:1 104, 2016.
- [93] J. Nilsson, A. H. Castro Neto, F. Guinea, and N. M. R. Peres. Phys. Rev. B, 76:165416, 2007.
- [94] E. V. Castro, K. S. Novoselov, S. V. Morozov, N. M. R. Peres, J. M. B. Lopes dos Santos, J. Nilsson, F. Guinea, A. K. Geim, and A. H. Castro Neto. *Journal of Physics:* Condensed Matter, 22(17):175503, 2010.
- [95] O. A. Pankratov. Semiconductor Science and Technology, 5(3S):S204, 1990.
- [96] E. Witten. Nuclear Physics B, 188(3):513 554, 1981.
- [97] A. A. Taskin, F. Yang, S. Sasaki, K. Segawa, and Y. Ando. Phys. Rev. B, 89:121302, 2014.
- [98] Y. J. Wang, W.-F. Tsai, H. Lin, S.-Y. Xu, M. Neupane, M. Z. Hasan, and A. Bansil. Phys. Rev. B, 87:235317, 2013.
- [99] S. Shallcross. Private Communication, 2017.
- [100] S. Safaei, P. Kacman, and R. Buczko. Phys. Rev. B, 88:045305, 2013.
- [101] M. Abramowitz and I. A. Stegun. *Handbook of Mathematical Functions*. Dover Publications, 1964.